Experimental and Finite Element Analysis of Residual Stress in Electroslag Butt Welds

Luoyang Institute of Science and Technology (B.S.)1989
Luoyang Institute of Science and Technology (M.S.)1992

Leilei Zhang

A dissertation submitted to the faculty of the
Oregon Graduate Institute of Science and Technology
in partial fulfillment of the
requirements for the degree
Doctor of Philosophy
in
Materials Science and Engineering

June 1999

The dissertation "Experimental and Finite Element Analysis of Residual Stress in Electroslag Butt Welds" by Leilei Zhang has been examined and approved by the following Examination Committee:

David G. Atteridge, Thesis Advisor
Professor

Martin Becker
Professor

Jack Devletian
Professor

Lemmy Meekisho
Associate Professor

ACKNOWLEDGEMENT

I would like to express my deep appreciation to Dr. David G. Atteridge for his encouragement, invaluable guidance and support during the course of this research work.

Special thanks are due to Dr. Martin Becker, Dr. Jack Devletian and Dr. Lemmy Meekisho for their guidance, time and effort in reviewing the dissertation.

I would also like to express my gratitude to all of the students, staff, and faculty in the Materials Science and Engineering Department.

Funding for this research was provided by Oregon Department of Transportation (ODOT). I am very grateful to Mr. Steve Lovejoy, Mr. Martin Layer and all of the other peoples in this project for their help.

Finally, and certainly not least, I would like to thank my parents for their patience, encouragement and support through my college life. I could not have come to this stage without their love and support.

TABLE OF CONTENTS

LIST OF TABLES

LIST OF FIGURES

ABSTRACT

The electroslag welding (ESW) process is an attractive operation for welding thick plates. However, low fracture toughness and the difficulty to detect weld defects are the main reasons for the ESW process not being used more extensively.

Electroslag (ES) weldments differ substantially from structural multipass arc-welded butt joints in that only a single pass and very high heat input is used. These differences are expected to have a major effect on the resultant residual stress pattern that in turn could affect the fatigue performance and propensity to cracking. To date, several thermal analysis have been completed using numerical analysis methods with only one residual stress measurement completed. Systematic analysis on the ESW processes is necessary to understand both thermal history and residual stress distribution of the ESW weldments.

Welding parameter data of the West Linn bridge on I-205 were not available. This necessitated the use of ESW cycle parameters and boundary conditions based on prior ESW research experience from work done at the Oregon Graduate Institute and open literatures, in addition to experimental determination of fusion zone characteristics for the West Linn Bridge ES weldments. Two-dimensional (2D) and three-dimensional (3D) models were developed using finite element methods (FEM) to simulate the ESW process and to analyze the effect of operating conditions on residual stress distribution. FEM uses both moving coordinate system (MCS) and fixed coordinate system (FCS). This study results reveal that 2D modeling gives incorrect residual stress predication and MCS is over 100 times efficient than FCS. MCS was used in 3D model. It predicts compressive stresses in the direction perpendicular to the welding direction and tensile stresses in the direction parallel to the welding direction in and around the fusion/HAZ zones. Both coring and sectioning techniques were used to measure residual stresses

inside the ESW weldments. Experimental results were found to be consistent with modeling results. This part of study is very useful in directing the future application of ESW process. At the same time, this study provides an initial attempt to evaluate residual stresses existing in ESW weldments.

CHAPTER 1
INTRODUCTION

Electroslag welding (ESW) was developed by Paton and his coworkers in the Paton Electric Welding Institute, USSR, in the early 1950's.[1] After that, research units in various countries, such as the U.S. Steel Corporation,[2] the British Welding Institute,[3] and the Oregon Graduate Institute of Science and Technology (OGI),[4] have performed further research on the ES butt welding processes.

There are two types of ESW, namely consumable and non-consumable ESW.[5] The type of ESW of interest with respect to this study is consumable guide electrode welding system, sketched in Figure 1-1. The consumable wire electrode guide (or in some cases, a plate electrode guide) is consumed as the process progresses. The actual wire electrode material feeds down the guide, is fed continuously into and melted in a molten slag pool which is resistively heated by the current that passes from the electrode wire/guide, through the molten slag and the metal pool below the slag pool, to the base plates. Two water-cooled copper "shoes" provide a mold through which a major portion of the thermal energy is removed from the system. The shoes assure that the molten metal and slag remain contained between the plate edges being welded.

The process is initiated by an electric arc between the electrode and the bottom of the joint. Powder flux is then added and melted by the heat of the arc. Once a layer of molten slag is established (1.5 to 2 inches (0.038 to 0.051 m)), the arc stops and welding current passes from the electrode through the slag by electrical conduction. At the start, the guide tube is positioned with its tip above the weld pool. During the processes, the guide tube is consumed into the weld pool. This method involves no moving parts except the welding electrode. The other type of ESW is conventional ESW which uses a non-consumable contact tube to direct the electrode into the molten slag

pool, as shown in Figure 1-2. The contact tube is maintained at about 2 inches (0.051 m) above the slag pool surface. The entire welding head along with cooling shoes is moved upward at a predetermined rate consistent with welding speed.

Electroslag welding process is performed in the vertical or the near vertical welding position. The welding technique utilizes a starting sump and a runoff block to eliminate defects associated with the initiation and the termination of the process, as shown in Figure 1-3. This practice also results in the weld being in quasi-steady state once the weld reaches the bottom of the plates to be welded and allows the weld to remain in quasi-equilibrium clear to the top of the plate to be welded.

The ESW process is an attractive operation for the welding of thick plates that include construction of ships, storage tanks, pressure vessels, bridges, buildings and other heavy structures. Sections that are several inches thickness can be welded in a single pass by selecting a suitable number of electrodes and/or electrode oscillation. The sections being welded do not need any edge preparation besides cutting because ESW exhibits a bigger weld pool size, higher heat input and a slower welding speed when compared with other welding methods. Preheating is generally not needed and, at the same time, distortion is minimum compared with other welding processes. If properly controlled, the slag/metal reaction involved in the ESW process results in sound, "defect-free" welds, as well as refinement of the chemical composition of the weld metal as molten metal drops pass through the molten slag.

However, low fracture toughness and the difficulty to detect weld defects are the main reasons for the ESW process not being used more extensively for welding thick plates in tensile applications. The large heat input associated with the process results in a coarse cast structure and extended large heat affected zone (HAZ) grains. The cast structure has anisotropic mechanical properties. The grain orientation and segregation can lead to hot cracking near the weld center line (WCL). The high heat input produces a coarse-grained HAZ that is more susceptible to brittle fracture than the parent material. Bridges fabricated using ESW have had a history of undetected fabrication defects and low weld metal and HAZ toughness.[6]

According to fracture mechanics, once a critical size flaw or crack is formed, the

structure is susceptible to catastrophic failure. When this critical size is reached, the crack propagates in a brittle fashion, which can lead to sudden catastrophic failure. Determination of whether a structure is safe or not is based mainly on the size of existing flaws or cracks (defects) relative to this critical size. Thus the ability to correctly evaluate the critical size is very important. Fracture toughness calculations are used to evaluate a weld-specific critical crack size. The larger this critical size, the easier and more reliable the possibility of detecting pre-critical-crack-size flaws becomes. A major factor in the determination of a weld-related critical crack size is the residual stress state related to the weldment. The residual stress field needs to be added to the expected structure/use induced load when calculating critical crack size.

It is generally assumed that the weld-induced stress field in, and close to, the fusion zone is tensile and of yield strength magnitude even though the stress field in a welded connection is both intense and complex. This assumption greatly reduces the allowable flaw size, especially when compared to the allowable flaw size when design stresses are considered alone. ES welded structures using standard welding techniques and filler metal tend to have poor fracture toughness, especially at the WCL and HAZ interface. Thus the calculated critical size for ESW, based on yield stress magnitude of residual stress, may well be expected to be smaller than that which can be reliably detected by standard non-destructive testing techniques. Thus the need for determining and/or estimating "exact" residual stresses associated with ESW.

In general, the total stress state at the tip of a crack or crack-like defect is one of the most important factors influencing the mechanisms of fatigue, brittle fracture, or stress corrosion cracking (SCC). In all of these failure mechanisms, the residual stress in the weldment can make a major contribution to the stress field at a crack tip.

Oregon has two steel bridges that were fabricated using ESW. One is the West Linn Bridge on I-205. The other is the approach structure to the Fremont Bridge on I-405. Because ES butt welded bridges have exhibited a low fracture toughness and conventional inspection of ES weldments under shop fabrication condition has historically failed to consistently detect and/or correctly size weld discontinuities, Federal Highway Administration (FHWA) banned ESW on "fracture critical" members of steel bridges in

1977 (a fracture critical member is a member of a structure that, if it were to fail, would be expected to produce a catastrophic failure on the given structure).

The FHWA has recommended that Oregon Department of Transportation (ODOT) either mount an intensive investigation oriented towards determination of critical flaw size associated with ESW on the bridges to "prove" the bridges are safe, or bolt splice the ESW flange welds located in the tensile portion of the spans. The bolt option for the West Linn Bridge alone is estimated to be between four to eight million dollars. Because of this high cost, an intensive effort is currently underway to evaluate the ESW welds on the West Linn Bridge and, in the future, evaluate the Fremont approach structure. At the same time, this research seeks to understand the residual stress development in A36 steel thick plates welded by ESW with an emphasis on the following:

(1) Assessment of welding parameters based on bridge core specimens.
(2) Assessment of residual stress state through evaluation of cored and sliced sections.
(3) Development and validation of 2D thermal and residual stress models.
(4) Development and validation of 3D thermal and residual stress models.

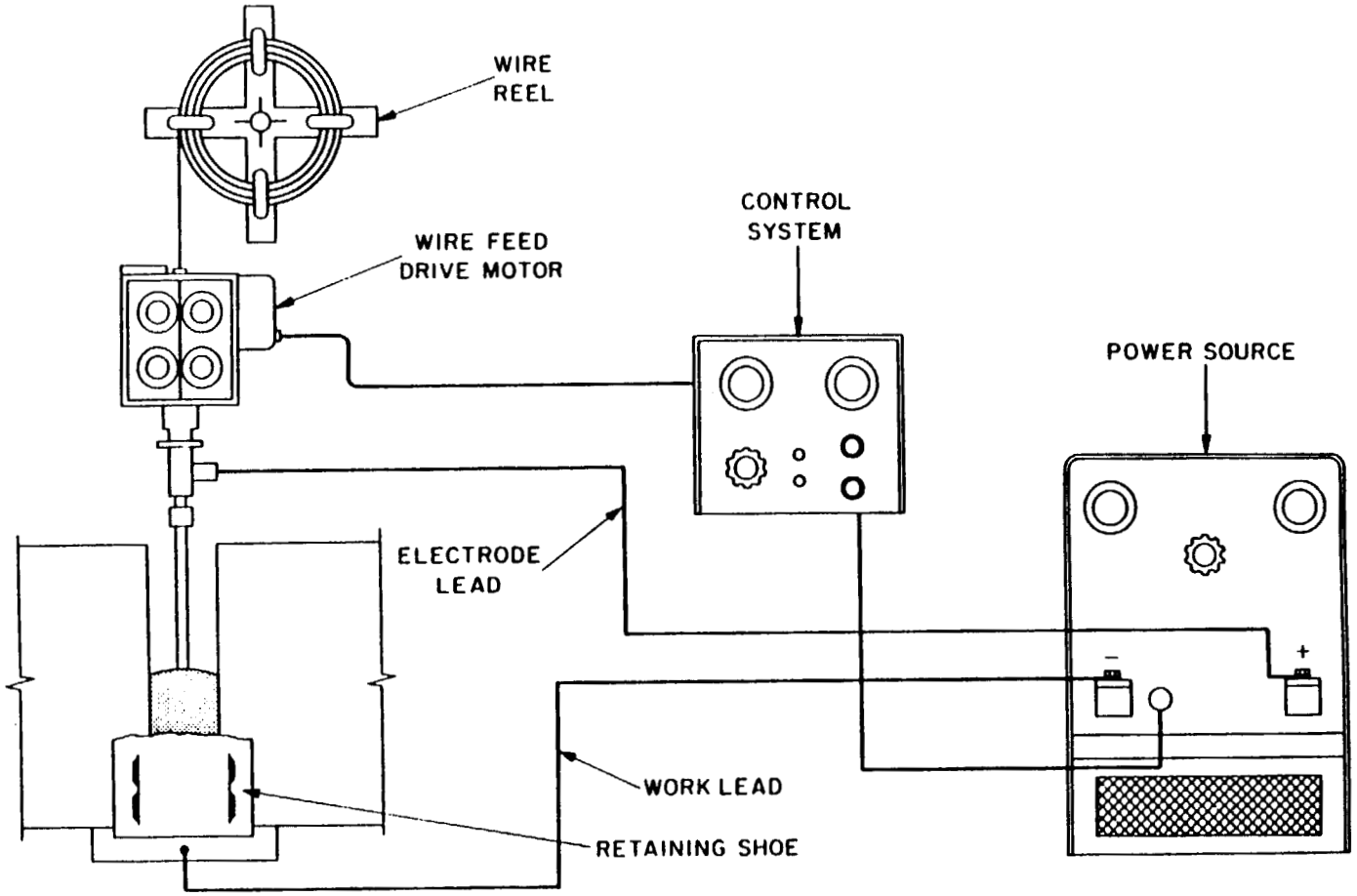

Figure 1-1 Physical Situation of Consumable Guide Electroslag Welding Process[5]

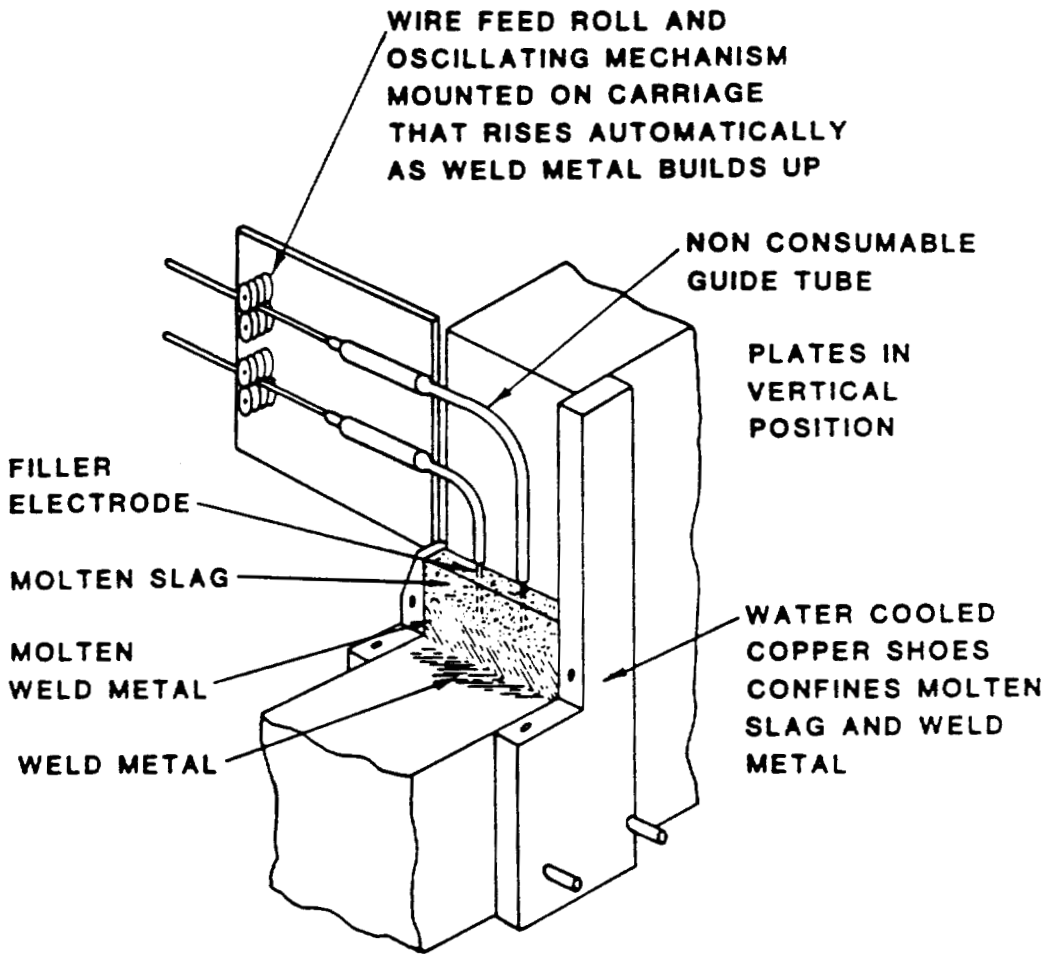

Figure 1-2 Schematic Representation of Conventional Electroslag Welding Process (Non-Consumable Guide)[5]

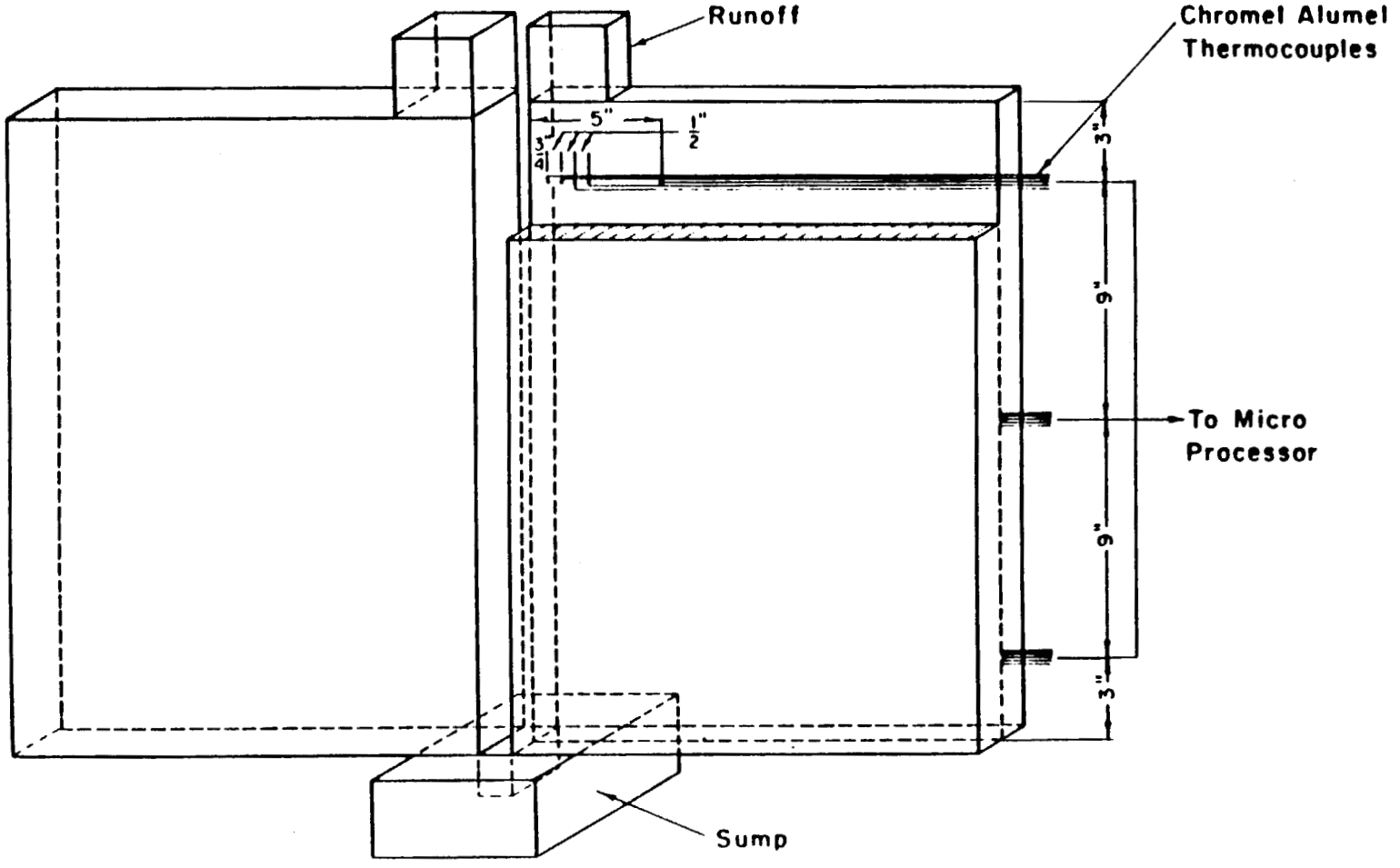

Figure 1-3 Schematic Representation of Electroslag Weld Plate with Sump and Runoff[5]

CHAPTER 2
BACKGROUND

2.1 RESIDUAL STRESS

PRINCIPAL OF RESIDUAL STRESS

Residual stresses are usually defined as the self-equilibration internal stresses existing in a free body with no external loads (mechanical, thermal or chemical) and restraints. They are also called internal stresses, initial stresses, locked-in stresses, and inherent stresses[7-9] and are formed when portions of a member undergo nonuniform permanent dimensional change. The permanent dimensional change usually occurs as plastic deformation. However, localized expansion or contraction of the metal lattice also can cause dimensional change with nitrating, carburizing, or phase transformation. Plastic deformation may be caused by large temperature gradients that can be produced by welding, quenching, or rapid heating. Residual stresses are usually detrimental but also may be beneficial especially for surface compressive stresses in components prone to fatigue failure or stress corrosion cracking. Also, stresses in the opposite direction to static load stresses may in effect increase the allowable design stress.[10]

CLASSIFICATION OF RESIDUAL STRESSES

Residual stresses can be commonly classified into two groups.

(1) Macroresidual stresses, or residual stresses of the first kind. Macroresidual stresses are those residual stresses that have an engineering nature and can be measured over a gauge length that encompasses several grains.

(2) Microresidual stresses are those stresses set by microstructural inhomogeneities. They can either be confined within a single grain or a particular set of grains of the same preferred orientation.

RESIDUAL STRESS IN WELDMENTS

Residual stresses in weldments are caused by uneven heating and cooling and also uneven distribution of nonelastic strains. Three sources of welding residual stresses are usually identified.[11-13]

1) Difference in shrinkage.

The weld metal, originally subjected to the highest temperature, tends upon cooling to contract more than all other areas. This is hindered by the other parts of the joint, thus resulting in the formation of high stresses perpendicular to welding direction in the weld metal. Similar tensile residual stresses develop in the direction parallel to welding but the magnitude is quite a bit smaller in magnitude.

2) Uneven cooling in the thickness direction of the weld.

The surface layers cool more rapidly than the interior ones, especially in thick plates. This gives rise to thermal stresses which can lead to nonuniform plastic deformation and thus to residual stresses, compressive at the surface and tensile in the interior.

3) Phase transformations.

Oregon Graduate Institute of Science and Technology (OGI) has made extensive studies of different welding processes including ESW.[14-35] The residual stress of "low" heat input weldments has been estimated. In general, the thin multi-pass butt welds have tensile residual stresses that are of the yield stress level through the thickness. For the thick section of multi-pass weldments, the residual stresses usually change from tension at the surface to compression in the middle. For the multi-pass thick plate V-grove welds, the mid-thickness region stress field is compressive stress that is of yield stress magnitude.[36-37]

Much less is known about the residual stress distribution of ESW weldments.

ESW is a single pass thick-section welding technique with much higher weld heat inputs than used in multi-pass welds. So ESW has a much wider melt zone and much slower cooling rates than standard multi-pass welding techniques. Thus the ESW residual stress fields would be expected to be lower in magnitude with shallower stress gradients than conventional multi-pass weldments. Therefore, there is a potential of larger allowable flaw sizes than can be predicated by simply assuming yield strength level residual stresses in the complete fusion zone and near fusion zone-HAZ. In fact, if some region of the weldments is in compression, flaws in compression will not propagate. Even if the stress field is found to be tensile in nature, but less than yield strength magnitude, accurate estimates of critical flaw size can be made which would be expected to greatly increase the expected critical flaw size.

MEASUREMENT OF RESIDUAL STRESS

Many techniques have been developed to measure the residual stress. They will be classified into two types: Destructive (or semi-destructive) measuring methods and Non-destructive measuring methods. During measuring, residual stress is treated as macrostresses contained within a metallic component or specimen. These stresses might be represented as a statistical average of stresses across a particular finite length in a component. Because destructive measuring methods were used in this study, emphasis was put on destructive measuring methods in this review.

Destructive measuring methods involve some degree of destruction. Most experimental techniques have been based on monitoring displacement over a defined gauge length, while physically relieving the residual stresses around the gauge by saw cutting, slicing, drilling or trepanning. They can be used to measure through thickness stress distributions, as well as surface stresses.

There are several destructive measuring methods that are based on stress-relaxation techniques[38-44] using mechanical methods to measure the macroscopic (long range) stress.

Sectioning, hole drilling and indentation with measurement of dimensional changes are examples of destructive residual stress measuring methods. During measuring, strain

gauges,[45] photoelastic coating, or brittle lacquer coatings are usually used to sense the resulting deformation. Hooke's Law is used to calculate the stress from the measured strains.

Many attempts have been made to measure residual stress. Rosenthal and Norton[46] proposed a method involving the removal and systematic destruction of blocks of steel. Although this method has been used by some laboratories, the Welding Institute's experience which this method has indicated several practical and theoretical limitations.

Ferrill et al[47] developed a method which was repeated by Bush and Kromer.[48] The method involves burying a multitude of strain gauges in a 279 mm thick weldment by bonding them to thin 6.4 mm diameter tubes into deep 6.4 mm diameter holes. Relaxation was obtained by removing long 25 mm square parallelepipeds containing the gauges. Sensible and consistent distributions were obtained, although, because of the large amount of damage caused by the hole drilling and the relatively large final section size, the absolute values obtained must remain questionable.

Vinokurov and Gazaryan[49] have outlined a procedure for the determination of residual stresses in thick weldments by inserting a strain gauged plug into specially prepared blind holes. The plug is in fact a hollow bolt with strain gauges fixed along its axis that is screwed into the hole to a predetermined tension. The plug is then removed by cutting a 40 mm square block out of the plate. The technique still has some problems.

These different experimental methods for measuring residual stresses are valuable engineering tools that can be used to establish a technical understanding of residual stress gradients and their magnitudes but all have measurement and/or interpretation problems. The most common and representative destructive technique is the "sectioning method" in which strain gauge rosettes are located at axial and circumferential locations. When the layers are removed from the sample, one could get the variation of residual stresses through the thickness.[38] This method is applicable to non-axisymmetric as well as axisymmetric residual stress distributions. A variation of this technique was used in this study.

Treuting and Reed[50] derived and documented a general method of layer removal

that is applicable to homogeneous elastic materials. This method has been successfully used to measure the residual stress alternations via cold rolling and stretching of an Aluminum alloy by W.E. Nickola.[51]

The hole drilling method that was proposed by Mathar, J in 1934[52] is always referred to as semi-destructive residual stress measuring method. Hole drilling method is based on the measurement of the change of surface strain caused by stresses relieved by machining a shallow hole in the test piece. Bonded electrical resistance strain gauges rosettes were used to measure the strain change. It is the most widely used modern technique for measuring residual stress. The measuring procedure has been standardized in ASTM Standard Test Method E837-85. The hole size typically ranges from 1.5 to 3.0 mm (1/16 to 1/8 in.) in both diameter and depth. In most practical applications of the method, the drilled hole is blind with a depth that is about equal to its diameter and small compared to the thickness of the test object. Most applications have been done on flat plate or cylindrically round parts.[53-55]

Figure 2-1 gives the design of a typical strain gauge rosette. The equations for calculating the principal residual stresses from the strain change readings provided by the change in the three strain gauges were was following:

$$\sigma_{max}=\frac{\varepsilon_a+\varepsilon_c}{4A}-\frac{\sqrt{2[(\varepsilon_a-\varepsilon_b)^2+(\varepsilon_b-\varepsilon_c)^2]}}{4B} \tag{2-1a}$$

$$\sigma_{min}=\frac{\varepsilon_a+\varepsilon_c}{4A}+\frac{\sqrt{2[(\varepsilon_a-\varepsilon_b)^2+(\varepsilon_b-\varepsilon_c)^2]}}{4B} \tag{2-1b}$$

$$\theta=\frac{1}{2}\arctan[\frac{2\varepsilon_b-(\varepsilon_a+\varepsilon_b)}{(\varepsilon_a-\varepsilon_c)}] \tag{2-1c}$$

$$A=-\frac{1+\nu}{2E}\frac{1}{r^2} \tag{2-1d}$$

$$B = -\frac{1+\nu}{2E}\left(\frac{4}{(1+\nu)r^2} - \frac{3}{r^4}\right) \qquad (2\text{-}1e)$$

where,

σ_{max}	=	Maximum principle stress.
σ_{min}	=	Minimum principle stress.
θ	=	Angle from which σ_{max} deviates from the ε_c direction.
E	=	Young's Modulus.
ν	=	Poisson's Ratio.
R	=	Distance from the center of the hole to a circle passing through the center of the three strain gauges.
R_0	=	Radius of the hole.
r	=	R/R_0.
ε_a, ε_b, ε_c	=	Strain gauge readings.

The most commonly used non-destructive measuring methods are: X-Ray Diffraction (XRD),[56-61] Neutron Diffraction,[62-68] Ultrasonic Methods,[69-73] and Electromagnetic Methods.[74-77]

2.2 COMPUTATIONAL MODEL

Beginning in the 1930's, researchers have tried to give a mathematical representation of the welding process. The work consists of two parts: heat flow analysis and thermal stress analysis. Both analytical models and numerical models have been used to predict temperatures and thermal stresses during welding processing.

HEAT FLOW ANALYSIS

The critical first step for accurate analyses of the welding process is to get the temperature profile T (x, y, z, t) at a point of interest (x, y, z) and at any instant of time

t. The governing equation of heat conduction analysis is based on the principle of energy conservation as following:

$$\frac{\partial}{\partial x}(K_x\frac{\partial T}{\partial x})+\frac{\partial}{\partial y}(K_y\frac{\partial T}{\partial y})+\frac{\partial}{\partial z}(K_z\frac{\partial T}{\partial z})+Q=\rho C\frac{\partial T}{\partial t} \qquad (2\text{-}2)$$

where,

Q	=	Heat from heat source or heat sink (w/m^3).
K_x, K_y, K_z	=	Thermal conductivities along x, y, z axes respectively (w/m^oC).
ρ	=	Density of Material (kg/m^3).
C	=	Mass specific heat (J/kg °C).

Equation (2-2) is the fundamental principle for analysis of heat flow. In order to compute the temperature profile of the domain, besides the governing equation, boundary and initial conditions must be defined.

There are three kinds of boundary conditions of the continuum domain:

1) Type I boundary condition (Dirichlet boundary condition or essential boundary condition)

   This kind of boundary condition prescribes the temperature values at the boundary S_I, i.e., $T(x, y, z) = T_s(x, y, z)$.

2) Type II boundary condition (Cauchy boundary condition or natural boundary condition)

   This kind of boundary condition prescribes the heat flux, convection and radiation at the outward surface S_{II} of the domain.

$$K_n\frac{\partial T_s}{\partial n}+h_c(T_s-T_A)+q+\sigma\epsilon(T_s^4-T_A^4)=0 \qquad (2\text{-}3)$$

where,

K_n	=	Thermal conductivity normal to the surface ($w/m\,^oC$).
h_c	=	Film coefficient for convectional heat transfer at the boundary.
T_s	=	Surface temperature.

T_A = Ambient temperature.

q = Prescribed heat flux at the boundary.

σ = Stefan-Boltzmann constant for radiative heat transfer.

ε = Emissity.

3) Adiabatic boundary conditions on insulated surfaces.

The initial condition must be specified for a transient analysis. In general one prescribes a temperature to all points in the domain, i.e., $T(x, y, z, 0) = T_0(x, y, z)$.

ANALYTICAL HEAT TRANSFER MODELS

Heat transfer and the temperature distribution during welding are complex. A closed form solution for practical welding is essentially impossible to obtained. In order to obtain analytical solutions,[78] the welding process is usually simplified with the following assumption:

1) The material is solid at all times and at all temperatures.
2) The material is isotropic and homogeneous without phase changes.
3) The thermal conductivity, density, and specific heat are constant, i.e., independent of temperature.
4) There are no heat losses at the boundary, i.e., the piece is insulated.
5) The piece is infinite except in the directions specifically noted.
6) Welding conditions analyzed remain steady with time, i.e. it is representation of being in the middle of a long weld where heat input, travel speeds, etc. are constant.
6) The heat source is assumed at a zero-volume point, line, or area.
7) There is no Joule ($I^2 R$) heating.

Two different sets of coordinates can be used for the weld modeling. One set is stationary with respect to the earth. The other coordinate set is stationary with respect to the heat source. Rosenthal[79-80] is the first one to give a closed form solution for heat flow analysis. He argued that, in the second coordinate system, the temperature profile

around the observer does not change after the initial period of welding. This phenomenon is called quasi-steady state condition. The analytical solution to the transient problem has been solved in the quasi-steady state condition by Rosenthal. Rosenthal gave the temperature at a point lying a distance from the weld line as a function of time, for a given energy input. Goldenberg[81] worked out a solution for spot welding (stationary line source in the middle of a large, thin plate), although, his solution is for the heating part of the cycle only. Tanaka[82] solved the welding heat flow equation without neglecting surface heat transfer. Naka and Masubuchi,[83,84] Masubuchi and Kusuda[85] also assumed line and point heat sources for two-dimensional and three-dimensional analytical solutions. They presented the solutions for the temperature distribution of welded plates under a transient state. Reference [78] gives a summary of the analytical solution.

These analytical solutions only emphasize some of the important parameters. The solutions are economic and could be used directly. All of the models provide limited accuracy because they are too idealized to be used in practice. Nippes et al.[86,87] found large discrepancies between Rosenthal's equation and experimental results for cooling rates in the weld HAZ. The error became significant in the vicinity of the idealized point heat source.

NUMERICAL SIMULATION MODELS

In many situations, the governing equations may be readily derived but their solutions by closed form methods may be difficult or impossible. With the advancement of computer technology, numerical simulation developed quickly. It could in principle permit nearly any complexity to be taken into account, however, economic requirements set a limit in practical terms.[88] Three main numerical methods have been developed. Both heat source model and kinematic model have been applied to welding process simulation. They are reviewed in the following sections with nonlinear material properties and heat losses being discussed.

Numerical Methods

Finite difference, finite element and boundary element analyses are the three strong candidates of numerical analysis. The boundary element method is not well developed for nonlinear analysis. During mid-1960's to mid-1970's, finite element and finite difference methods were competing with each other. The finite difference method[89] is quite simple in concept, i.e., derivations in the equation are replaced by using a finite difference approximation. However, inaccuracy of the derivative can render this modeling inappropriate for weld modeling. Also difficulty of imposing boundary condition on curved boundary with complex geometries and difficulty with non-uniform grids hinder the use of this technique. Thus most recent weld modeling work, as well as the work reported herein, uses the finite element method.

Model of Welding Process

Normally, heat source model and kinematic model are used to simulate the welding process.

Heat Source Model

In analytic models, the heat source is assumed to be a point or line. These models neglect the spatial distribution of the arc energy and typically ignore the temperature dependence of material properties. The great advantage of numerical modeling is that it allows distribution of the heat source. The simplest function is a constant distribution. The next simplest is a Gaussian distribution function. The simplest shape is a circle in 2D model or a sphere in 3D model. A more complex shape of energy distribution in the arc is an ellipse or double ellipse in 2D model or ellipsoids or double ellipsoids in 3D model.

In 1973, Bonacina et al.[90,91] developed a finite difference model to solve non-linear heat conduction problems. Westby[92] was probably the first one to compute the

temperature distribution in welds using finite difference method. He assumed the weld energy distributed throughout the molten zone with a constant power density. Pavelic et al[93] also used finite difference method to compute temperature histories in gas tungsten arc welding of thin plates and compared them with experimental data. The heat source was treated as a flux disc with Gaussian distribution. Provision was also made for inclusion of convective and radiative losses from the heat plate to the surroundings as well as variable properties of the metal. Much better agreement was obtained between experimental measurements and numerical computations than analytical models. In 1974, Parley and Hibbert[94] added several capabilities to Westby's finite difference model. They analyzed non-rectangular cross sections such as single and double V and U grooves in welding practice with non-uniform mesh. The welding heat source was simulated by designating one or more elements as heated elements with Gaussian distribution of heat flux. The model included temperature dependent material properties but did not incorporate the heat loss from boundaries.[95]

In 1974, Comini et al[96] successfully included nonlinear material properties and latent heat effects in their finite element model. Latent heat effect was incorporated as variation in heat capacity. Kohler et al.[97] reported a better stability of the solution for transient temperature field problems with finite element discretization of time. A comparison in terms of accuracy, stability and computational cost of different numerical schemes for the finite element and finite difference methods in 2D heat conduction problems was done by Thomas el al.[98]

Prescribed temperature boundary conditions and natural boundary conditions are used to solve the energy equation. In general, greatest success has been achieved by constraining the heat input to the region of the weld pool. In this way, heat transfer is not used to predict the shape and size of the weld pool. It can only predict the temperature field outside of the experimentally determined or estimated weld pool. Prescribed temperature boundary condition is only valid when welding process reaches the steady-state region. In this region, it is possible to analyze more complex weld pool shapes. On the other hand, the distributed flux and power density computed from the prescribed temperature model can be applied to analyze the starting and ending transients.

Up to now, the most realistic arc energy models are due to Galdak's double ellipsoidal model. In this model, a Gaussian heat flux distribution on the top of weld pool is simulated by one half ellipsoid and a Gaussian power density distribution in the weld is imitated by one half of another ellipsoid (see Figure 2-2). It requires an estimate of the net heat into the weld and the distribution of this net heat into each of the ellipsoids to properly simulate the heat flow in the longitudinal direction. The net heat input to the weld could be represented in the following formulation:

$$Q=\eta VI \tag{2-4}$$

where,

η = Efficiency of heat source.

V = Welding voltage.

I = Welding current.

This model also allows changing the heat distribution by a simple change of various geometric parameters rather than changes to the finite element mesh. It is a very practical and useful in attempting to simulate a weld pool.

One problem with the heat source modeling is the stirring effect. During the welding process, the molten zone is stirred intensively. In this way, the heat source should be simulated by solving the magnetohydrodynamics of the arc and the fluid mechanics of the molten zone. This is a problem of extreme difficulty from mathematical, numerical, computational, and experimental view point. The flow patterns inside the molten pool are the result of the competing forces of gravity, buoyancy, surface tension, electromagnetic force, droplet momentum and surface drag from gas flow. These are in turn affected by the arc voltage, current, shielding and chemistry. The most comprehensive review of the physics of arc and the molten pool is Lancaster's book.[99] The model proposed by Dilawari, Eagar, and Szekely[100,101] considered the effects of stirring and mixing in weldments. Although the coupling between the arc and the weld pool is strong and this coupling is the proper method for determining the energy distribution, solutions have not been derived.[102-108]

Kinematic model

Besides the heat source models described above, kinematic model is also used for heat transfer in welds. For kinematic model, once after a model for the heat source has been selected, one could assume the heat flows only in cross sectional planes, only in the plane of the plate, only in radial direction or is free to flow in all three dimensions (see Figure 2-3). Then the feature of the selected model is that the direction of the thermal gradient has been restricted. There are 2D cross-sectional models, 2D in-plane models and 3D models in kinematic models. Analyst must balance accuracy against cost. 3D modeling is most accurate with the highest cost. Restricting heat flow to the plane of the plate can achieve useful accuracy for thin plates, particularly with deep penetration plasma, electron and laser beam welds. Assuming heat flows only in the cross-sectional plane can provide a useful and economical approximation for many welding situations. In particular, the results from a low cost cross-sectional analysis can be helpful in designing an efficient 3D mesh.

Thermal Material Properties

Nonlinear material properties have been used in recent welding numerical simulation work. Although material properties at room temperature are easier to get than the high temperature properties different data should be tried to match the experimental data during a numerical simulation. Rohsenow[109] provided the detailed measurement techniques for high temperature heat transfer. References [110,116] summarizes much of the published data.

HEAT LOSSES

Heat losses are, in general, composed of the heat transferred from the weld pool to the parent metal by conduction and convection and the heat lost by free convection and radiation from the exposed surface. For the heat transferred to the parent metal, many

researchers use artificially high conductivity for the metal in the weld pool.[117,118] It is conventional to use conductivities an order of magnitudes higher than its value at the solidus temperature. The problem with this method is that various values of conductivity for the molten metal must be tried until a reasonable weld pool shape and temperature distribution within the weld pool are obtained. Heat loss due to thermal radiation is dominant in the vicinity of the weld pool where the temperature difference between the weldment and the environment is large. Radiative heat loss can be calculated with the Stefan Boltzman equation that requires a value of the surface emissivity. Heat losses due to surface convection are dominant away from the weld pool and appear to have a significant effect on the cooling rate of the weld. It is often compensated by decreasing the welding efficiency during welding process to adjust the heat loss effect. The heat loss by free convection can be modeled by Newton's cooling law that requires a knowledge of the surface heat transfer coefficient. This coefficient will vary with the orientation of the surface and may not be readily available for some orientations and surface finishes.

THERMAL STRESS MODELS

Basic Principle of Mechanics

There are three elastic theories: elasticity, hyperelasticity and hypoelasticity. Elasticity is based on the thermodynamic equilibrium principle. Hyperelasticity theory is based on assuming reversible thermodynamics, i.e., strain energy density is an analytic function of strain and temperature. Hypoelastic theory is based on assuming irreversible thermodynamics. The stress and strain relationship depends on the previous stress state. This theory is also called the rate theory. As for the welding process, the stress and strain relationship strongly depends on the welding procedure, stress relief, etc. So only hypoelastic theory is applicable to welding process.

Elasticity is only applicable for sufficiently small strains. For large strains, new phenomenon occurs and other theories are needed to describe it. For welding mechanics problems, a plasticity or viscoplasticity theory should be used, so a thermo-elasto-

plasticity theory has been widely used to analyze welding mechanics.

Thermo-Elasto-Plasticity Theory

In each time increment, Δt, at each point in the material during welding process, the change in temperature, ΔT, is calculated first. Then the total strain increment, $d\varepsilon_{ij}^{Tot}$ could be calculated. The $d\varepsilon_{ij}^{Tot}$ is decomposed into three parts: elastic strain increment, $d\varepsilon_{ij}^{Elas}$, thermal strain increment $d\varepsilon_{ij}^{Therm}$ and plastic strain increment $d\varepsilon_{ij}^{Plas}$. Then the stress increment associated with above three strain increments can be obtained.

During thermo-elasto-plastic analysis of welds, some fundamental equations are necessary to compute the thermal stress in weldments.[119,120]

1) A change in temperature, ΔT, causes a volumetric strain $\alpha \Delta T$.

$$\varepsilon_{ij} = \alpha \Delta T \tag{2-5}$$

2) At each point, the strain increment can be defined as:

$$d\varepsilon_{ij}^{Tot} = d\varepsilon_{ij}^{Elas} + d\varepsilon_{ij}^{Plas} + d\varepsilon_{ij}^{Therm} \tag{2-6}$$

$$d\varepsilon_{ij}^{Therm} = \alpha \Delta T \delta_{ij} \tag{2-7}$$

3) The Young's modulus and Poisson's ratio are assumed to be temperature dependent.

4) The total strain rate could be in the form as :

$$d\varepsilon_{ij}^{Elas} = D_{ijkl}^{-1} d\sigma_{ij} \tag{2-8}$$

$$d\varepsilon_{ij}^{Plas} = \lambda \frac{\partial f}{\partial \sigma_{ij}} \tag{2-9}$$

$$\varepsilon_{ij}=\frac{1-2\nu}{E}\sigma\delta_{ij}+\frac{\sigma_{ij}'}{2G}+\frac{3\sigma_{ij}'}{2\sigma\overline{H'}}\overline{\sigma}+\varepsilon_{ij}^{\theta}\delta_{ij}-\frac{1-2\nu}{E^2}E\sigma\delta_{ij}-\frac{1}{2G^2}G\sigma_{ij}'+\frac{3\sigma_{ij}'}{2\overline{\sigma}H'}\frac{\partial f}{\partial T}T \qquad (2\text{-}10)$$

$$\overline{\sigma}=\sqrt{\frac{3\sigma_{ij}\sigma_{ij}'}{2}} \qquad (2\text{-}11)$$

$$H'=-\frac{\partial f}{\partial\overline{\varepsilon}^{(p)}} \qquad (2\text{-}12)$$

where,

f = Yield function. It is assumed as:

$$f(\sigma_{ij},\varepsilon_{ij}^{(P)},K(\varepsilon_{ij}^{(p)}),T)=0 \qquad (2\text{-}13)$$

$$f=\overline{\sigma}-c(\varepsilon_{ij}^{(p)},T) \qquad (2\text{-}14)$$

K = Strain hardening parameter.

T = Temperature.

σ = Average hydrostatic stress.

δ_{ij} = Kronecker symbol.

υ = Poisson's ratio.

E = Young's modulus.

G = Shear modulus.

ε^{θ} = Thermal strain caused by the temperature distribution.

σ_{ij}' = Stress deviation.

D = Matrix of coefficients.

If an element in question is plastic, the element takes one of the following states

at the next time increment:

$f = 0$	$f_j' < 0$	(unloading)
$f = 0$	$f_j' = 0$	(neutral)
$f = 0$	$f_j' > 0$	(loading)

where,

$$f' = \sigma_{ij} \frac{\partial f}{\partial \sigma_{ij}} + T \frac{\partial f}{\partial T} \tag{2-15}$$

If the yield function does not move and does not change the size, the loading in the element does not occur. In other words, unloading or neutral state is possible.

5) Conservation of linear momentum and angular momentum

The Von Mises yield criteria states that attainable stress states are constrained to lie within a cylinder in stress space or, equivalently, a sphere in deviatoric stress space. Strain hardening that changes the radius of the sphere, while holding its center fixed, is called isotropic hardening. Strain hardening that maintains the radius fixed but moves the center of the sphere is called kinematic hardening, (as shown in Figures 2-4 and 2-5). Zeigler[121] stated that the center must move in the direction normal to the yield function evaluated at the location of the stress state on the yield surface. Isotropic-kinematic hardening permits both the position of the center and the radius to change with strain hardening. Among kinematic hardening model, isotropic hardening model and isotropic-kinematic hardening model, kinematic hardening model is used to characterize the material behavior during welding. The reason for this is:

1) Kinematic hardening theory is the simplest theory to simulate the reverse plasticity and Bauschinger effect that is expected to occur during welding. For this theory, work-hardening in the plastic region is linearized to be a constant.

2) The combined kinematic-isotropic hardening model is more accurate than kinematic model,[122,123] although, unless more accurate stress-strain curves are available, it will not improve the accuracy of the results.

During the welding process, the time for material to stay at a high temperature is short, so time dependent creep effects are generally not considered.[124]

In addition to strain hardening, the yield function is a function of temperature. Usually the radius decreases at higher temperatures. However, metallurgical phenomenon, such as precipitation hardening, can cause hardening as the temperature is increased. In passing through a phase change, such as the austenite-ferrite transformation in steel, the yield strength may be very low. It is preferred that the yield strength data that is dependent on temperature is measured by experiment.

The plastic strain increment can be computed in four ways: the exact, radial return, secant and tangential predictor-radial corrector algorithms.[125,126] Currently the radial return algorithm is recommended because it becomes exact for both very large and very small strain increments and it is computationally efficient. For large increments, the exact method, which requires roughly twice the computational effort, may be more efficient. The basic step in all of these methods is to project the plastic component of the trial strain increment onto the normal to the yield surface.

Jones and Albert[127], Greenwood and Johnson[128,129] have worked on the effect of the phase transformation on welding processes. They observed that the yield strength drops to zero during the transformation until the strain due to the transformation volume change is accommodated. At higher stress levels, the plastic strain is greater. Hence, it is very difficult to simulate the welding process with phase transformations rigorously. Most analysts ignore this effect entirely.

If feasible, temperature dependent effect due to rate of change in Young's Modulus, Poisson's Ratio and the coefficient of thermal expansion with temperature should also be considered. Most formulations ignore these terms that can be significant.

Mechanical Material Properties

The Virgin Yield Stress and Tangent Modulus are the critical material properties. For the kinematic hardening model, the Tangent Modulus is set to zero above melting temperature so that the molten material can re-solidify as damage-free material. The Virgin Yield Stress at melting temperature should be very small but not zero. Otherwise, it may produce "divided by zero" problems in the computation.

For the residual stress and strain analysis of welding, in order to save computing cost, some researchers set a cut off temperature. They assume that the thermal strains, Young's Modules and Yield Strength do not change above a cut off temperature.

History of Thermal Stress in Welds

At the end of the 1970's, efforts were begun to develop analytical models to predict the thermal-mechanical response of welded structures . Before that time, various approaches had been taken to establish empirical methods for understanding material behavior during welding.

Analytical models for calculating stresses during welding have been developed based on the line heat source and moving point heat source.[130-138] These techniques generally show good agreement between residual stresses of the model and experimental data but are often limited to single pass welds. As for the complex welding process, for example, irregular geometries, inelastic material response and material loading, unloading, etc., the problem could not be solved with a closed-form solution. Numerical methods should be used to analyze the residual stress in welded structures. The finite element method has been applied to study the behavior of welded structures.

Veda[139] was the first to compute the residual stress in a welded structure using finite element method. Wilson and Nickell[140] were the pioneers in applying the finite-element method to transient heat conduction in solids. Sagalevich and Mezentseva[141] developed a method for calculating residual stresses and strains during welding of circular tubes. Their method recognized each weld pass as it was laid down. Kamichika, Yada and Okamoto[142] applied the finite element method to determine residual stresses in low alloy carbon steel plates for a case where a wide band of austenitic stainless steel was laid on top of the plate.

The next attempt to compute residual stress due to welding with finite element method was mad by Hibbitt and Marcal.[143] They presented a thermo-mechanical model for the welding and loading of fabricated structures, describing the development of numerical analysis techniques that account for many welding parameters. The model

simulates the gas-metal arc-welding process and accounts for temperature dependent material properties, phase changes, and deposition of filler material. Their expertise in finite element method is demonstrated by the fact that MARC, developed by Marcal and Hibbitt, and ABACUS, developed by Hibbitt, are the most highly regarded commercial programs for nonlinear finite element analysis.

Nickell and Hibbitt[144] presented thermal and mechanical analysis procedures for welded structures that take into account latent heat effects and weld metal deposition. Their paper also discusses methods for handling floating solid regions that could occur during cooling.

Following Hibbitt and Marcal, Andersson[145] was the next to attempt a rigorous finite element method analysis of residual stresses. He used an enthalpy method to deal with latent heat effects. The arc was modeled as a constant surface flux. The stress analysis appears to be based on the correct thermo-elasto-plastic equations for hypoelasticity, with a Von Mises yield criterion and isotropic hardening.

Friedman[146] applied finite element analysis procedures to calculate temperature, stresses and distortions in longitudinal butt welds. The analysis procedures presented by Friedman are applicable to planar or axisymmetric welds under quasi-stationary conditions.

An analysis procedure for analyzing transient residual stresses and deformations due to flame forming applied to a flat plate has been developed by Iwamura and Rybicki.[147] The model gives residual stresses that vary through the plate thickness. A simple finite-element representation for deformations is used. However, complex constitutive relations to represent material unloading and temperature-dependent properties are included. Rybicki, Ghadiali and Schmtteser[148] developed a simple mathematical model to predict deformations of butt welded flat plats. Weld distortions due to each pass are included in the finite-element model by updating the geometry of the finite element grid after each pass. The predicted results of this model show good agreement with experimentally measured data.

RESEARCH DIRECTION

Recent modeling results give increasingly reasonable simulation results of residual stresses with increasing distance from the weld fusion line.[149] That is because the weld fusion line experiences high temperature cycles during the welding process, thus experiencing the highest plastic strain. At the same time, the absence of accurate thermal/mechanical material properties and accurate work-hardening data at high temperatures leads to added inaccuracy in residual stress results.

Normally some type of heat flux/heat source model is used for numerical simulation of fusion zone. It is based on the known welding operation parameters and their experimentally determined effects on the slag weld pool geometry. However, for the weldments with unknown operation parameters during welding process, such as in the case of this study, the heat flux/heat source model is not applicable. Because of this, a different heat source model was developed. The weld/fusion zone boundary was experimentally determined from the core material removed from the bridge and used to define fusion boundary for the models developed in this study.

Solving the 3D problem is very time consuming. Although a 2D model could yield approximate results of 3D model, some problems like ES welding residual stresses through whole plate thickness must be modeled in 3D. Another problem is how to reduce the cost of computation that can be tremendous for some 3D model simulations even though accurate modeling of the residual stress in weldments has become cheaper and cheaper with the rapid development of computer technology.

One research direction for reducing the cost of computing is using the moving coordinate steady state system to replace the fixed coordinate transient state system which is used in most finite elements analysis. Commercial software (SYSWELD) based on this kind of coordinate replacement is readily available. With moving coordinate system, the computational time can be dramatically reduced. Therefore, the moving coordinate system is used during 3D model of ES modeling process in the study reported here in Chapter 7 will demonstrate the advantage of using the moving coordinate system.

2.3 MODELING OF ELECTROSLAG WELDING PROCESS

The thermal history of ESW differs markedly from that of conventional arc welds. That leads to different analysis methods. ES welding began in 1950's. However, low fracture toughness has been found in the fusion and HAZ in ESW. This greatly restricted its usage. Thus the modeling work on the ESW process is not as detailed as for arc welding process. However, modeling work has also been done on ES remelting, a billet remelting process similar to ESW except that the ES remelting billet is entirely surrounded by a copper water-cooled mold.

THERMAL MODELING OF ESW PROCESSES

Molten pool size and shape are the controlling factors in the production of sound welds. The physical properties of heat flow in welding are the same as in casting. Muehlbauer and Sunderland[150] reviewed the techniques of analysis in heat conduction with freezing and melting conditions. Further work in this area has been done by Tien and Geiger[151] and Cho and Sunderland.[152]

Using the above theory of heat conduction during solidification processes, Carvajal and Geiger[153] analyzed the temperature distribution and the location of the solidus, mushy and liquids zones for the ES remelting of an Al-4.5% Cu binary alloy. In their analysis a parabolic temperature distribution was applied to the top of the ingot to represent the heat generation in the slag. The results agreed qualitatively with experimental evidence of the shape of the molten pool.

Campbell[154] developed a transparent model to directly observe phenomena occurring in the slag and metal layers during ES remelting. The major means of heat transfer from slag pool to metal pool is the fall of droplets of consumable electrode. Edwards and Spittle[153] collaborated the results by an experimental investigation. These investigators found that the metal pool depth was proportional to the slag temperature and is defined, to a large extent, by heat transfer to the pool by molten metal droplets.

The heat generation pattern is modeled by the resistance heating of the slag.

Current and voltage profiles in the slag are important in determining the shape of the molten metal pool.

The most detailed modeling work of ESW process has been done by Dilawari, Szekely, and Eagar of M.I.T. Their work can be divided into two parts. One part[100,101] has put emphasis on the role of the electromagnetic and buoyancy fields in determining the velocity and temperature profiles of molten metal in the weld pool. In this part of their work, idealized two-dimensional (axisymmetrical or plate-like) systems have been used. The rectangular system modeled is a reasonably good approximation of ES welding with a strip electrode. Only the shape of the metal pool appears to be over-idealized.

It was found that the buoyancy and electromagnetic forces produce vigorous agitation in the molten weld pool. The nature of this agitation is quite markedly affected by the geometry. When the current field is non-parallel, as in the case of wire electrodes, the electromagnetic force field plays a major role, while for parallel fields, as produced by flat plates, the flow field is driven essentially by buoyancy forces. This part of work established the existence of vigorous agitation in the weld pool and indicated the important role played by the system geometry.

The other part of their work[155,158] uses truly three-dimensional system to examine the heat generation patterns and the resultant temperature distribution in the molten slag, the metal pool, HAZ and base metal. The idealized 3D model for heat flow analysis were schematically illustrated in Figure 2-6. However, their work did not consider the phase transformation effect during heat flow and the shape of the molten pool is idealized in their model. At the same time, all of their modeling work is based on the known welding operation parameters and their effect on slag/weld pool shape.

MECHANICAL MODELING OF ESW

Until now, no report has been found on thermal stress finite element analysis of ES welding process. Thermal stress will affect the fracture and fatigue property of welded structures. It is necessary and important to make a detailed study on this subject. Such a study is reported herein.

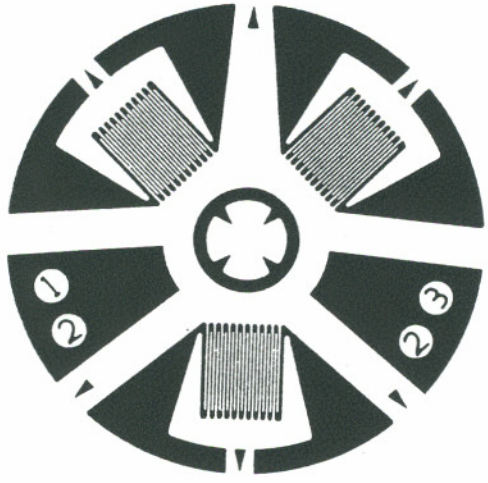

Figure 2-1 Design of Strain Gage Rosette

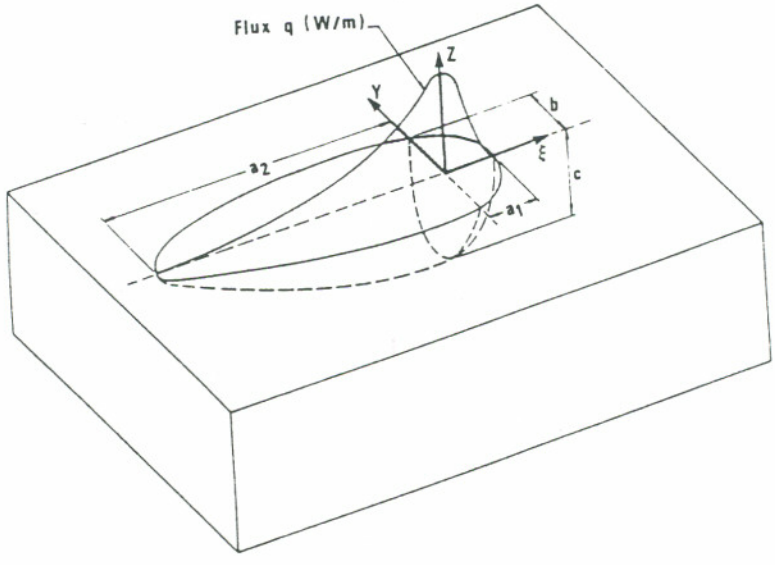

Figure 2-2 Arc Heat Source Model with a Distribution of Flux over the Surface and the Power Density throughout the Volume of the Double Ellipsoid[90]

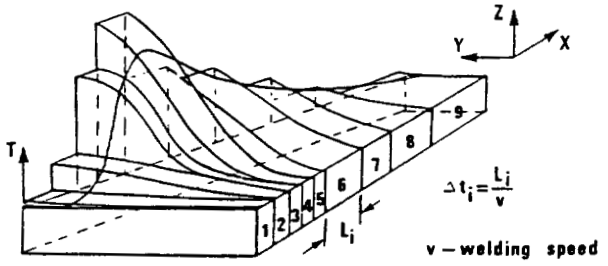

(*a*)

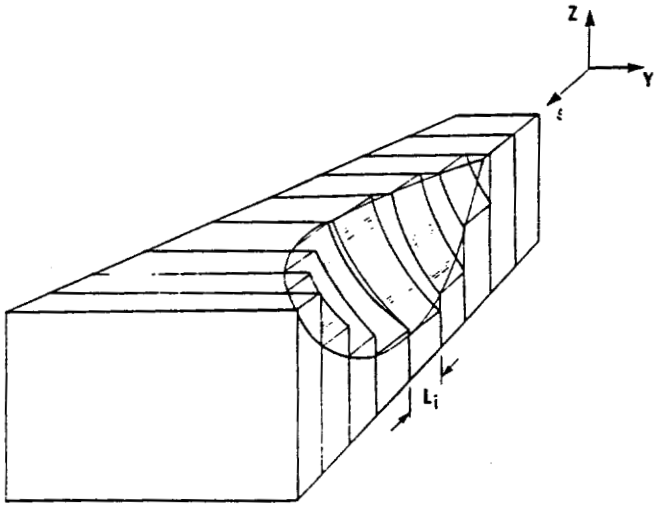

(*b*)

Figure 2-3 (a) For Cross-Sectional Model, the Temperature Distribution on a Series of Slices to Show the Temperature Field at Several Instants Time
(b) Approximate 3D Steady State FZ Boundary Obtained from the Cross-Sectional Model[90]

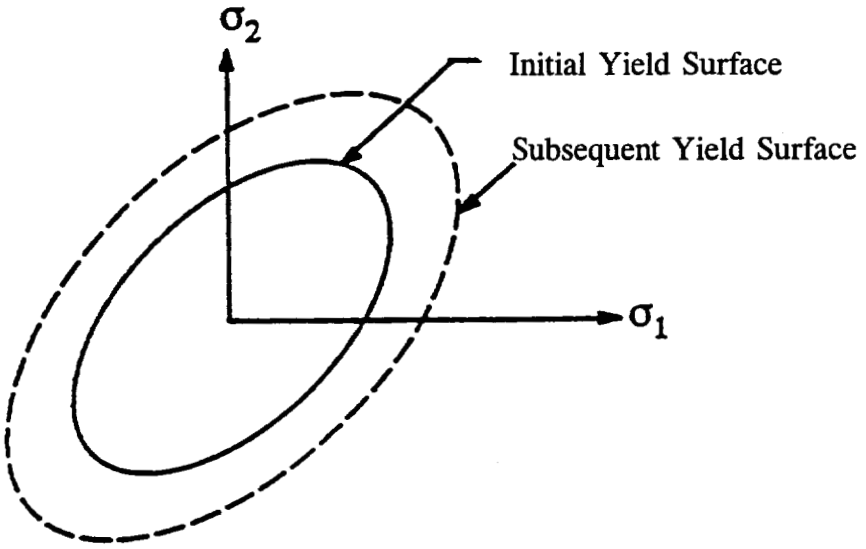

Figure 2-4 Isotropic Work Hardening Rule

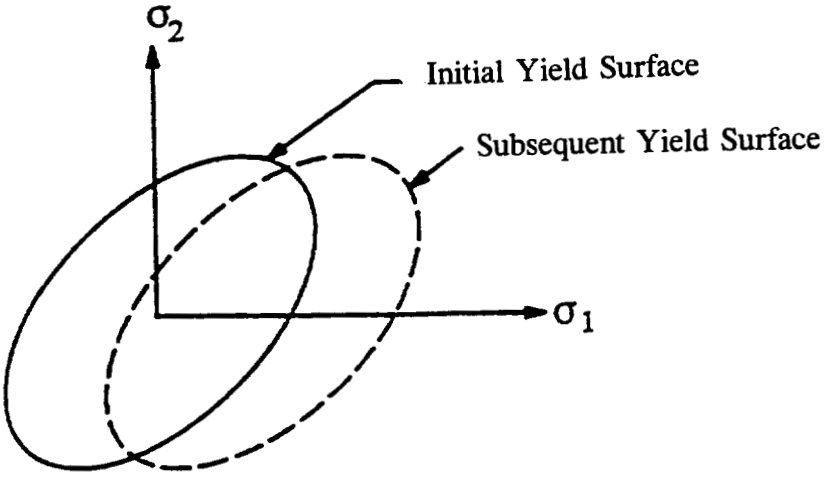

Figure 2-5 Kinematic Work Hardening Rule

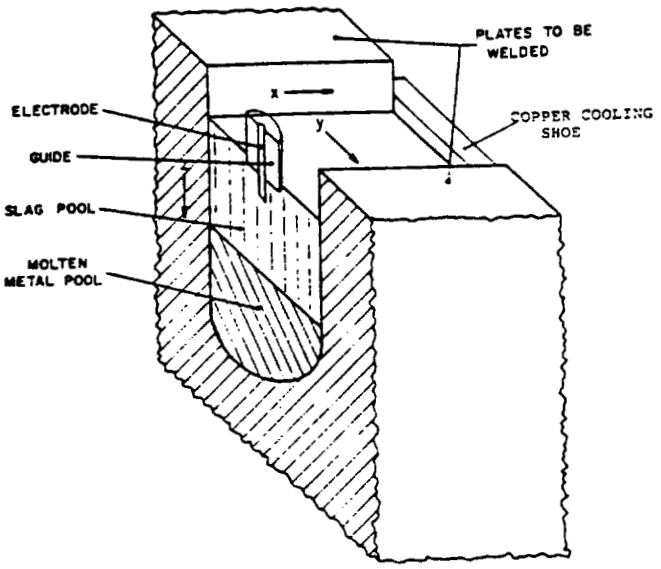

Figure 2-6 Schematic Representation of 3D Model

CHAPTER 3
CORE FUSION BOUNDARY ASSESSMENT

3.1 INTRODUCTION

The Welded Plates of the West Linn Bridge have been in service for almost 30 years (the bridge was built in 1968). The ES welding process was used to shop-weld plates together to form the top and bottom flanges of the box girders. The operation parameters that were used during the ES welding process for the welded plates on the West Linn Bridge are not known now. One generally develops weld models based on a set of operating parameters. However, the major effect of ESW operation parameters is the determination of the shape characteristics of the molten weld pool during the welding process. The size and shape of the molten pool are the most important factors in determing the weldment properties and residual stress distribution. This means that if one can determine the molten weld pool shape present during welding of the plate, the residual stress distribution inside the plate could be estimated without detailed information of welding process operation parameters. Experimental work was performed to determine the molten pool shape and size present during the West Linn Bridge ESW process. This information was then used as input for numerical analysis of the residual stress field.

It is well known that the welded region in general can be classified into three zones: fusion zone, HAZ and base metal. The easiest to distinguish is the fusion line during welding from weldments using microanalysis. It is very difficult to identify the extent of the HAZ. The HAZ lies between base metal and fusion zone. The width of HAZ is several millimeters which is negligible compared to the fusion zone dimension of centimeters. The parameter assessment work was done by measuring the position of fusion line without assessing the HAZ.

The results of preliminary FEA research reveal that molten pool shape/size are very important to the accuracy of simulating a welding process. Thus the need to experimentally determine the bridge-specific ESW weld pool shape/size. The molten metal pool of ESW is idealized to be a half sphere or square. The half sphere shape model is more accurate than the square shape model. The results of simulation using a half sphere molten metal shape yield a good agreement with the experimental results in some cases. However, half sphere molten pool shape is still an idealized one. Normally, the more accurate the weld pool shape simulated in model, the more reliable the FEA calculation results. However, the weld pool shape effect on ESW process is still not known. The remainder of this chapter will analyze the effect of weld pool shape on ESW process.

Operation parameters affect residual stress. Different operation parameters will change the residual stress distribution. This part of the study is needed for analysis of the residual stress results measured as a result of core removal and subsequent core slicing. For example, the residual stress will be different for a steady welding process versus an unsteady welding process.

During the solidification process, liquid does not solidify continuously. Solidification bands formed because of segregation of elements during discontinuous solidification processing. The shape of the molten metal pool during welding can be inferred from the geometry of solidification bands. Weld pool measurement was based on the microanalysis results. The results will be used as input data for further finite element analysis of residual stress during ES welding processing.

The West Linn bridge-specific ES weld fusion zone characteristics were assessed by analysis of cores removed from the weld area by ODOT personnel for subsequent material toughness assessment. This core material was macro-etched to yield fusion zone structure.

3.2 EQUIPMENT

The equipment that was used during this part of the work were the core drilling

system and mechanical band saw machine. The core drilling system was mainly used to drill cores from the bridge. The saw was used to cut the cores into several slices.

3.3 PROCEDURE

The procedures for this part of the work are as following:

1) Removing Cores from Bridge

Multiple cores were removed from box girders of the West Linn 205 Bridge. Plate girders versus box girders support the approach structures to the West Linn Bridge. Two box girders support each traffic deck on the main channel crossing structure, with each traffic direction deck structure being totally independent of the other as shown in Figures 3-1 (a) and (b). The four box girders are sequentially lettered from A to D, starting with A-girder on the external, down-stream side of the south-bound traffic deck as shown in Figure 3-1 (c). The 14 support piers for the approach structures and main channel crossing structure are numbered sequentially from 1 to 14 beginning on the east side of the river and ending on the west side of the river. The main channel crossing structure begins at pier 3 and ends at pier 6. Multiple girder sections make up a given main channel crossing box girder. In fact, each box girder is made up of nine shop-fabricated girder sections that are then field bolted to yield the final main channel crossing girder.

The individual box girder sections are numbered 1 to 9, starting on the east side of the river and running to the west side of the river as shown in Figure 3-1 (d). Each individual girder section is further characterized by a letter designation from A to D before the girder section number to identify the specific box girder it is associated with. The shop-fabricated ES weldments for each girder section are identified by position and number of welds from the east end of the girder section, as well as the overall girder section number. The position identification designates whether the weldments is at the top of the box girder (T), and thus under the roadway, or at the bottom of the box girder (B), thus facing down to the river as shown in Figure 3-1 (d). A complete ES weldment identification number would be D3B1; ES weldment would be the first weldment from

east side in the third box girder section in the external, up-river side box girder under the north-bound traffic deck of the main channel crossing support structure. The bolted connection attaching one box girder section to another are designated as "field splices" and are numbered 1 through 8, starting at the splice between the eastern-most box girder sections (Girders 1 and 2) and ending at the western-most box girder sections (girders 8 and 9).

The cores were taken from three out of four (B, C and D) of the box girders of the channel crossing structure from ESW weldments on the bottom floor of the box girder which were in compression loading. A core drilling machine was placed over the spot to be core-drilled, and bolted in place using 5/8 inch bolts screwed 1 to 1-1/2 inch into the box girder plate in threaded holes specially pre-drilled for this operation. The girder was 3.5 inches thick, and the core diameter was 3.5 inches. It took about 1 to 1-1/2 minutes to drill each core. The core was drilled from inside the box girder toward the outside, or down toward the Willamette River. A hydraulic bucket was positioned below the expected point of exit, and the cores were "caught" as they fell away from the bottom of the girder bottom plate. Special compression load-bearing devices were installed into the core holes after each core drilled. The two-piece units were pulled together by torquing a connection bolt until they snugly contacted the core hole edges. The bolt holes were assumed to have essentially no effect on subsequent load distribution, and were simply filled with grease to deter liquid penetration.

Fourteen cores have been removed from the bridge. Two were base metal cores, four were weld centerline specimens and eight were HAZ specimens, which had the core center point 1/2 inch out from the fusion line edge. One base metal core was drilled 8 feet from the D3B1 core. The other base metal core was drilled on B girder 72" from the end. The base metal cores are assumed not to be affected by the ES welding process. The base metal cores were drilled to allow assessment of the stress distribution inside the plate without the effect of thermal stress from the welding process. The actual core designations are given in Table 3-1. Core drilling position is determined by core identification number. For example, the position of cores taken from the bottom flange of box girder section D on the welded plate is shown in Figure 3-2.

2) Sectioning Cores

The core specimens were cut into several slices using a band saw. The thickness of each slice was decided by the type of mechanical test specimens to be subsequently machined from the slice. For example, if the slice was to be machined into a fracture toughness test specimen after being cut from core, a one inch plus clean up thickness was used during the slice cutting. If the slice was to be used for Charpy-V-Notch (CVN) test specimens, CVN specimen thickness plus clean up would be the slice thickness. The core mechanical property testing type identification number and their description are given in Table 3-1. All of the cores were cut at the same slow cutting speed with water cooling during the cutting process.

3) Polishing Slices

In order to get a smooth slice surface, the slices that were to be etched were polished using silicon dioxide grind sand paper.

4) Etching Slices

A 5% nitric acid solution was used to etch each slice. After each etching, the fusion line and solidification bands can be easily seen. Figures 3-2 (a) and 3-2 (b) show the topography after etching B3B1 weld center line specimen and B7B2 HAZ specimen, respectively. It can also be seen from Figure 3-3 (c) (center piece topography of C3B1 HAZ specimen), that solidification band lines sometimes can not be easily seen.

5) Measuring Position of the Fusion Line

The fusion line position variation with thickness and the solidification band shape was measured to get molten pool shape during welding process. Weld center line specimens are better candidates for this work because the complete fusion zone is present during analysis of slices. Assessment of the weld center line specimens indicate that the fusion zone is symmetrical. Thus HAZ cores could be used to measure the fusion line position through thickness knowing the HAZ core position related to the welded plate and the assumption of weld symmetry.

Each core exhibited slightly different operation parameters during welding process. For example, some cores had an obvious restart operation during the welding process, as that leads to a double fusion line. Fusion line shape variation allows assessment of the

consistency between welders. General data for all of the cores should be summarized prior to being used as input data for further finite element analysis. Even through the operator is fabricating each weld according to the same welding code, operating variations may cause different operation results in practice. Fusion line position assessment can indicate the differences for all of the weldments that were studied.

3.4 RESULTS

FUSION LINE SHAPE FOR EACH CORE

Two kinds of WCL specimen fusion line shapes were formed, as shown in Figure 3-4. B3B1 and D3B1 cores were drilled slightly off center and have incomplete fusion zone, as shown in Figure 3-4 (a). C7B2 and C3B2 cores contain the complete fusion zone as shown in Figure 3-4 (b). The reason for the fusion line shape difference between Figures 3-4 (a) and 3-4 (b) is the drilling position deviation for C7B2 and C3B2 on welded plate. This is because the presence of fusion line weld repairs made it impossible to correctly judge where the actual ESW surface fusion line was.

There are three kinds of HAZ specimen fusion line shapes as shown in Figure 3-5. C7B1, B7B1, B7B2, B3B2 and D3B2 core specimens have one distinct fusion line shape over the complete specimen length as shown in Figure 3-5 (a). The fusion line shape of D7B1 exhibits a "double" fusion line near the bottom of the specimen with a distinct difference in the bottom surface intercept placement between the two fusion line as shown in Figure 3-5 (b). The fusion line shape of C3B1 core specimen exhibits a double fusion line with the same bottom surface intercept placement as shown in Figure 3-5 (c).

FUSION LINE POSITION FOR WELD CENTER LINE SPECIMENS

Fusion zone width, measured as illustrated by line AB in Figure 3-3 (a), varies through thickness. The relationship between fusion zone width and slice thickness is shown in Figures 3-6 (a) and (b) for B3B1 and D3B. Solidification band shapes for

center slice of B3B1 and D3B1 are shown in Figures 3-7 (a) and (b), respectively.

FUSION LINE POSITION FOR HEAT AFFECTED ZONE SPECIMENS

Fusion line position of HAZ specimens (C7B1, B7B1, B7B2 B3B2 and D3B2) were measured. The results are shown in Figures 3-8 (a) to (e). The relative position for each slice has been measured by determining the specimen centerline distance from fusion line to the base metal edge of the specimen perpendicular to fusion line direction, as illustrated by line CD in Figure 3-3 (b).

3.5 DISCUSSION

FUSION LINE DETECTION

Solidification band line detection difficulty varies from weld to weld. Figure 3-3 (b) reveals the situation where solidification line is easily detected. On the contrary, the solidification line of Figure 3-3 (c) is not easily detected. Figures 3-3 (b) and 3-3 (c) are from HAZ specimens of different welded plates. The reason for the detection difference is due to the slightly different welding condition. Differences in oscillation of the weld pool caused by mechanical oscillation of the electrode during welding is felt to be a major detection variable. Bigger weld pool oscillation will lead to a greater distance between solidification band lines while smaller weld pool oscillation will lead to a finer solidification band structure. The greater the distance between the solidification bands, the easier post-etch detection becomes. Another factor contributing to the spacing between the solidification band lines is wire guide arcing to the slag pool surface. Also, the presence of double fusion lines as shown in Figure 3-3 (c) in these welds made fusion zone size and shape interpretation difficult. This can be caused by improper electrode oscillation during the welding process as well. The presence of two fusion lines means that solidification band lines may interrupt each other and make it hard to determine the weld pool shape.

FUSION LINE SHAPE

Fusion line shape reveals the operation procedure characteristic during the welding process. For weld center line specimens, from Figures 3-4 (a) and (b), it is evident that C7B2 and C3B2 come from a good, steady welding process and B3B1 and D3B1 from an unsteady welding process because the fusion line has an obvious oscillation. For HAZ specimens, from Figures 3-5 (a), (b) and (c), it could be seen that C7B1, B7B1, B7B2, B3B2 and D3B2 probably come from a good, steady welding process. D7B1 and C3B1 have different fusion line shape from above specimens. The different fusion line shape for HAZ specimens originates from stop and restart operation during welding process. That is why Figure 3-4 (b) has a double fusion line for the same thickness position. Another reason for the different fusion line shape, as shown in Figure 3-5 (c), is that the electrodes improperly oscillated during the welding process.

It can be seen that the fusion line shape is not the same for all of the specimens through the thickness of the welded plate. The width of the fusion zones at the top and bottom plate surface remained nominally constant but the mid-thickness width of the weldments were found to vary. Point P on the fusion line defines where the weld was the widest. Assume the distance from P to a projection of the fusion line position on the top surface is PT as defined in Figure 3-9. Normally it can be classified into two groups: one with PT $>$ 4 cm as shown in Figures 3-6 (a), 3-6 (b), 3-8 (a), 3-8 (c) and 3-8 (d) and the other with PT $<$ 4 cm as shown in Figures 3-8 (b) and 3-8 (e). The relationship between weld number and PT values is illustrated in Figure 3-10.

The fusion line shape through the thickness of the core specimens reveals effectiveness of the heat transfer of the copper shoes during ESW process. In conjunction with the through thickness results, the solidification band line shape reveals the heat transfer property effect along the weld pool depth direction and along the welded plate longitudinal direction. From Figures 3-6, 3-7 and 3-8, it can be seen that the fusion line shape is steeper in through thickness direction than along the weld pool depth direction and along welded plate longitudinal direction. That is to say the heat loss is much greater through the copper shoes than any other direction.

FORM FACTOR

A main weld characteristics in ESW is the width of the weld b (see Figure 3-11). As applied to ESW, the term "depth of penetration" loses much of its meaning since welding is usually done in the vertical position. It is therefore legitimate to speak of the "depth of the weld pool" but not of the depth of penetration. The form factor ψ, which is the ratio of the width of the weld b to the depth of the weld pool h (see Figure 3-11), is an extremely important characteristic in ES welding and to a great extent determines the resistance of the weld to intergranular cracks. The width or depth of penetration can vary according to the thickness of the metal. However, if the welding procedure is correctly chosen, these variations are negligible. The weld-form factor in ESW may vary between 0.8 and 10, the mean value is 1.5-4. From Figures 3-7 (a) and (b), it can be seen that the weld form factor for these tests vary in the mean value range. The weld form factor is about 2.5 for B3B1 weld center line specimen. The weld form factor is about 3.8 for D3B1 weld center line specimen.

FUSION ZONE WIDTH

From the fusion line shape of WCL and HAZ specimens, it can be seen that the narrowest fusion zone is at the top and bottom of the core, i.e., at the plate surface in contact with the copper shoes. The widest fusion zone is near the center of core. From Figure 3-6, it can be seen that the narrowest width of the fusion zone is about 4 cm and the widest width of the fusion zone is about 8 cm for fusion zone cores. For the HAZ cores, the width of widest fusion zone d_{max} can be calculated from Figure 3-8. If the fusion zone width at the top of core is d_{min}, and if the difference between the fusion line on top and at the center of the core along welded plate longitudinal direction is PT, then $d_{max}=d_{min}+2PT$. The measured PT with each cores is given in Table 3-2. It can be seen that 2PT is about 4 cm and d_{max} is about 8 cm, with good agreement between weld centerline cores and HAZ cores.

The position of the fusion line on top of the HAZ specimens reveals the actual

drilling position. If all of the HAZ cores had been drilled in the same position, i.e., 0.5" out from the fusion line as the center of the core, then all of the fusion line positions should have the same CD length on top of the core. Table 3-2 also gives the values of CD length on top of HAZ cores. The values reveal that most cores were drilled at nominally the same position, with B7B2 being drilled farther away from the fusion zone than other cores. This variation is mainly due to the difficulty in determine the ESW fusion line on the plate surface in situ by macro-etching the welds. This difficulty was caused by the cosmetic weld repairs linearly along the fusion lines on both sides of essentially all the welds to compensate for lack of fill due to poor shoe design.

FUSION LINE CURVE EQUATION

It is necessary to get the general curve equation of the fusion line for further numerical simulation work. Because solidification band shape varies through the thickness, a general equation about solidification band line couldn't be generated. As for the fusion line through the thickness, there is a definite one for each weldment. According to Figure 3-8, the fusion line contour can be summarized by the following equation:

$$y=6-0.7X-0.04X^2+0.03X^3-0.002X^4 \qquad (3\text{-}1)$$

3.6 CONCLUSIONS

1) The operation parameters that were used during ESW process were slightly different from weld to weld.
2) The heat loss is much great through the copper shoes than any other direction.
3) The weld form factor is in the mean value ranges.
4) The widest fusion zone width is about 8 cm. The fusion zone width at the surface of the welded plates is about 4 cm.

5) The depth of the weld pool at mid-thickness is expected to vary from 2.1 to 3.2 cm, based on 8 cm average maximum width and a form factor variation from 2.5 to 3.8.

6) Fusion Line curve equation through thickness is as following:

$$y=6-0.7X-0.04X^2+0.03X^3-0.002X^4$$

Table 3-1 Core Mechanical Property Testing Type Identification Number and Description

Number	Specimen ID	Mechanical Test Type	Core Type
1	B1+4	Fracture Toughness	Base Metal
2	B3B1	Fracture Toughness	Weld Center Line
3	B3B2	Fracture Toughness	Weld HAZ
4	B7B1	Fracture Toughness	Weld HAZ
5	B7B2	Fracture Toughness	Weld HAZ
6	C3B1	Fracture Toughness	Weld HAZ
7	C3B2	Fracture Toughness	Weld Center Line
8	C7B1	Fracture Toughness	Weld HAZ
9	C7B2	Fracture Toughness	Weld Center Line
10	D3B1+8	Charpy Impact	Base Metal
11	D3B1	Fracture Toughness	Weld Center Line
12	D3B2	Charpy Impact	Weld HAZ
13	D7B1	Fracture Toughness	Weld HAZ
14	D7B2	Charpy Impact	Weld Center Line

Table 3-2 Difference between Widest Fusion Zone and Narrowest Fusion Zone 2PT and Position of Fusion Line on Top of HAZ Specimens CD_{top}

Specimen ID	2PT (cm)	CD_{top} (cm)	d_{max} (cm)
C7B1	3	6	7
B7B1	4	5.8	8
B7B2	4	6.9	8
B3B2	4.4	5.8	8.4
D3B2	4.8	5.9	8.8

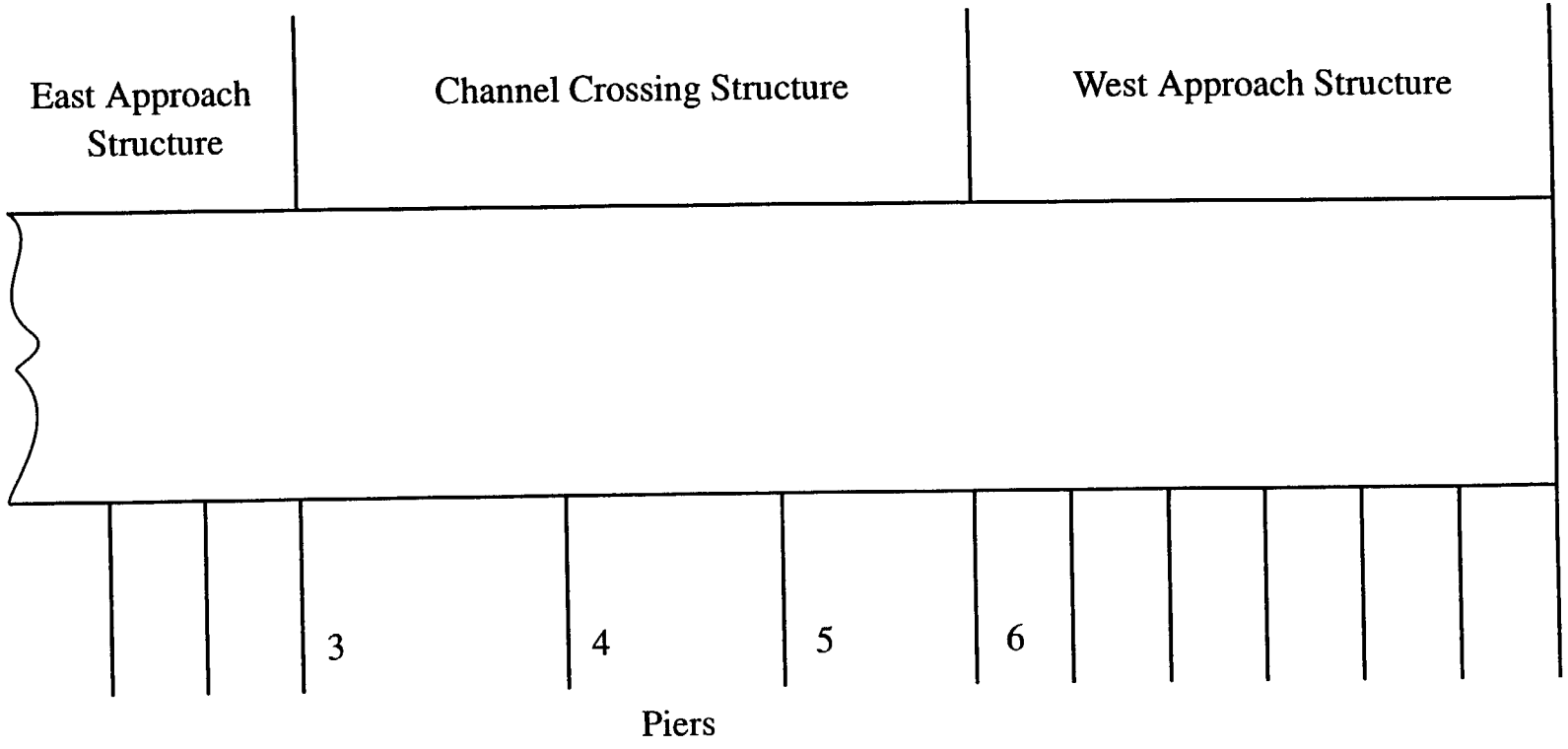

Figure 3-1 (a) Schematic Illustration of The West Linn Bridge Showing Relationship of the Main Channel Crossing Structure to Support Piers and Approach Structures

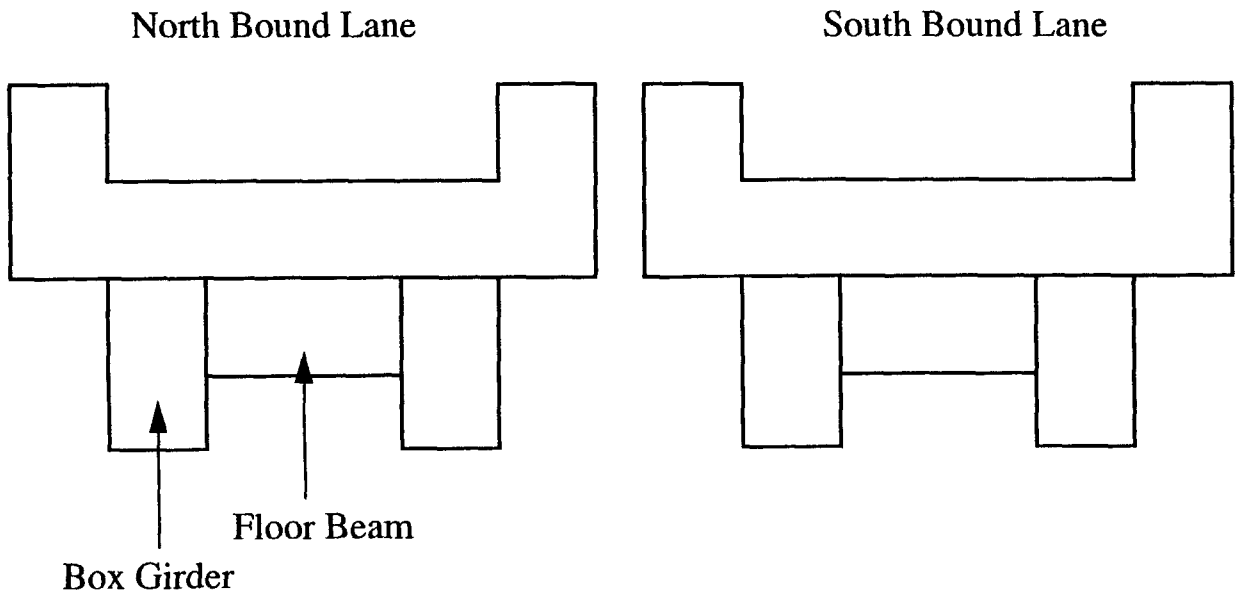

Figure 3-1 (b) Schematic Illustration of the Main Channel Crossing Support Structure Illustrating the Independence of the North-Bound and South-Bound Lanes, and the Placement of the Box Girders

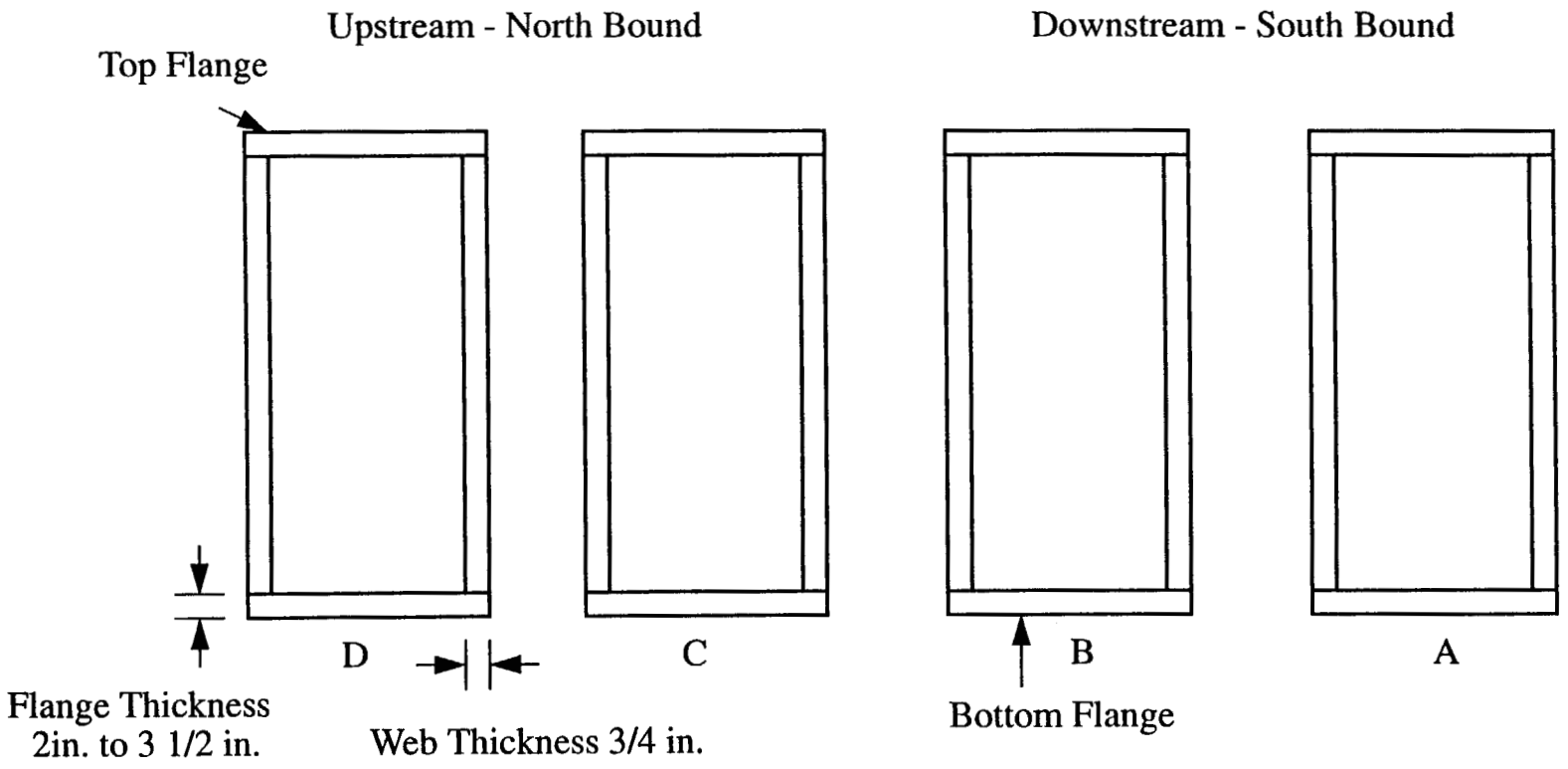

Figure 3-1 (c) Schematic Cross-Sectional View of the Box Girders Illustrating Their Labeling Sequence

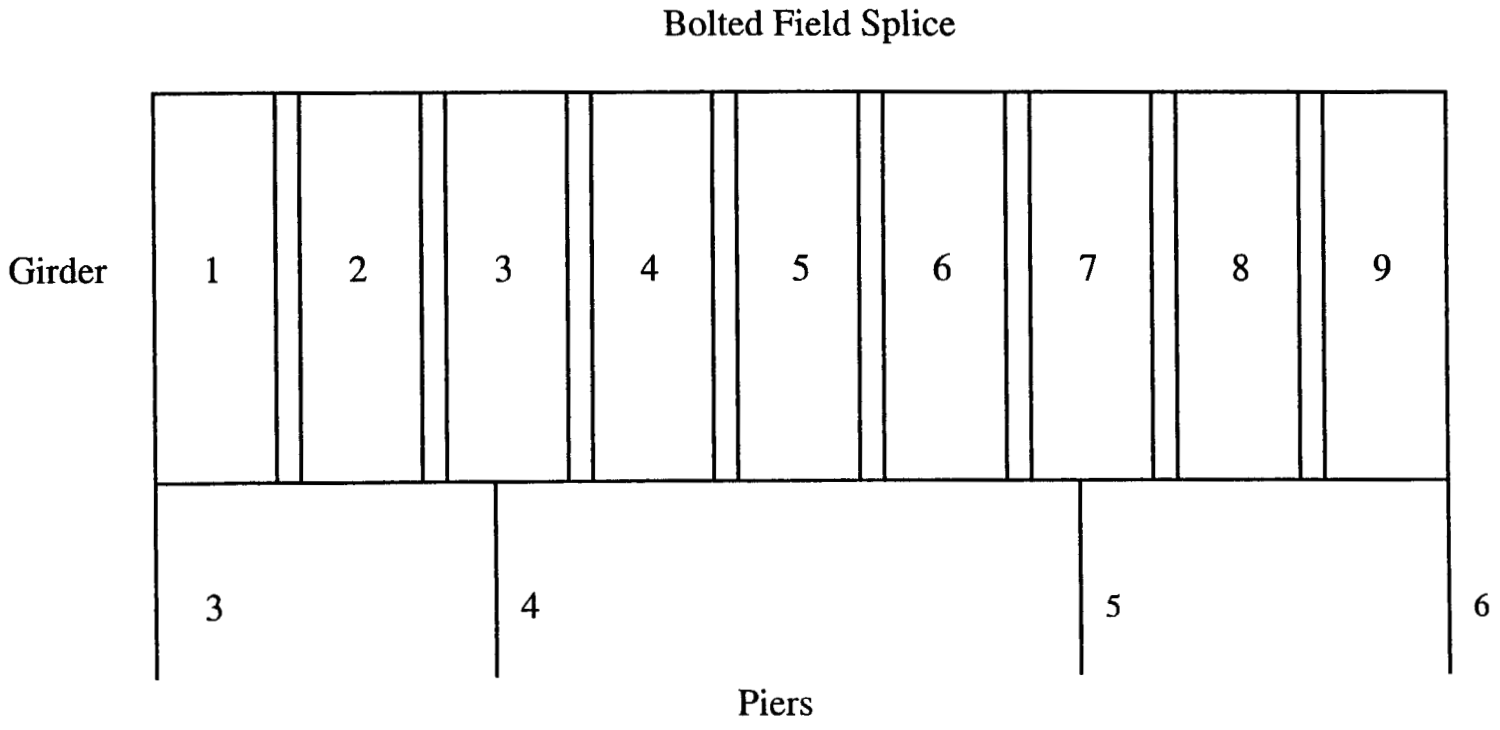

Figure 3-1 (d) Schematic Illustration of the Box Beam Girder Sections Bolted Together to Make Up the Main Channel Crossing Structure

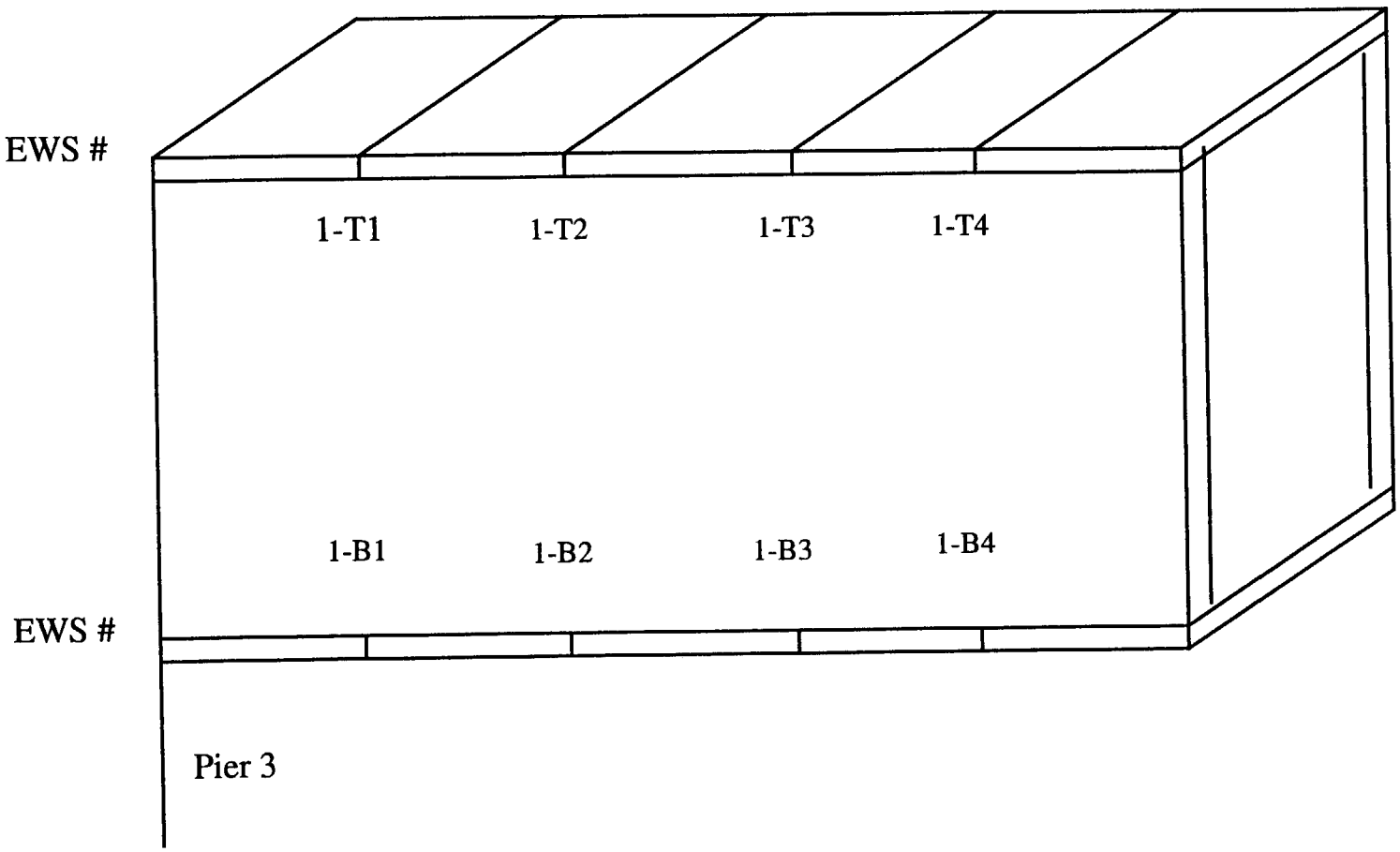

Figure 3-1 (e) Schematic Illustration of the Box Girder Section 1 and the Electroslag Welds Needed in the Fabrication of the Girder Section

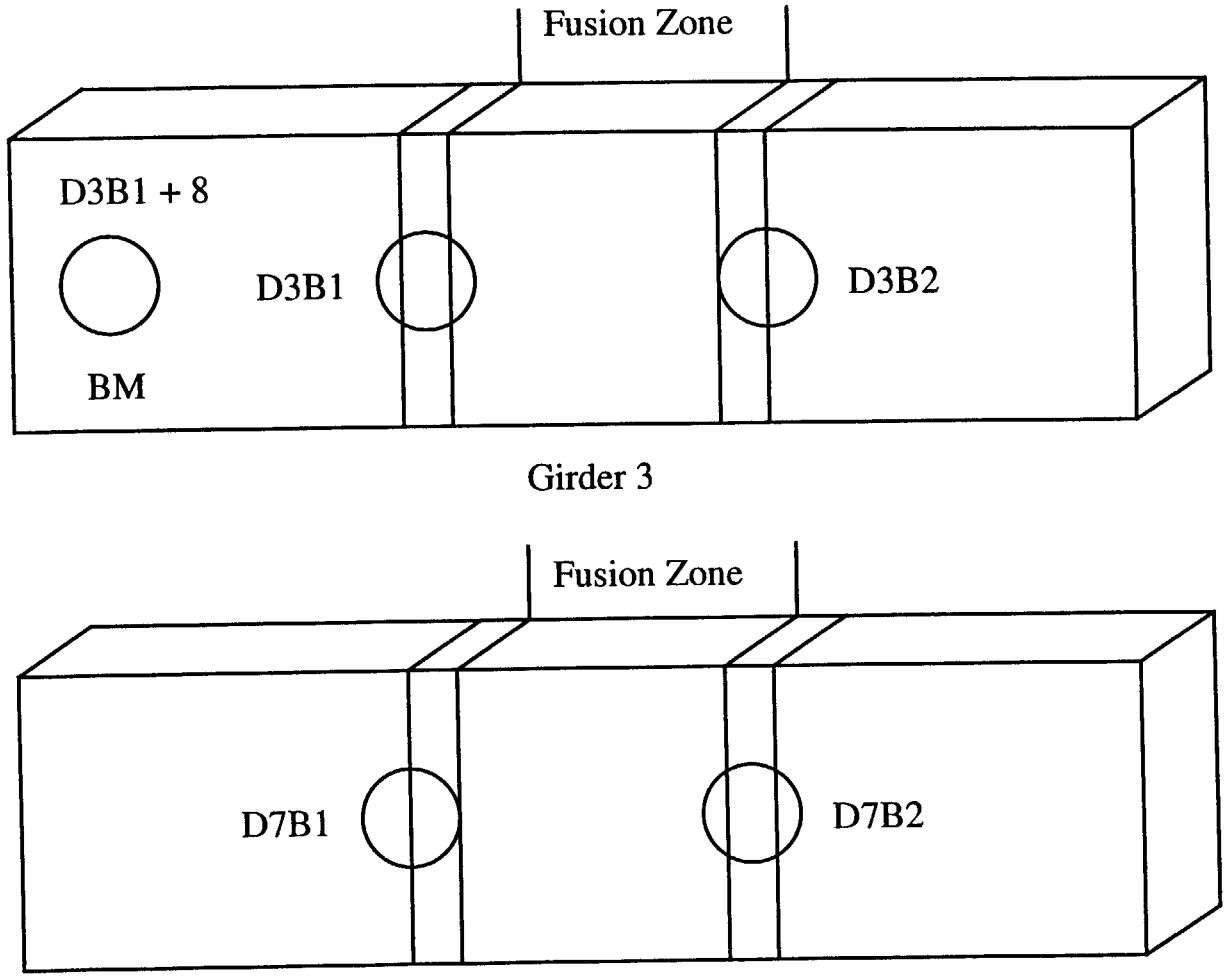

Figure 3-2 Schematic Illustration of Electroslag Weld Core Position Taken from the Bottom Flange of Box Girder Section D

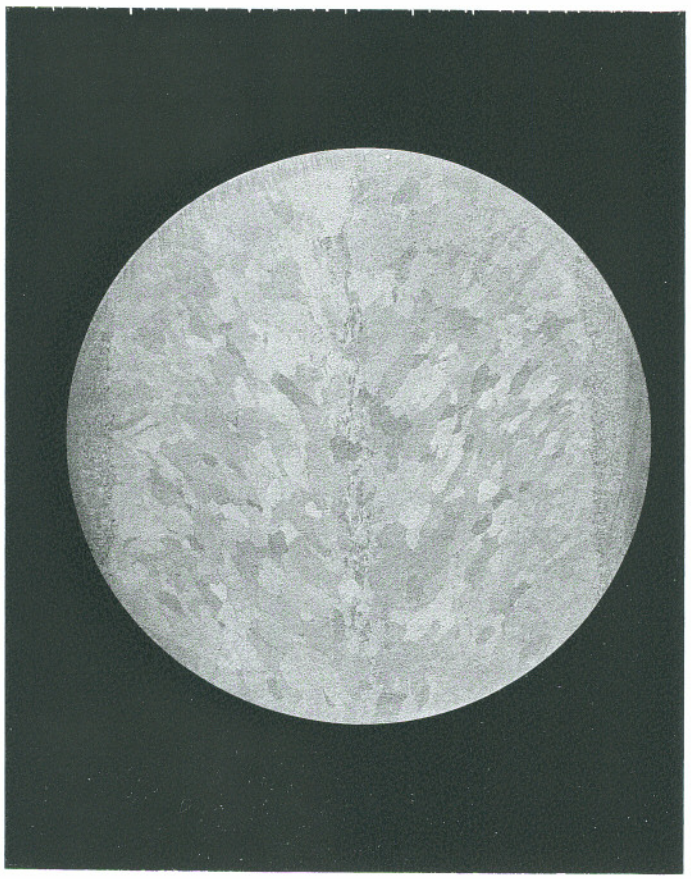

Figure 3-3 (a) Topography after Etching of B3B1 Core Specimen

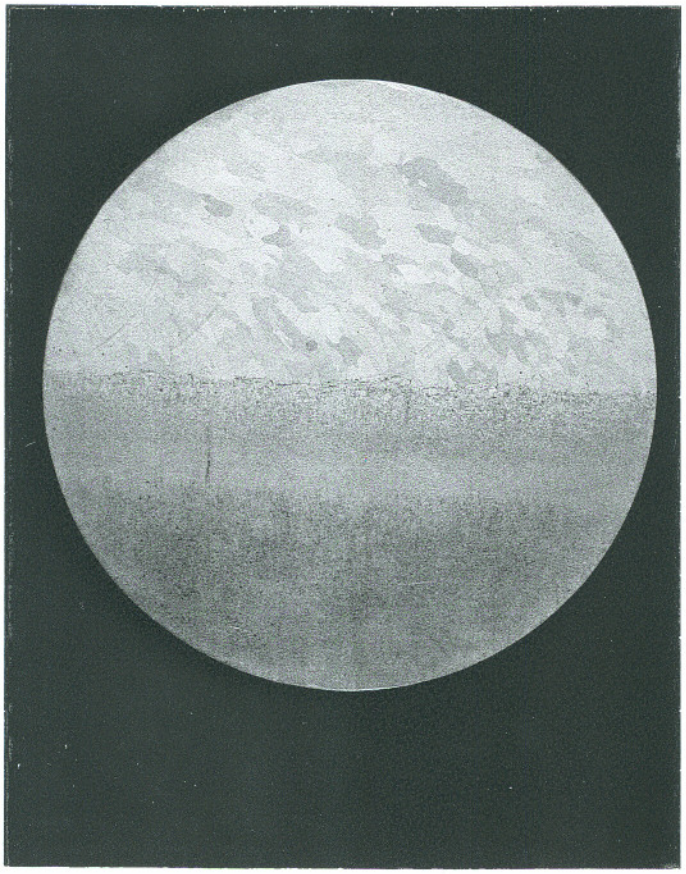

Figure 3-3 (b) Topography after Etching of B7B2 Core Specimen

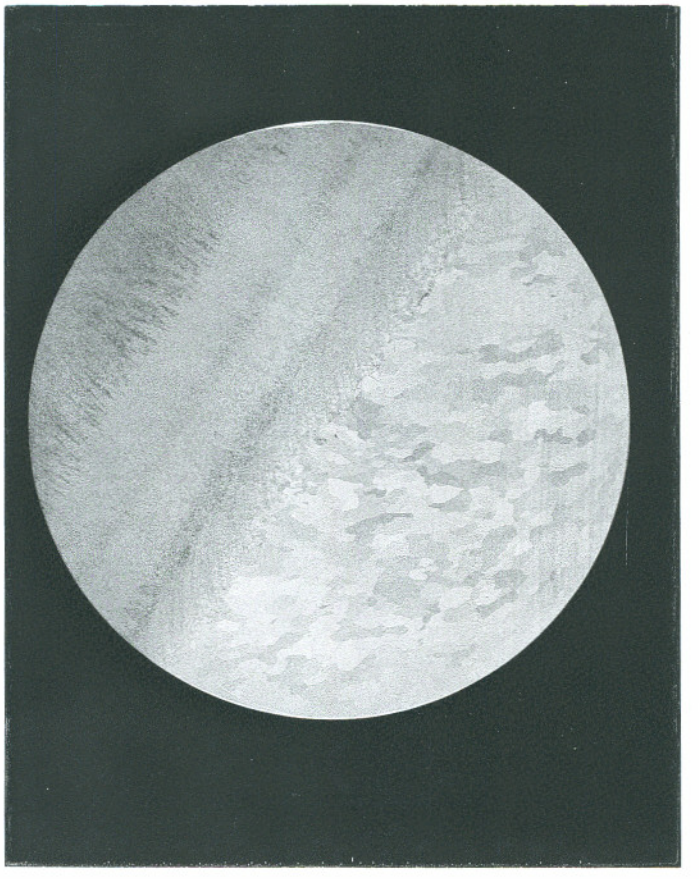

Figure 3-3 (c) Topography after Etching of C3B1 Core Specimen

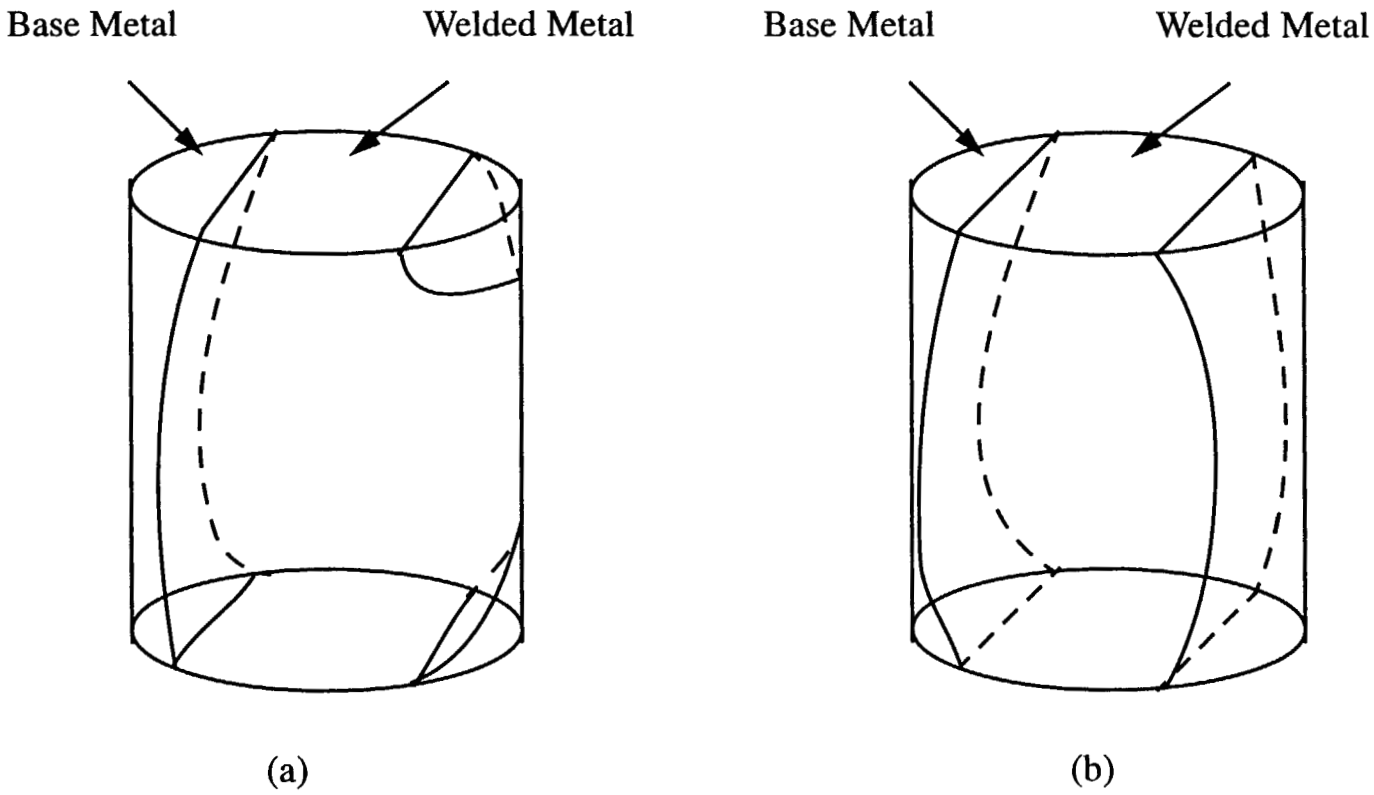

Figure 3-4 (a) Schematic Illustration of the Fusion Line Shape of B3B1 and D3B1 WCL Specimen
(b) Schematic Illustration of the Fusion Line Shape of C7B2 and C3B2 WCL Specimen

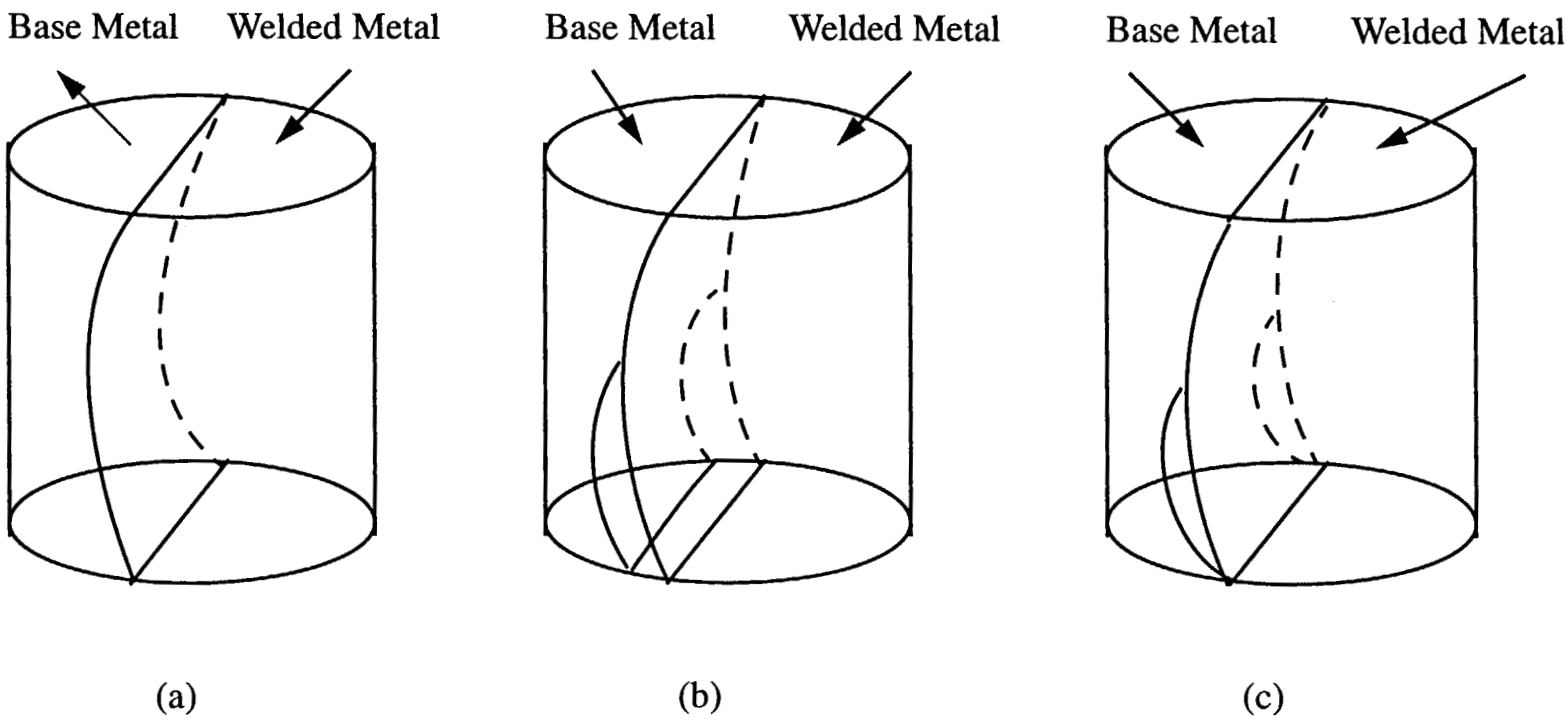

Figure 3-5 (a) Schematic Illustration of the Fusion Line Shape of C7B1, B7B1, B7B2, B3B2 and D3B2 HAZ Specimen
(b) Schematic Illustration of the Fusion Line Shape of D7B1 HAZ Specimen
(c) Schematic Illustration of the Fusion Line Shape of C3B1 HAZ Specimen

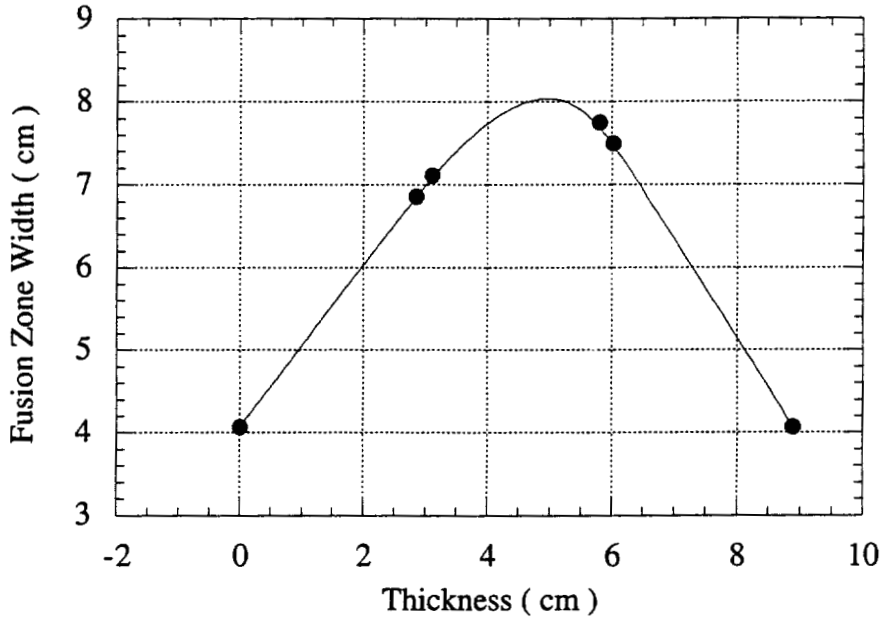

Figure 3-6 (a) Relationship of Fusion Zone Width with Thickness of B3B1 WCL Specimen

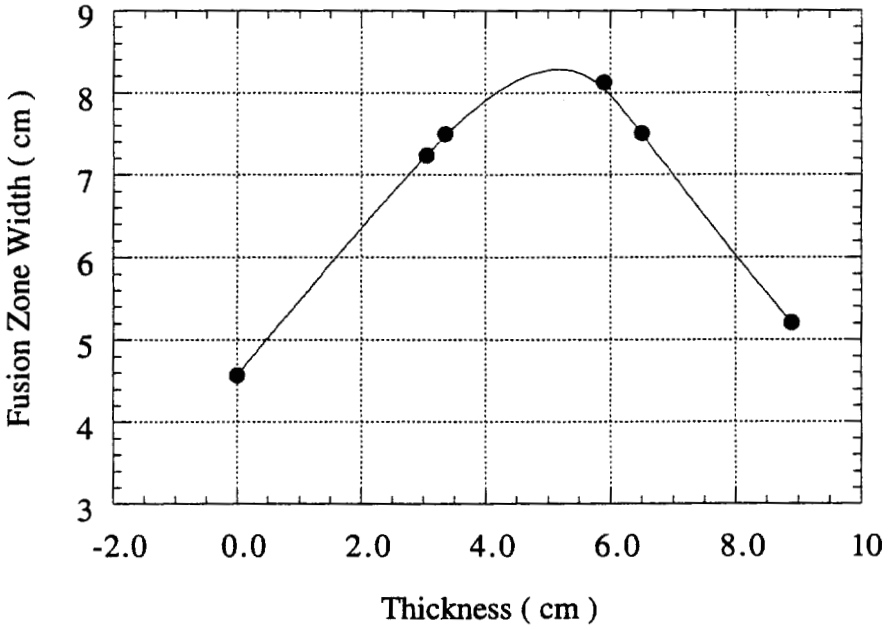

Figure 3-6 (b) Relationship of Fusion Zone Width with Thickness of D3B1 WCL Specimen

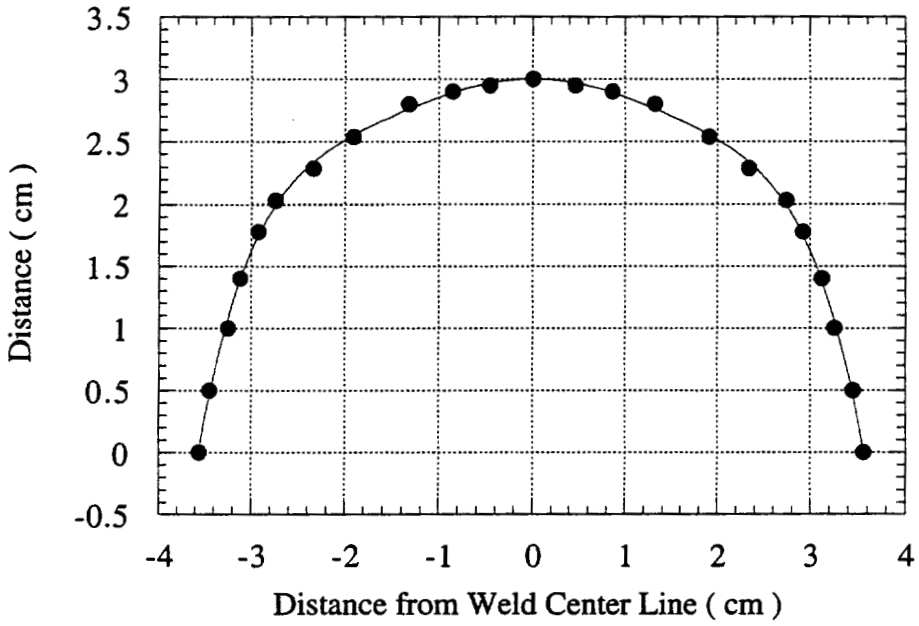

Figure 3-7 (a) Solidification Band Shape of B3B1 WCL Specimen
Curve Fit:

$Y=3+1.52x10^{-14}X-0.16X^2-4.3x10^{-15}X^3+0.018X^4+2.6x10^{-16}X^5-0.002X^6$

(R=0.99931)

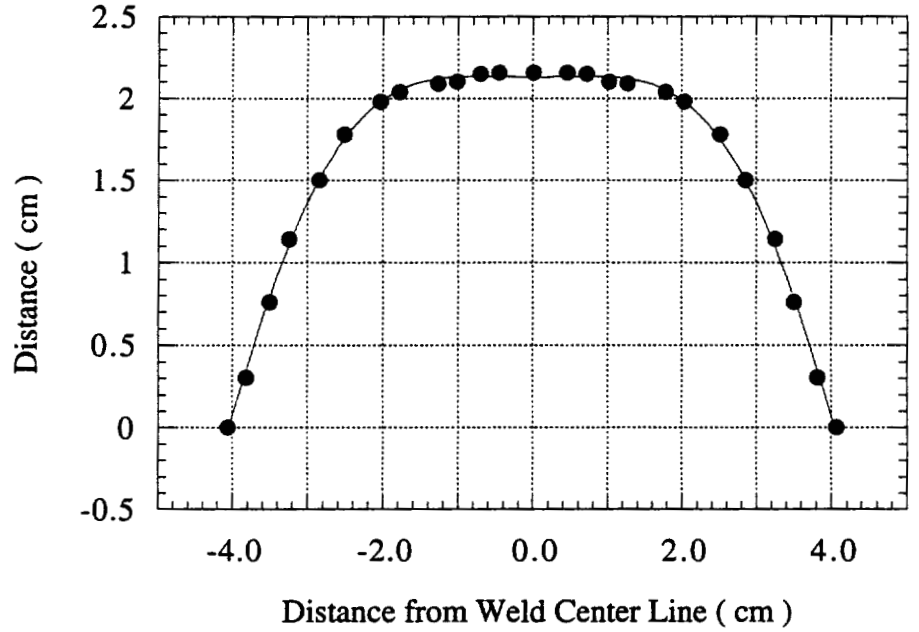

Figure 3-7 (b) Solidification Band Shape of D3B1 WCL Specimen
Curve Fit :

$y=2.13+6.14x10^{-11}\ X\ +0.017X^2-1.19x10^{-11}X^3-0.014X^4+5.16x10^{-13}X^5+0.0003X^6$

(R=0.99933)

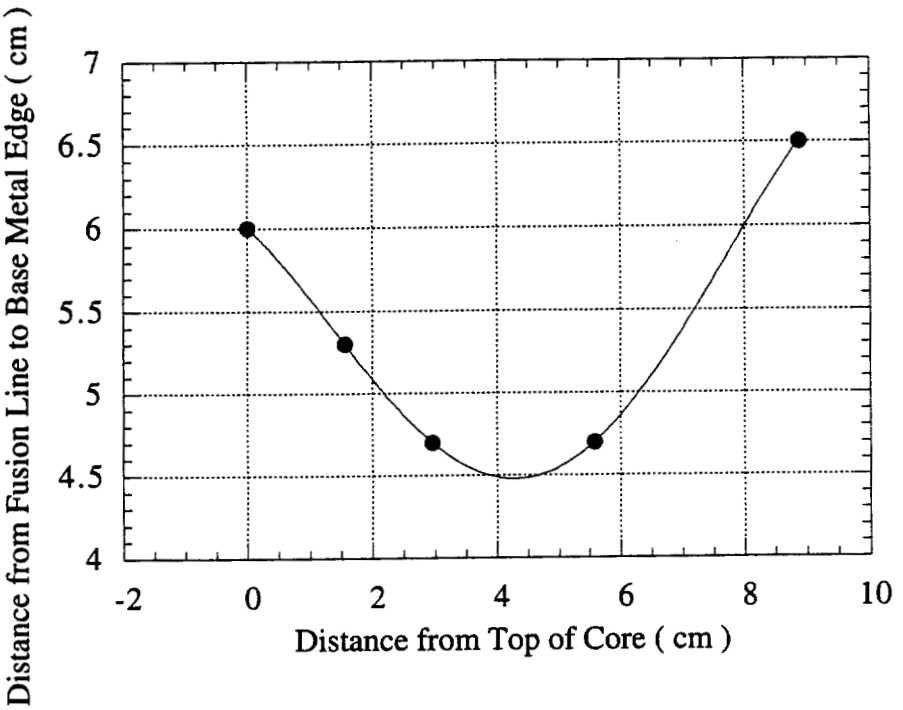

Figure 3-8 (a) Relationship of Fusion Line Position with Thickness of C7B1 HAZ Specimen Curve Fit:

$Y=6-0.32X-0.14X^2+0.04X^3-0.002X^4$ (R=1)

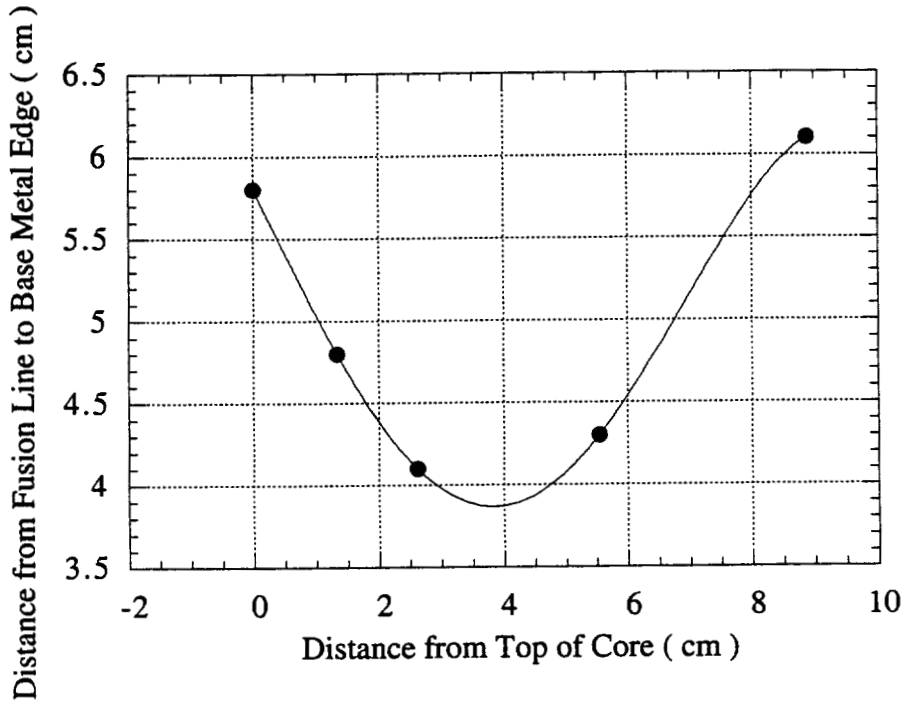

Figure 3-8 (b) Relationship of Fusion Line Position with Thickness of B7B1 HAZ Specimen Curve Fit:

$Y=5.8-0.77X-0.027X^2+0.034X^3-0.002X^4$ (R=1)

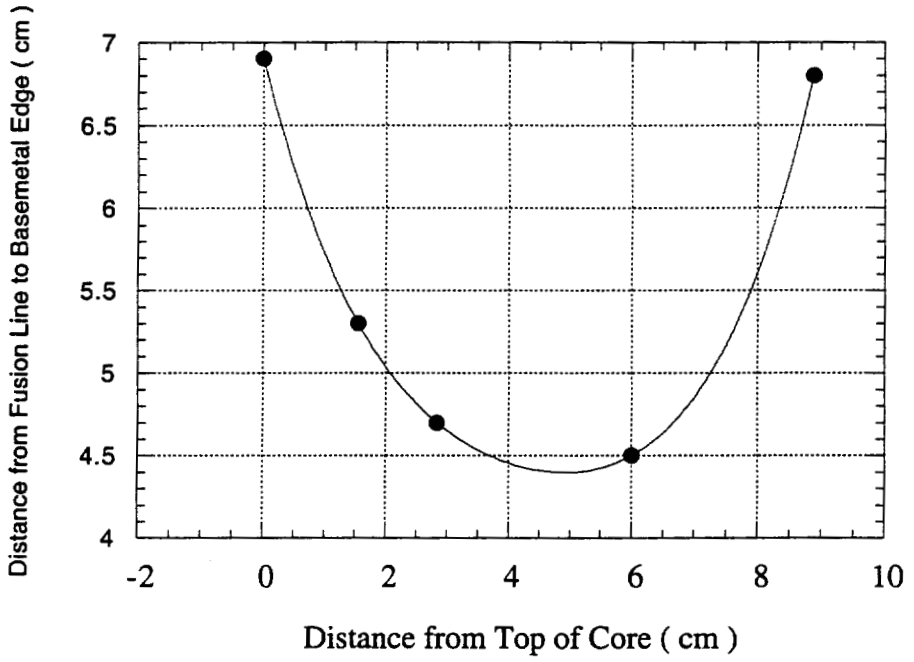

Figure 3-8 (c) Relationship of Fusion Line Position with Thickness of B7B2 HAZ Specimen Curve Fit:
$Y=6.9-1.5X+0.37X^2-0.05X^3+0.0028X^4$ (R=1)

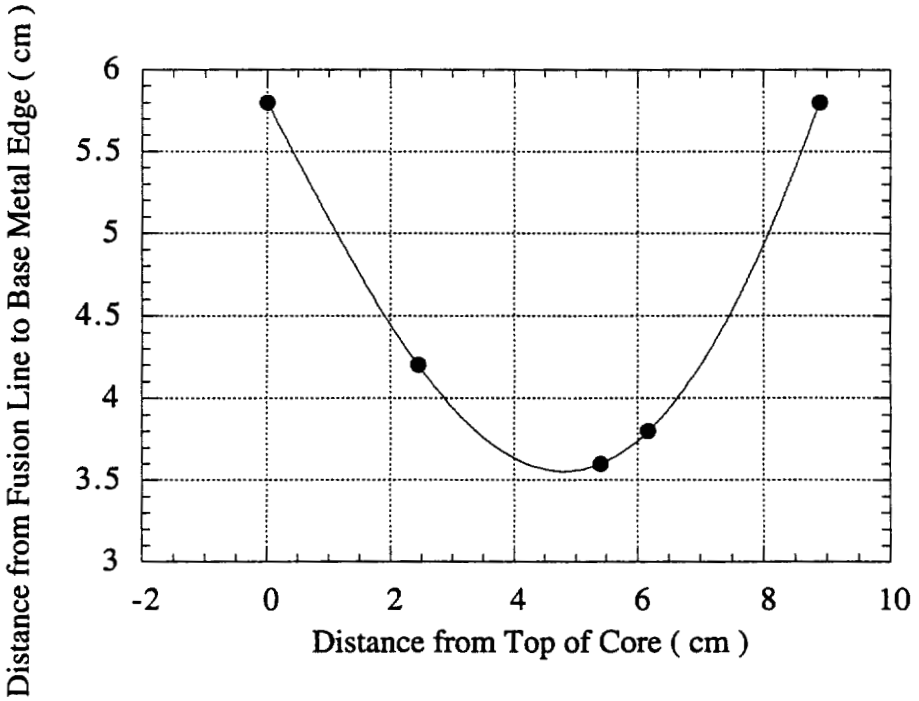

Figure 3-8 (d) Relationship of Fusion Line Position with Thickness of B3B2 HAZ Specimen Curve Fit:
$Y=5.8-0.72X-0.0029X^2+0.014X^3-0.00055X^4$ (R=1)

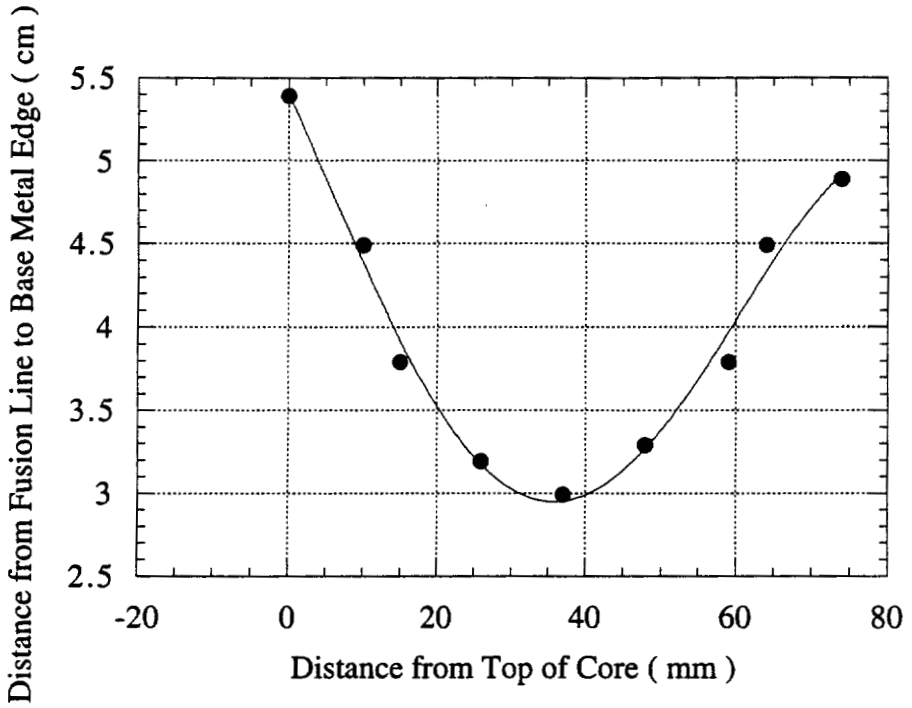

Figure 3-8 (e) Relationship of Fusion Line Position with Thickness of D3B2 HAZ Specimen Curve Fit:

$Y=5.4-0.1X-0.00077X^2+6.38x10^{-5}X^3-4.9x10^{-7}X^4$ (R=0.99191)

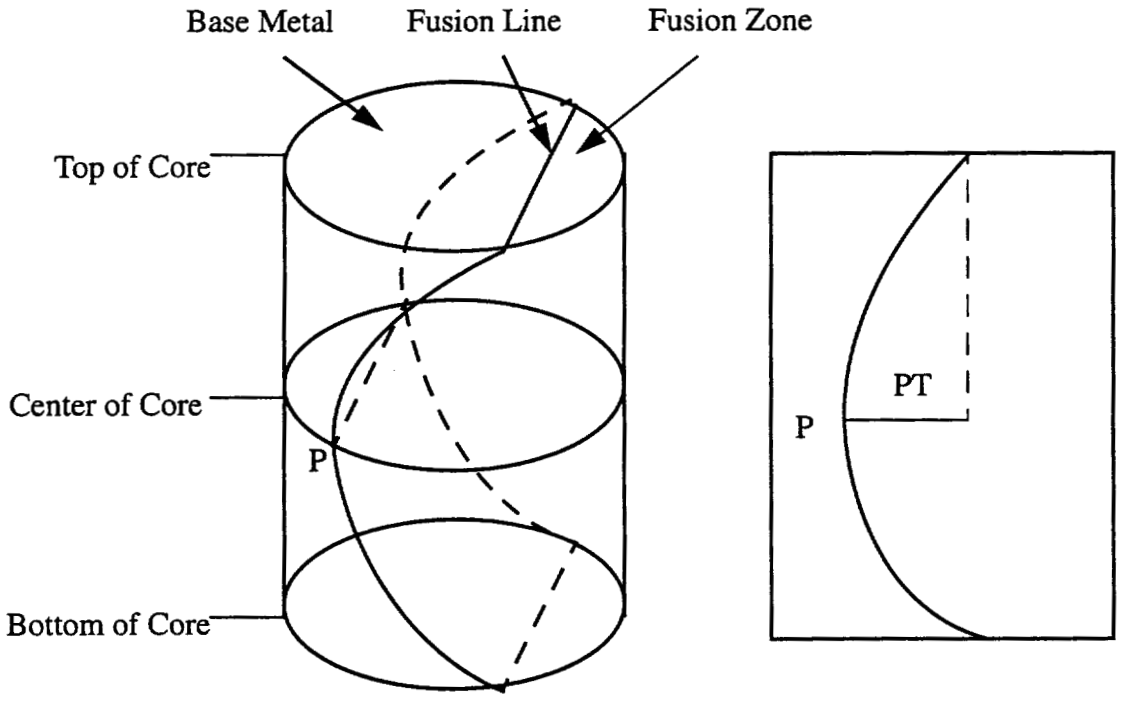

Figure 3-9 PT Position for Heat Affected Zone Specimens

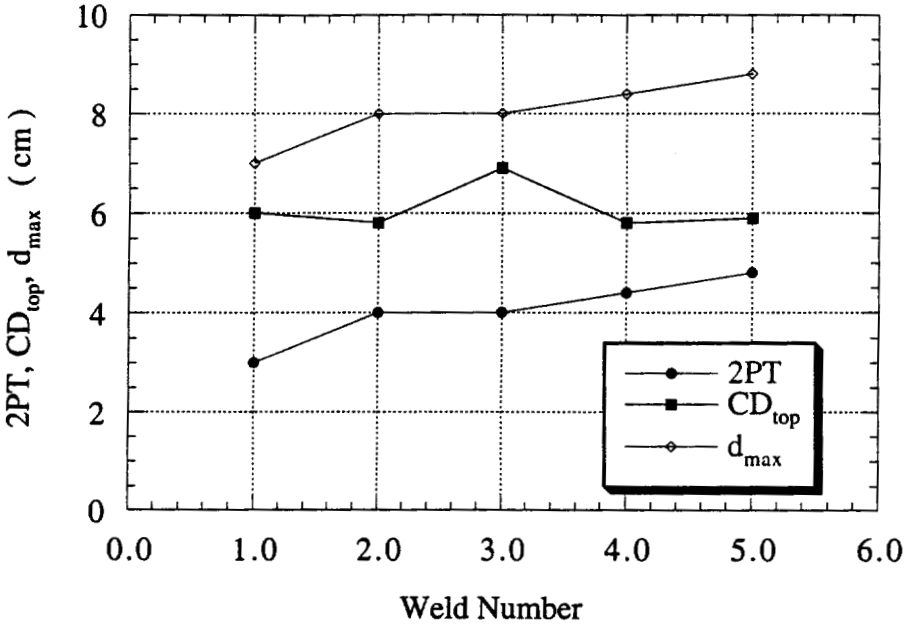

Figure 3-10 Relationship between Weld Number and 2Pt, CD_{top} and d_{max}
(C7B1, B7B1, B7B2, B3B2 and D3B2 for weld number 1 to 5 sequentially)

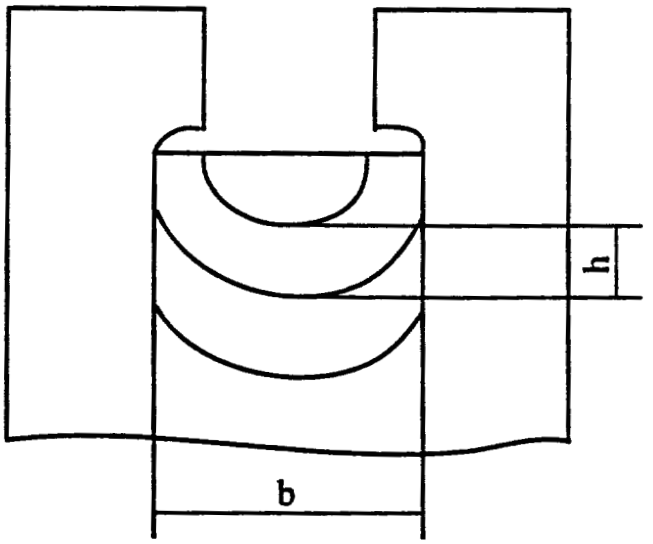

Figure 3-11 Weld Pool Shape During Electroslag Welding Process

CHAPTER 4

RESIDUAL STRESS MEASUREMENT

4.1 INTRODUCTION

Oregon has two steel bridges that were fabricated using electroslag (ES) butt welds, namely, the West Linn Bridge on 1-205 and the approach structure to the Fremont Bridge on I-405. The work reported herein is directed towards assessment of the residual stress fields associated with ES welding in the West Linn Bridge. The objective of this work is to develop an experimental database that can be used to assist in quantifying the residual stress/strain field in ES butt welded steel plates. The specimens used to obtain this database are 3.5" diameter through-thickness "cores" removed from the West Linn Bridge. Strain relief measurements were first taken to determine the relief present due to initial core removal from the bridge. A second set of strain relief measurements was taken as the cores were being sectioned for subsequent machining into fracture toughness specimens. This chapter summarizes the measurement results and interpretation of these results.

Relief strain of the cored material is what is measured experimentally. These core-related strain measurements can then be used to calculate "nominal" core-related relief stresses. Residual stress present in the structure prior to core removal is equal in magnitude and opposite in sign to relief stress. However, simply taking the measured relief stresses and changing their sign can not, in general, be used to make assessment of the actual residual stress distribution. The measured relief stresses yield general information on the change in dimension/stress state of the individual cut "sections" of the structural component under investigation, but do not necessarily readily yield a composite

picture of the actual residual stress state of the original "uncut" structure. The relief stress measurements can be used as an indication of the residual stress state in the original structure, but the actual residual stress state analysis is complex and can not be determined by simple analysis of core-related relief stresses.

A major problem with using the core-related strain relief measurements for subsequent residual stress analysis is that the strain relief sample geometry was decided based on the need for fracture toughness specimens, which was not a desirable strain relief measurement geometry. Strain relief specimen geometry is preferably a narrow slice of material parallel to the desired strain/stress direction to be measured. This allows one to consider the strain/stress perpendicular to the analyzed direction to be essentially zero for simple result interpretation. A cylindrical specimen geometry, such as the one used in this study, results in the need to measure and to assess strains parallel to and perpendicular to the desired analysis direction, thus greatly complicating data interpretation. Complete interpretation of the complex stress/strain changes measured in this study would require complex FEA. The measured relief strain/stress results from this study will simply be assessed as being indicators of surface related strain/stress. This approach is in actuality correct as the experimentally measured strains are surface strains. The initial coring operation would be expected to generate the major amount of surface core relief, with the subsequent sectioning of the core yielding a second-order effect on relieved strain/stress.

It is desirable to determine the relieved surface strain/stress by "tree-panning" out a thin, strain-gaged, surface layer of material directly from the bridge. Or, at a minimum, tree pan out a surface layer the thickness of the sectioning slice nearest the gage surface. However, one can postulate that the relief strains/stresses seen by a tree-panned slice will be closely associated with the final cumulative cored and sliced results, as these multiple cuttings essentially "free" the last slice of all connections to the rest of the bridge material. A first approximation of the stress state of the surface material associated with the bridge will be given below. The initial coring results are assessed first, and then the cumulative coring plus slice results are assessed. These results/trends are then compared with the ESW FEA model results in Chapter 8.

4.2 STRAIN MEASUREMENT

Electrical-resistance strain gages are normally employed on the free surface of a specimen to measure the stress at a particular point. Three strains at a point should be measured to completely define either the stress or the strain field. With three strains at a particular point, principal strains and principal angle can be calculated. The principal angle is defined as the angle between x axis and one of the principal strain directions. The elastic constants such as elastic modules and Poisson's ratio of the specimen material should be known for conversion of the strains into stresses.

Stress state decides which kind of strain gages to be used - a one element gage or multiple element gage. In certain special cases, the state of stress can be established with a single strain gage. This requires a uniaxial state of stress where $\sigma_{yy}=\tau_{xy}=0$ with the known direction of σ_{xx}. In this case a single-element strain gage is mounted with its axis coincident with the x-axis. The stress σ_{xx} is given as :

$$\sigma_{xx}=E\varepsilon_{xx} \tag{4-1}$$

For an isotropic stress state where $\sigma_{xx}=\sigma_{yy}$ and $\tau_{xy}=0$, a strain gage may be mounted in any direction, and the magnitude of the stress can be established as following:

$$\sigma_{xx}=\sigma_{yy}=\frac{E}{1-\mu}\varepsilon_{\theta} \tag{4-2}$$

where

σ_{xx}	=	Stress along x-axis.
σ_{yy}	=	Stress along y-axis.
τ_{xy}	=	Shear stress.
ε_{θ}	=	Strain measured in any direction in the isotropic stress field.
E	=	Elastic modules.
μ	=	Poission's Ratio.

When less is known beforehand regarding the state of stress in the specimen, it

is necessary to employ multiple-element strain gages to establish the magnitude of the stress field. If the specimen has axis symmetry, or if a brittle-coating analysis has been conducted to establish the principal-stress directions, this knowledge can be used to reduce the number of gage elements required from three to two.

The work reported herein entails the use of strain gages to measure the residual stress distribution through the thickness of the core specimens which have been drilled from the West Linn Bridge on I-205. Because all of the core specimens were to be cut into several slices in preparation for subsequent CVN or fracture toughness testing, the residual stress measurement sectioning method was used instead of using the hole drilling or nondestructive methods. The triaxial relieved stress distribution through the thickness of the welded plate can be inferred from the measured residual stress after each cut. In order to know the thermally induced stress of welding inside the welded plate, the dead load of the bridge structure as well as the weld induced residual stress relieved by the coring operation should be considered. A 90° rosette strain gage was welded on the top of the cores before the cores were removed from the bridge. In this way, the relief of the dead load plus the weld induced stresses incurred due to core removal from the bridge structure can be measured by using the weld on strain gages. An initial post-core-removal residual stress analysis on D3B2 WCL core and D3B1+8 Base Metal core specimens involved the use of three more gages glued to the core. One was glued to the bottom surface of the core and the other two on circumference of the core specimen to get detailed information of the residual stress inside the core. The original two element gages and additional three element gages on the top and bottom of the cores were used to determine the magnitude and direction of principal stresses. The two element gages on the circumference of the cores were intended to investigate the stress distribution along circumference directions of cores. The results of D3B2 and D3B1+8 core specimens revealed that residual stress is mainly parallel to or perpendicular to welding direction, as discussed below. The residual stress along circumference and axial direction of the core was found to be very small. Based on the results of D3B2 and D3B1+8 core specimens, all of the other cores only had one more three element gage added on the bottom of the cores without any two element gage along the circumference of the cores.

4.3 PRINCIPAL STRESS CALCULATION

This study uses one-element, two-element and three-element gages. With different gages there are different principal stress calculation methods. It is important to note that when a strain gage is used under any condition other than those employed in the gage-factor calibration, there is always some degree of error due to transverse sensitivity. The error can be compensated with the transverse-sensitivity factor for each gage, and coordinate stress can then be calculated from the adjusted strain. With the three element gage, principal strain, principal stress and principal stress direction can be calculated. As for the two element gage and one element gage, it is assumed that the principal stress direction was known and the gages were glued along the principal stress directions. The principles for calculating stresses from measured strains for different gages were as following.

THREE-ELEMENT RECTANGULAR ROSETTE

The strain measured by the three gage rectangular (45-degree) rosette should be adjusted with the following formulation:

$$\varepsilon_A = \frac{\varepsilon_1'(1-\nu_0 K_{t1}) - K_{t1}\varepsilon_3'(1-\nu_0 K_{t3})}{1-K_{t1}K_{t3}} \tag{4-3a}$$

$$\varepsilon_B = \frac{\varepsilon_2'(1-\nu_0 K_{t2})}{1-K_{t2}} - \frac{K_{t2}[\varepsilon_1'(1-\nu_0 K_{t1})(1-K_{t3}) + \varepsilon_3'(1-\nu_0 K_{t3})(1-K_{t1})]}{(1-K_{t1}K_{t3})(1-K_{t2})} \tag{4-3b}$$

$$\varepsilon_C = \frac{\varepsilon_3'(1-\nu_0 K_{t3}) - K_{t3}\varepsilon_1'(1-\nu_0 K_{t1})}{1-K_{t1}K_{t3}} \tag{4-3c}$$

Since the transverse sensitivities of the orthogonal gages (1) and (3) are nominally

the same, then let

$$K_{t1}=K_{t3}=K_{t13} \tag{4-4}$$

$$\varepsilon_A=\frac{1-\nu_0 K_{t13}}{1-K_{t13}^2}(\varepsilon_1'-K_{t13}\varepsilon_3') \tag{4-5a}$$

$$\varepsilon_B=\frac{(1-\nu_0 K_{t2})(1+K_{t13})\varepsilon_2'-K_{t2}(1-\nu_0 K_{t13})(\varepsilon_1'+\varepsilon_3')}{(1+K_{t13})(1-K_{t2})} \tag{4-5b}$$

$$\varepsilon_C=\frac{1-\nu_0 K_{t13}}{1-K_{t13}^2}(\varepsilon_3'-K_{t13}\varepsilon_1') \tag{4-5c}$$

where,

ε_1', ε_2', ε_3' = Measured strains (unadjusted) from gage element No.1, No.2 and No.3, unadjusted with transverse sensitivity.

K_{t1}, K_{t2}, K_{t3} = Transverse sensitivity of gage element No.1, No.2 and No.3.

ε_A, ε_B, ε_C = Adjusted strains along gage element No.1, No.2 and No.3.

K_{t13} = Transverse sensitivity of orthogonal gage element No.1 and No.3.

υ_0 = Poission's ratio of the material on which the manufacturer's gage factor was measured (usually 0.285).

The three-element rectangular rosette gages were placed at the 0°, 45°, and 90°. Assume the measured strain is in the Cartesian system, $\varepsilon_A=\varepsilon_{xx}$, $\varepsilon_B=\varepsilon_{yy}$ and $\varepsilon_C=(\varepsilon_{xx}+\varepsilon_{yy}+\gamma_{xy})/2$. $\gamma_{xy}=2\varepsilon_B-\varepsilon_A-\varepsilon_C$, the adjusted strains ε_A, ε_B, ε_C can be used to calculate the principal strain and principal stress. The principal strains ε_1, ε_2 and principal stress direction can be established as following:

$$\varepsilon_1=\frac{1}{2}(\varepsilon_A+\varepsilon_c)+\frac{1}{2}\sqrt{(\varepsilon_A-\varepsilon_c)^2+(2\varepsilon_B-\varepsilon_A-\varepsilon_c)^2} \tag{4-6a}$$

$$\varepsilon_2=\frac{1}{2}(\varepsilon_A+\varepsilon_c)-\frac{1}{2}\sqrt{(\varepsilon_A-\varepsilon_c)^2+(2\varepsilon_B-\varepsilon_A-\varepsilon_c)^2} \tag{4-6b}$$

$$\tan 2\phi=\frac{2\varepsilon_B-\varepsilon_A-\varepsilon_c}{\varepsilon_A-\varepsilon_c} \tag{4-7}$$

The value of ϕ has two values, ϕ_1 and ϕ_2. ϕ_1 refers to the angle between the x-axis and the axis of the maximum principal strain ε_1. ϕ_2 is the angle between the x axis and the axis of the minimum principal strain ε_2.

The principal stresses could be calculated in the following formulation:

$$\sigma_1=E[\frac{\varepsilon_A+\varepsilon_c}{2(1-\mu)}+\frac{1}{2(1+\mu)}\sqrt{(\varepsilon_A-\varepsilon_c)^2+(2\varepsilon_B-\varepsilon_A-\varepsilon_c)^2}] \tag{4-8a}$$

$$\sigma_2=E[\frac{\varepsilon_A+\varepsilon_c}{2(1-\mu)}-\frac{1}{2(1+\mu)}\sqrt{(\varepsilon_A-\varepsilon_c)^2+(2\varepsilon_B-\varepsilon_A-\varepsilon_c)^2}] \tag{4-8b}$$

where,

μ = Poission's Ratio (0.3) of measured specimen material.

σ_1, σ_2 = Adjusted principal stresses.

TWO ELEMENT-90-DEGREE ROSETTE

It is assumed that the two gages of the rosette gage were employed along principal stress direction. The principal strain can be calculated with the transverse sensitivity correction. The adjusted strains along any two perpendicular axes can always be calculated from the following equations in terms of the measured strains along those axes:

$$\varepsilon_1=\frac{(1-\nu_0 K_t)(\varepsilon_1'-K_t\varepsilon_2')}{1-K_t^2} \tag{4-9a}$$

$$\varepsilon_2 = \frac{(1-\nu_0 K_t)(\varepsilon_2' - K_t \varepsilon_1')}{1-K_t^2} \qquad (4\text{-}9b)$$

where,

K_t = Transverse sensitivity.

ε_1 = Adjusted strain of gage element No. 1.

ε_2 = Adjusted strain of gage element No. 2.

If the two gages of the two-element rosette have different values of transverse sensitivity, the actual strain can be calculated from the following equation:

$$\varepsilon_1 = \frac{\varepsilon_1'(1-\nu_0 K_{t1}) - K_{t1}\varepsilon_2'(1-\nu_0 K_{t2})}{1-K_{t1}K_{t2}} \qquad (4\text{-}10a)$$

$$\varepsilon_2 = \frac{\varepsilon_2'(1-\nu_0 K_{t2}) - K_{t2}\varepsilon_1'(1-\nu_0 K_{t1})}{1-K_{t1}K_{t2}} \qquad (4\text{-}10b)$$

The coordinate stress can be calculated in the following way:

$$\sigma_1 = \frac{E}{1-\mu^2}(\varepsilon_1 + \mu\varepsilon_2) \qquad (4\text{-}11a)$$

$$\sigma_2 = \frac{E}{1-\mu^2}(\varepsilon_2 + \mu\varepsilon_1) \qquad (4\text{-}11b)$$

ONE ELEMENT ROSETTE

The error due to transverse sensitivity for a strain gage orientated at any angle in

any strain field, on any material can be expressed as:

$$n_{\epsilon}=100\frac{K_t(\frac{\epsilon_t}{\epsilon_a}+\nu_0)}{1-\nu_0 K_t} \tag{4-12}$$

Where,

ε_a, ε_t = The actual strains parallel and perpendicular to the primary sensing axis of the gage respectively. $\varepsilon_t/\varepsilon_a=-\mu^{-1}$.

If the test specimen is steel, with $\mu=0.285$, then $\varepsilon_t/\varepsilon_a=-3.5$. Assuming that the transverse sensitivity of the strain gage is -3%, then the error is +9.6%. The stress coordinate to the adjusted stress equals the adjusted strain times Poission's ratio of the measured material.

4.4 EQUIPMENT

The equipment that was used in this experiment are as follows:

1. Model 2100 strain gage conditioner and amplifier system.
2. Marvel (Armstrong - Blum MFG Co. Series and Mark II)
   5 - 8 varipitch m42
3. Strain Gauges:

Six types of strain gauges that were used for the residual stress measurement.

1) Strain Gauge A: LWK-06-W250D-350

Resistance in OHMS at 24 °C: 350.0±0.4%

Transverse Sensitivity at 24°C: (-4.0±0.2)% Gage Factor: 2.04±1.0%

2) Strain Gauge B: CEA-06-250UR-350

Resistance in OHMS at 24 °C: 350.0±0.4%

Transverse Sensitivity at 24°C: section 1: (0.4±0.2)% section 2: (0.2±0.2)%

Gage Factor: section 1: 2.095±0.5% section 2: 2.105±0.5%

3) Strain Gauge C: CEA-06-125UT-350

Resistance in OHMS at 24 °C: 350.0±0.4 %

Transverse Sensitivity at 24 °C: section 1: (0.7±0.2)% section 2: (0.5±0.2)%

Gage Factor: section 1: 2.105±0.5% section 2: 2.120±0.5%

4) Strain gauge D: LWK-06-W250B-350

Resistance in OHMS at 24 °C: 350.0±0.4%

Transverse Sensitivity at 24 °C: (-4.7±0.2)% Gage Factor: 2.02±1.0%

5) Strain gauge E: WK-06-125AD-350

Resistance in OHMS at 24 °C: 350.0±0.3%

Transverse Sensitivity at 24 °C: (-2.1±0.2)% Gage Factor: 2.02±1.0%

6) Strain gauge F: EA-06-062RB-120

Resistance in OHMS at 24 °C: 120.0±0.4%

Transverse Sensitivity at 24 °C: section 1,3: (1.3±0.2)% section 2: (0.8±0.2)%

Gage Factor: section 1,3: 2.04±0.5% section 2: 2.045±0.5%

4.5 SECTIONING PROCESS PROCEDURE

1) Glue strain gage on the core specimen.

Besides the weld-on gage on the top of core before the core was removed from the bridge, one or three more gages were glued on the cores to measure the residual stress inside the core specimens along all directions. Initial post-core-removal relief strain/stress analysis on D3B2 HAZ and D3B1+8 base metal core specimens involved the use of three more strain gage rosettes glued to the core. One rosette was glued to the bottom surface of the core and the other two on the circumference of the core specimen to get detailed information of the residual stress inside the core. The original core top two element rosettes and additional core bottom three element rosettes were used to determine the magnitude and direction of principal stresses. The two element rosettes on

the circumference of the cores were used to investigate the stress distribution along the circumferential and axial directions of core. The gauge type and their coordinate glue position on each cores were given in Figure 4-1.

2) Setup and AC/DC power check

Check each 2110A module to set the proper AC line voltage before installing a 2110A Power Supply module in each cabinet. The Power switch on the front panel should be set at OFF position. Install the Power Supply in the right hand position of the cabinet; push in to engage the input/output plug, and secure the thumb screws. Install 2120A Conditioners in the remaining positions in the cabinet. Push the modules in to engage the power-input plugs, and secure the thumb screws. Plug the line cord into an AC receptacle to make certain that the third pin goes to a good ground. The equipment must be grounded for best performance. On each channel, make certain that the EXCITE switches are OFF (thus removing excitation to all gage circuits) and the CAL switchers are in the center (OFF) position. On each Power Supply, turn the CHANNEL selector to "AC". Turn the POWER switch on. The red pilot lamp should light and the meter should read between 9 and 11. Then turn the CHANNEL selector to "DC". The meter should read near the line at 10.

3) Excitation

Set desired excitation on each channel: turn the CHANNEL selector to channel 1; on the left most channel, adjust BRIDGE EXCITE (using a small screwdriver) to read the desired BRIDGE VOLTS on the Power Supply Meter. Turn CHANNEL selector to channel 2 and repeat the above procedure adjusting BRIDGE EXCITE on the next channel; continue until all installed channels are satisfactorily adjusted. 10v bridge excitation voltage was chosen for these experiments. Connect the gage INPUT plugs. The system is now ready for use. If it is planned to use the system immediately, it is suggested that the POWER be left on (for warm-up); otherwise turn all POWER to OFF.

4) Zero Amplifier

Adjust the AMP to zero for each channel.

5) Bridge Balance

For each channel, turn the EXCITE switch to ON; then turn the BALANCE

control to extinguish the OUTPUT lamps. Connect OUTPUT plugs for each channel.

6) Shunt Calibration

It should be noted that the purpose of shunt calibration is to determine the performance of the circuit into which the gage is wired, and in no way does it verify the ability of the gage itself to measure strain or the characteristics of its performance. Shunt calibration can be achieved by shunting any one of the four arms of the input bridge. The calibration equation is as following:

$$\mu\varepsilon = \frac{R_A}{K(R_{cal}+R_A)} \times 10^6 \qquad (4\text{-}13)$$

where,

$\mu\varepsilon$ = Standard calibration value (microstrain).

K = Effective gage factor of strain gage.

R_A = Precise effective resistance of arm shunted (ohms).

R_{CAL} = Resistance of calibration resistor (ohms).

K may be the actual package gage factor of the strain gage in use. It may also be adjusted for leadwire desensitization with the following equation:

$$K = k' \frac{R_G}{R_G+R_L} \qquad (4\text{-}14)$$

Where,

K' = Package gage factor of active gage.

R_G = Resistance of strain gage (ohms).

R_L = Resistance of leadwire in series with active gage (usually the resistance of one leadwire) (ohms).

Package gage factor of active gage was used to do the shunt calibration in this experimental work.

7) Cut Core Specimens

Cores were sectioned at OGI by using an automatic-feed band saw with a slow cutting speed of 50 feet/minute, 30 pounds load and continuous coolant to minimize heating. The thickness for each slice and the cut sequence are shown in Figure 4-1 for each core specimens.

8) Measurement of strain relieved after each section

The given strain gages were zeroed prior to core sectioning. The core was then cut and the specimen was taken back to the 2100 strain gage conditioner and amplifier system to determine the change is strain due to slicing. This procedure was repeated for each slice.

4.6 RESULTS

Relief strain measurements were not made during the coring operation on all cores, as summarized in Table 4-1. The strain relief measurements taken by ODOT personnel during the coring operation are presented in Table 4-2. Each core is identified by core number and core type, i.e., base metal, WCL or HAZ. The strain relief measurements for both the coring and sectioning operation for all cores are given in Table 4-3 to Table 4-24 and Figure 4-2 to Figure 4-4. One thing that needs to be pointed out is that all of the figures have been labled as "residual stress through thickness" which is just for illustration of the data when a given slice was cut at a certain thickness. It does not actually represent the residual stress at that thickness point.

The actual measured strain values, as well as the corrected calculated strain values are given in the tables. The relief stress values derived from the calculated strain values are also presented. Detailed information is summarized in the following sections: Base Metal Core Results, WCL Core Results and HAZ Core Results. It should be noted that two kinds of stain/stress concepts are employed in this chapter. The measured strain/stress relief data, which come from the reading results during coring or sectioning process, are listed in tables for each core specimen. These data are associated with the cores only. The other kind of strain/stress is associated with the plate and is relieved

residual stress. The residual strain/residual stress has the same absolute value as the measured strain/stress with opposite sign. This kind of data is shown in figures for each specimens. In order to distinguish these two kinds of strain/stress, the measured strain/stress is just named as strain/stress. The strain/ stress which are associated with plate are named as residual strain/residual stress.

BASE METAL CORE RESULTS

Three base metal cores were taken. Two base metal core specimens, B1+4 and D3B1+8, were drilled from the bridge. A third core was a feasibility plate core. The B1+4 core was taken from a 2.5 inch (6.35 cm) thick plate at a location where the bridge loading is expected to be approximately zero. The D3B1+8 core was taken from a 3.5 inch (8.89 cm) thick plate in a region where rolling-induced residual stress and bridge loading is expected, similar to the loading expected in the areas of the weldment cores; the thickness of this plate material was the same as that for the welded plates. The feasibility core was taken from an A36 plate of intermediate thickness, namely 3 inch (7.62 cm). This plate certainly was under zero external load. The data from B1+4 core and the feasibility core can be used to evaluate the rolling stress.

The base metal coring results for the cores from bridge are listed in Table 4-2 and for the feasibility core in Table 4-25. The calculated strain and stress measured by the three element gage on the bottom of D3B1+8 during sectioning operation are given in Table 4-3. The calculated strain and stress measured by the two element weld-on gage on top of D3B1+8 during sectioning operation are given in Table 4-4. The calculated strain and stress measured by the two element gage on the circumference of D3B1+8 during sectioning operation are given in Tables 4-5 and 4-6. During the measurements for D3B1+8, when the saw got close to the side gage, some damage took place and it was impossible to get meaningful data for some readings. The calculated strain and stress measured by the three element gage on the bottom and two element weld on gage on the top of B1+4 during sectioning operation are given in Table 4-7. Because the angle between element F1 and F2 is 45°, according to the results in Table 4-6 of B1+4, the

principal residual stress is along longitudinal and lateral to box girder direction inside base metal core. It can be further inferred that the maximum principal stress value measured by the D3B1+8 is lateral to box girder direction and minimum principal stress is longitudinal to box girder direction.

The residual stress through thickness distribution for D3B1+8 base metal core is shown in Figures 4-2 (a) and (b) and for B1+4 base metal core in Figure 4-2 (c). The residual stresses measured by both the top and the bottom strain gage are plotted in the same figure. There are two stress values for the 45 mm position, one from each gage, as the specimen was first cut in the middle. The plots in Figure 4-2 (b) are similar as one of the circumference gages was glued at the bottom and the other one at the top. The duplicate stress relief readings presented in Figure 4-2 (c) are at the 10 mm level, as the first core parting cut was made off the center. Thus the bottom gage readings are 10 mm or less and the top gage readings are for 10 mm or more. The difference in placement of the first and subsequent core sectioning cuts are related to whether the resulting mechanical property specimens were CVN (center line cut) or K/J (off-center line cut). There were two extra two-element gages on the circumference of the D3B1+8 core with one near the bottom of the core and one near the top of the core.

WCL CORE RESULTS

A total of four WCL core specimens were drilled from the bridge-B3B1, D3B1, C3B2 and C7B2. The residual bridge stresses relieved by the coring operation are presented in Table 4-2. The measured strain and stress of B3B1, D3B1, C3B2 and C7B2 during core sectioning process are given in Tables 4-8 to 4-12.

The residual stress through thickness distributions for B3B1, D3B1, C3B2 and C7B2 WCL cores are shown in Figures 4-3 (a) to (d). As for Figures 4-3 (a) to (c), the data to the left of 30 mm on the figure was from the three element gage on the bottom of the core. All of the remaining data was from the two element gage which is on the top of the core. As for Figure 4-3 (d), the data for thickness less than 26 mm is measured by the three element gage on the bottom of the core and for thickness bigger

than 26 mm by the two element gage on the top of the core. The data at 26 mm has two values for each direction with one from two element gage on top of the core and the other one from three element gage on the bottom of the core.

HAZ CORE RESULTS

A total of eight HAZ specimens were drilled from the bridge: B3B2, B7B1, B7B2, C3B1, C7B1, D3B2, D7B1 and D7B2. Six HAZ cores were strain gaged prior to coring. There were no gages applied to the D7B2 specimen before coring from the bridge and sectioning. So no relief stresses were measured on D7B2. The residual bridge stresses relieved by the coring operation are presented in Table 4-2. The measured strain and stresses of all of the other core specimens during sectioning process are shown in Tables 4-13 to 4-24.

The residual stress through thickness distribution for B3B2, C3B1, B7B1, B7B2, C7B1, D7B1 and D3B2 HAZ cores are shown in Figures 4-4 (a) to (h). When thickness is near 60 mm for Figures 4-4 (a) and (b), 30 mm for Figures 4-4 (c) to (f), there are two data for the same position and same direction. One is from the two element gage on the top of core and the other one from three element gage on the bottom of the core. Figures 4-4 (g) and (h) show the data from thickness less than 45 mm measured by three element gage on the bottom of the core. The data from the thickness bigger than 45 mm is measured by two element gage on the top of the core. The data at 45 mm has two values with one from two element gage on the top of the core and the other one from three element gage on the bottom of the core.

4.7 DISCUSSION

The general pattern of the experimentally determined residual stress seen in the majority of the results is as follows:

1. The major stress relief takes place during the coring operation.
2. A secondary "major" change of the opposite sign to that exhibited during coring

takes place when the cut farthest away from the strain gaged surface is cut.

3. Subsequent sectioning operation closer to the strain-gaged surface results in decreasing change in relief stress.
4. All sectioning-induced changes tend to yield stress relief of the opposite sign observed in the original coring operation.

The residual stress in and near the weldments on the bridge consisted of three parts: one from the dead load of the bridge, one from rolling induced stresses in the plate and the other one from the thermally induced stresses during welding. The effect of each kind of stress on residual stress measurement of this study is discussed in following four major categories.

DEAD LOAD FROM BRIDGE AND ROLLING STRESS

As the base metal cores are far away from fusion zone, it is assumed that they are not affected by the thermally induced stress from welding. The results of base metal cores give information about dead load stress distribution of the bridge and rolling induced stresses.

All of these cores exhibited stress relief due to the coring operation, and the relieved strain indicated that the cored material was under a compressive residual stress prior to the coring operation. The coring-induced results indicate that the rolling-induced residual stresses are significant when compared with the expected bridge loading stresses. These results indicate that the rolling stresses relieved by the coring operation are in the range of 10 ksi (70 MPa) and are compressive. There are differences between the two zero-load plate coring residual stress results. It is not surprising to have such differences since the plates have different thickness and are from different heats as well as from different steel producers. Note that the coring operation does not necessarily relieve all of the rolling-induced residual stresses in the cored material, as will be evident from the core sectioning results. The observed difference between longitudinal beam stresses (the same as stresses perpendicular to the ESW welding direction) for the zero (bridge) load condition and the bridge load condition appears to be around -15 ksi (-105 MPa). The

observed difference between lateral beam stresses (the same as stresses parallel to the ESW welding direction) for the zero (bridge) load condition and the bridge load condition appears to be around -8 ksi (-56 MPa) which is expected to be almost zero. It is assumed that this difference should represent the dead load condition, which is expected to be nominally -10 ksi (70 MPa) for longitudinal beam stress, and will be completely relieved by the coring operation. It is not known how much significance should be put on this difference, as we do not know the expected statistical variance of a given reading, and the residual stress state of the 3.5 inch (8.89 cm) plate may well be somewhat different from either of the two thinner plates. However, the order of magnitude change is correct and of the right sign.

Figure 4-5 presented the base plate rolling-induced relieved stresses as a function of plate thickness. The measured transverse stresses are plotted as the actual measured values since it is assumed that there are no bridge loading transverse stresses present. It is interesting to note that the relieved internal stresses appear to decrease linearly with increasing plate thickness. The longitudinal stress relief values for the two no-load condition are plotted and found to also decrease with increasing plate thickness, although at a much lower rate. A linear extrapolation value of around 9 ksi (63 MPa) for longitudinal stress and 8 ksi (56 Mpa) for lateral stress is predicated for the 3.5 inch thick plate from these results. This indicates that the bridge dead load induced a compressive stress of approximately -16 ksi (-112 MPa) versus the expected -10 ksi (-70 MPa) longitudinal stress and zero lateral stress. This is only a bridge loading assessment. It is not known how realistic it is. However, it can be inferred that the longitudinal load stress is in the range of lower than half yield stress level and very low lateral stress. In the following discussion, -15 ksi (105 Mpa) longitudinal dead load and zero lateral dead load of the bridge were used for thermal stress analysis.

Rolling stress will be released when the parts are heated up and cooled down naturally. So there is no rolling stress is expected in and near the fusion zone of the weldments. How far away from the fusion zone the rolling stress has been released during ESW welding process is unknown. Based on the thermal modeling results of this study, the rolling stress has minimum effect on the experimental results among the three

kinds of stress. The effect of rolling stress is almost negligible for WCL cores and HAZ cores. The detailed discussion is given in Chapter 8. So for WCL core results and HAZ core results analysis, only dead load of the bridge and thermal stress from welding process were discussed.

THERMAL RESIDUAL STRESS FROM CORING RESULTS

Visualization of a simplified meaning of the original coring operation results is much easier than that of the core sectioning results. Assuming that the core material relaxation takes place uniformly through-thickness, the coring-induced strains/stresses can be visualized as acting over the complete core cylinder.

The WCL core results are summarized in Table 4-26. The thermal residual stress found from coring operation for WCL core is expected to be coring results minus dead load of the bridge. The results indicate that the thermal longitudinal residual stress (perpendicular to ES welding direction) is in the range from -5 ksi (35 MPa) to 10 ksi (70 MPa) and the thermal parallel residual stress (parallel to the ES welding direction) is about 30 ksi (210 MPa). The average results reveal that the thermal longitudinal stress is very low and negligible and thermal parallel stress is close to yield stress range.

The HAZ core results are summarized in the same way as WCL core in Table 4-27. The results reveal that the thermal longitudinal stress is in the compression stress state range from -4 ksi (28 MPa) to -14 ksi (98 MPa) and the thermal parallel stress is in tension stress range from 13 ksi (91 MPa) to 29 ksi (203 MPa). The average thermal longitudinal stress is in very low compression range which is almost negligible and the thermal parallel stress is in half yield stress range. The results also reveal that HAZ core results are more scatter than WCL core results which is as expected, because HAZ core has mixed material. Geometrically speaking, they are not HAZ cores as the HAZ region is small compared to either the amount of fusion zone or base metal material in the core. Attempt was made to cut the cores so that the HAZ material at the center of the core would be at the center of the core cross-section to allow subsequent mechanical property evaluation. This results in approximately half the core being fusion zone material and the

other half being base metal material with the HAZ zone separating these two material regions. In this complex material state, the stress state is also expected to be complex. In this complex stress state, gage position on the core will also affect the experimental data, i.e., the gage may have been glued on fusion zone, HAZ zone or base metal part of the core. As for WCL core, most material of the core is fusion zone material. The stress data is more simple and most likely the gage can be glued on the fusion zone. However, all of the HAZ core results are very reasonable and basically consistent with each other.

Combing the results of WCL core and HAZ core, the thermal stress is substantially decreased in HAZ core compared to WCL core. In general, the strain gage on HAZ core has been glued farther away from weld center line than the strain gage on WCL core. The strain gage position difference from weld center line is about half the fusion zone. Thus the thermal stress has substantially changed from weld center line to heat affected zone. The general thermal stress distribution in these ES weldments are as following:

1. The longitudinal thermal stress is very low and changes from tension stress to compression stress as the distance from WCL increases to near HAZ.
2. The parallel thermal stress is in tension stress range and changes from around material yield stress to around half yield stress as the distance from WCL increases to near HAZ.

THERMAL RESIDUAL STRESS FROM CORING PLUS SECTIONING RESULTS

In this study, two kinds of process (coring and sectioning) have been applied to release the residual stress inside the weldments. If one assumes the stresses are uniformally distributed along core thickness direction, one expects the major surface strain/stress relief contribution when the core is initially cut out of the bridge, as this directly relieves strains present in the plane of the surface. The major effect of subsequent core sectioning would be expected to be the release of strains/stresses in the through-thickness direction with a related Poisson's relief effect in the surface plane, i.e.,

the core sectioning results in this study is core thickness dependent and closely related to the coring operation results. It is necessary to combine the two results together to analize the thermal stress state inside the ES weldments.

Because the gages are glued on the top of the gage, the cut position will affect the measured results of the outer plate surfaces during sectioning process. Even so, the core thickness only affects core sectioning results magnitude not general trend. So one can still get the stress distribution trend based on the measured results without correction for the effect of variable thickness. In this sutdy, the measurement results of the gage during sectioning process have been taken for thermal residual stress analysis without correction for through thickness effect. The thermal residual stress has been calculated by adding the measured residual stress for the same gage during coring process and sectioning process minus the dead load from bridge.

The thermal residual stress from coring plus sectioning results are summarized in Table 4-26 for WCL core and Table 4-27 for HAZ core. The thermal residual stress in certain direction is calculated from coring results plus average sectioning results minus the dead load from bridge. From both tables, it can be seen that the thermal residual stress from coring plus sectioning results are very comparable with the thermal stress from coring results. At the same time, it is very obviously to see that the coring operation released most of the thermal stress inside the ES weldments.

SUMMARY

Based on the above discussion, the general thermal stress distribution trend has been summarized. However, the following issues need to be considered and may be improved in future experimental work to get more accurate thermal stress data in ES weldments:

1. The metallographic examination of weld reveals that essentially all welds has full length fusion line repair welds. These repairs were made from one to several passes. One repair weld sequence had a repair weld completely across the fusion zone surface. The gage has been mounted on the plate surface. The repair will

affect the measurement results. However, the weld repair was assumed to not change the thermal stress distribution trend inside the weldments which was measured in this study.

2. The specimens of this study are from the real world which lack control and record of what went on during the ES welding process.
3. Placement of gages on cores were determined by etching techniques, which, inretrospect, really assessed where and how wide the fusion zone weld repairs were. This means that the gages were centered or off-centered, as was the case for the HAZ cores by the placement of the weld repairs.
4. The core specimens were drilled and sectioned for mechanical property test not merely for residual stress measurement. This part of experimental work was based on this situation and was restricted by the mechanical property test requirement. The biggest issue is the cutting sequence and section thickness during sectioning process. For example, if the section material will be further machined to be fracture toughness test specimen, only three sections were cut from a core with each of them one inch thick. In addition, most sectioning was not done symmetrically, which makes data interpretation difficult. In this situation, it will be very hard to fully understand the exact residual stress inside the core based on the existing experimental results.
5. Normally the cores were cut into 3 pieces. There are three cores that had been cut into more than 3 pieces: D3B1+8 (base metal core), C7B2 (weld center line core) and D3B2 (heat affected zone core). All of these three cores have strain gages glued on both top and bottom. The sectioning results reveal the same phenomena. The longitudinal stress distribution trend for both top gage and bottom gage is the same, i.e., both gages revealing either tension stress or compression stress. Discrepancy existed for parallel stress distribution trend for top gage and bottom gage, i.e., the top gage and bottom gage revealing tension stress for top gage and compression stress for bottom gage. Even base metal core, which had compressive longitudinal stress versus WCL core and HAZ core which had tension longitudinal stress, had tension parallel stress on top gage and

compression stress on bottom gage. So it is expected that all of them have been affected by same factor on the parallel stress distribution. There are five known factors may have effect on this phenomena: dead load of bridge, thermal stress, rolling stress, weld repair and gage related issues like gage position on plate. Because the dead load of bridge had been released during coring process, none of the cores were affected by dead load during sectioning process. Thus dead load of bridge is not the factor causing parallel stress discrepancy for top gage and bottom gage. Based on the following chapters modeling results, it is concluded that rolling stress has negligible effect on residual stress measurement in this study. This is particularly true for WCL core. So rolling stress is not expected to be the factor causing parallel stress discrepancy for top gage and bottom gage either. Base metal core has neither weld repair nor thermal stress effect. The only factor left is the gage related issues. However, it may caused by other unknown factors. For example, the set up of the experiment. What is the exact effect and how it affected the parallel stress measurement still needs to be further study. By the way, because most stress has been released during coring operation, the lack of accuracy of the sectioning results are postulated only affect the data magnitude and not affect the general trend.

6. It is not an unreasonable assumption to make for an idealistic weld modeling situation. It is more difficult to justify in a "real world" situation where grossly off -centered weldments are possible. However, the West Linn Bridge specific fusion line assessments given in Chapter 3 indicate that the assessed welds are reasonable symmetrical, even with the noted fabrication perturbations.

In general, the general trend that has been gotten from coring results and coring results plus sectioning results is reliable and reasonable. However, further work is needed get more accurate stress distribution data.

4.8 CONCLUSION

1) The major stress relief takes place during the coring operation.
2) The longitudinal thermal stress is very low and changes from tension stress to compression stress as the distance from WCL increasing to near HAZ.
3) The parallel thermal stress is in tension stress range and changes from around material yield stress to around half yield stress as the distance from WCL increasing to near HAZ.

Table 4-1 Core Identification Number and Description

Number	Core ID	Core Type	Strain Gaged		Test Type
			Coring	Sectioning	
1	B1+4	Base Metal	Yes	Yes	FT
2	B3B1	WCL	Yes	Yes	FT
3	B3B2	HAZ	Yes	Yes	FT
4	B7B1	HAZ	Yes	Yes	FT
5	B7B2	HAZ	Yes	Yes	FT
6	C3B1	HAZ	No	Yes	FT
7	C3B2	WCL	No	Yes	FT
8	C7B1	HAZ	Yes	Yes	FT
9	C7B2	WCL	Yes	Yes	FT
10	D3B1+8	Base Metal	Yes	Yes	CVN
11	D3B1	WCL	Yes	Yes	FT
12	D3B2	HAZ	Yes	Yes	CVN
13	D7B1	HAZ	Yes	Yes	FT
14	D7B2	WCL	No	No	CVN

Table 4-2 Bridge Core Strain Gage Information and Strain Stress Relief Information

Core ID	Strain Gage Direction Relate to Box Girder Length or ES Welding Direction		Measured Strain (ue)	Calculated Strain (ue)	Stress Relief Associated with Core (Psi)
	Girder	ES Weld			
B1+4	Longitudinal		160	179.5	10289
	Lateral		429.9	442	16346
B3B1	Longitudinal	Perpendicular	799.8	762.4	13632
	Lateral	Parallel	-1180	-1163	-30799
B3B2	Longitudinal	Perpendicular	959.8	924.5	19040
	Lateral	Parallel	-1180	1156.5	-28982
B7B1	Longitudinal	Perpendicular	879.8	864.1	22129
	Lateral	Parallel	-669.8	-642.9	-12647
B7B2	Longitudinal	Perpendicular	709.8	683.4	13998
	Lateral	Parallel	-879.9	-862.6	-21678
C7B1	Longitudinal	Perpendicular	1139.7	978.7	29361
	Lateral	Parallel	-619.8	-532.2	-15967
C7B2	Longitudinal	Perpendicular	789.9	678.3	20349
	Lateral	Parallel	-1180	-1013.3	-30398
D3B1 +8	Longitudinal		759.6	769.1	25559
	Lateral		-10	20.6	8287
D3B1	Longitudinal	Perpendicular	509.7	473	5081
	Lateral	Parallel	-1069.6	-1062.9	-30362
D3B2	Longitudinal	Perpendicular	919.5	894.2	20635
	Lateral	Parallel	-919.6	-894.3	-20639
D7B1	Longitudinal	Perpendicular	919.5	902.7	23018
	Lateral	Parallel	-709.7	-681.7	-13545

Note: C3B1, C3B2 and D7B2 Core Specimens did not strain gaged

Table 4-3 Principal Strain and Principal Stress Measured by Strain Gage B on D3B1+8 Base Metal Core Specimen

Cut Sequence		Maximum Values	Minimum Values	Direction of Principle Strain
First Cut	strain (ue)	97	-141	-26 degree form grid 1 to the maximum principle strain
	stress (psi)	1788	-3707	
Third Cut	strain (ue)	154	-292	-27 degree from grid 1 to the maximum principle strain
	stress (psi)	2180	-8107	
Fifth Cut	strain (ue)	246	-384	-26 degree from grid 1 to the maximum principle strain
	stress (psi)	4300	-10227	
Seventh Cut	strain (ue)	369	-455	-25 degree from grid 1 to the maximum principle strain
	stress (psi)	7675	-11342	

Table 4-4 Strain and Stress Measured by Strain Gage A on D3B1+8 Base Metal Core Specimen

Cut Sequence		Calculated Values for Gage 1	Calculated Values for Gage 2
Drilled from Bridge	strain (ue)	769.1	20.6
	stress (psi)	25559	8287
First Cut	strain (ue)	79	3
	stress (psi)	2630	880
Second Cut	strain (ue)	138	72
	stress (psi)	5260	3740
Fourth Cut	strain (ue)	204	117
	stress (psi)	7880	5870

Note: Gage 1 along the longitudinal to box girder direction

Table 4-5 Strain and Stress Measured by Strain Gage C on Circumferential Side of D3B1+8 Base Metal Core Specimen

Cut Sequence		Parallel Flat Plane Values	Perpendicular Flat Plane Values
First Cut	strain (ue)	32	-11
	stress (psi)	935	-56
Second Cut	strain (ue)	44	-22
	stress (psi)	1220	- 302
Third Cut	strain (ue)	23	-32
	stress (psi)	434	-833

Table 4-6 Strain and Stress Measured by Strain Gage D on Circumferential Side of D3B1+8 Base Metal Core Specimen

Cut Sequence		Parallel Flat Plane Value	Perpendicular Flat Plane Values
First Cut	strain (ue)	123	1
	stress (psi)	4020	1210
Second Cut	strain (ue)	115	11
	stress (psi)	3860	1460

Table 4-7 Strain and Stress of B1+4 Base Metal Core Specimen

Gage Element Number	Drilled from Bridge		Cut Sequence					
			First Cut		Second Cut		Third Cut	
	Strain (ue)	Stress (Psi)	Strain (ue)	Stress (Psi)	Strain (ue)	Stress (Psi)	Strain (ue)	Stress (Psi)
A1	442	16346	19	960	30	1366	-15	-427
A2	179.5	10289	32	1252	39	1568	6	66
F1			25	Maximum Strain and Minimum Strain are 70 and -25 ue. Maximum Stress and Minimum Stress are 2065 and -126 Psi. +44 degree from gage element F1 to the Maximum Principal Strain				
F2			70					
F3			21					

Note:

1. A1 and A2 are the two element of gage A on top of B1+4 Core. Element A1 is along lateral to box girder direction. Element A2 is along longitudinal to box girder direction.
2. F1, F2 and F3 are the three element of gage F on the bottom of B1+4 Core. F2 is along lateral to box girder direction.
3. All of the stress value is associated to the core not to the bridge.

Table 4-8 Strain and Stress of B3B1 WCL Core Specimen

Gage Element Number	Cut Sequence				Drilled from Bridge	
	First Cut		Second Cut			
	Strain (ue)	Stress (Psi)	Strain (ue)	Stress (Psi)	Strain (ue)	Stress (Psi)
A1	24	-40	106	1890	-1163	-30799
A2	-84	-2532	-162	-4281	762.4	13632
B1	-554	Maximum Strain and Minimum Strain are -206 and -562 ue. Maximum Stress and Minimum Stress are -12346 and -20571 Psi. -81 degree from gage element B1 to the Maximum Principal Strain				
B2	-439					
B3	-215					

Note:

1. A1 and A2 are the two element of gage A on top of B3B1 Core. Element A1 is parallel to welding direction. Element A2 is perpendicular to welding direction.
2. B1, B2 and B3 are the three element of gage B on the bottom of B3B1 Core. B3 is parallel to welding direction.
3. All of the stress value is associated to the core not to the bridge.

Table 4-9 Strain and Stress of D3B1 WCL Core Specimen

Gage Element Number	Cut Sequence				Drilled from Bridge	
	First Cut		Second Cut			
	Strain (ue)	Stress (Psi)	Strain (ue)	Stress (Psi)	Strain (ue)	Stress (Psi)
A1	23	-201	100	-392	-1062.9	-30362
A2	-97	-2970	-373	-11308	473	5081
B1	-240	Maximum Strain and Minimum Strain are -12 and -240 ue. Maximum Stress and Minimum Stress are -2758 and -8029 Psi. +88 degree from gage element B1 to the Maximum Principal Strain				
B2	-117					
B3	-12					

Note:

1. A1 and A2 are the two element of gage A on top of D3B1 Core. Element A1 is parallel to welding direction. Element A2 is perpendicular to welding direction.
2. B1, B2 and B3 are the three element of gage B on the bottom of D3B1 Core. B3 is parallel to welding direction.
3. All of the stress value is associated to the core not to the bridge.

Table 4-10 Strain and Stress of C3B2 WCL Core Specimen

Gage Element Number	Cut Sequence				Drilled from Bridge	
	First Cut		Second Cut			
	Strain (ue)	Stress (Psi)	Strain (ue)	Stress (Psi)	Strain (ue)	Stress (Psi)
C1	29	432	49.4	-511	No strain gaged before drilled from bridge	
C2	-53	-1460	-215	-6603		
F1	-175	Maximum Strain and Minimum Strain are -10 and -258 ue. Maximum Stress and Minimum Stress are -2887 and -8620 Psi. +55 degree from gage element F1 to the Maximum Principal Strain				
F2	-17					
F3	-93					

Note:

1. C1 and C2 are the two one element gage on top of C3B2 Core. Gage C1 is parallel to welding direction. Gage C2 is perpendicular to welding direction.
2. F1, F2 and F3 are the three element of gage F on the bottom of C3B2 Core. F2 is parallel to welding direction.
3. All of the stress value is associated to the core not to the bridge.

Table 4-11 Principal Strain and Principal Stress Measured by Three Element Gage B on C7B2 WCL Core Specimen

Cut Sequence		Maximum Values	Minimum Values	Direction of the Principal Strain
First Cut	strain (ue)	4	-374	+87 degree from element B1 to maximum principal strain
	stress (psi)	-3563	-12298	
Second Cut	strain (ue)	-159	-777	+83 degree from element B1 to maximum principal strain
	stress (psi)	-12936	-27186	

Note: Element B3 of gage B is along parallel to welding direction.

Table 4-12 Calculated Principal Strain and Principal Stress of C7B2 Core Specimen

Gage	Drilled from Bridge		Cut Sequence					
			First Cut		Second Cut		Fourth Cut	
	Strain (ue)	Stress (Psi)	Strain (ue)	Stress (Psi)	Strain (ue)	Stress (Psi)	Strain (ue)	Stress (Psi)
D1	-1013	-30398	21	630	74	2220	816	24473
D2	678.3	20349	-89	-2670	-432	-12960	-627	-18806

Note: D1 and D2 are the two one element gage D on top of C7B2 Core. Gage D1 is along parallel to welding direction. Gage D2 is along perpendicular to welding direction.

Table 4-13 Principal Strain and Principal Stress Measured by Three Element Gage F on B3B2 HAZ Core Specimen

Cut Sequence		Maximum Values	Minimum Values	Direction of the Principal Strain
First Cut	strain (ue)	32	-55	+42 degree form grid F1 to maximum principal strain
	stress (psi)	497	-1509	
Second Cut	strain (ue)	134	-236	+44 degree form grid F1 to maximum principal strain
	stress (psi)	2076	-6460	
Third Cut	strain (ue)	116	-183	+48 degree from grid F1 to maximum principal strain
	stress (psi)	2015	-4881	

Note: Gride F2 of gage F is along parallel to welding direction.

Table 4-14 Strain and Stress of B3B2 HAZ Core Specimen

Gage Element Number	Drilled from Bridge		1st Cut	
	Strain (ue)	Stress (Psi)	Strain (ue)	Stress (Psi)
A1	-1156.5	-28982	128	2985
A2	924.5	19040	-123	-2805

Note: A1 and A2 are the two element of gage A on top of B3B2 Core. Gage A1 is along parallel to welding direction. Gage A2 is along perpendicular to welding direction.

Table 4-15 Strain and Stress of B7B1 HAZ Core Specimen

Gage Element Number	Cut Sequence						Drilled from Bridge	
	First Cut		Second Cut		Third Cut			
	Strain (ue)	Stress (Psi)	Strain (ue)	Stress (Psi)	Strain (ue)	Stress (Psi)	Strain (ue)	Stress (Psi)
A1	38	671	81	3102	115	4274	-642.9	-12647
A2	-59	-1574	45	2271	48	2725	864.1	22129
F1	-117	Maximum Strain and Minimum Strain are 27 and -337 ue. Maximum Stress and Minimum Stress are -2457 and -10862 Psi. +39 degree from gage element F1 to Maximum Principal Strain						
F2	23							
F3	-194							

Note:

1. A1 and A2 are the two element of gage A on top of B7B1 Core. Element A1 is parallel to welding direction. Element A2 is perpendicular to welding direction.
2. F1, F2 and F3 are the three element of gage F on the bottom of B7B1 Core. F2 is parallel to welding direction.
3. All of the stress value is associated to the core not to the bridge.

Table 4-16 Strain and Stress of B7B2 HAZ Core Specimen

Gage Element Number	Cut Sequence						Drilled from Bridge	
	First Cut		Second Cut		Third Cut			
	Strain (ue)	Stress (Psi)	Strain (ue)	Stress (Psi)	Strain (ue)	Stress (Psi)	Strain (ue)	Stress (Psi)
A1	43	442	108	650	76	-3433	-862.6	-21678
A2	-97	-2790	-293	-8596	-601	-19053	683.4	13998
F1	26	Maximum Strain and Minimum Strain are 118 and -70 ue. Maximum Stress and Minimum Stress are 3207 and -1141 Psi. +45 degree from gage element F1 to Maximum Principal Strain.						
F2	118							
F3	23							

Note:

1. A1 and A2 are the two element of gage A on top of B7B2 Core. Element A1 is parallel to welding direction. Element A2 is perpendicular to welding direction.
2. F1, F2 and F3 are the three element of gage F on the bottom of B7B2 Core. F2 is parallel to welding direction.
3. All of the stress value is associated to the core not to the bridge.

Table 4-17 Principal Strain and Principal Stress Measured by Three Element Gage F on C3B1 HAZ Core Specimen

Cut Sequence		Maximum Values	Minimum Values	Direction of the Principal Strain
First Cut	strain (ue)	45	-64	+44 degree form grid F1 to maximum principal strain
	stress (psi)	84	-1664	
Second Cut	strain (ue)	-28	-428	+44 degree form grid F1 to maximum principal strain
	stress (psi)	-5168	-14390	
Third Cut	strain (ue)	-198	-727	+41 degree from grid F1 to maximum principal strain
	stress (psi)	-13707	-25914	

Note: Gride F2 of gage F is along parallel to welding direction.

Table 4-18 Strain and Stress of C3B1 HAZ Core Specimen

Gage Element Number	Drilled from Bridge		1st Cut	
	Strain (ue)	Stress (Psi)	Strain (ue)	Stress (Psi)
D1	No strain gaged before drilled from bridge		58	1740
D2			-144	-4320

Note: D1 and D2 are the two one element gage D on top of C3B1 Core. Gage D1 is along parallel to welding direction. Gage D2 is along perpendicular to welding direction.

Table 4-19 Strain and Stress of C7B1 HAZ Core Specimen

Gage Element Number	Cut Sequence						Drilled from Bridge	
	First Cut		Second Cut		Third Cut			
	Strain (ue)	Stress (Psi)	Strain (ue)	Stress (Psi)	Strain (ue)	Stress (Psi)	Strain (ue)	Stress (Psi)
D1	30	900	62	1860	-41	-1230	-532.2	-15967
D2	-20	-600	9	270	-158	-4740	978.7	29361
F1	63	Maximum Strain and Minimum Strain are 28 and -169 ue. Maximum Stress and Minimum Stress are -763 and -5306 Psi. +43 degree from gage element F1 to Maximum Principal Strain						
F2	27							
F3	-79							

Note:

1. D1 and D2 are the two one element gage on top of C7B1 Core. Gage D1 is parallel to welding direction. Gage D2 is perpendicular to welding direction.
2. F1, F2 and F3 are the three element of gage F on the bottom of C7B1 Core. F2 is parallel to welding direction.
3. All of the stress value is associated to the core not to the bridge.

Table 4-20 Principal Strain and Principal Stress Measured by Three Element Gage B on Top of D3B2 HAZ Core Specimen

Cut Sequence		Maximum Values	Minimum Values	Direction of the Principal Strain
First Cut	strain (ue)	67	-201	+87 degree form grid B1 to maximum principal strain
	stress (psi)	233	-5947	
Third Cut	strain (ue)	39	-359	+87 degree from grid B1 to maximum principal strain
	stress (psi)	-2273	-11456	
Fifth Cut	strain (ue)	-16	-695	+89 degree from grid B1 to maximum principal strain
	stress (psi)	-7407	-23079	
Seventh Cut	strain (ue)	-58	-920	-88 degree from grid B1 to maximum principal strain
	stress (psi)	-11005	-30908	

Note: Grid B3 is along parallel to welding direction.

Table 4-21 Calculated Strain and Stress Measured by Two Element Gage A On D3B2 HAZ Core Specimen

Cut Sequence		Parallel to Weld Direction	Perpendicular to Weld Direction
First Cut	strain (ue)	84	-154
	stress (psi)	1246	-4246
Second Cut	strain (ue)	516	-263
	stress (psi)	14410	-3567
Fourth Cut	strain (ue)	20	-409
	stress (psi)	-3386	-13286
Sixth Cut	strain (ue)	48	-517
	stress (psi)	-3531	-16569
Drilled from Bridge	strain (ue)	-894.3	894.2
	stress (psi)	-20639	20635

Table 4-22 Strain and Stress Measured by Strain Gage D on the Bottom Circumferencial Side of D3B2T HAZ Core Specimen

Cut Sequence		Parallel Flat Plane Values	Perpendicular Flat Plane Values
First Cut	strain (ue)	2	-10
	stress (psi)	-30	-306
Third Cut	strain (ue)	-23	-16
	stress (psi)	-910	-749
Fifth Cut	strain (ue)	-79	-34
	stress (psi)	-2925	-1889

Table 4-23 Strain and Stress Measured by Strain Gage C on the Top Circumferencial Side of the D3B2 HAZ Core Specimen

Cut Sequence		Parallel Flat Plane Values	Perpendicular Flat Plane Values
First Cut	strain (ue)	20	-17
	stress (psi)	495	-357
Second Cut	strain (ue)	-455	-24
	stress (psi)	-15232	-5283
Fourth Cut	strain (ue)	4	-45
	stress (psi)	-300	-1428

Table 4-24 Strain and Stress of D7B1 HAZ Core Specimen

Gage Element Number	Cut Sequence						Drilled from Bridge	
	First Cut		Second Cut		Third Cut			
	Strain (ue)	Stress (Psi)	Strain (ue)	Stress (Psi)	Strain (ue)	Stress (Psi)	Strain (ue)	Stress (Psi)
A1	-6	-362	-31	-1286	-130	-4394	-681.7	-13545
A2	-17	-631	-26	-1152	-11	-1656	902.7	23018
F1	-24	Maximum Strain and Minimum Strain are 94 and -39 ue. Maximum Stress and Minimum Stress are 2705 and -345 Psi. +71 degree from gage element F1 to the Maximum Principal Strain						
F2	69							
F3	79							

Note:

1. A1 and A2 are the two element of gage A on top of D7B1 Core. Element A1 is parallel to welding direction. Element A2 is perpendicular to welding direction.
2. F1, F2 and F3 are the three element of gage F on the bottom of D7B1 Core. F2 is parallel to welding direction.
3. All of the stress value is associated to the core not to the bridge.

Table 4-25 Flat Plate Coring Strain Gage Results

Flat Plate Strain gage Identification	Coring Induced Strain gage Differences	Rolling-Induced Residual Stress
	Microstrain	Psi
FP-GAGE-1	300	-11868
FP-GAGE-2	200	-9560

Table 4-26 Summary of Weld Center Line Core Results

Core ID	Stress Relate to Welding Direction	Dead Load from Bridge (Ksi)	Residual Stress from Coring		Residual Stress from Coring plus Sectioning	
			Coring Results (Ksi)	Coring Results - Dead Load (Ksi)	Average Sectioning Results (Ksi)	Coring + Sectioning - Dead Load (Ksi)
B3B1	Perpendicular	-15	-14	1	3	4
	Parallel	0	31	31	-1	30
C7B2	Perpendicular	-15	-20	-5	11	6
	Parallel	0	30	30	-9	21
D3B1	Perpendicular	-15	-5	10	-7	3
	Parallel	0	30	30	0	30
Average	Perpendicular			2		4
	Parallel			30		27

Table 4-27 Summary of Heat Affected Zone Core Results

Core ID	Stress Relate to Welding Direction	Dead Load from Bridge (Ksi)	Residual Stress from Coring		Residual Stress from Coring plus Sectioning	
			Coring Results (Ksi)	Coring Results - Dead Load (Ksi)	Average Sectioning Results (Ksi)	Coring + Sectioning - Dead Load (Ksi)
B3B2	Perpendicular	-15	-19	-4	3	-1
	Parallel	0	29	29	-3	26
B7B1	Perpendicular	-15	-22	-7	-1	-8
	Parallel	0	13	13	-3	10
B7B2	Perpendicular	-15	-14	1	10	11
	Parallel	0	22	22	0	22
C7B1	Perpendicular	-15	-29	-14	-2	-16
	Parallel	0	16	16	0	16
D3B2	Perpendicular	-15	-21	-6	10	4
	Parallel	0	21	21	-2	19
D7B1	Perpendicular	-15	-23	-8	1	-7
	Parallel	0	14	14	2	16
Average	Perpendicular			-6		-3
	Parallel			19		18

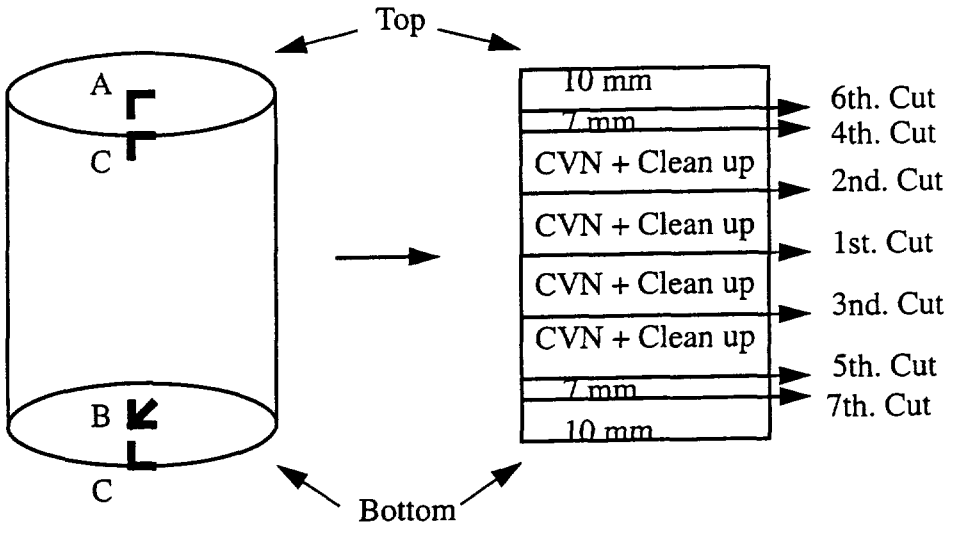

Figure 4-1 (a) Gage Position, Cut Sequence and Slice Thickness of D3B2 Core Specimen

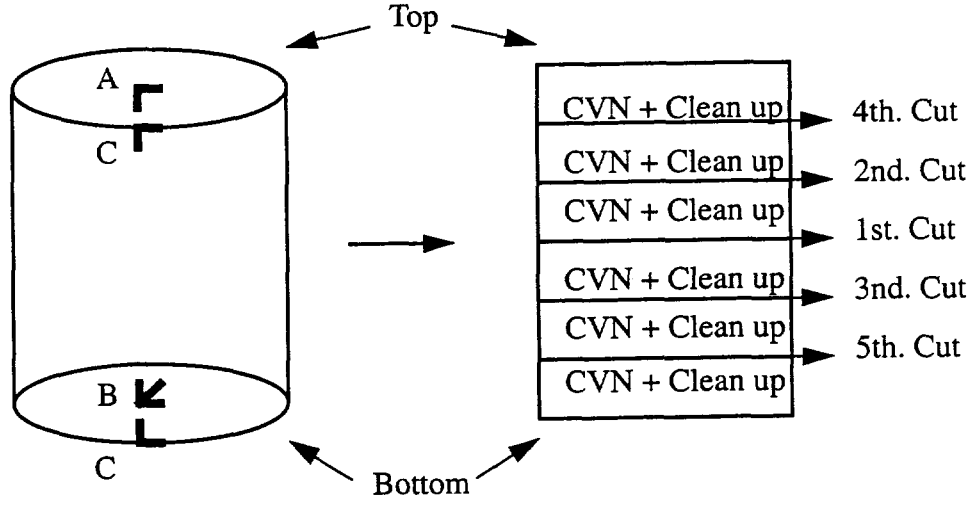

Figure 4-1 (b) Gage Position, Cut Sequence and Slice Thickness of D3B1+8 Core Specimen

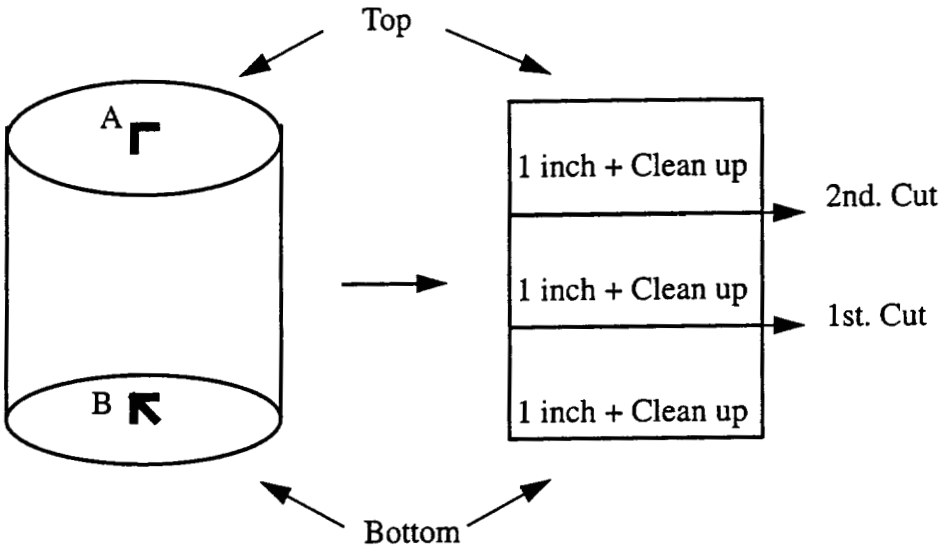

Figure 4-1 (c) Gage Position, Cut Sequence and Slice Thickness
of B3B1, D3B1 Core Specimen

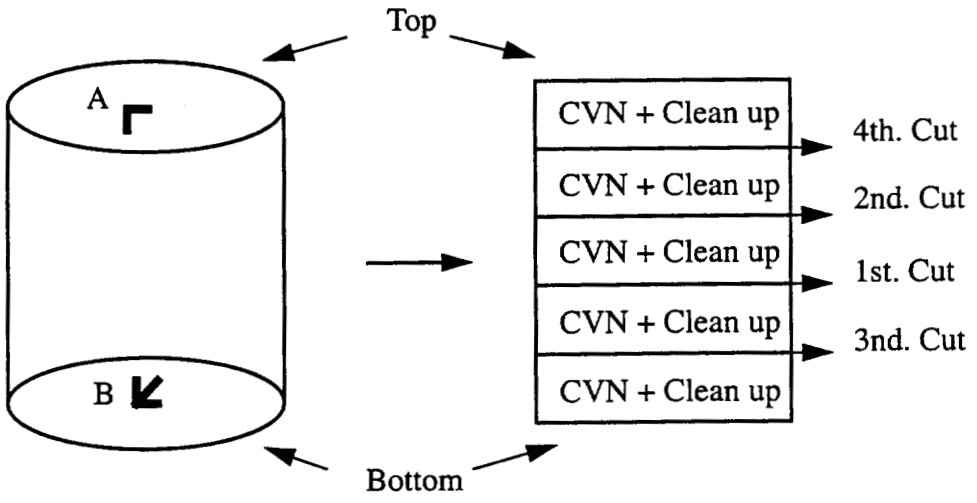

Figure 4-1 (d) Gage Position, Cut Sequence and Slice Thickness
of C7B2 Core Specimen

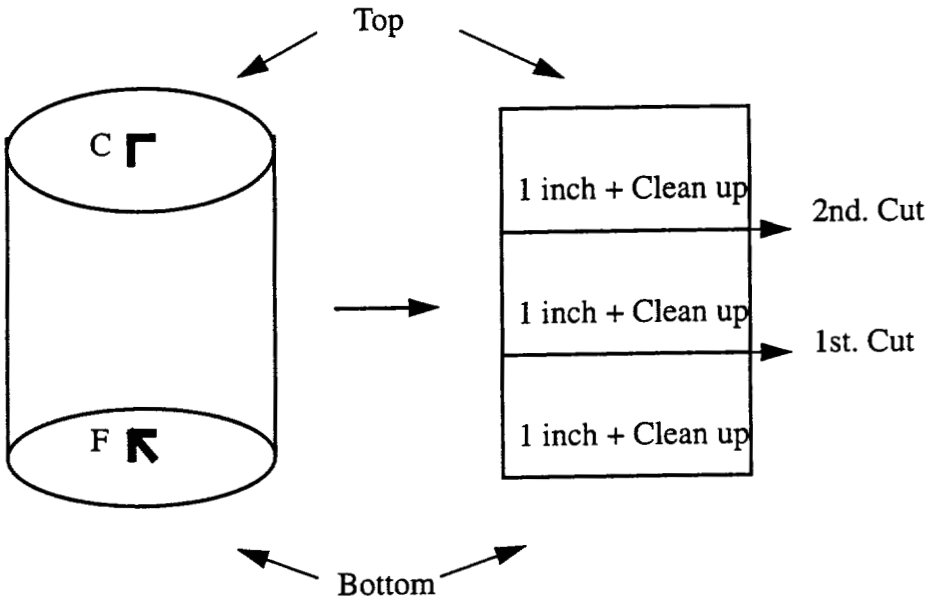

Figure 4-1 (e) Gage Position, Cut Sequence and Slice Thickness of C3B2 Core Specimen

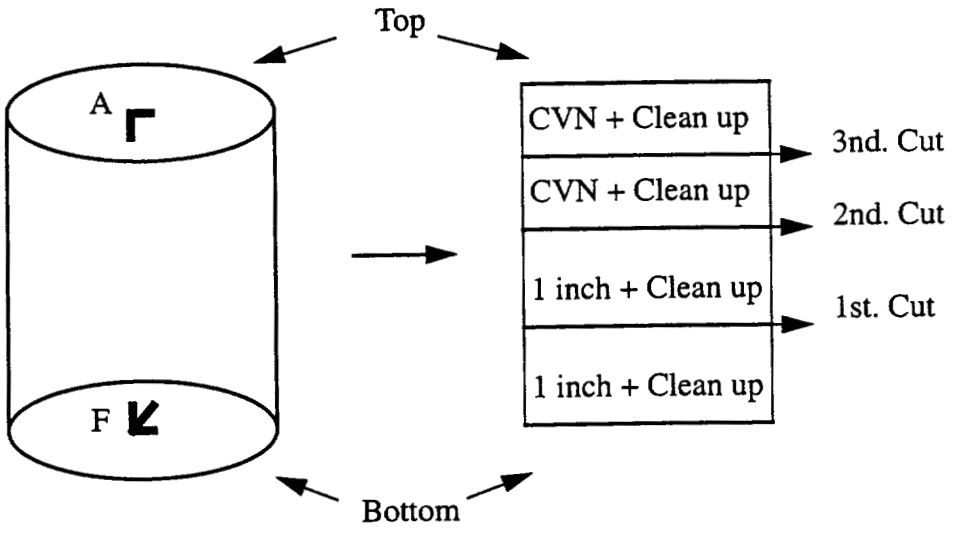

Figure 4-1 (f) Gage Position, Cut Sequence and Slice Thickness of D7B1, B7B2, B7B1 Core Specimen

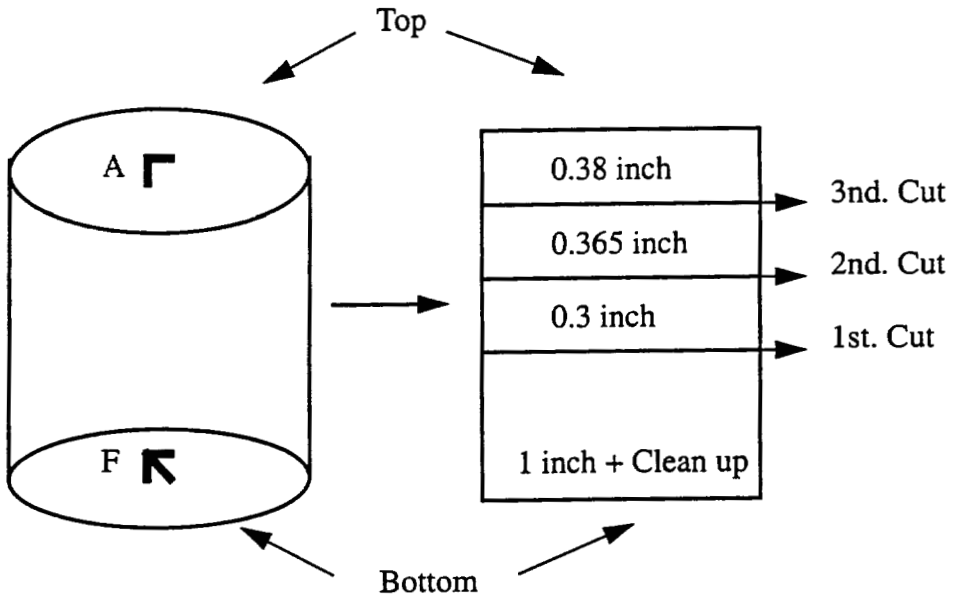

Figure 4-1 (g) Gage Position, Cut Sequence and Slice Thickness of B1 Core Specimen

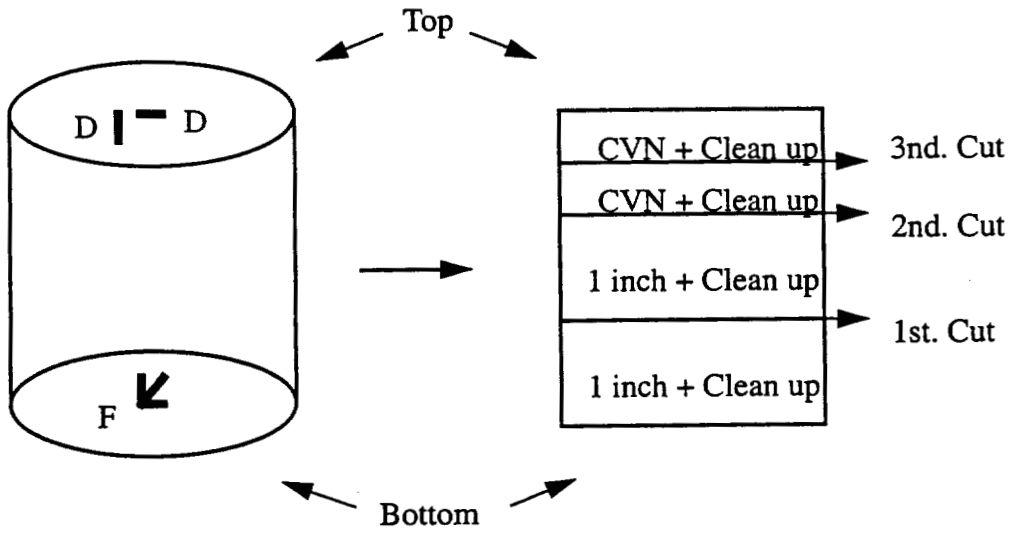

Figure 4-1 (h) Gage Position, Cut Sequence and Slice Thickness of C7B1 Core Specimen

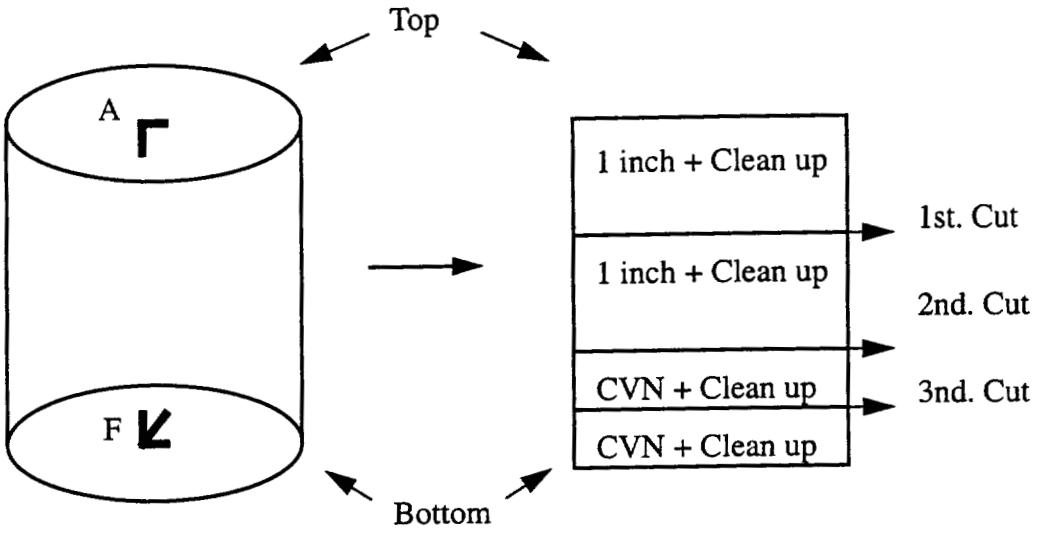

Figure 4-1 (i) Gage Position, Cut Sequence and Slice Thickness of B3B2 Core Specimen

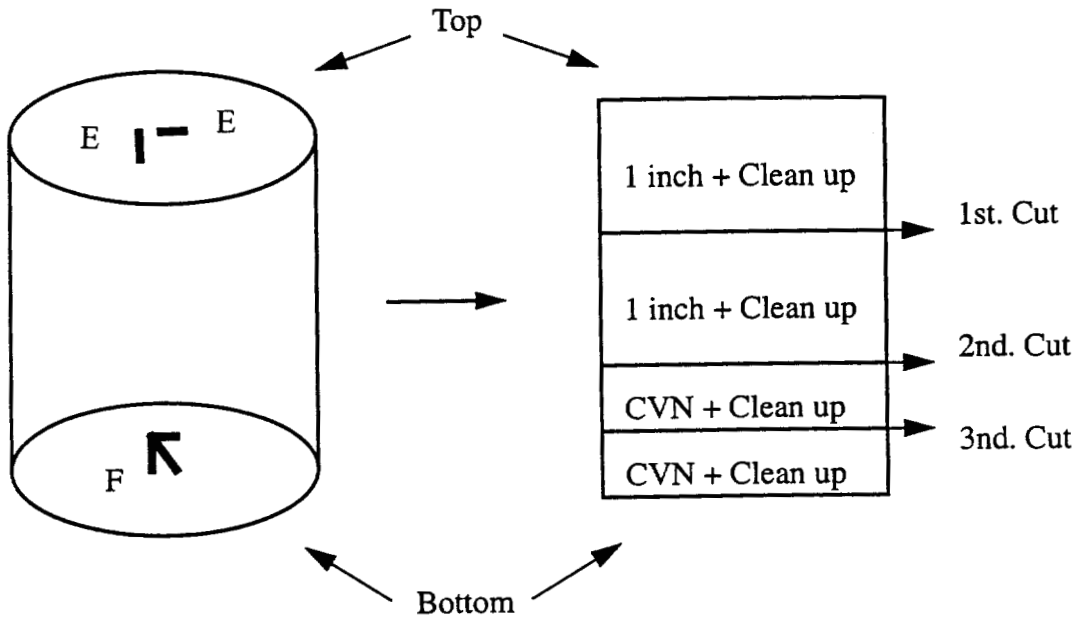

Figure 4-1 (j) Gage Position, Cut Sequence and Slice Thickness of C3B1 Core Specimen

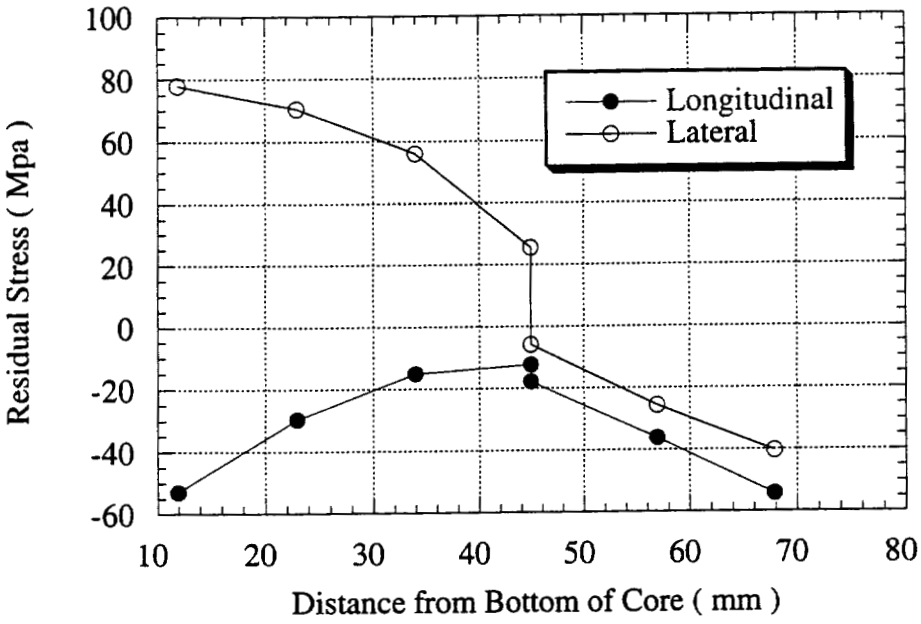

Figure 4-2 (a) Residual Stress Distribution through Thickness along Longitudinal and Lateral to Box Girder Direction of D3B1+8 Base Metal Core

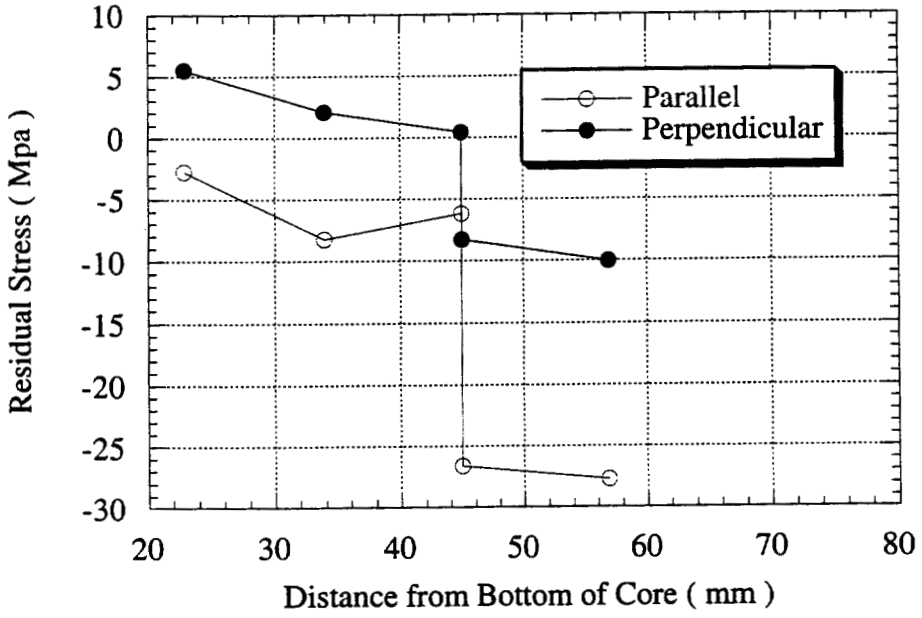

Figure 4-2 (b) Residual Stress Distribution through Thickness Parallel and Perpendicular to Core Top Flat Surface of D3B1+8 Base Metal Core

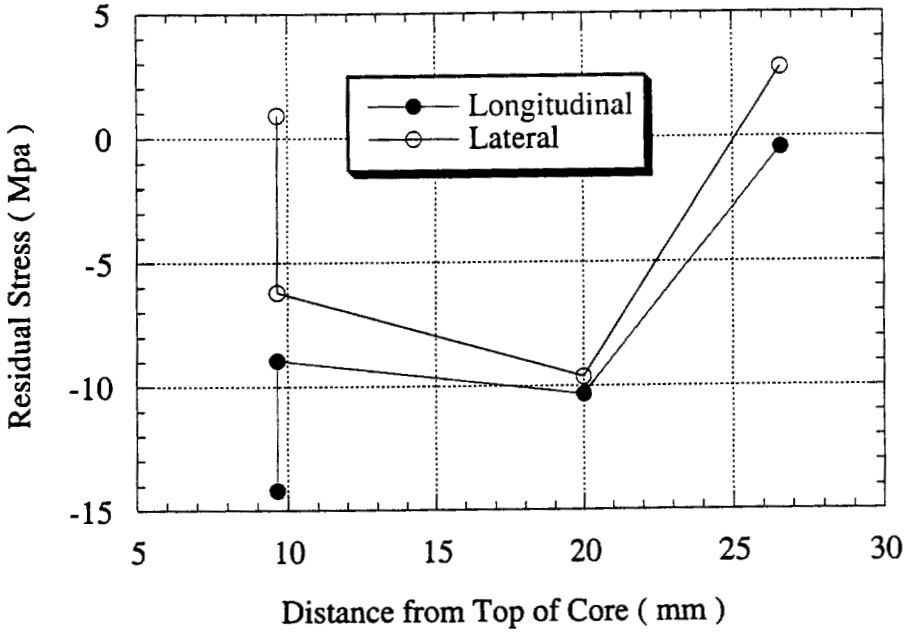

Figure 4-2 (c) Residual Stress Distribution through Thickness along Longitudinal and Lateral to Box Birder Direction of B1+4 Base Metal Core

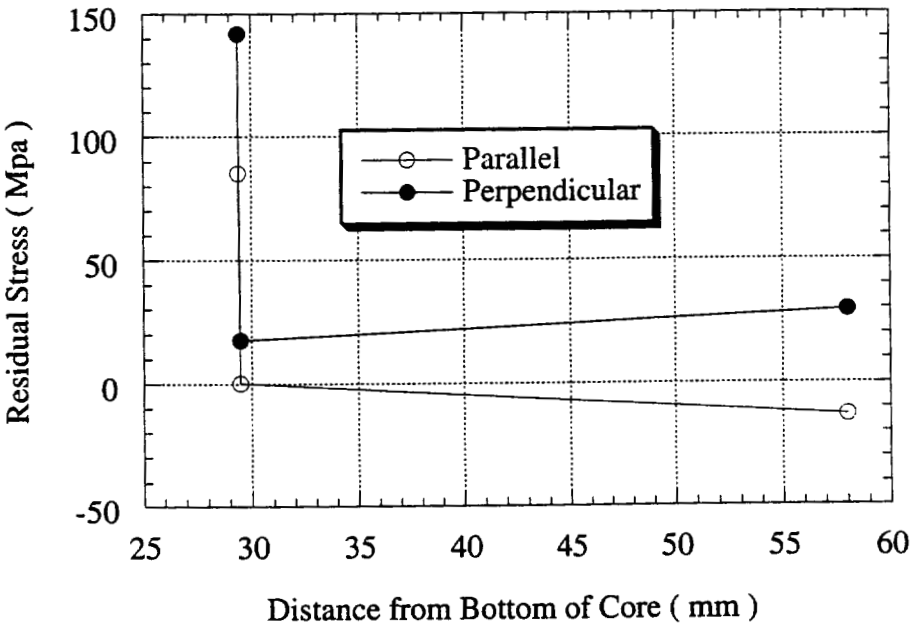

Figure 4-3 (a) Residual Stress Distribution through Thickness Parallel and Perpendicular to Welding Direction of B3B1 WCL Core

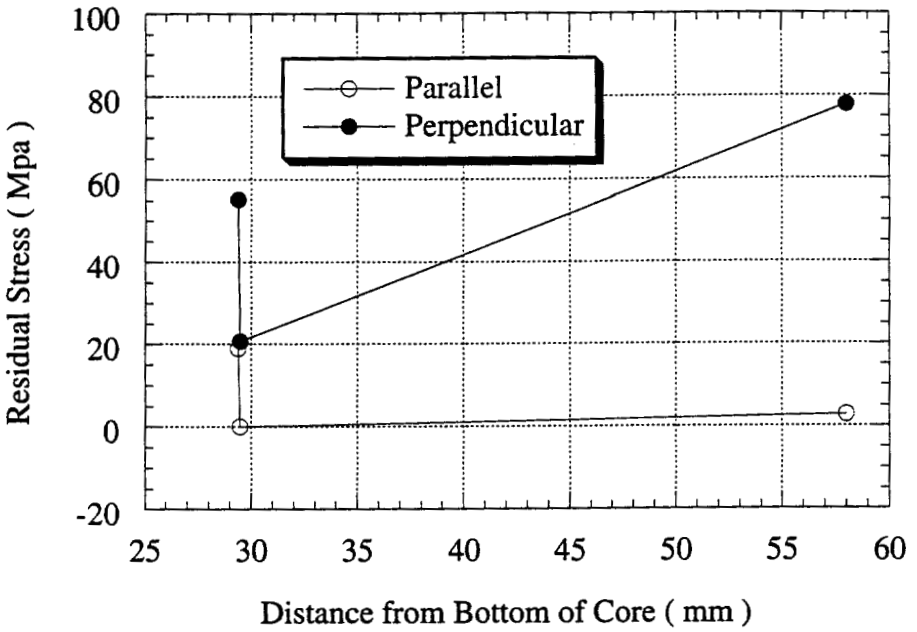

Figure 4-3 (b) Residual Stress Distribution through Thickness
Parallel and Perpendicular to Welding Direction of D3B1 WCL Core

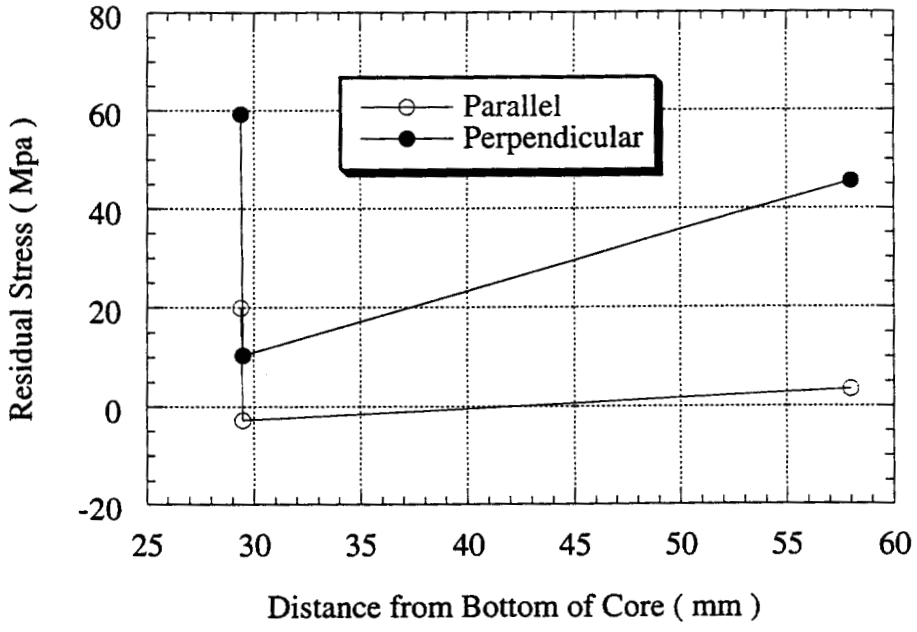

Figure 4-3 (c) Residual Stress Distribution through Thickness
Parallel and Perpendicular to Welding Direction of C3B2 WCL Core

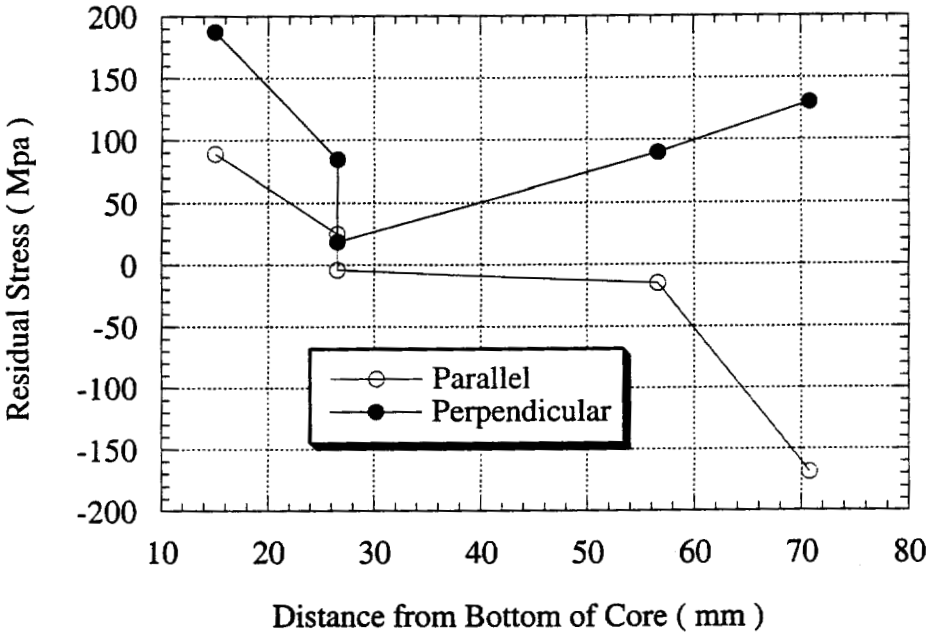

Figure 4-3 (d) Residual Stress Distribution through Thickness
along Parallel and perpendicular to Welding Direction of C7B2 WCL Core

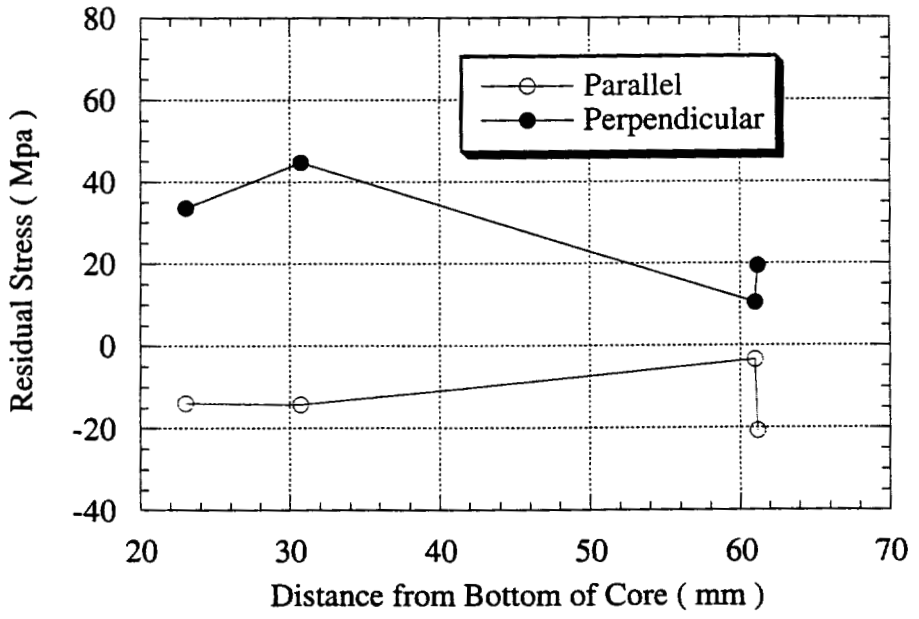

Figure 4-4 (a) Residual Stress Distribution through Thickness
Parallel and Perpendicular to Welding Direction of B3B2 HAZ Core

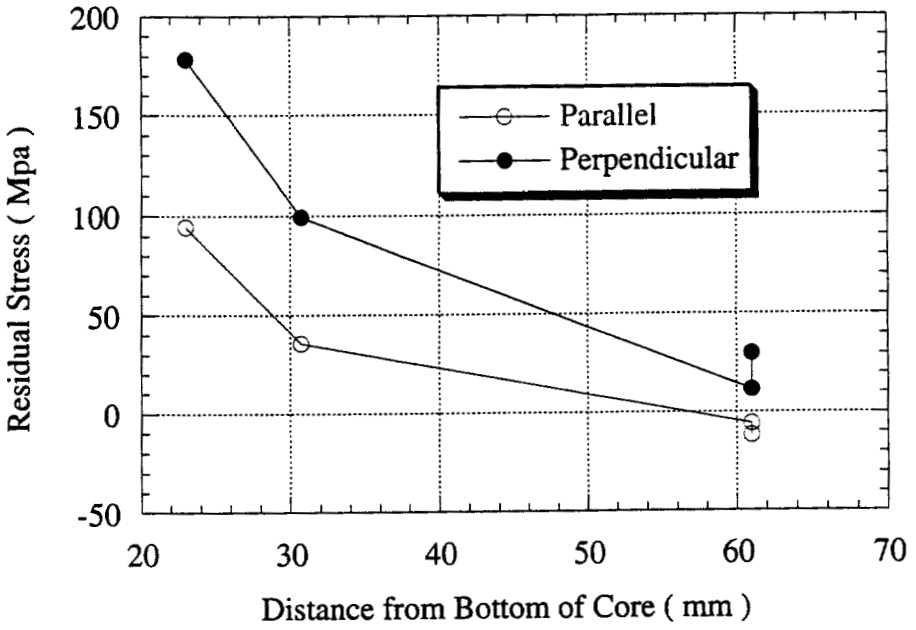

Figure 4-4 (b) Residual Stress Distribution through Thickness
Parallel and Perpendiculat to Welding Direction of C3B1 HAZ Core

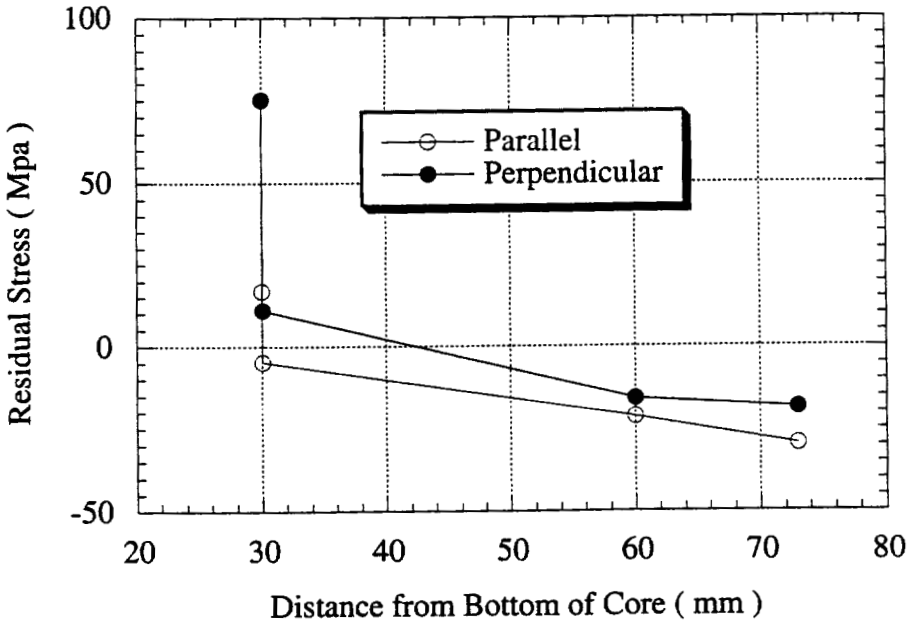

Figure 4-4 (c) Residual Stress Distribution through Thickness
Parallel and Perpendicular to Welding Direction of B7B1 HAZ Core

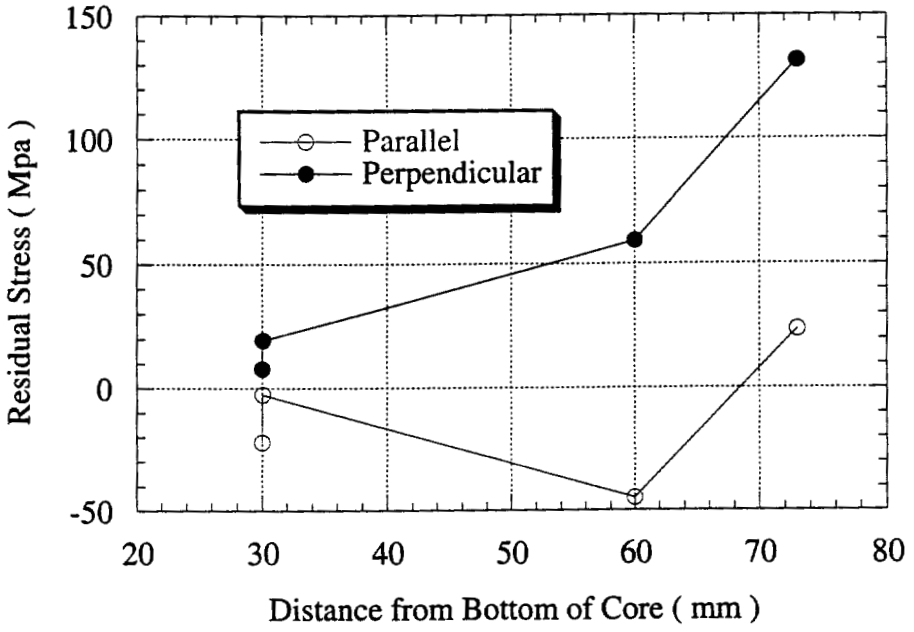

Figure 4-4 (d) Residual Stress Distribution through Thickness
Parallel and Perpendicular to Welding Direction of B7B2 HAZ Core

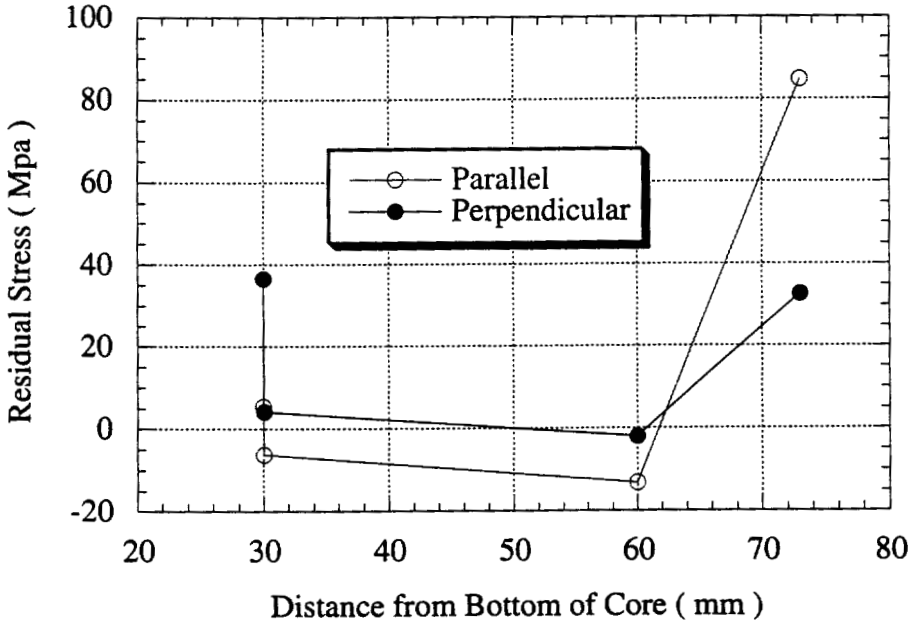

Figure 4-4 (e) Residual Stress Distribution through Thickness
Parallel and Perpendicular to Welding Direction of C7B1 HAZ Core

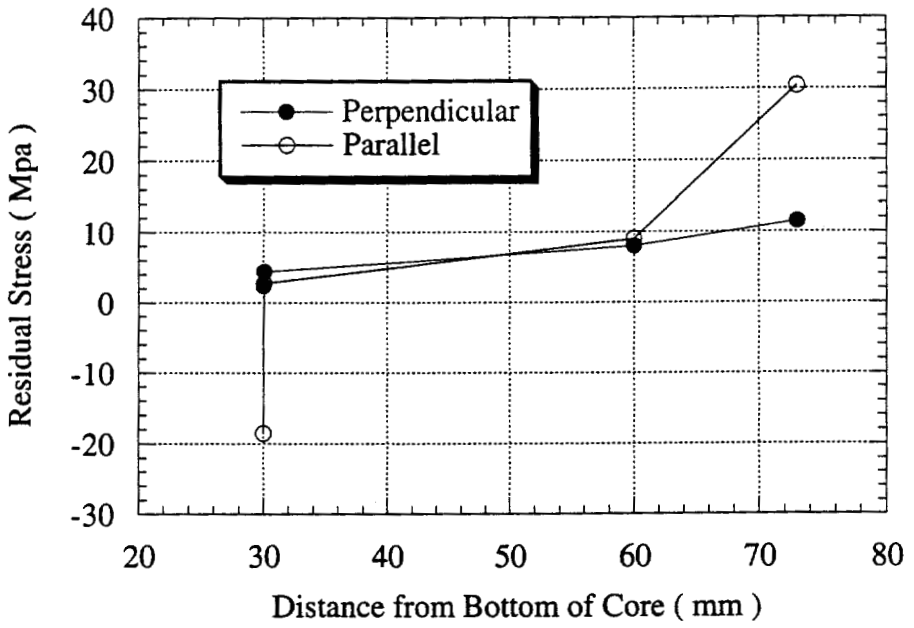

Figure 4-4 (f) Residual Stress Distribution through Thickness
Parallel and Perpendicular to Welding Direction of D7B1HAZ Core

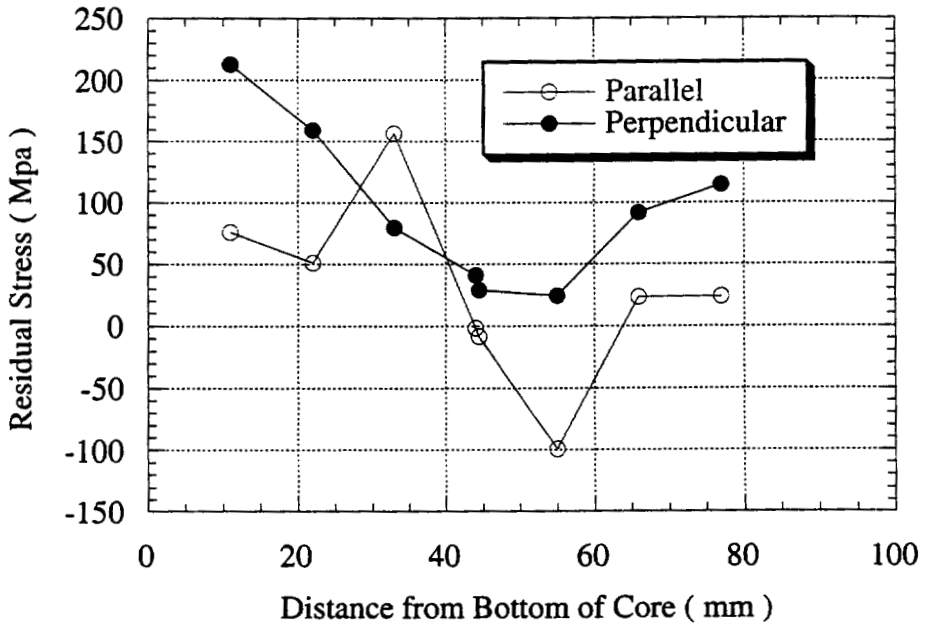

Figure 4-4 (g) Residual Stress Distribution through Thickness
Parallel and Perpendicular to Welding Direction of D3B2 HAZ Core

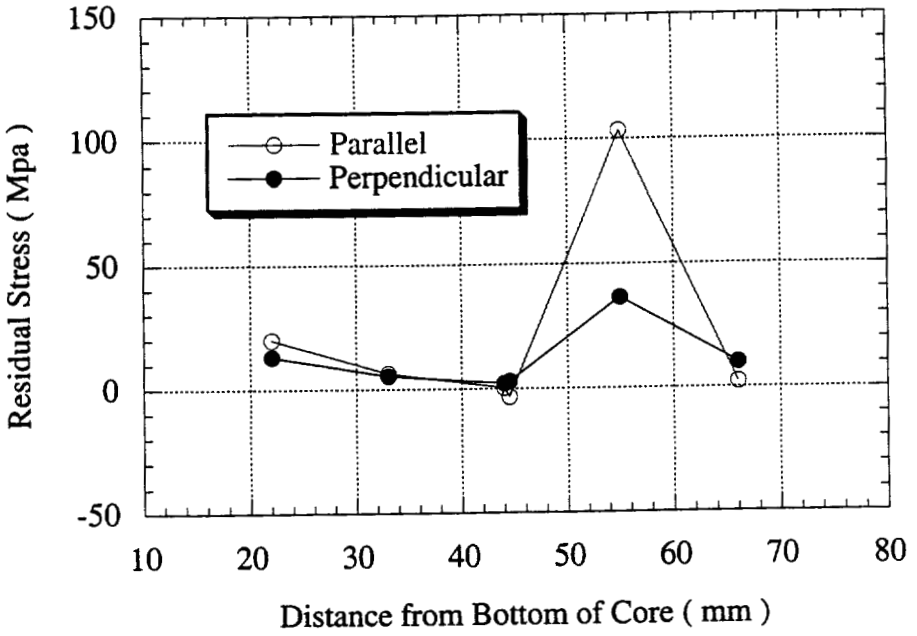

Figure 4-4 (h) Residual Stress Distribution through Thickness
Parallel and Perpendicular to Top Flat Surface of D3B2 HAZ Core

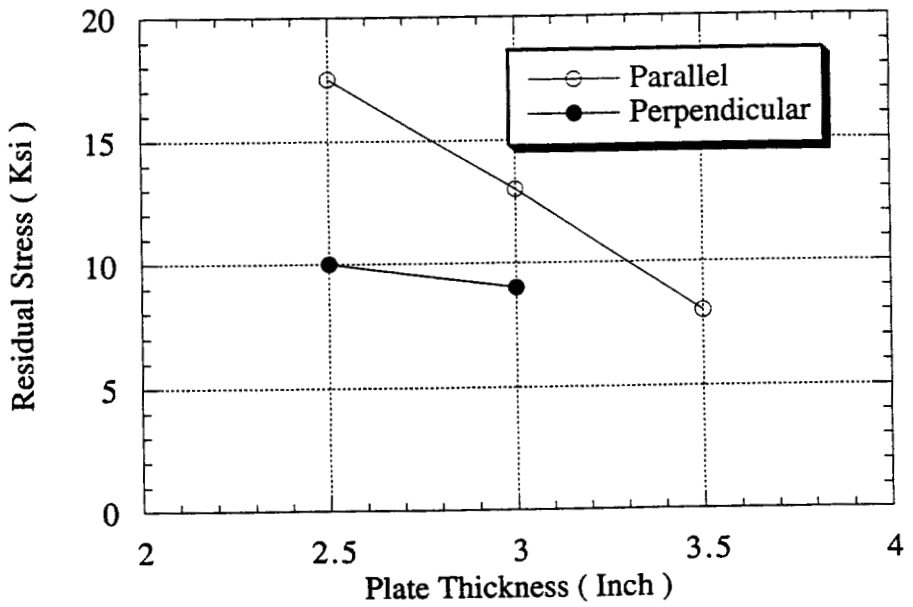

Figure 4-5 Base Plate Rolling-Induced
Relieved Stresses as a Function of Plate Thickness

CHAPTER 5
TWO DIMENSIONAL NUMERICAL ANALYSIS OF TEMPERATURE DISTRIBUTION IN A WELDMENT DURING ELECTROSLAG WELDING PROCESS

5.1 INTRODUCTION

It is well known that residual stresses in weldments derive from three principal sources: uneven heating and cooling along the welding direction, uneven heating and cooling perpendicular to the welding line, and phase transformation. The first modeling work on the ESW process was presented by Dallier, Szekely, and Eagar. They calculated the heat and fluid flow in the liquid slag and liquid metal regions in an idealized two-dimensional (2D) system using finite differential methods. After that they used a three-dimensional (3D) model to calculate the temperature distribution associated with different ESW operation parameters. However, they did not consider phase transformation effects on thermal distribution during the welding process and did not predict the resultant residual stress distributions. Because the objectives of the current study differ substantially from the work of Eagar's, the basis of model and simulation procedure of necessity will differ from his. Eagar's work was conducted on the basis of known operation parameters and unknown weld results. In the case of this study, the work will be done based on the completed weldments and unknown operation parameters. The primary importance will be the investigation of residual stresses in the weldment. Two dimensional numerical simulation work has been done for the ESW process when in reality, it is a three dimensional problem. In order to verify the results and get general information about the residual stress variation with operation parameters in fixed

coordinate system, this part of work uses 2D numerical models. It should be noticed that all of the 2D models were based on some assumptions which idealize the process, i.e., only part of process or welding facility was included in the 2D models. Two 2D models were developed - mid-plane model and cross-sectional model. The mid-plane model does not consider the effect of copper shoe. The cross-sectional model does not simulate the whole process.

During welding process, the weldment can be divided into weld pool part and base metal part. By measuring the position of the fusion line, the weld pool shape can be characterized. At the interface between the weld pool and base metal, the temperature boundary condition can be effectively incorporated into the simulation model. Given these conditions, all remaining effective operation parameters, excluding welding speed, can be simulated. The other effect of weld pool on base metal is the radiation from the surface of the slag to the side of the base metal. As for this effect, one can assume the heat flux into this side or reduce the heat transfer coefficient on this side. If the heat flux methods is used, the operation parameters must be known to calculate the temperature distribution in the weld pool. The most convenient way for such simulation work is using the reduced thermal coefficient to simulate the process. At the same time, because of the complexities of the underlying phenomena, unavailability of a material property database and limited computer configuration, simplifying assumptions were necessary. Various simplifications commonly adopted in FEA of welding processes are applied below.

5.2 MODELS

ASSUMPTIONS

The following assumptions have been made in this ESW thermal analysis:

1) The weld pool remains in a steady state condition during the ESW process.
2) The melting point of the metal is used as the boundary conditions at the contact layers between molten metal/base metal, molten metal/plate and molten slag/plate.
3) The weld pool shape is simplified to be rectangular for the slag phase and half

circle for the metal phase.

4) The convection boundary condition has been used for the remaining sides of plate.

5) The heat generated by the deformed solid is negligible.

6) All of the thermal coefficient that has been used in this study remains constant through the welding process simulation.

7) Mid-plane model assumes the plate are one element thick with plate surface insulated during welding process, i.e., no effect of the copper shoe.

8) Cross-sectional model assumes no or little heat transfer along either up or down plate in the height direction. The heat transfer is mainly through copper shoe and plate in longitudinal direction.

GOVERNING EQUATION

The fundamental principle for heat flow analysis is based on thermal energy conservation in the solid as following:

$$\frac{\partial}{\partial x}(K_x\frac{\partial T}{\partial x})+\frac{\partial}{\partial y}(K_y\frac{\partial T}{\partial y})+\frac{\partial}{\partial z}(K_z\frac{\partial T}{\partial z})+Q=\rho C\frac{\partial T}{\partial t} \qquad (5\text{-}1)$$

where,

Q	=	Internal heat generation rate per unit volume (w/m^3).
K_x, K_y, K_z	=	Thermal conductivities along x, y and z principal axes direction respectively (w/m^oC).
ρ	=	Density of Material (kg/m^3).
C	=	Mass specific heat (J/kg^oC).
t	=	Time (s).

GEOMETRY DEFINITION FOR TWO DIMENSIONAL MODEL

During this study, two discrete 2D models were developed. One modeled the

mid-plane of the weldment, while the other modeled the cross-sectional plane perpendicular to the mid-plane, as illustrated in Figures 5-1 (a) and (b) respectively. The mid-plane model allowed for heat transfer up and down the height and down the length of the weldment, but did not include the thickness of the weldment. In this model, the shape of the heat source remained the same for every increment of time. This model therefore represents a case in which residual stress build-up is not influenced by heat transfer towards the edges of the plate, i.e., the results are unaffected both by the presence of the water-cooled copper shoes pressed against the sides of the weldment, and/or the heat transfer from the plate surface to the atmosphere. The cross-sectional model described heat transfer across the thickness and down the length of the weldment, but not up and down the height of the weldment. Thus the residual stress build-up for this model was unaffected by the heat transfer up the unwelded portion of the plates above the welded section, and/or by heat transfer down into the weldment during subsequent weldment cooling. The entire ESW process has not yet been simulated in a cross-sectional model. Both models utilized here represent idealized approximations of a complex three dimensional problem, but were expected to allow for both assessment of approximate residual stress distributions, and to illustrate trends in welding parameter effects.

In order to save calculation time, only a part of the welded plate has been modeled; a half-plane for the mid-plane model and a quarter-plane for the cross-sectional model. In addition the CD side, a dimension in Figures 5-1 (a) and (b), is not the actual end of the welded plate. Preliminary work has been done to decide how long a plate should be modeled to represent the whole situation. The CD side length has been chosen at which, during the ESW process, the temperature is almost room temperature because of the length of the plate compared to the heat flow process. From the following equations of heat flow through conduction and convection, the heat conduction process in the welded plate at which the temperature is room temperature could be simulated using heat convection. That is to say, of the two following equations for heat flow, the simulation utilized the heat convection rather than heat conduction to characterize the boundary condition.

The equation for convection is known as Newton's Law of Cooling:

$$q=hA(T_s-T_b) \tag{5-2}$$

where,

q	=	Heat flow rate (J/s).
h	=	Film coefficient.
A	=	Area of surface (m^2).
T_s	=	Surface temperature of the object (K).
T_b	=	Bulk temperature of the surrounding fluid (K).

The equation for conductive heat transfer through a wall processing uniform thermal conductivity is known as Fourrier's Law:

$$q=-kA\frac{(T_2-T_1)}{L} \tag{5-3}$$

where,

q	=	Heat flow rate (J/s).
k	=	Thermal conductivity (w/m°C).
A	=	Area (m^2).
T	=	Temperature (K).
L	=	Wall thickness (m).

According to Equation 5-3, the heat flow behavior through the unmodeled part of the welded plate could be simplified by utilizing the heat convection boundary condition. The only additional step necessary is to calculate the convection coefficient from the conductivity and length of the welded plate, i.e., h=k/L was prescribed as the convection coefficient on the CD side, where L is the unmodeled plate length.

HEAT SOURCE

Normally the concentrated heat input is simplified for heat transfer analysis. The temperature near the source is determined by the energy density distribution. At the same time, the heat source and the geometric condition determine the temperature distribution. During the ESW process, the weld pool may be considered as a heat source. The heat flow behavior in welded plate is affected by the shape of the weld pool. The heat source distribution can be modeled by utilizing the essential boundary condition ($T(x,y,z)=T_s(x,y,z)$), where $T_s(x,y,z)$ is the melting temperature of the welded plate. That is to say, a temperature boundary versus a heat flux heat source model was used in this study. It greatly simplifies the numerical simulation work on ESW processing. At the same time, welding operation parameters can be unknown. For mid-plane model (Figure 5-1 (a)), $A_1B_1B_2$ is the heat source at a certain time step. For cross-sectional model (Figure 5-1 (b)), A_1B_1 is the heat source at a certain time step. At that certain time step, the melting temperature of the welded plate was used along $A_1B_1B_2$ and A_1B_1 for mid-plane model and cross-sectional model, respectively.

INITIAL AND BOUNDARY CONDITIONS

The heat transfer field equation is solved under the given initial and boundary conditions. Three types of boundary conditions were used during the calculation.

Initial Condition

Room temperature ($T=298K$) is prescribed as the initial condition for the calculation to all points in the domain except those at the heat source boundary.

Essential Boundary Condition

At the heat source boundary, the melting temperature of welded plate $T=1773K$

is prescribed during a given time step. The surface defined as $A_1B_1B_2$ in the mid-plane model, Figure 5-1 (a), is the heat source at a certain time step. A_1B_1 defines the fusion line of the molten metal pool (modeled as quarter circle of radius 0.04 m (1.6 inch) while B_1B_2 defines the slag pool to plate boundary. Note that the temperature of the complete $A_1B_1B_2$ surface is defined as the steel melting point, 1773K. This heat source configuration is stepped from the bottom to the top of the plate at a given welding speed. Equilibrium configuration of the weld pool is assumed as starting and stopping blocks are used during the process to allow pool development prior to plate welding initiation and to assure the pool is above the top of the plate prior to weld termination.

The slag/weld pool in the mid-plane model retains a constant configuration throughout the model calculation. This is not true for the cross-sectional model pool. Here the pool starts at a maximum dimension, holds that dimension as the slag pool traverses the cross-sectional plane, and then continuously decreases in cross section until the weld pool completely disappears, as illustrated in Figure 5-1 (b). A total of five time steps have been used to simulate the heat source passing through the OA_2CD plane of the welded plate. A_1B_1, A_2B_2, A_3B_3, A_4B_4, O is applied with steel melting temperature for each time step. This is because the molten pool approaches, intersects, and then passes through the cross-sectional model plane position. Note that the effect of the copper shoe was simulated by an increase in surface heat transfer coefficient in the shoe contact area.

Natural Boundary Condition

The heat transfer through the surrounding medium can be specified through the heat transfer coefficients.

$$K_n \frac{\partial T_s}{\partial n} + h_c(T_s - T_A) = 0 \qquad (5\text{-}4)$$

where,

K_n = Thermal conductivity normal to the surface (w/m°C).

h_c = Film coefficient for convectional heat transfer at the boundary.

T_s = Surface temperature.

T_A = Ambient temperature.

At B_2B_n (when heat source is at $A_1B_1B_2$ position), B_nC, CD, DB_1 for mid-plane model and A_2C, CD, DB_1 (when heat source is at A_1B_1 position) for cross-sectional model, the convection heat transfer boundary condition is prescribed.

It should be noticed that unlike in cross-sectional model, the effect of copper shoe was not included in mid-plane model. C_1A_2 is the position where copper shoe was pressed against the welded plate. AC_1 is the position where copper shoe contacts with base metal and A_1A_2 is the position where copper shoe contacts with fusion zone. Higher thermal coefficient was used to simulate the effect of copper shoe, as mentioned above. According to the temperature field calculation results of Eagar's,[150-152] thermal coefficient values of 130 and 1670 Jm/sK on A_1C_1 side and A_1A_2 side, respectively, were used in this study.

Adiabatic Boundary Condition

The symmetry surfaces in the ANSYS program were prescribed by the adiabatic boundary condition. Side A_1A_n for mid-plane model and OD, OA_2 for cross-sectional model are the symmetry axes and adiabatic boundary condition were prescribed.

SPATIAL DISCRETIZATION

To balance the calculation cost and desired accuracy, the finite element mesh needs to be optimized. Finer mesh will help getting desired results but will be cost-prohibitive whereas the use of a coarse mesh comes at the expense of accuracy of the results. A carefully graded mesh is the solution but not necessarily easy to obtain. Some guidelines must be met to obtain better results. The mesh should be sufficiently fine to model the heat source with acceptable accuracy. Regions close to heat source should be

discretized with smaller elements than in regions far away from the heat source. At the same time, element types such as linear or quadratic elements will also affect the mesh coarseness. Pammer[154] has determined the criterion for the element size near the hot boundary to achieve accurate results in the analysis. Finer mesh should be used in conjunction with fine time increments to get accurate results. Also, Thomas et al[155] have shown that every given mesh has an inherent limit of achievable accuracy. Therefore continuous refinement of spatial increments will not continuously improve the accuracy of the results.

Because of the symmetry nature of the ESW weldment, only half of the weldment for mid-plane model and one quarter of the weldment in the cross-sectional model with one end at the weld center plane were modeled. Illustration of the two models were shown in Figures 5-1 (a) and (b) for mid-plane model and cross-sectional model respectively, where A_1A_n for mid-plane model and OA_2 for cross-sectional model are the WCL. In this chapter, the results that were shown are applied to the plate 0.08 m (3.15 inch) in thickness and 0.8 m (31.5 inch) in length for both models. Note that the "effective" plate length of each welded plate was 6.12 m (20 ft) due to use of a length-specific modified heat conductivity as a plate and boundary condition.

A nonuniform mesh with 1419 elements and 1456 nodes was generated over the domain for mid-plane model. 154 elements and 183 nodes were generated for cross-sectional model. The density of elements varies as a function of distance from the weld center line. A total of 656 elements for mid-plane model and 72 elements for cross-sectional model were placed in the weld area (about 0.04 m from weld center line). The meshes for both mid-plane model and cross-sectional model were given in Figures 5-2 (a) and (b).

TIME DISCRETIZATION

In transient heat transfer analysis, faster convergence and reasonable accuracy can be achieved by an appropriate time-stepping scheme. Due to the sharp temperature rise in the initial heating period, short time increments and relatively large temperature

convergence tolerance should be used while longer time increments and smaller tolerances should be used during cooling.

THERMAL MATERIAL PROPERTIES

The finite element transient heat transfer analysis requires accurate values of thermal conductivity, specific heat, material density and latent heat of fusion and phase transformations up to the melting point. Due to lack of measured data for high temperature, the low temperature data is usually used to extrapolate data for high temperature.

The thermal material properties which were used in this study are summarized as following.

Density

Density is measured at room temperature and converted through the mean, linear thermal expansion coefficient at higher temperature. It decreases with increasing temperature. At the same time, a discontinuity density changs occurs due to denser atom packing of face-centered austenite compared to the body centered ferrite at the transformation temperature. However, because material density has a minor effect on the heat transfer, density can be assumed to be constant during the whole process.

Thermal Conductivity

Thermal conductivity and diffusivity are based on the mobility of free electrons in the metallic lattice and decreases as the temperature increases. They decrease at a given temperature as the alloying content increases. In the current model, continuously decreasing thermal conductivity was prescribed. This is shown in Figure 5-3 and can be expressed as[150-152]:

$$K = 9.2 \times 10^{-2} - 5.86 \times 10^{-5} T \qquad T < 1050 \text{ K}$$

$K = 3.05 \times 10^{-2}$ $T > 1050$ K

Enthalpy

A phase change was modeled by defining the enthalpy of the material as a function of temperature (see Figure 5-4). Enthalpy, which has unites of heat/volume, is defined as the integral of density times specific heat with respect to temperature:

$$H = \int \rho C_p(T) dT \tag{5-5}$$

Where,

H	=	Enthalpy (J/m^3).
ρ	=	Density (g/m^3).
C_p	=	Specific heat (J/gK).
T	=	Temperature (K).

The specific heat is applied for the entire duration of the time increment. If the specific heat value undergoes a dramatic change in the phase transformation range, a large time step will introduce a significant error in the results. So fine time-steps should be used in transient heat transfer analysis.

5.3 FINITE ELEMENT CODE

ANSYS 5.3 was used to model the ESW processes. The ANSYS program is a general purpose finite element program which can be used in all disciplines of engineering-structural, mechanical, electrical, electromagnetic, electronic, thermal, fluid, and biomedical. It is constantly updated with new features, enhancements of existing features and error corrections. Revision 5.3 version of the ANSYS program allows the implementation of the current state-of-the art technology. Enhanced nonlinear capabilities were also developed. It has elements with the death and birth feature which is very critical in terms of modeling welding processes. It can also model the phase change of

metal by applying enthalpy (including heat of fusion) as a function of temperature.

5.4 SOLUTION PROCEDURE

The transient heat transfer of the ESW welding process was modeled using the ANSYS 5.3 commercial software. Plane55 thermal solid element in ANSYS was chosen in thermal analysis. Temperature dependent material properties were defined, followed by the meshing of the domain. Preparation part of the ANSYS thermal analysis was finished by the above procedures. The parameters that were used to calculate temperature field were given in Table 5-1.

For the solution part of ANSYS program, transient analysis option was chosen first, followed by a full Newton-Raphson solution procedure. The initial temperature was specified by the TUNIF command in the ANSYS program. Convection heat transfer was activated on all the sides except the symmetry line as soon as welding was initiated. Welding was initiated by selecting nodes at the heat source boundary and prescribed the melting temperature of welded plate. Heat source movement and addition of filler material were modeled by element death and birth procedures. Thus, in the model, the weld metal part elements are deactivated before the start of the welding process. The addition of filler material was modeled by activating previously deactivated elements one set by one set as the weld and heat source progressed from one time step to the next time step. The heat source movement was modeled by prescribing and deleting the temperature in incremental fashion for given time intervals. The continuous moving of the weld and heat source were modeled by using discontinuous time step Δt, i.e., the weld and heat source would stay in one area within one time step and would advance to the next adjacent area for next time step. There were 42 areas along the fusion line between weld metal and plate for mid-plane model. Therefore, 42 time steps would be applied for whole processing for mid-plane model. Thus Δt can be represented as:

$$\Delta t = \frac{d}{42v} \tag{5-6}$$

where,

v = Welding speed (m/s).

d = Height of the welded plate (m).

One time step was automatically adjusted to several sub-time steps to make sure the numerical process was stable. At the end of welding, the specimens were allowed to cool down. Only convection heat transfer was allowed during this time period. The thermal analysis was carried out until the specimens reached room temperature.

An automatic convergence criterion was used through out the thermal analysis to optimize the solutions. During the welding part, a larger convergence criterion was used, since steeper temperature gradients are encountered. As soon as welding was over, smaller convergence criterion was used as the temperature gradients are less steep.

5.5 RESULTS

TEMPERATURE PROFILE

The temperature profile for mid-plane model and cross-sectional model during welding process are shown in Figures 5-5 and 5-6, respectively. From Figure 5-5, it can be seen that the temperature profile around heat source stays the same for the different time steps. It is consistent with the assumption of steady state heat transfer for each time step.

Some operation parameter effect on welding process have been studied with cross-sectional model. The results are given in next chapter from residual stress view of point.

PEAK TEMPERATURE

During the welding process, each point in the welded plate will endure certain thermal cycle with the heat source coming to and away from the point. The thermal models yielded reasonable temperature profiles as a function of distance from the WCL,

as illustrated for the mid-plane model in Figure 5-7. Note that increasing node number corresponds to increasing distance from WCL.

In order to compare the differences of the two models, the temperature profile with temperature on equivalent nodes for both models were given. Figure 5-8 (a) illustrates the temperature as a function of time of node point 927 in mid-plane model. Figure 5-8 (b) illustrates the temperature as a function of time of node point equivalent to mid-plane node point 927 in cross-sectional model.

5.6 DISCUSSION

COMPARING WITH EXPERIMENTAL RESULTS

Previous experimental results which used thermocouple to measure temperature at different time during ESW process were shown in Figure 5-9. Comparing Figures 5-7 with 5-9, both of them have similar temperature history profile. The modeling results are dependable and the simplifying of the ESW process is acceptable from this point of view.

HEAT TRANSFER PATTERN

Mid-plane model simulates very thin plate with no heat transfer through the plate surface, i.e., the plate surface is insulated during welding process. Obviously there is no effect of copper shoe in this model. Without the copper shoe, the heat transfer was conducted through the plate length direction and plate up and down direction because mid-plane model was calculated with the assumption that the heat source was moving in steady state. There was no edge effect with this assumption. The plate height is long enough for the heat transfer to reach steady state. The steady state will also be reached along plate length.

The temperature profile for each time step is decided by the heat conduction inside the plate. However, the heat convection at the boundary still affects the heat transfer pattern. During welding process, the effect of heat conduction inside the plate is more

important than the heat convection through the boundary on the temperature profile.

Cross-sectional model presents the heat transfer pattern of ESW process from a different aspect than mid-plane model. In this model, the effect of the copper shoe is included. Between the height versus thickness direction, only part of the welding process was simulated as compared to the whole process being modeled in mid-plane model. The results in Figure 5-6 reveal that the heat loss from copper shoe is bigger than other direction. The results are reasonable since the plate thickness is very small comparing with the plate length. At the same time, heat transfer coefficient is very high due to the effect of copper shoe. In this model, the heat convection through copper shoe is more important than the heat conduction inside the plate. Comparing the effect of plate length and plate thickness, the later is a more important factor on heat transfer pattern during welding process.

It should be noted that none of the results of two 2D models included all of the effects which are very important during welding process. Copper shoe is an very important factor during ESW, however, mid-plane model does not include it in the model. With cross-sectional model, it only models the part when the heat source pass through the studied plane. In general, the results of both 2D models reveal that ESW process is in reality a three dimensional problem. In order to simulate the 3D process with all of the important factors included, 3D modeling is needed to fully understand the details of the heat transfer pattern of ESW.

MODELING RESULTS COMPARING

The two 2D models reveal the heat transfer pattern of ESW process from different aspects with the same object. Therefore, their results can be associated. At the same time, differences should be presented in these two models, because of the different assumptions associated with each process.

The two models did exhibit different heating and cooling characteristics at equal distances from WCL/fusion line at mid-thickness, as illustrated in Figures 5-8 (a) and (b). The mid-plane model results yielded higher peak temperature and longer cooling time

than the cross-sectional model. The difference is because of the effect of the copper shoe which pulls the heat out better than the plate length and plate up and down direction.

5.7 CONCLUSIONS

1) Copper shoe is an important factor during ESW process.
2) 3D modeling is needed to fully understand the details of the heat transfer pattern of ESW.

Table 5-1 Parameters Used for Temperature Field Calculation of 2D Models

Parameters	Mid-Plane Model	Cross-Sectional Model
Plate Thickness	0.08m	0.08m, 0.06m
Plate Length	6.12m	6.12m, 0.8m, 0.3m
Initial Plate Gap	0.04m	0.04m
Width of Copper Shoe	N/A	0.08m
Radius of Metal Pool	0.04m	0.04m
Depth of Slag Pool	0.04m	0.04m
Convection Heat Transfer Coefficient at the Base Plate Surfaces	h_1= 84 Jm/sK	h_1=84 Jm/sK
Convection Heat Transfer Coefficient at the Plate-Copper Shoe	N/A	h_2=130 Jm/sK h_3=1670 Jm/sK

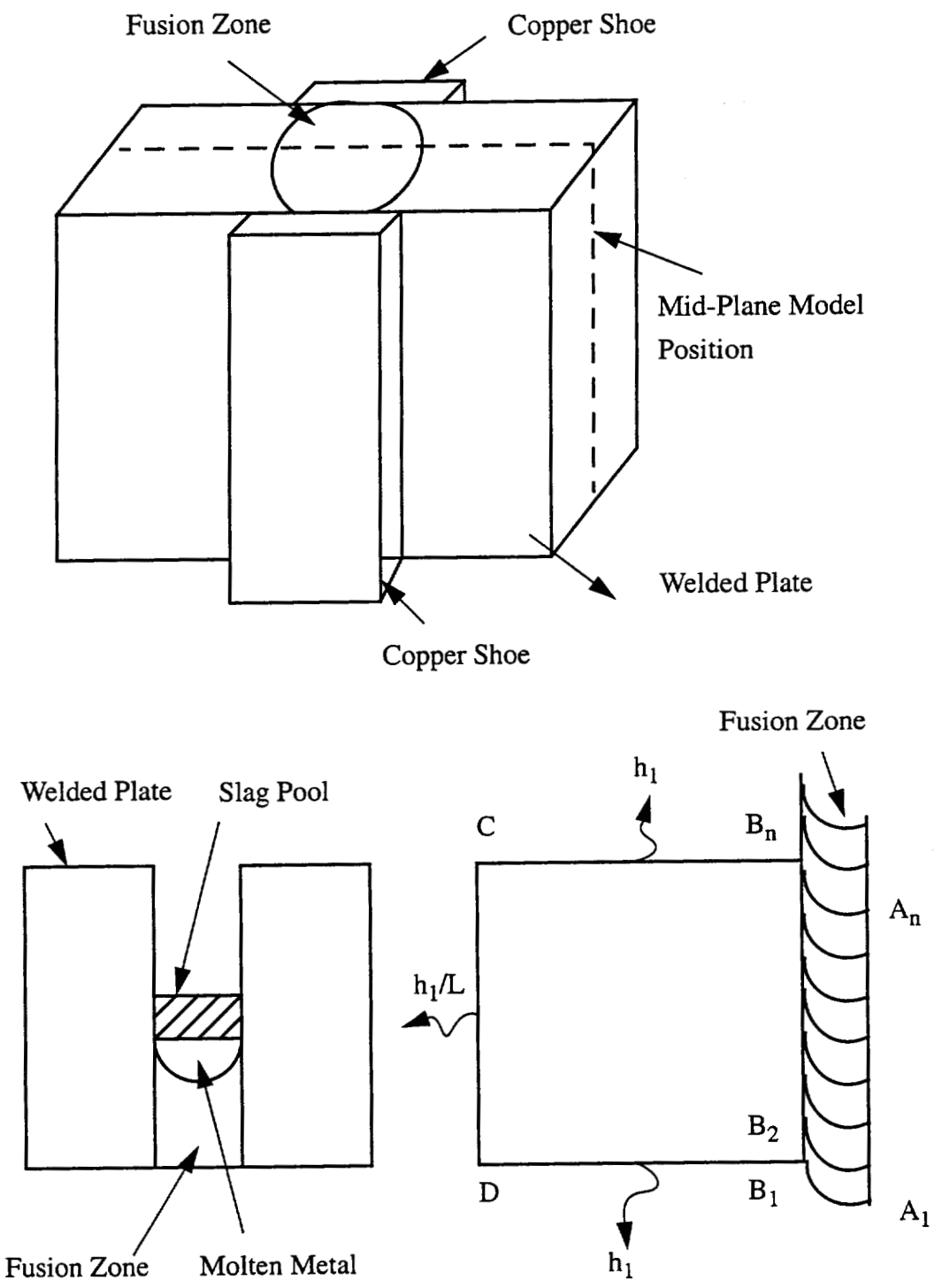

Figure 5-1 (a) Illustration of Mid-Plane Model Position and Shape

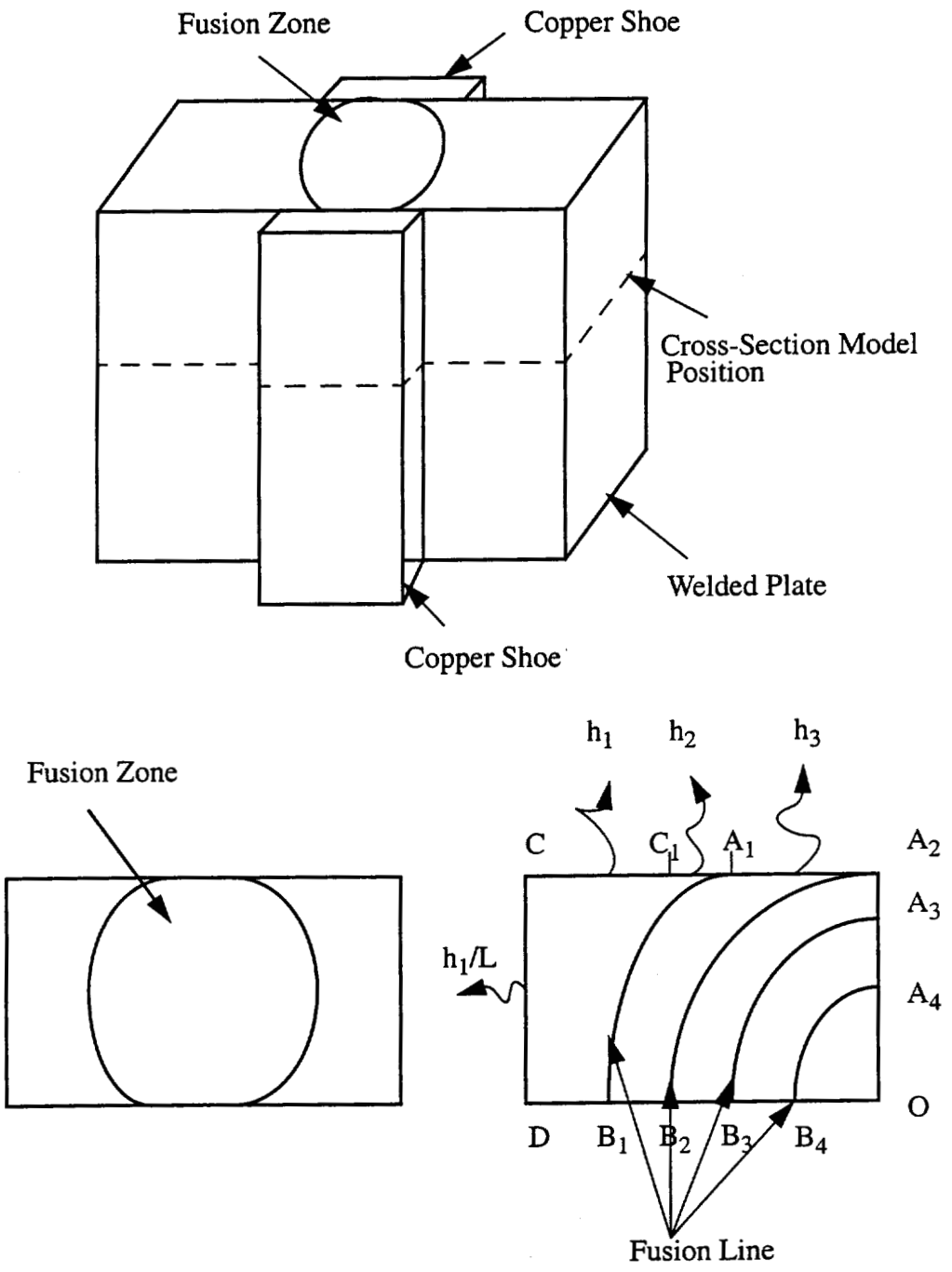

Figure 5-1 (b) Illustration of Cross-Section Model Position and Shape

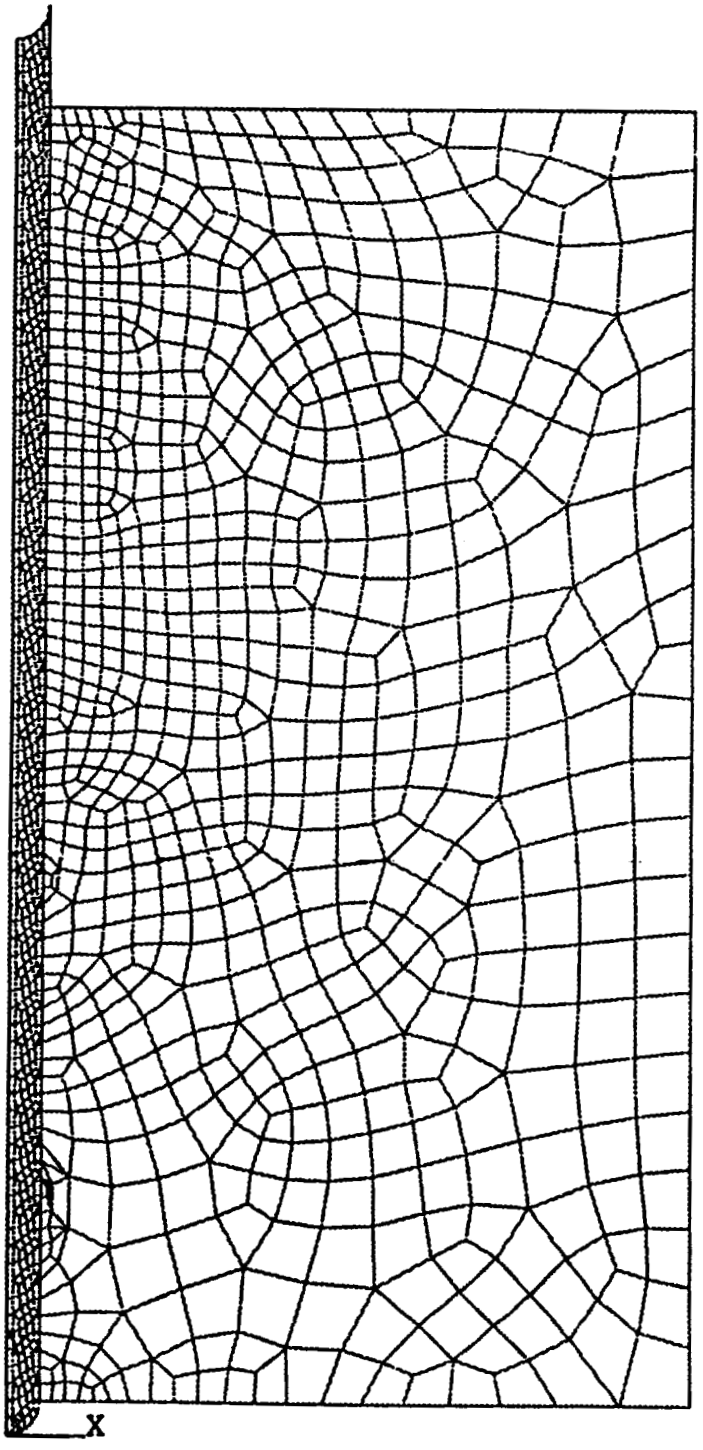

Figure 5-2 (a) Mesh of Mid-Plane Model

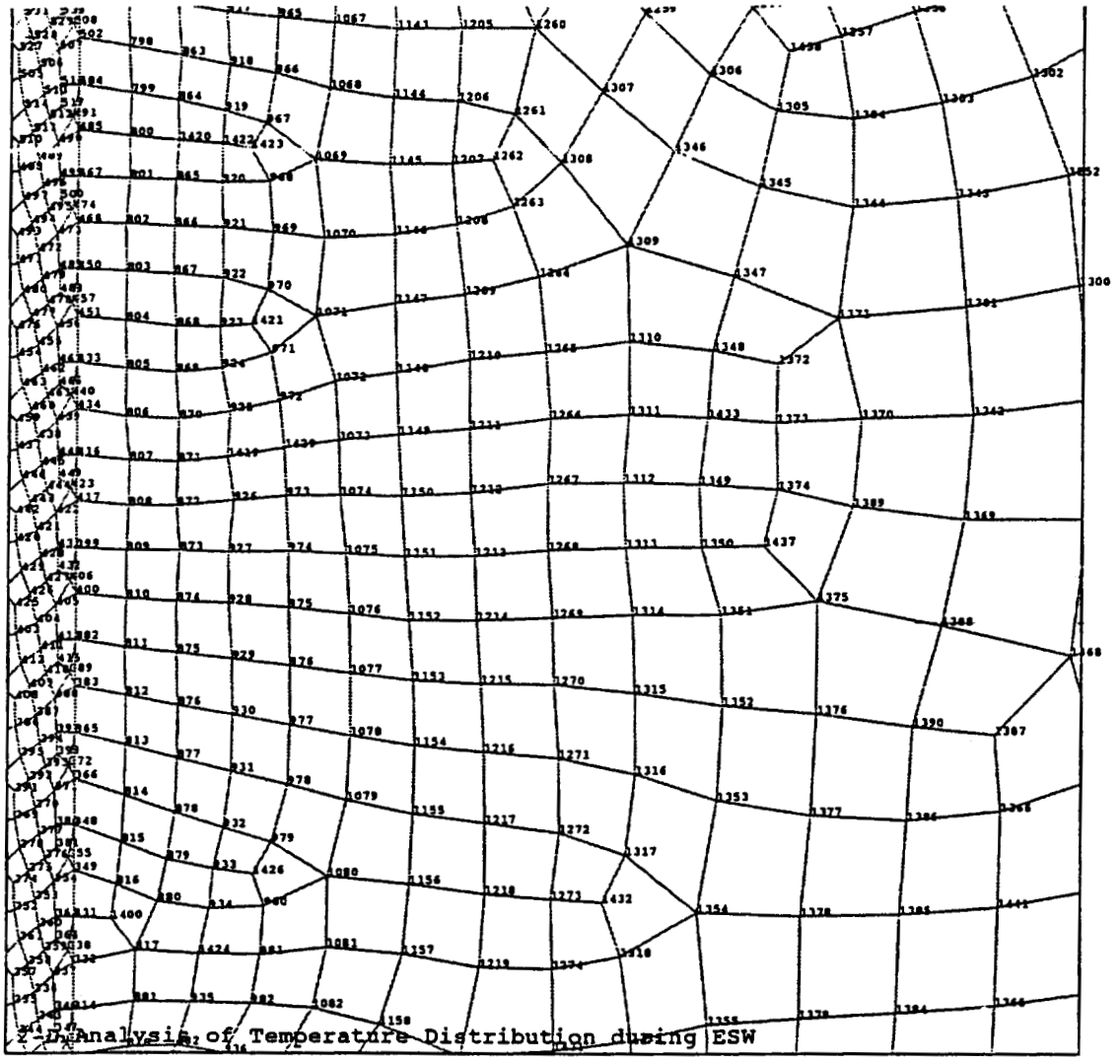

Figure 5-2 (b) Enlarged View of Mesh of Mid-Plane Model

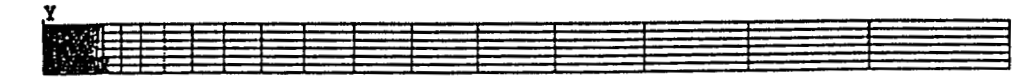

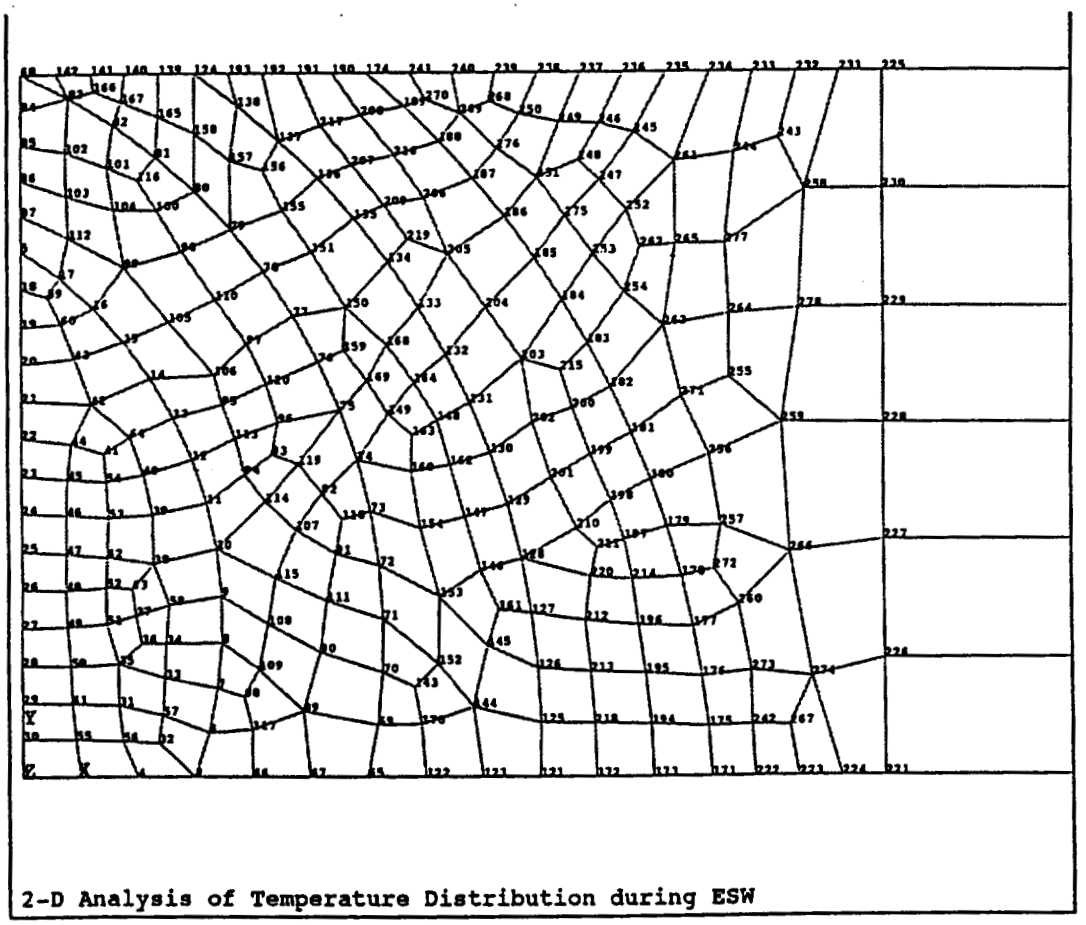

Figure 5-2 (c) Mesh of Cross-Sectional Model

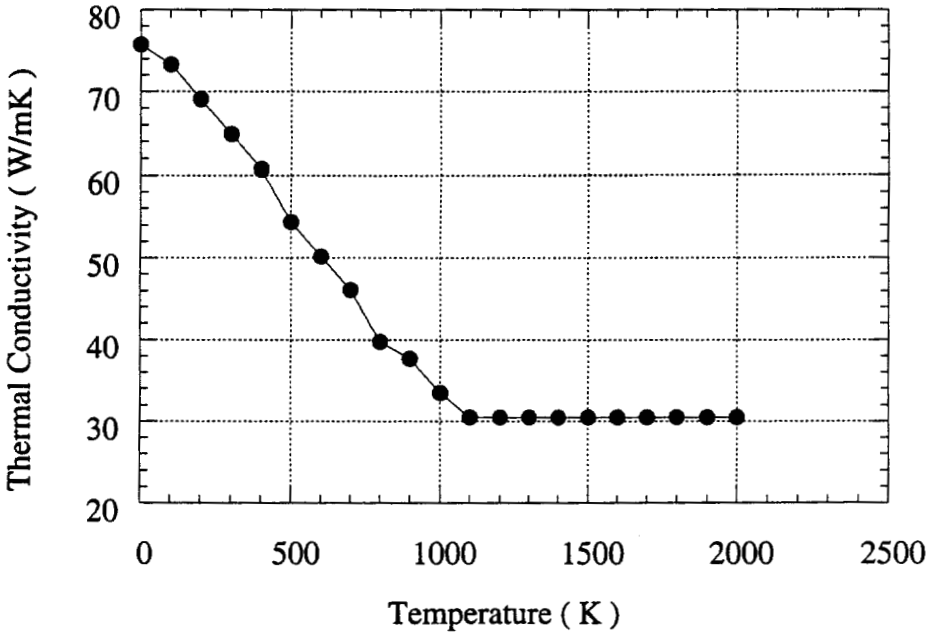

Figure 5-3 Temperature Dependent Thermal Conductivity

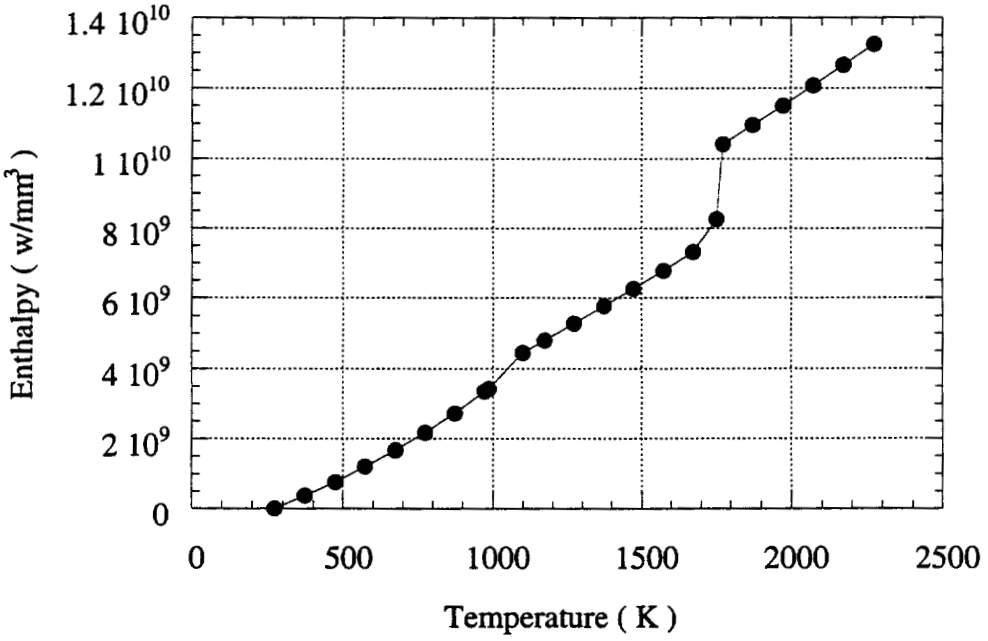

Figure 5-4 Temperature Dependent Enthalpy

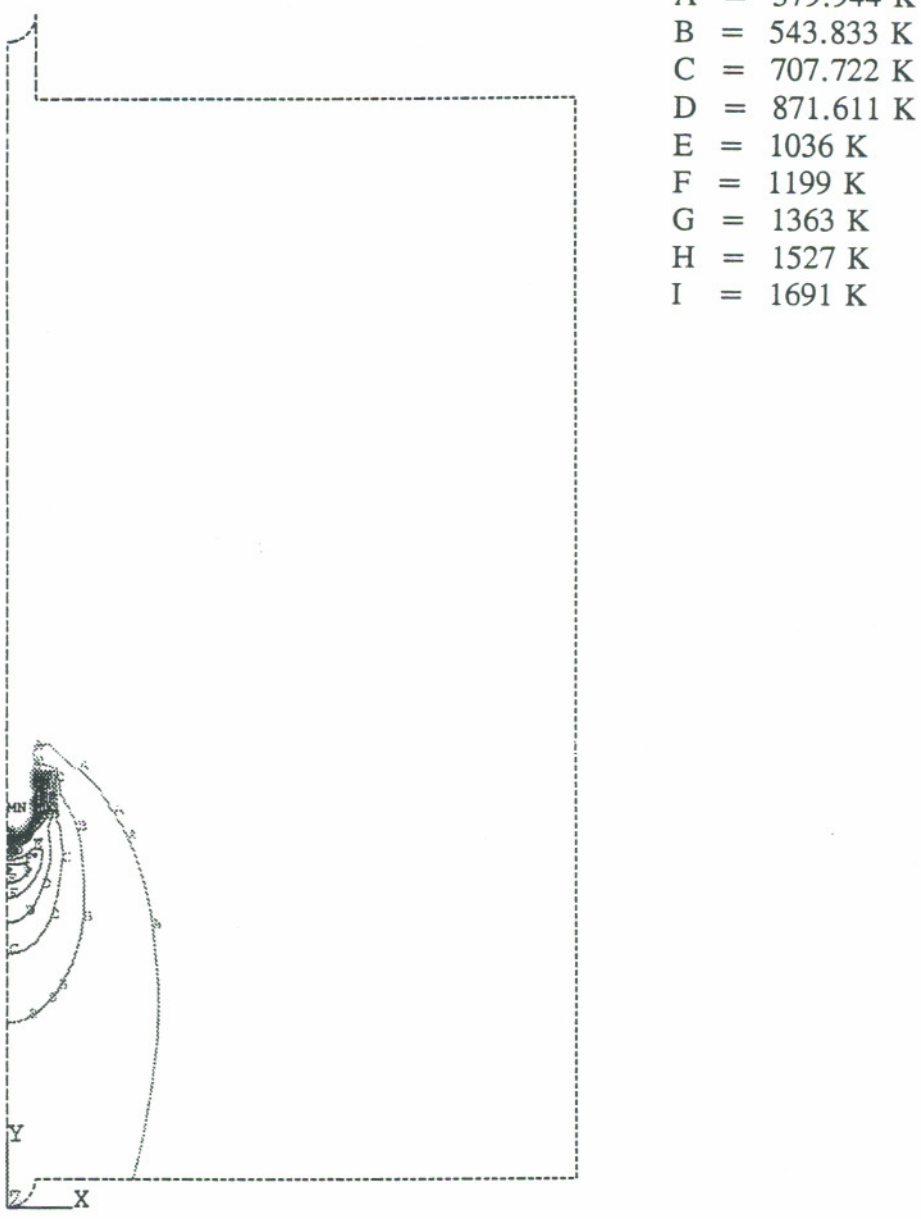

Fgure 5-5 (a) Temperature Profile at Time=1757 Seconds for Mid-Plane Model

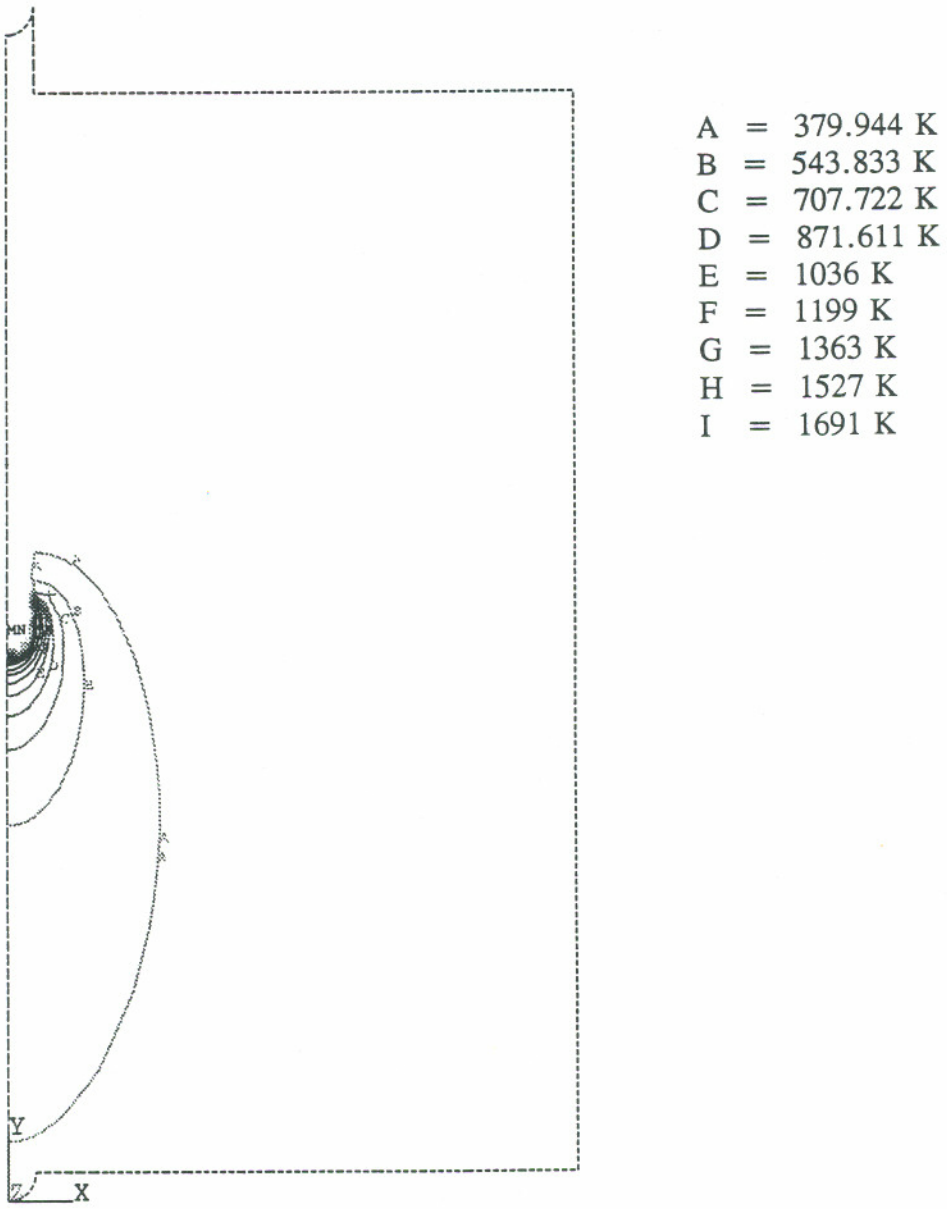

Fgure 5-5 (b) Temperature Profile at Time=2667 Seconds for Mid-Plane Model

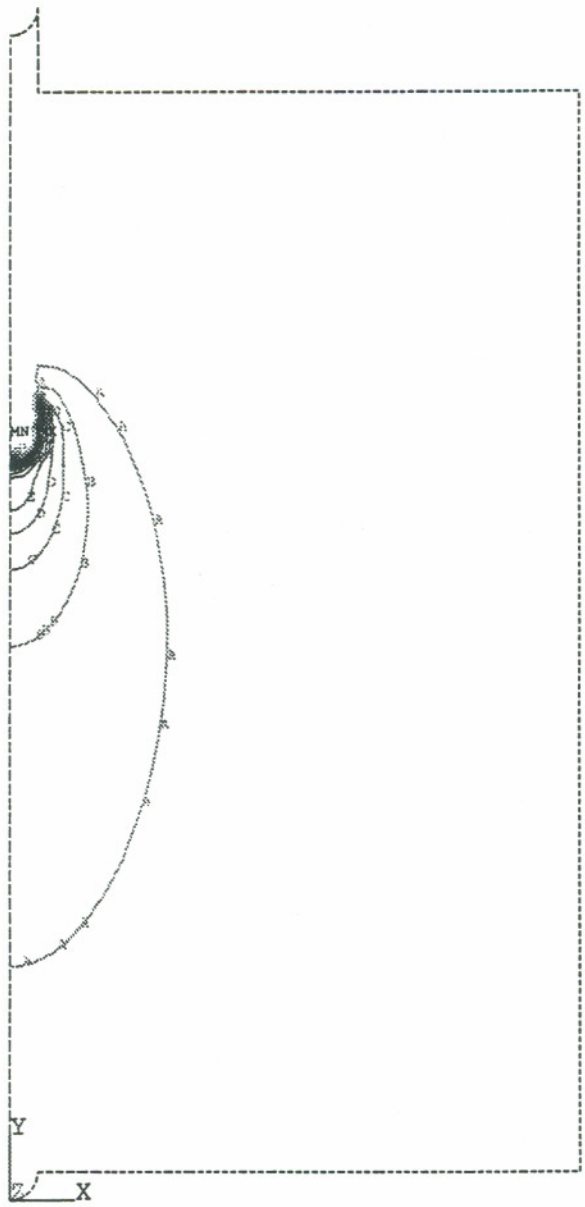

Fgure 5-5 (c) Temperature Profile at Time=3533 Seconds for Mid-Plane Model

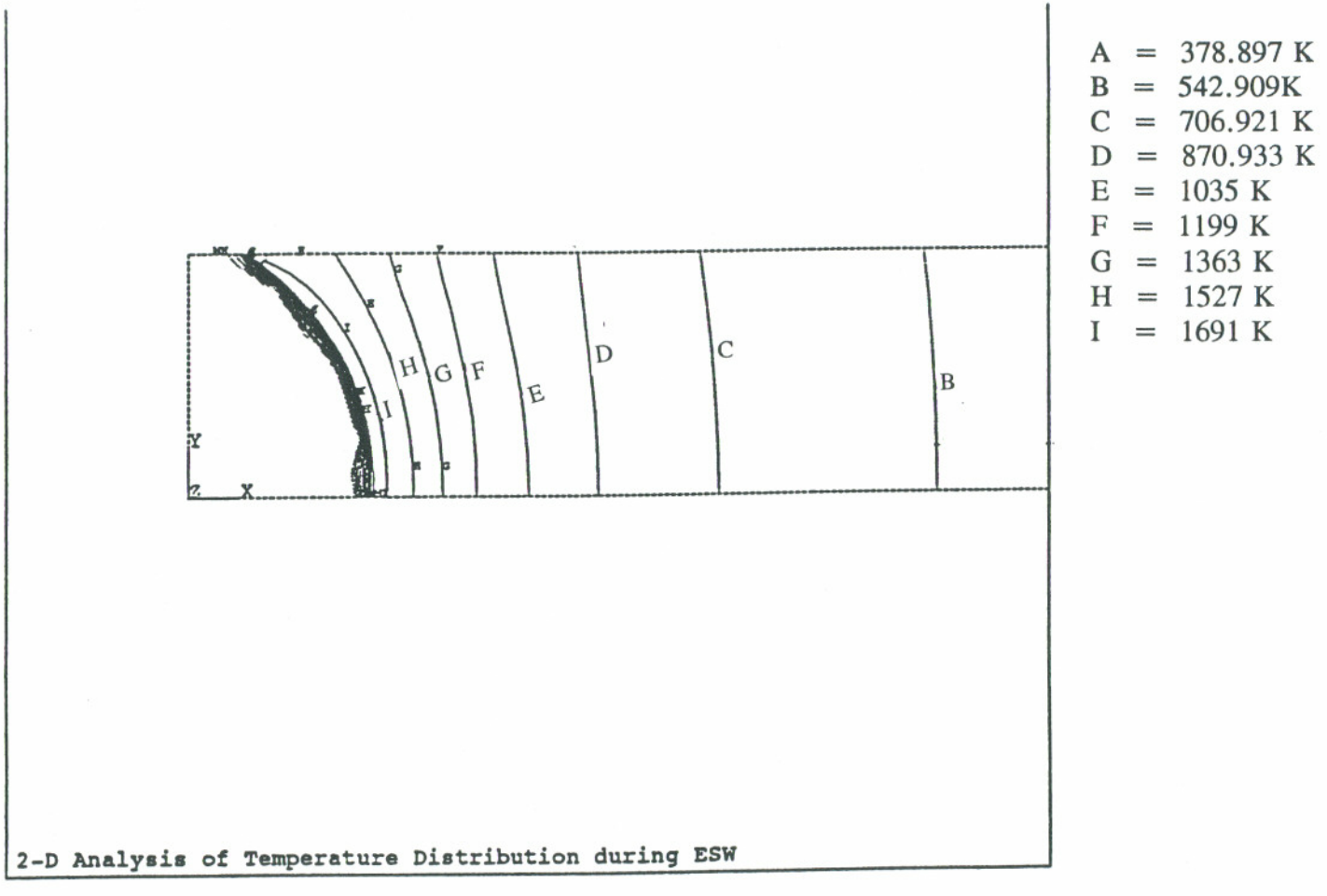

Figure 5-6 Temperature Profile at Time=41.42 Seconds for Cross-Sectional Model

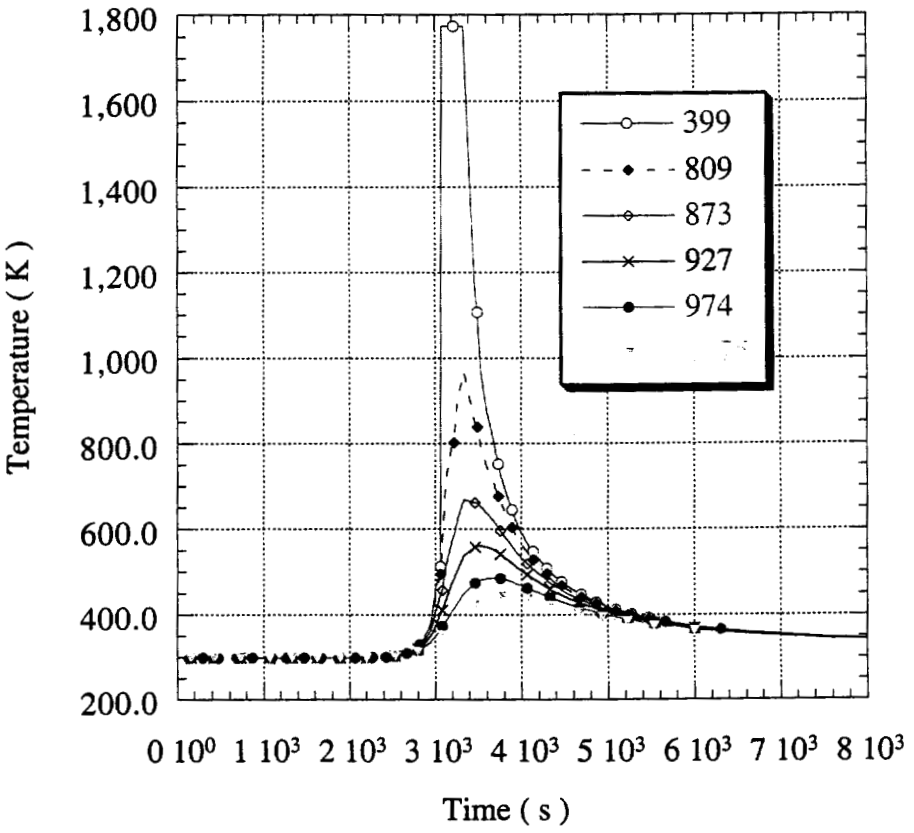

Figure 5-7 Illustration of Temperature as a Function of Time of Node Point 399,809,873,972,974 and 1075 on Mid-Plane Model

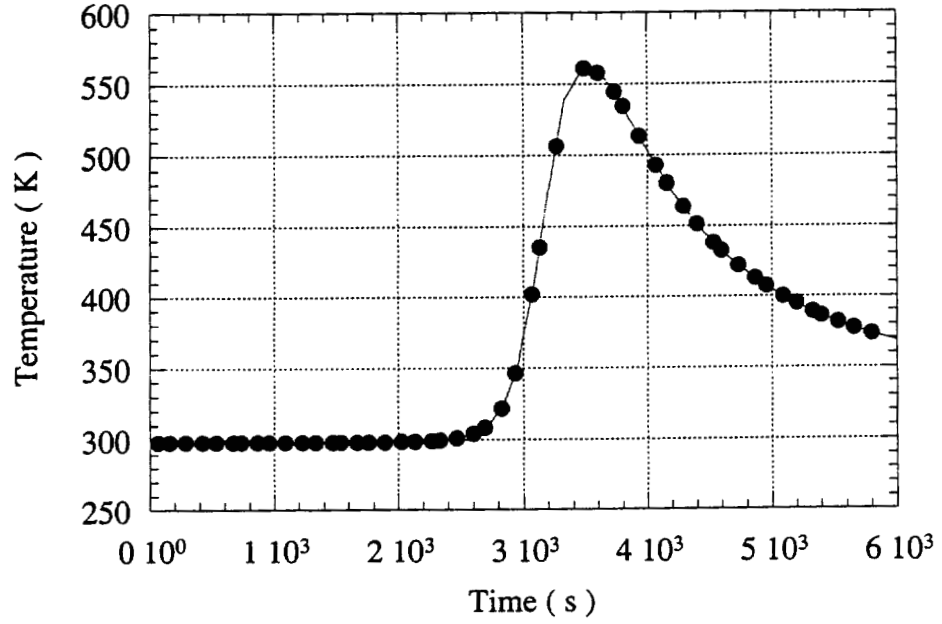

Figure 5-8 (a) Illustration of Temperature as a Function of Time of Node Point 927 in Mid-Plane Model

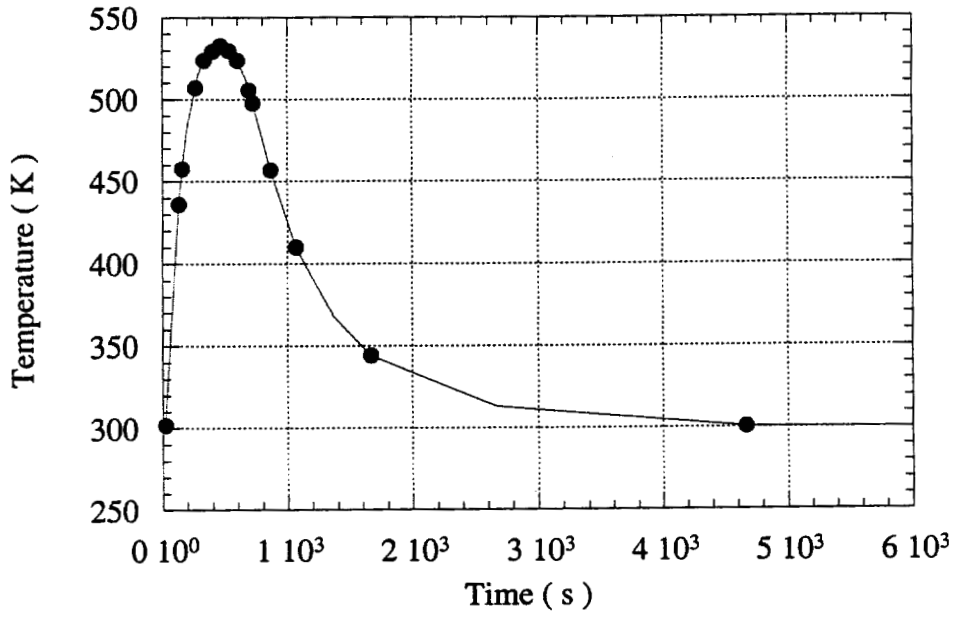

Figure 5-8 (b) Illustration of Temperature as a Function of Time of Node Point Equivalent to Mid-Plane Node Point in Cross-sectional Model

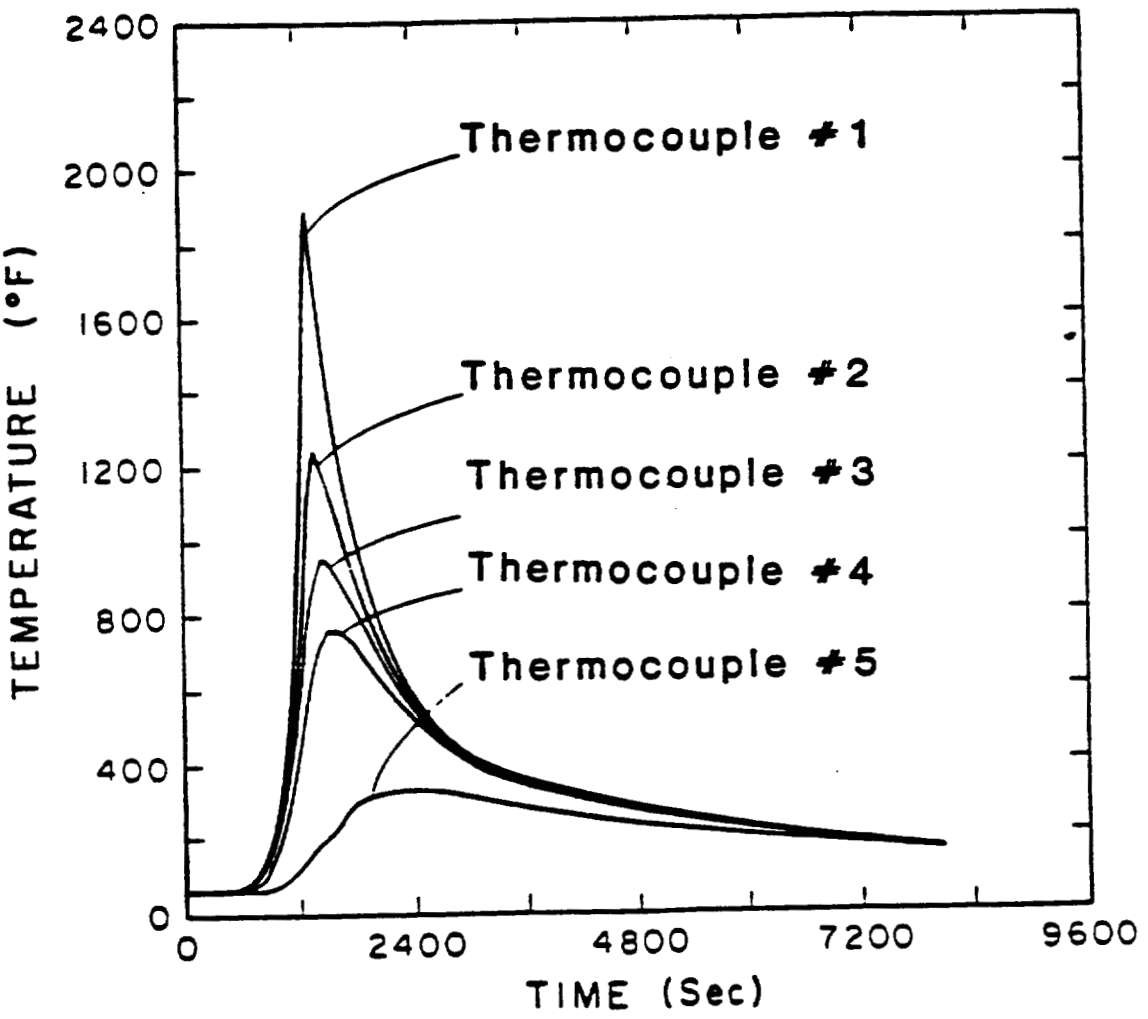

Figure 5-9 Experimental Results of Temperature as a Function of Time

CHAPTER 6
TWO DIMENSIONAL NUMERICAL ANALYSIS OF RESIDUAL STRESS IN A WELDMENT DURING ELECTROSLAG WELDING PROCESS

6.1 INTRODUCTION

Residual stress analysis was performed based on the results of thermal analysis, i.e., decouping analysis being used in this study. Because of the decouping of the thermal and stress processes, the same geometry was used in the residual stress analysis as in the thermal analysis. At the same time, simplifying assumptions are necessary due to the complexities of underlying phenomena, unavailability of material property database and limited computer configuration. It should be noticed that these simplifications only affect the magnitude of residual stresses but not the residual stress distribution.

6.2 MODELS

ASSUMPTION

The following assumptions were made in this study for residual stress analysis:

1) Reduce the non-linear thermoelastic-viscoplastic model to a linear thermoelastic model. A linear elastic-plastic stress-strain relation was assumed. The elastic and plastic regions were defined by elastic modules and plastic modules with yield stress separating them.
2) Ignore potential defect or crack formation.
3) Ignore creep and hardening, as well as introduce simplification in yield laws.

Von-Mises yield criterion and associated flow rule with kinematic hardening were assumed to consider the Bauschinger effect. As in most welding problems, on the basis that time spent at high temperature is short for a weld, creep effects were neglected.

4) The phase transformation expansion effect was considered to be similar during heating as well as cooling because of the available thermal expansion coefficient values. Plastic strain due to the change in volume during allotropic phase transformation is neglected in this study. A more representative treatment would involve incorporating the transformation of plasticity effect for weld metal as well as different HAZ regions.

5) The same material properties were used for base metal, weld metal and HAZ. This will change the magnitude of the resulting residual stresses even though the overall residual stress distribution will be unchanged. Since the objective of this research work is to study the residual stress distribution instead of specific stress values, this assumption will not cause too much difference in the final conclusions.

GOVERNING EQUATION

The numerical simulation of welding process is based on a series of small time increments from the start to the finish. During each time step, at each point of the domain, the temperature increment is calculated first with the total strain increment calculated following. In the first iteration of each time increment, the material stiffness was calculated under the elastic assumption. This method allows the incremental solution to be obtained in one iteration if elastic unloading takes place in that increment. If yield was reached in the following iteration, the elastic-plastic stiffness matrix was used during the calculation. According to the new calculated total strain increment, the associated stress increment is calculated while satisfying the yield criterion. The combination of yield condition, yield law and hardening law applies to the plastic strain. The yield condition designates the initiation of the yield of the material under multi-axial stress state. The yield law correlates the plastic strain increments with the momentary stress

state and with stress increments. The hardening law states how the yield limit is changed by yielding. Von Mises yield criteria and kinematic hardening law were chosen in this study. The stress, strain and temperature are related as following:

$$\epsilon_{ij}=\epsilon^{e}{}_{ij}+\epsilon^{p}{}_{ij}+\epsilon^{T}{}_{ij} \tag{6-1}$$

where the e, p and T refer to elastic, plastic and thermal strains. Creep strain and plastic strain were neglected in this study. Plastic flow occurs when equation 6-3 and equation 6-4 are satisfied.

$$\frac{\partial\sigma_{ij}}{\partial\tau}=D_{ijkl}(T)\frac{\partial\varepsilon^{e}{}_{ij}}{\partial\tau}+\frac{\partial D_{ijkl}}{\partial T}\varepsilon^{e}{}_{kl} \tag{6-2}$$

$$\kappa(\sigma_{e},\epsilon^{p}{}_{e},T)=0 \tag{6-3}$$

$$\frac{\partial\kappa}{\partial\sigma_{ij}}\cdot\frac{\partial\sigma_{ij}}{\partial\tau}>0 \tag{6-4}$$

where,

$$\sigma_{e}=\sqrt{\frac{3\sigma_{ij}\sigma_{ij}'}{2}} \tag{6-5}$$

$$\epsilon^{p}{}_{e}=\int_{0}^{\tau}\sqrt{\frac{2}{3}\cdot\frac{\partial\epsilon_{ij}}{\partial\tau}\cdot\frac{\partial\epsilon_{ji}}{\partial\tau}}d\tau \tag{6-6}$$

$$\kappa(\sigma_{e},\epsilon^{p}{}_{e},T)=\sigma_{e}-y(\epsilon^{p}{}_{e},T) \tag{6-7}$$

where,

κ	=	Flow surface.
σ_e	=	Von Mises equivalent stress.
$\varepsilon^p{}_e$	=	Equivalent plastic strain.
σ_{ij}	=	Deviation stress component.

y = Flow stress for uniaxial tensile test under plastic strain and temperature.

$D_{ijkl}(T)$ = Temperature dependent elastic stiffness matrix and repeated indices summed.

The strain hardening results from the following plastic work:

$$\int \sigma_{ij}'(\frac{\partial \epsilon}{\partial \tau})dt \tag{6-8}$$

While considering large strains and finite displacements, the equilibrium condition is satisfied by the application of the principle of virtual work as following:

$$\int_s t_i V_i^* ds + \int f_i V_i^* dv = \int \frac{1}{2}\sigma_{ij}(\frac{\partial V_i^*}{\partial x_j} + \frac{\partial v_j^*}{\partial x_i})dv \tag{6-9}$$

where,

t_i = Boundary traction.

f_i = Components of the body force.

S = The surface of the body

V = The volume of the body.

V* = Virtual velocity field that satisfies the imposed displacement boundary conditions.

BOUNDARY CONDITIONS

Only symmetry boundary conditions were used during the residual stress analysis. The residual stress was modeled under self-restraint only. No external restraints were applied in the analysis. To prevent rigid body motion during the finite element analysis, only two nodes on the domain edge were fully restrained. This suggests that the welded plate is not restrained but is pivoted around these restrained nodes and the restraint free condition is realized.

The applied boundary condition for mid-plane model and cross-sectional model is shown in figure 6-1 (a) and figure 6-1 (b), respectively.

MECHANICAL MATERIAL PROPERTIES

The temperature dependent mechanical properties of A36 used in the model are summarized below. Thermal expansion coefficient, Elastic modules, Poisons ratio, Yield strength and plastic modules are given a the function of temperature during the residual stress analysis.

Thermal Expansion Coefficient

Tekriwal[118] used thermal Expansion Coefficient values which increased with temperature up to 700°C and then decreased due to phase transformation from ferrite to austenite between 700°C and 900°C and again increased above 900°C. Patel[156] used gradually increasing values until 700°C and then maintained it at a constant level for higher temperature. During this study, gradually increasing thermal coefficient values are used until 1000°C and then it is maintained at a constant for higher temperature (as shown in Figure 6-2).

Elastic Modules

Elastic modules of metals depend on temperature, strain rate and thermal history. It generally decreases with increasing temperature and decreases sharply when temperature reaches a certain level. The elastic modules decreases rapidly near the transformation temperature A_{c1} while Poisson's ratio rises sharply. This point corresponds approximately to one half of the melting temperature. The deformation in high temperature range is elasto-plastic due to the low plastic modules. Since the stiffness matrix is formed initially based on elastic modules, which are higher than plastic modules, it takes more iterations and consequently more time for convergence. Because

of this, some researchers have adopted lower than actual values for the elastic modules in the high temperature range. Temperature dependent elastic modules used in this study are shown in Figure 6-3.

Yield Stress

Yielding is defined by von Mises criterion. It generally decreases as temperature increases. Once yielding has occurred, an associated flow rule is used to calculate the incremental plastic strains. The kinematic theory simplistically models reverse plasticity and Bauschinger effect that is expected during welding. The plastic behavior is assumed through a constant work-hardening slope.

Tekriwal[118] used yield strength value of 1 Mpa for mild steel at the liquid temperature which was approximately 0.4% of the value at room temperature. Temperature dependent yield strengths used in this study are shown in Figure 6-4.

Plastic Modules

As for kinematic hardening model, a zero plastic modules must be specified at temperatures above melting temperature so that the molten material can resolidify as damage-free material. The yield strength at melting temperature should be very low but not zero as this may create division problems in computation. Leung[119] found that a value of about 0.5% of the room temperature value for temperatures above melting would give reasonable results. The temperature dependent plastic modules can be approximated based on the assumption that elastic modules versus plastic modules ratio remains constant up to the melting temperature. Tekriwal[118] used very low plastic modules value of 10^{-6} MPa which will introduce insignificant error. Patel[156] assumed that plastic modules is 11.1% of elastic modules at all temperatures for a 0.23% steel and this generated higher plastic modules values. In this study, Patel's methods were used. Temperature dependent plastic modules used in this study is shown in Figure 6-5.

Poisson's Ratio

Poisson's ratio generally increases with temperature. The data at temperatures above 1000°C are not available. Patel[156] used a Poisson's ratio which varies from 0.29 at room temperature to 0.48 at 1000°C and above for a 0.23% carbon steel. Tekriwal[118] studied the effect of three different values of Poisson's ratio as a function of temperature on residual stress distribution and found that poisons ratio had no significant effect on final residual stress distribution. At higher temperatures, where the material behaves in a plastic manner, the elastic modules and Poisson's ratio have little influence on the calculated stresses. Temperature dependent Poisson's ratios used in this study are shown in Figure 6-6.

Density

Density generally decreases with increasing temperature. It is usually measured at the room temperature. The high temperature density value is usually calculated using linear thermal expansion. Because density has a minor effect on heat transfer, it is usually assumed to be constant during thermal analysis. A constant density of 7800 kg/m^3 was used in this study.

6.3 SOLUTION PROCEDURE

A transient thermal analysis which was illustrated in last chapter was first performed to obtain nodal temperature solution. The nodal thermal history was saved as the thermal load in the mechanical analysis. The same geometry and finite element mesh was employed in both the thermal and mechanical analysis. In this way, node temperature history could be directly inputted to perform mechanical analysis. The mechanical finite element model was obtained directly from the thermal model by using the conversion ETCHG in ANSYS. Plane42 element was used to perform thermal mechanical analysis. The element is defined by four nodes with each node having two

degrees of freedom (translation in the x and y direction). The temperature dependent mechanical material properties were defined. This is the PREP part of ANSYS program.

Under current computing conditions (computer capacity and speed), it is impossible to conduct stress analysis at every time solution for the thermal analysis due to extremely high computational time involved. During the solution part of ANSYS analysis, static stress analysis instead of transient stress analysis was used in this part of calculation. The reason to use static analysis instead of the transient analysis is to reduce the computing cost while still achieving reasonable results at the same time. The boundary conditions were inputted next, followed by definition of the numerical procedure option, such as autoloading to track the load and monitor convergence, and selection of the large strain option, Newton-Raphson solution procedure. The loads which were chosen from the thermal analysis should represent thermal history as close as possible. Preliminary study shows that with reasonably reduced number of sequential structural solutions, the results are still acceptable while saving substantial computer calculation time. A stringent convergence criteria of 1 % plasticity ratio was specified and time-step optimization was employed to automatically determine convergence checking and optimize on the number of iteration. Different load steps were defined by reading nodal temperatures corresponding to certain time intervals. This load stepping scheme was essentially the same as the temperature history from the thermal analysis. That is to say, the time stepping was much finer in initial part of the thermal cycle and gradually coarsened in the later part of the weld cooling. From the experimental results, the stresses of most interest were the stresses perpendicular to welding direction and the stresses parallel to welding direction. Because of this, the hydrostatic stress and Von Mises stress was not included in this part of study. The obtained results are summarized in the next section.

Because cross-sectional model is less time consuming compared with mid-plane model, only one set of operation parameters was studied for mid-plane model and several sets of operation parameters of plate length, plate thickness and welding speed were studied with cross-sectional model. It also should be noted that the mid-plane model and cross-sectional model have the mid-plane centerline in common (OD in cross-sectional

model (Figure 6-1 (b) is the place where mid-plane was positioned) in both of the models. The two models represent same process from different view point. Mid-plane model illustrates the whole process while cross-sectional model only describe part of the process. Therefore, some differences should be expected between the residual stress distribution on OD side for cross-sectional model and line parallel to CB_n inside the mid-plane model (Figure 6-1). The results for the two models on the same line were compared in the discussion section.

6.4 RESULTS

In order to compare mid-plane model and cross-sectional model, one set of same parameters were used for both of them. Several other sets of operation parameters were run using cross-sectional model to evaluate the effect of welding speed, plate length and plate thickness on residual stress distribution during ESW processing. Figure 6-8 illustrates the residual stress distribution for cross-sectional model which was run under the same parameters as mid-plane model. The cross-sectional model results for residual stress distribution change with the variation of welding speed, plate length, plate thickness are illustrated in Figures 6-9 to 6-11. The results for were summarized as follows.

MID-PLANE MODEL RESULTS

Only one model was run with mid-plane model, i.e., with one set of operation parameters. Figure 6-7 illustrates the residual stress in the weldment longitudinally down the plate length as a function of distance from the weld center line (WCL) for mid-plane model. Residual stress perpendicular to the welding direction and parallel to the longitudinal direction of the plate (longitudinal residual stress) shown in Figure 6-7 (a) begins at a high tensile value at WCL, decreases slightly and then increases into the fusion zone/HAZ, and then decreases to zero with increasing distance down the weldment. Its initial value is set at about plate material yield strength level of 250 MPa (36 ksi) with its maximum approximately 0.025 m (1 inch) from WCL, and decreases to

zero around 0.2 m (8 inch) from WCL. Residual stress parallel to the welding direction (parallel residual stress) shown in Figure 6-7(b) begins at a tensile stress approximately 170 percent of plate material yield strength at WCL, decreases to a compression value near 33 percent of yield strength, and then increases to zero as distance from WCL increases. Maximum compression residual stress occurs around 0.15 m (6 inch) from WCL and zero residual stress is approached near 0.4 m (16 inch) from WCL.

CROSS-SECTIONAL MODEL RESULTS

Mid-Plate Results

The cross-sectional plane model results for residual stress distribution at "mid-plate" (OD side) along the length of the weldment with the same operation parameters as mid-plane model are illustrated in Figure 6-8. Longitudinal residual stress (Figure 6-8 (a)) begins at a tensile value at WCL, decreases rapidly and then increases into the fusion zone/HAZ, and then decreases to zero with increasing distance down the weldment. Its initial value is approximately 45 percent of the plate yield strength, decreases to a tensile stress of 15 percent of the yield strength, rises to a tensile value of approximately 90 percent of yield approximately 0.05 m (1.6 inch) from WCL, and then decreases to zero around 0.2 m (8 inch) from WCL. Residual stress perpendicular to the welding direction and in the short transverse (through-thickness) direction of the plate (transverse residual stress) as shown in Figure 6-8 (b) begins at a compressive stress approximately 50 percent of yield at WCL, decreases to a compressive stress of 90 percent of yield, increases to a tensile stress of approximately 110 percent of plate yield at 0.05 m (2 inch) form WCL, decreases to a compressive strength of 30 percent of yield and then increases to zero as distance from WCL increases at about 0.14 m (0.55 inch) from WCL.

Parameter Effect

Residual stress perpendicular to welding direction along middle plane of ESW

process (longitudinal residual stress) as a function of distance from the weld centerline for a variety of ES welding occasions is shown in Figures 6-8 (a), 6-9 (a), 6-10 (a) and 6-11 (a). The centerline residual stress increased with decreasing welding speed (see in Figure 6-9 (a)). The distance from WCL needed before the tension stress to dies out increased with decreasing welding speed.

Residual stress in the parallel (through plate height) direction of the plate (parallel residual stress) along middle plane of ESW process as a function of distance from the WCL for a variety of ES welding occasions is shown in Figures 6-8 (b), 6-9 (b), 6-10 (b) and 6-11 (b). The trends and residual stress values are the same after the distance from WCL reaches 0.1 m for all welding speed (see in Figure 6-9 (b)). The only real difference is at WCL. It means that parallel residual stress at WCL changes with the welding parameters. WCL residual stress increases with decreasing speed going from compression (-200 MPa) at $1x10^{-3}$ m/s to tension (180 MPa) at $1x10^{-4}$ m/s. At a welding speed of $1x10^{-4}$ m/s, even though transverse stress is in high tension stress range at the center of the welded plate, the tension stress drops sharply to compression stress along this direction with increasing distance from WCL.

Residual stress perpendicular to welding direction (longitudinal residual stress) along the WCL as a function of distance from the middle of welded plate for a variety of ES welding occasions is shown in Figures 6-9 (c), 6-10 (c) and 6-11 (c). The longitudinal residual stresses were tensile stress for all welding speed (see in Figure 6-9 (c)). Tensile stress decreases with increasing distance from the middle plane of welded plate when the distance is less than 0.006 m (0.0236 inch) and increases when the distance is bigger than 0.006 m (0.0236 inch). The highest longitudinal tensile stress along the weld line exists at the plate surface. The WCL residual stress values increased with decreasing welding speed.

Residual stress in through thickness direction (transverse residual stresses) along the WCL as a function of distance from the middle of welded plate for a variety of ES welding occasions is shown in Figures 6-9 (d), 6-10 (d) and 6-11 (d). The transverse residual stress is more complicated than both longitudinal stress and parallel stress. In most cases, the transverse residual stress decreases with increasing distance from the

middle plane of welded plate when the distance is less than 0.01 m (0.4 inch), increases with the increasing distance from middle plane of welded plate when the distance is greater than 0.01 m (0.4 inch). At the WCL, the residual stress is compression stress except tension stress when welding speed reaches $1x10^{-4}$ m/s.

Residual stress distribution as a function of distance from center of welded plate along middle plane of the welded plate and along WCL with different deposition speed were shown in Figures 6-9 (a), (b), (c) and (d). From Figures 6-9 (a) and (b), it can be seen that the stress distribution curves shift to right with decreasing deposition speed. The high tension stress decreases as welding speed decreasing. From Figures 6-9 (c) and (d), it can be seen that in most cases the transverse residual stress shows compression stress at center of welded plate. Although, at the center of the welded plate, it was a high tension stress instead of compression stress with the lowest welding speed. In all cases, high tension stress level was found in the direction perpendicular to weld line, and both tension stress and compression stress were found in the direction parallel to welding line.

Residual stress distribution along middle plane of the welded plate and along WCL with different plate lengths were shown in Figures 6-10 (a), (b) and (c). It can be seen that residual stress distribution in the welded plate with lengths of 6.12 m and 0.8 m are almost the same. When the plate length decreases to 0.3 m, the longitudinal residual stress shifted to right and no parallel compression residual stress was found in the HAZ. The length change caused little variation in the through thickness residual stress along WCL. These results reveal that plate length mainly affects the heat transfer behavior in the longitudinal direction of the welded plate and it has no effect on the heat transfer in the through thickness along WCL direction with copper shoe pressed on the welded plate. The results also show that the effect of plate length on residual stress distribution in the welded plate is less than the effect of deposition speed on both heat transfer pattern and residual stress distribution.

Residual stress distribution along middle plane of the welded plate and along WCL with a plate thickness of 0.06 m instead of the 0.08 m for the other cases were shown in Figures 6-11 (a) and (b). The results also show that residual stress in the through thickness direction at the center of welded plate is tensile stress instead of compression

stress. The residual stress along middle plane of welded plate in the direction shows compression stress near HAZ instead tensile stress with thickness of 0.08 m welded plate. Such occurrence reveals that the effect of the welded plate thickness is more important than that of plate length.

In general, the residual stress along middle plane of welded plate in the direction perpendicular to weld line was shown as tensile stress. The residual stress along middle plane of welded plate in the direction parallel to weld line was shown as tensile or compression stress at center of welded plate. Residual stress will reach the peak tensile stress in HAZ, drop to compression and then recover to zero residual stress with increasing distance from WCL. Whether the residual stress at center of welded plate is tensile stress or compression stress is decided by the welding operation parameters. Among the parameters, plate thickness and deposition speed are important. Plate length has little effect on residual stress distribution. As for the residual stress along WCL, high tensile stress can be found at plate surface in the direction perpendicular to weld direction. In most cases, the transverse residual stress was compressive stress with small tensile stresses at plate surface.

6.5 DISCUSSION

The residual stress results for both 2D models are comparable. Figures 6-7 and 6-8 have the same operation parameters while modeling different planes of the same process with mid-plane model for Figure 6-7 and cross-sectional model for Figure 6-8, respectively. They exhibit similar general trends while at the same time exhibit different model-specific results, as should be expected as they model different cooling scenarios. Both models exhibit similar trends for the distribution of residual stress perpendicular to weld centerline (Figures 6-7 (a) and 6-8 (a)). The difference between their WCL residual stress results may come from the effect of the copper shoe in the cross-sectional model and the presence of the height of the weld in the mid-plane model. The copper shoe results in a more complicated centerline residual stress pattern in the cross-sectional model than that for mid-plane model. Residual stress starts with tensile stress at weld

centerline, decreases and then increases with distance from weld centerline, and then decreases to zero. Comparing with cross-sectional model, the mid-plane model needs a shorter distance from the WCL to reach the maximum residuals tensile stress and then to go down to zero. It should be noted that residual stresses for both mid-plane model and cross-sectional model displayed the same trend. Both of them have "dip" at WCL to fusion boundary. The only differences are that "dip" in cross-sectional model is much greater than that in mid-plane model and mid-plane model possesses much higher residual stress than cross-sectional model. Both models also have peak residual stress at 0.05 m from WCL and then decrease as the distance from WCL increases. Thus the only real difference between the two models results occurs in the fusion region. This difference may be caused by the effect of copper shoe. At the same time, both models have the same trend for parallel residual stress. Parallel residual stress distribution (Figures 6-7 (b) and 6-8 (b)) exhibits a high tensile residual stress at/near weld centerline decreasing to a compressive stress and then increasing to zero residual stress with increasing distance from WCL with maximum compressive stress being essentially equal for both models. The maximum tensile stress in mid-plane model is greater than that for the cross-sectional model and its residual stress approaches zero at a shorter distance than the cross-sectional model. Another difference between model results is the presence of a compressive region at weld centerline in the cross-sectional model.

Assessment of the overall results of the mid-plane analysis indicates that the effect of the copper cooling shoes/surface cooling can not be ignored at middle plane even for a plate of 0.08 m in thickness.

Residual stress is decided by the thermal loads during process. The temperature distribution is affected by heat transfer behavior in the welded plate. As for the ESW process, copper shoes play an important role in the welding process. The heat transfer through welded plate thickness direction is more important than that for plate longitudinal direction and plate up and down direction. This phenomena controls the residual stress distribution inside the welded plate. The effect of welding parameters on residual stress distribution is through the effect on heat transfer process.

When the welded plate is long enough, plate length has almost no effect on

residual stress distribution because temperature drops to room temperature in the middle of welded plate instead of at the end of welded plate. When the plate length is short enough, the heat transfer along welded plate will be affected by the convection effect at the end of welded plate. That is why residual stress is almost the same for the welded plate which has the length of 6.12 m and 0.8 m and different thermal stresses distribution for the welded plate which has the length of 0.3 m.

As for the effect of deposition speed, it can be understood from aspect of heat transfer. When the deposition speed is slow, the model configuration, i.e., a constant slag, fusion zone value leads to higher heat input during unit time, which in turn decrease heat dissipation in the welded plate during welding while decreasing the temperature gradient. That also may be one of the reasons that when the deposition speed drops low enough, the residual stress at the center of welded plate could turn from high value compression stress to tensile stress. Figure 6-9 (c) shows that the stress gradient is small at the deposition speed of $1x10^{-4}$ m/s. The effect of welded plate thickness on residual stress distribution is closely connected with the effect of copper shoes. The less the plate thickness, the higher rate of heat loss in the thickness direction with less heat loss along welded plate direction. That is to say, the effect of decreasing plate thickness has similar effect as increasing deposition speed on residual stress along welded plate direction. Decreasing thickness corresponds with faster deposition speed and long plate length.

The longitudinal residual stress in mid-plane model approaches zero near 0.2 m from WCL (see in Figure 6-7 (a)) while longitudinal residual stress along middle plane of welded plate in cross-sectional model approaches zero near 0.4 m from WCL (see in Figure 6-10 (a)). This phenomena could be explained from the effect of copper shoe on heat transfer behavior in welded plate during ESW welding process. The mid-plane model did not consider the effect of copper shoe. The heat transfer for mid-plane model is mainly from the welded plate boundary. Cross-sectional model, which includes the effect of copper shoe, leads to much less heat loss in the direction along welded plate. That will cause less gradient stress distribution along welded plate direction in cross sectional plane model. That is why the cross-sectional model stress drops to zero at near 0.4 m instead of mid-plane model at 0.2 m.

In general, three dimensional model is needed for this study to understand the thermal and mechanical phenomena of ESW welding process.

6.6 CONCLUSIONS

1) Three dimensional model is needed to fully understand residual stress distribution in ESW weldments.
2) Among welding parameters (plate thickness, welding speed and plate length), the effect of plate thickness and welding speed on residual stress distribution in ESW weldments is greater than that of plate length.
3) Residual stress distribution is not uniformly.

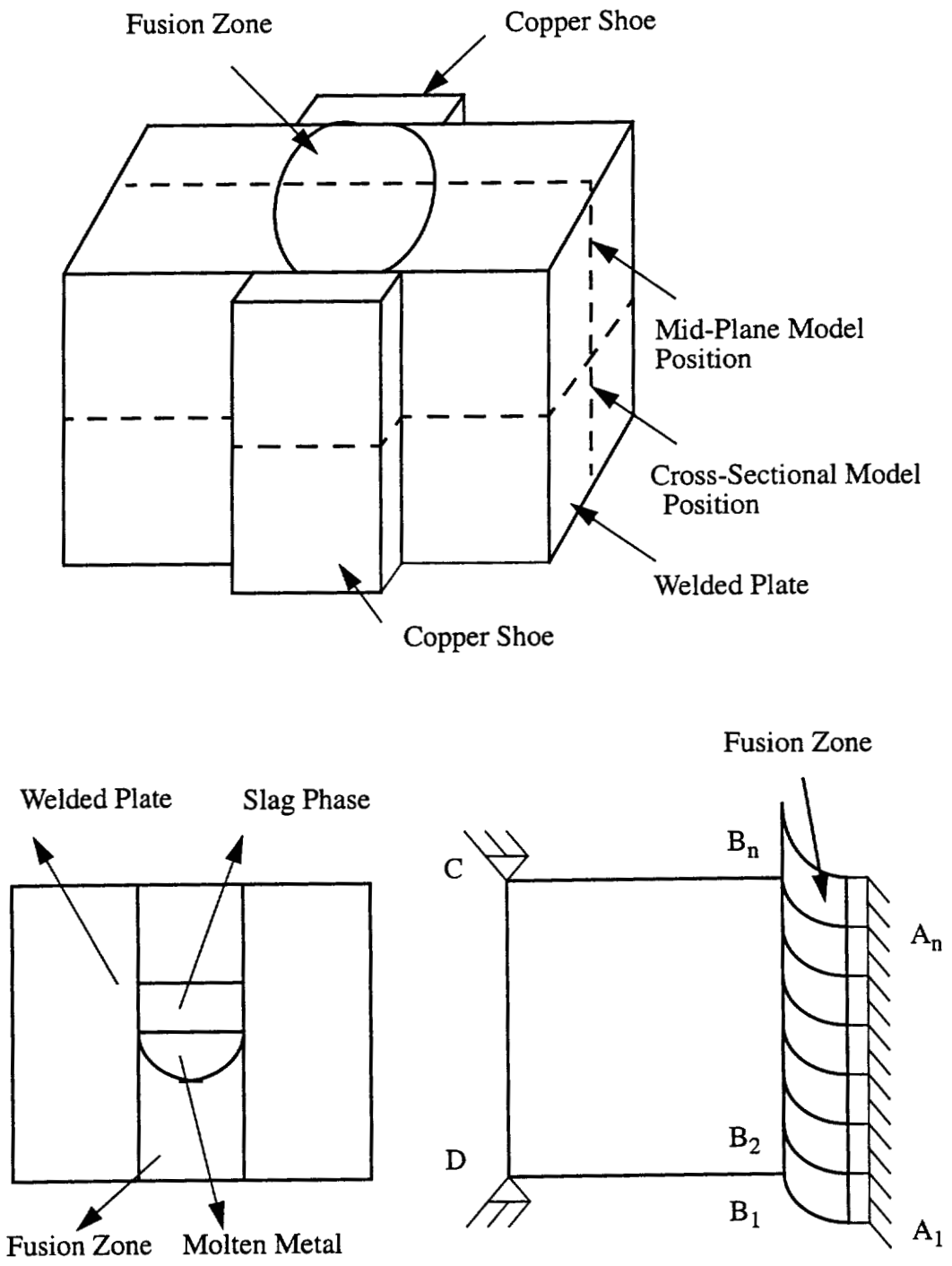

Figure 6-1 (a) Illustration of Boundary Condiction for Thermal Stress Analysis in Mid-Plane Model

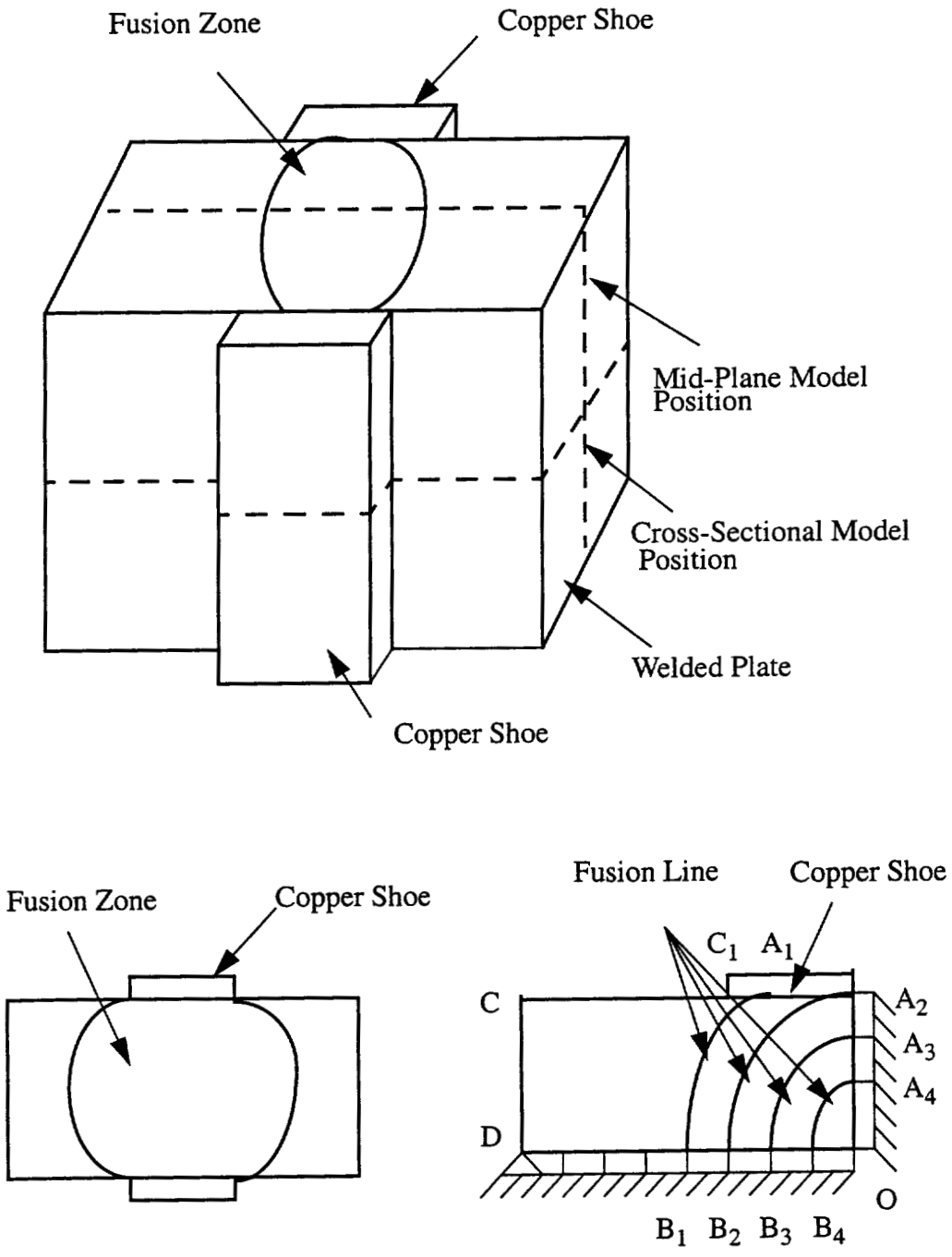

Figu 6-1(b) Illustration of Boundary Condition for Thermal Stress Analysis in Cross-Sectional Model

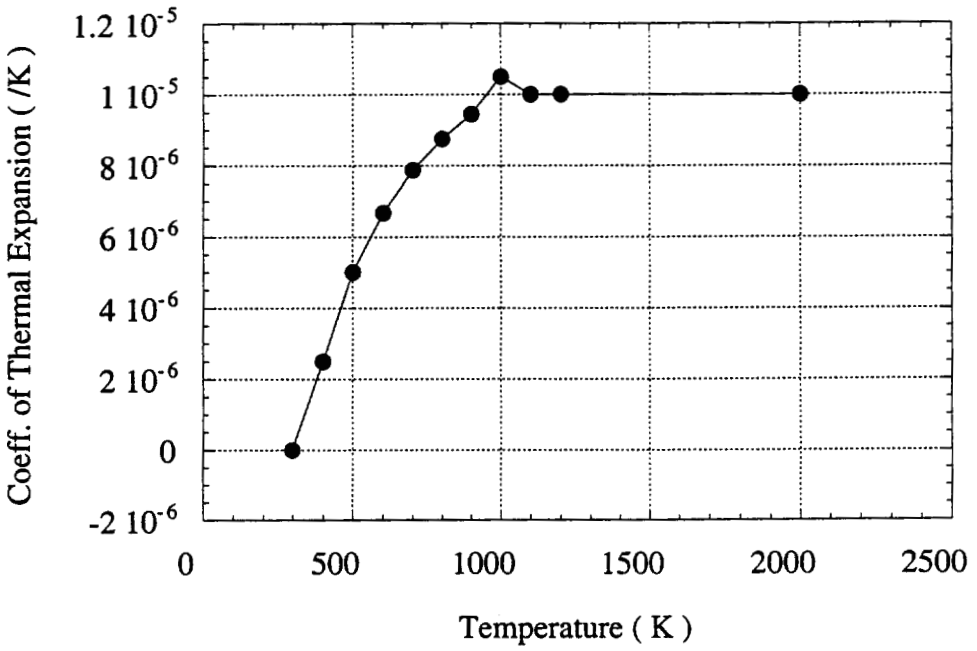

Figure 6-2 Temperature Dependent Coeff. of Thermal Expansion

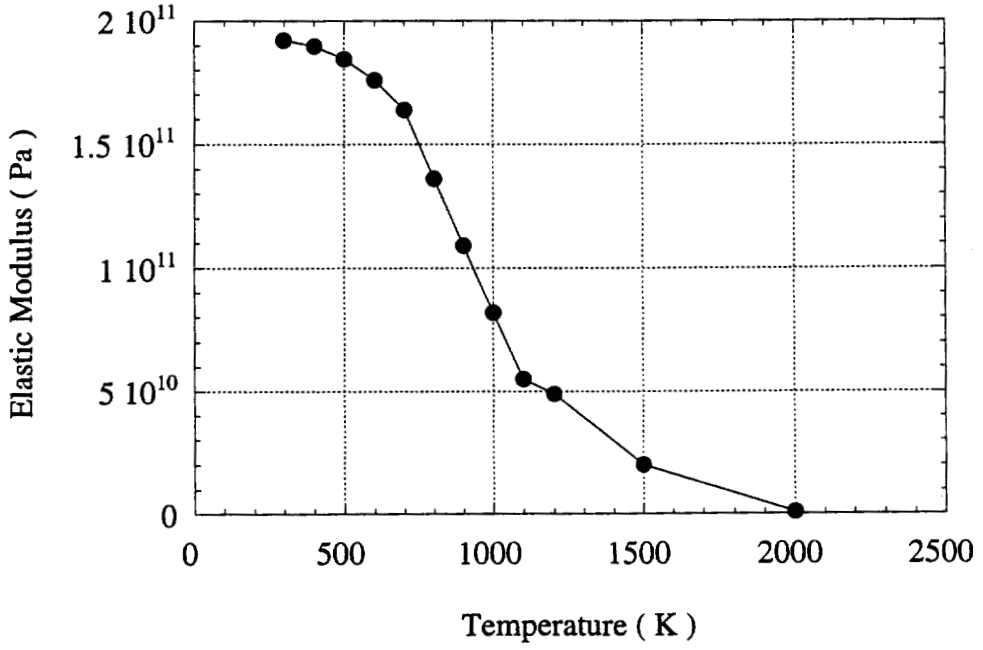

Figure 6-3 Temperature Dependent Elastic Modulus

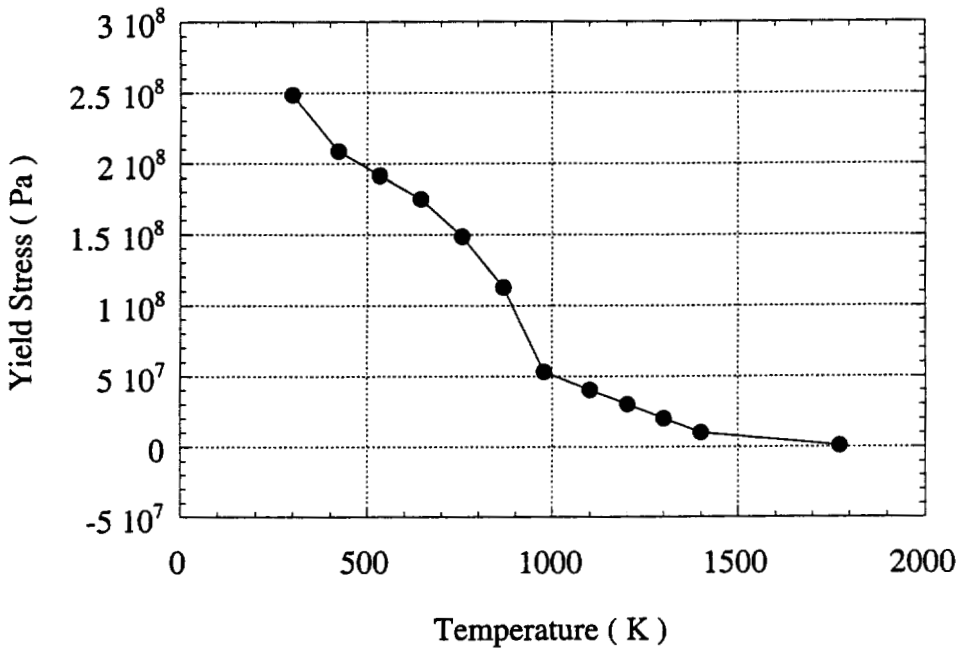

Figure 6-4 Temperature Dependent Yield Stress

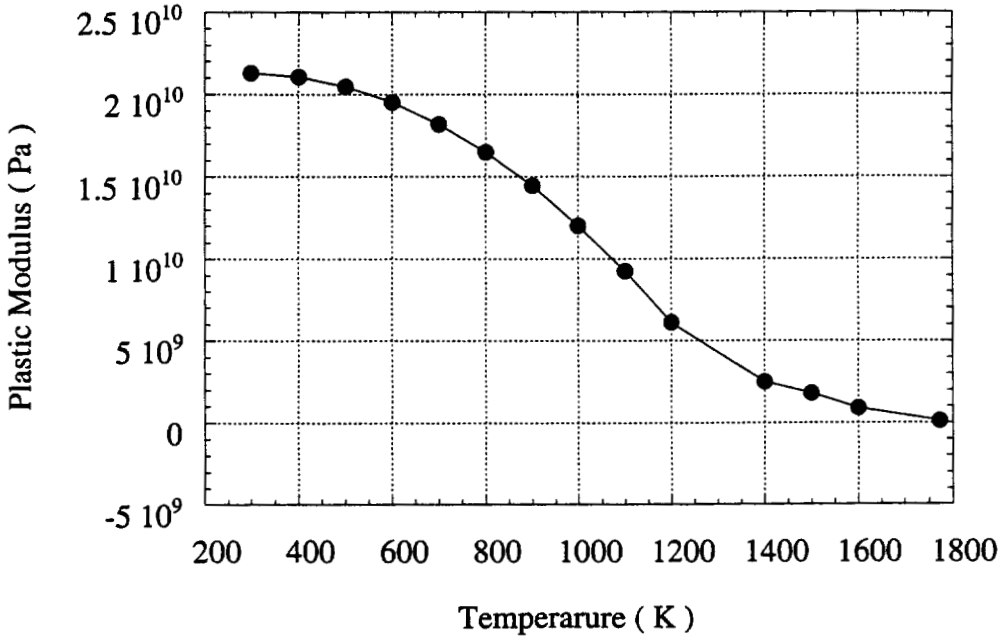

Figure 6-5 Temperature Dependent Plastic Modulus

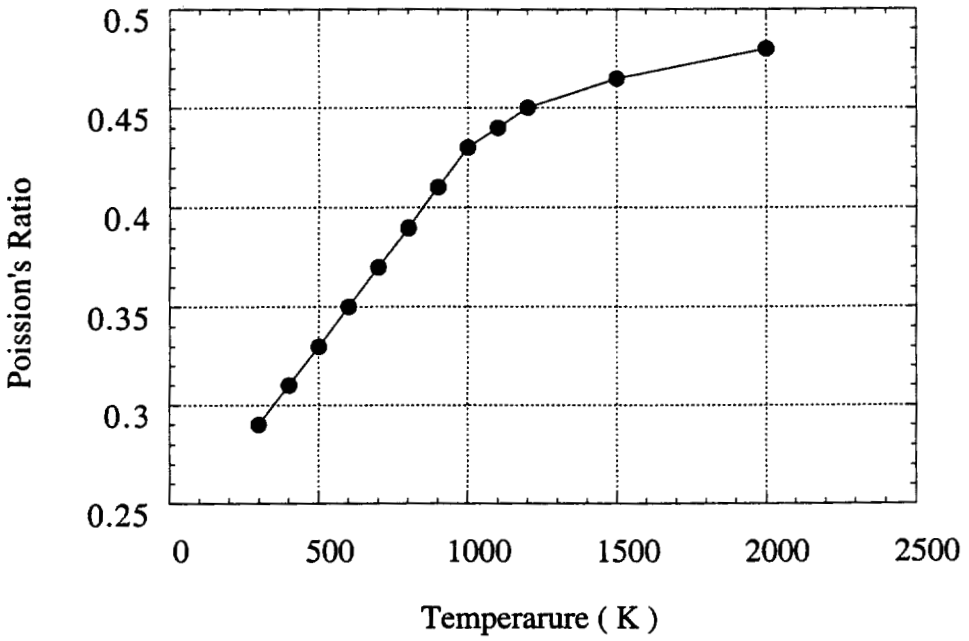

Figure 6-6 Temperature Dependent Poission's Ratio

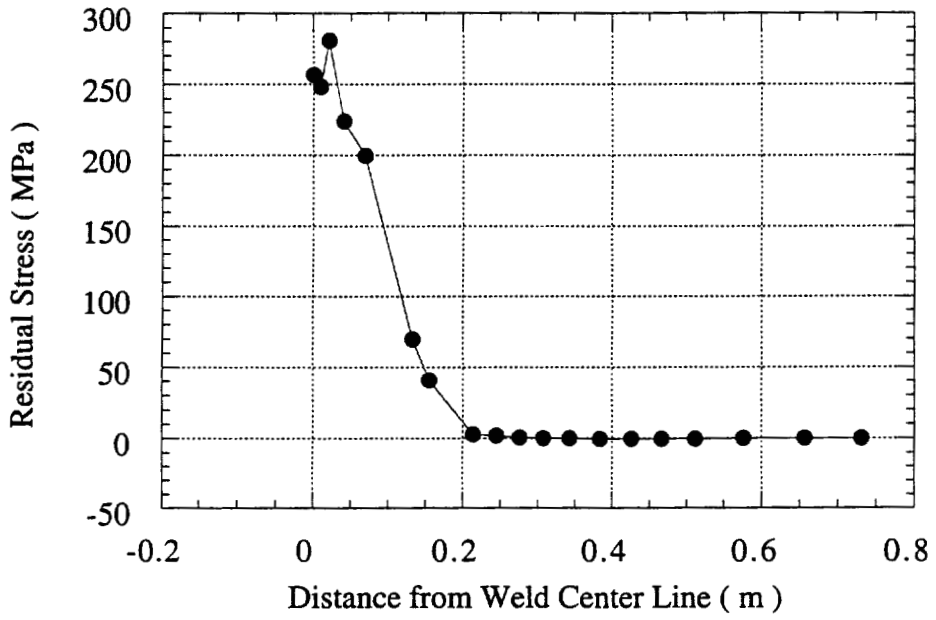

Figure 6-7 (a) Longitudinal Residual Stress as a Function of Distance from WCL
(Mid-Plane Model, v= $3x10^{-4}$m/s, l=6.12m, t=0.08m)

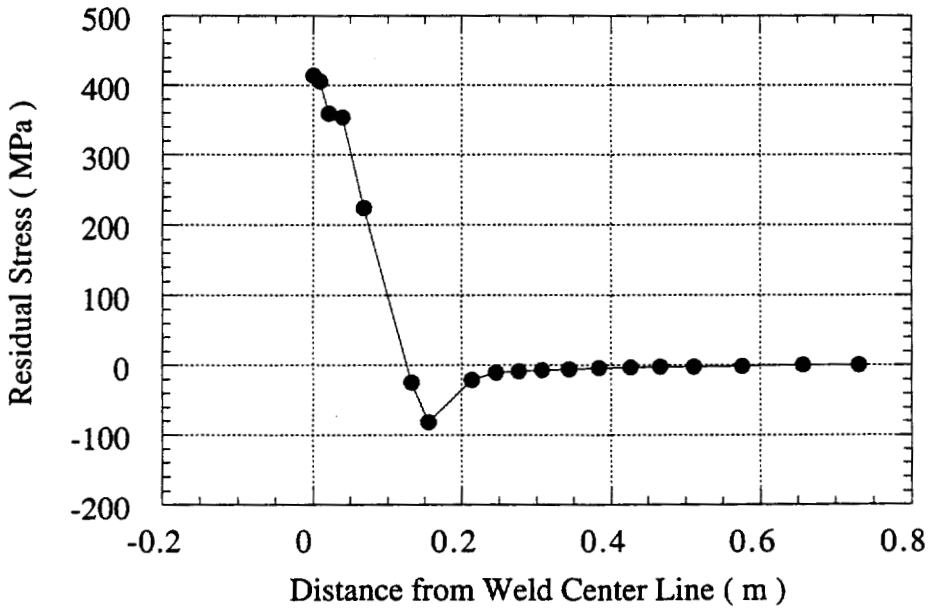

Figure 6-7 (b) Parallel Residual Stress as a Function of Distance from WCL
(Mid-Plane Model with v=$3x10^{-4}$m/s, l=6.12m, t=0.08m)

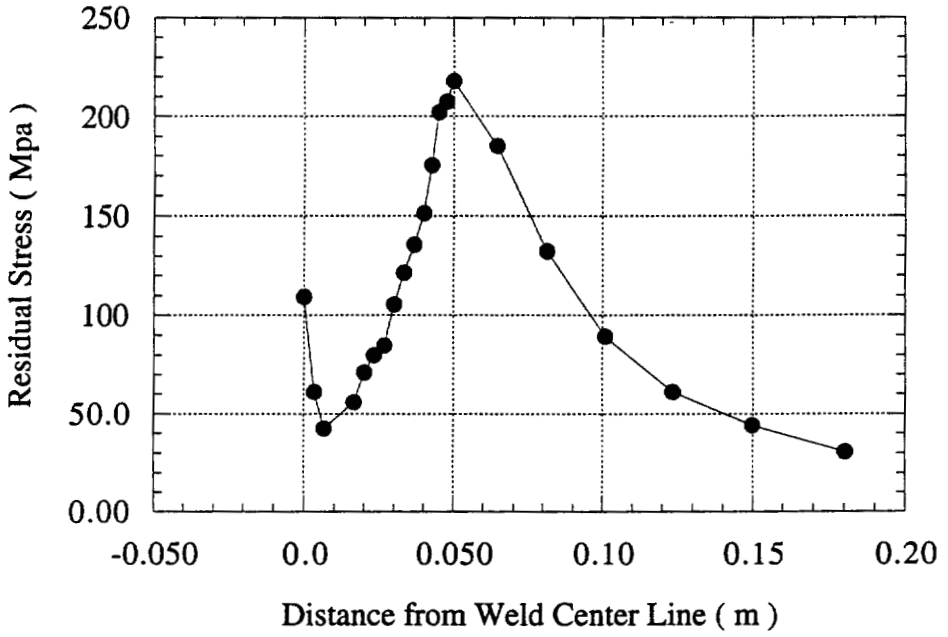

Figure 6-8 (a) Longitudinal Residual Stress along Middle Plane of Welded Plate as a Function of Distance from WCL
(Cross-Sectional Model, l=6.12m, t=0.08m, v=3x10^{-4} m/s)

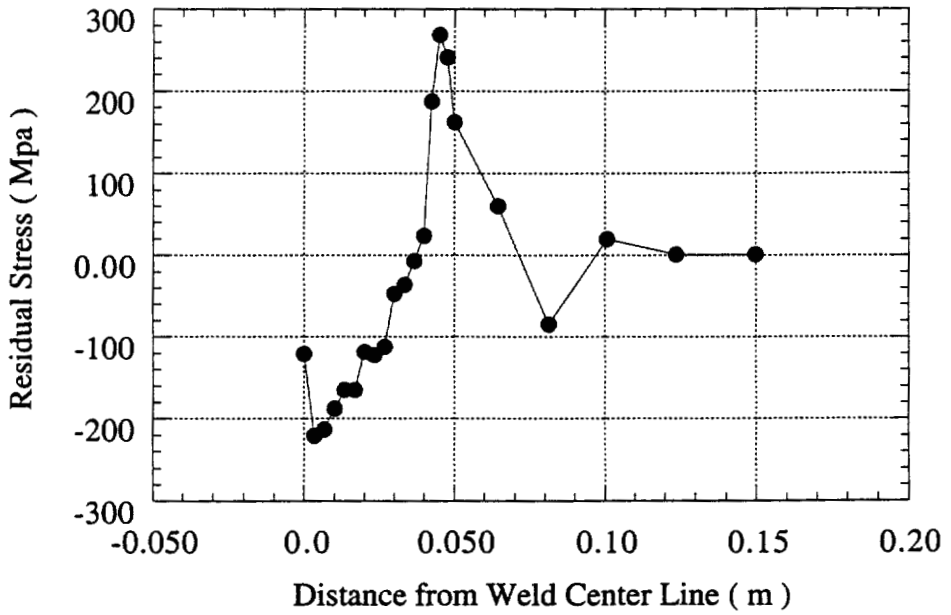

Figure 6-8 (b) Parallel Residual Stress along Middle Plane of Welded Plate as a Function of Distance from WCL
(Cross-Sectional Model,l=6.12m, t=0.08m, v=3x10^{-4} m/s)

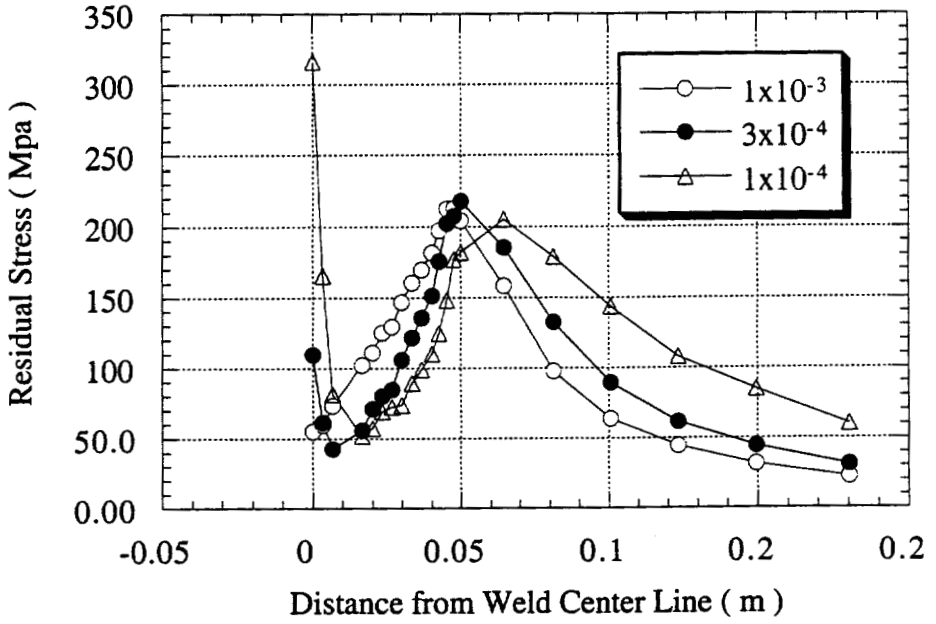

Figure 6-9 (a) Effect of Welding Speed on Longitudinal Residual Stress along Middle Plane of Welded Plate
(Cross-Sectional Model, l=6.12m, t=0.08m)

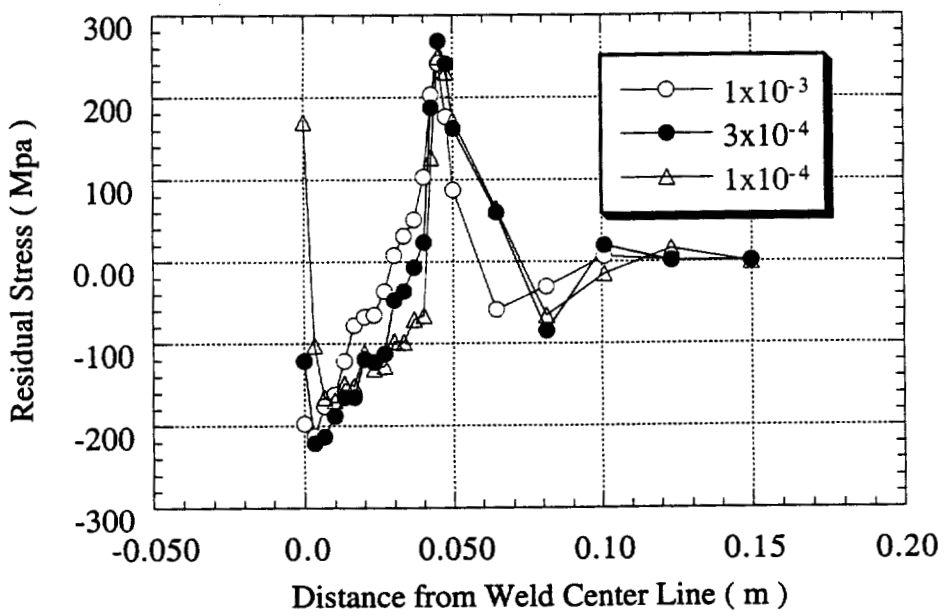

Figure 6-9 (b) Effect of Welding Speed on Parallel Residual Stress along Middle Plane of Welded Plate
(Cross-Sectional Model, l=6.12m, t=0.08m)

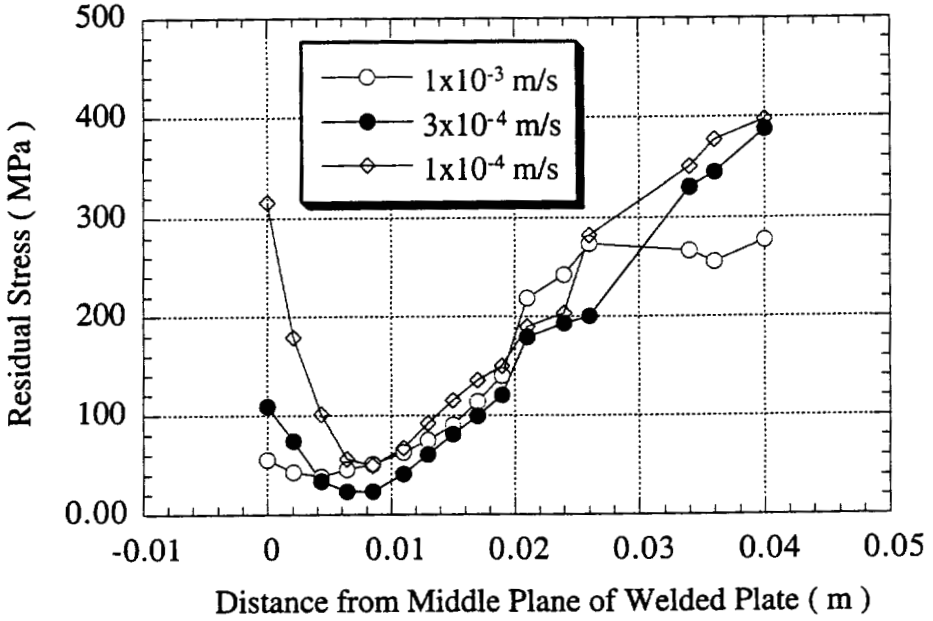

Figure 6-9 (c) Effect of Welding Speed on Longitudinal Residual Stress along Welded Plate Thickness
(Cross-Sectional Model, l=6.12m, t=0.08m)

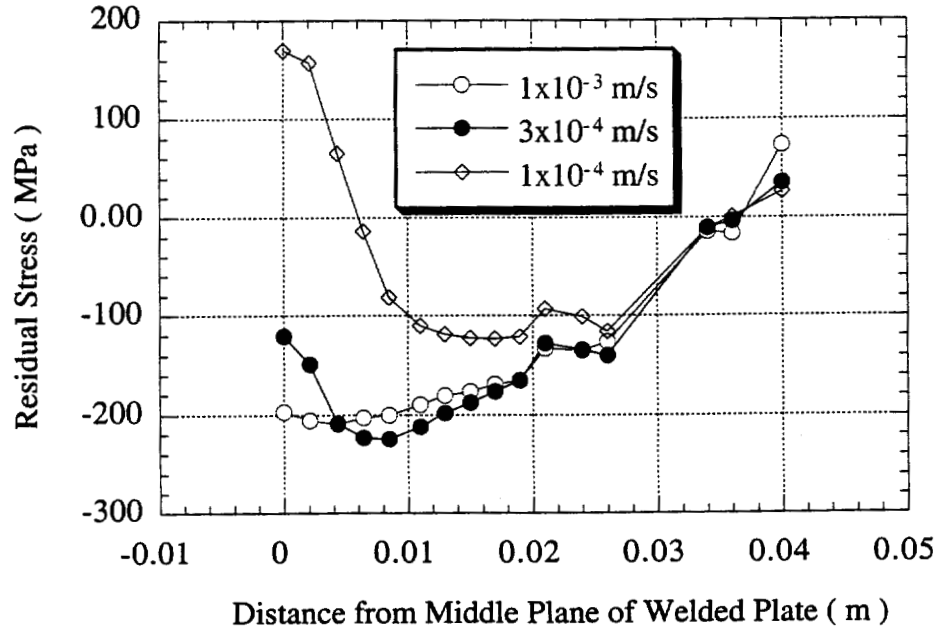

Figure 6-9 (d) Effect of Welding Speed on Transverse Residual Stress along Welded Plate Thickness
(Cross-Sectional Model, l=6.12m, t=0.08m)

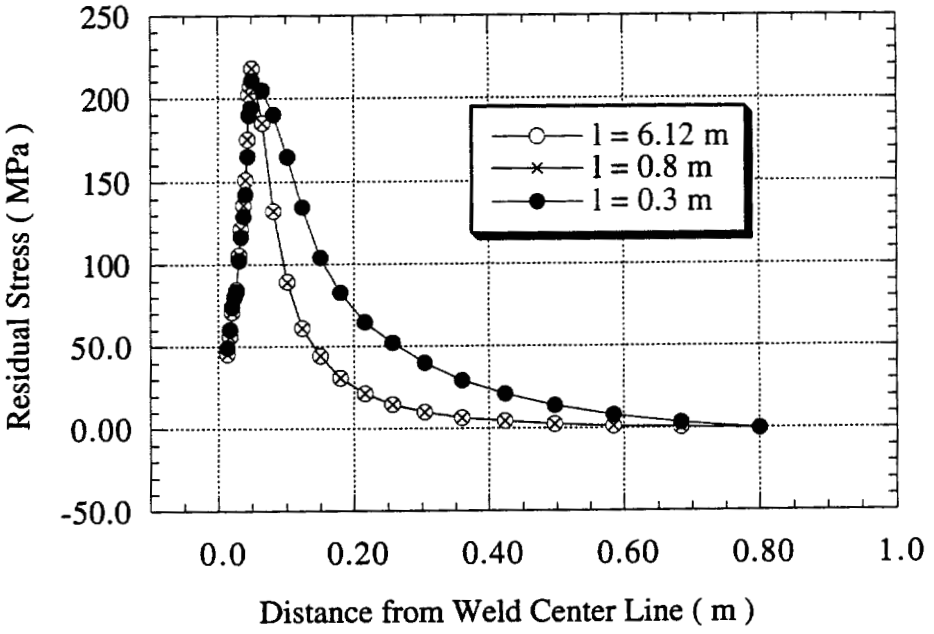

Figure 6-10 (a) Effect of Plate Length on Longitudinal Residual Stress along Middle Plane of Welded Plate
(Cross-Sectional Model, $v=3x10^{-4}$m/s, t=0.08m)

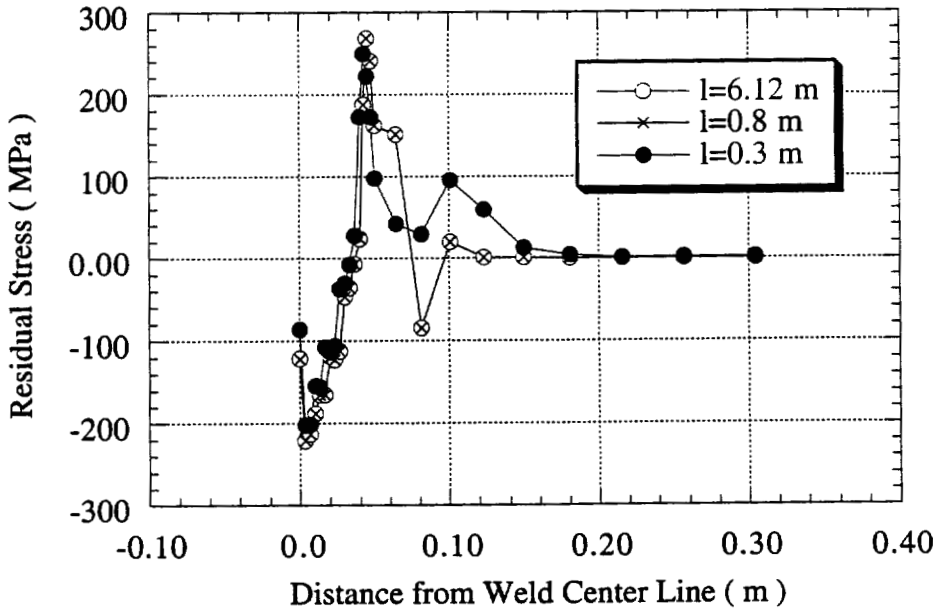

Figure 6-10 (b) Effect of Plate Length on Parallel Residual Stress along Middle Plane of Welded Plate
(Cross-Sectional Model, $v=3x10^{-4}$ m/s, t=0.08 m)

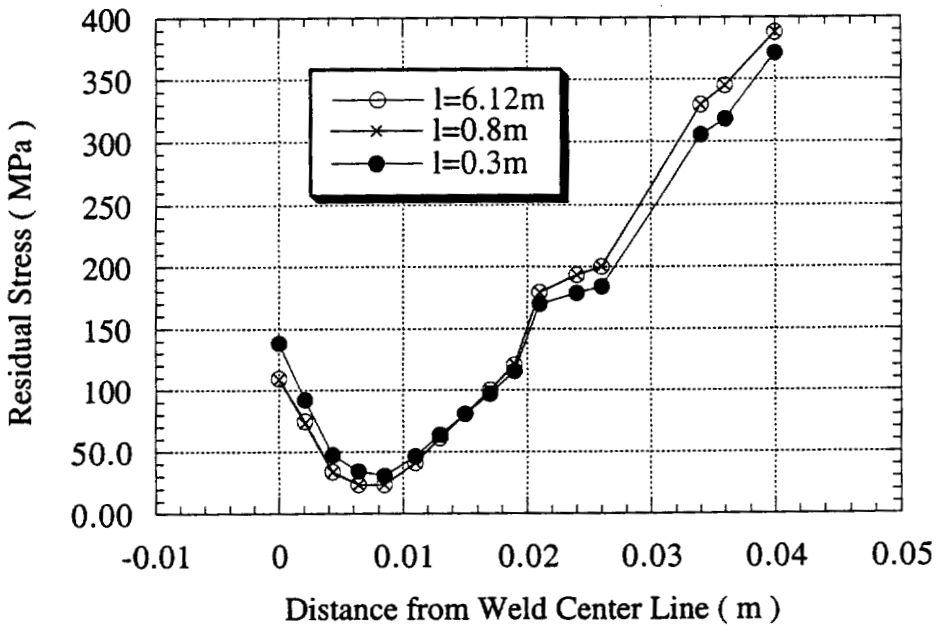

Figure 6-10 (c) Effect of Plate Length on Longitudinal Stress along Through Thickness Direction of Welded Plate
(Cross-Sectional Model, V=3x10^{-4} m/s, t=0.08 m)

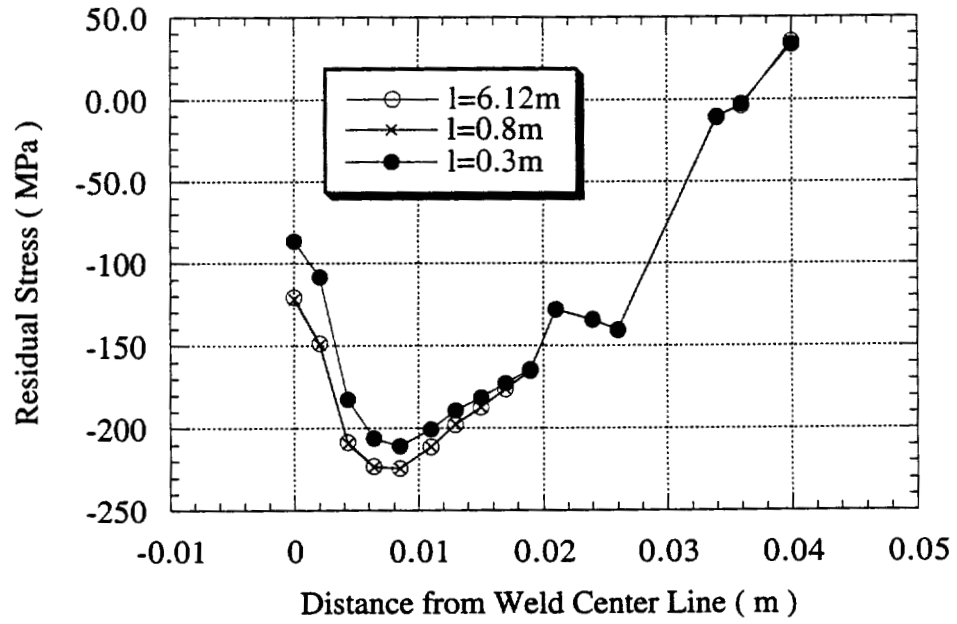

Figure 6-10 (d) Effect of Plate Length on Transverse Residual Stress along Through Thickness Direction of Welded Plate
(Cross-Sectional Model, V=3x10^{-4} m/s, t=0.08m)

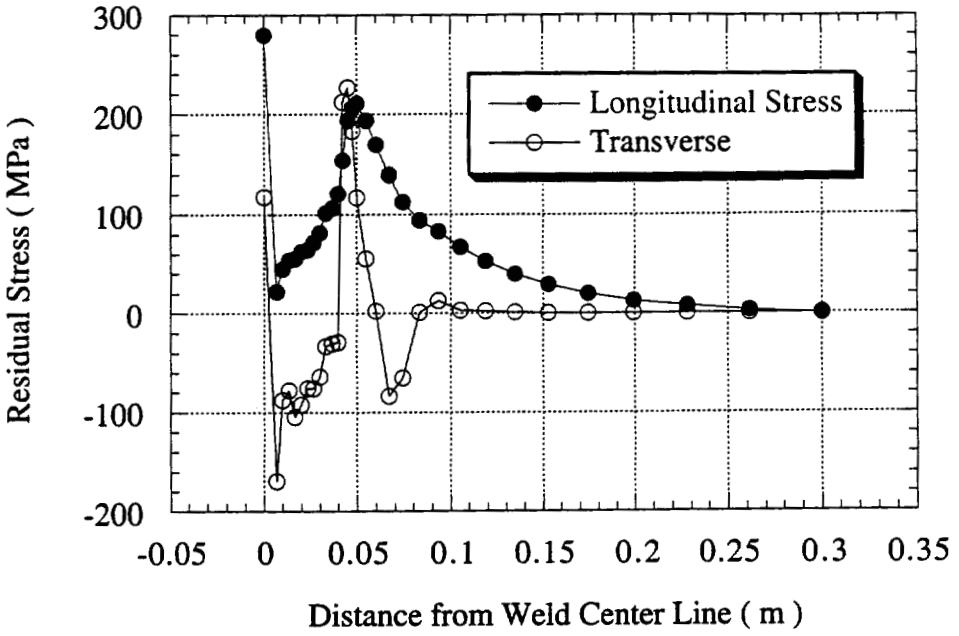

Figure 6-11 (a) Longitudinal and Transverse Stress along Middle Plane of Welded Plate

(Cross-Sectional Model, V=3x10^{-4} m/s, l=0.3 m, t=0.06 m)

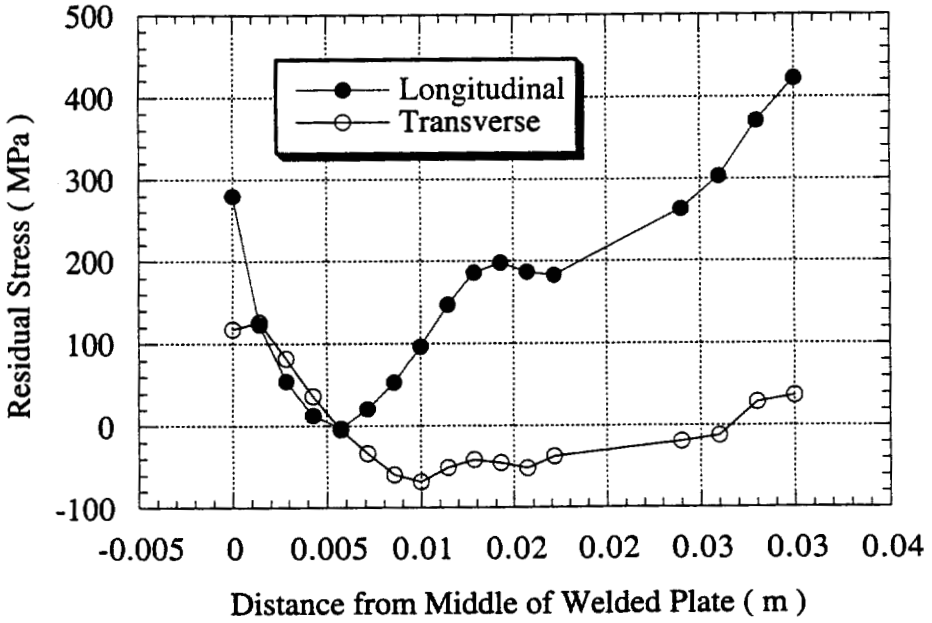

Figure 6-11 (b) Longitudinal and Transverse Residual Stress along Through Thickness Direction of Welded Plate

(Cross-Sectional Model, V=3x10^{-4} m/s, l=0.3m, t=0.06m)

CHAPTER 7
THREE DIMENSIONAL NUMERICAL ANALYSIS OF RESIDUAL STRESS IN A WELDMENT DURING ELECTROSLAG WELDING PROCESS

7.1 INTRODUCTION

From the previous two chapters, it is known that the ES welding process is actually a 3D problem. The 2D analysis results just partially reveal the characteristics of the process with some effects being ignored. Mid-plane model does not consider the effect of copper shoes. Cross-sectional model does not simulate the whole ESW process. 3D numerical simulation is needed to correctly characterize the ES welding process. However, 3D model is geometrically complicated and very time consuming using the fixed coordinate system (FCS). In order to solve this problem, the moving coordinate system (MCS) is applied to obtain the results efficiently.

In this chapter, the thermal results for the FCS and the MCS for 3D models were analyzed with ANSYS commercial software. The results reveal that the two different coordinate system results are very comparable. At the same time, the calculation time for the FCS is more than one hundred times the time for the MCS. The calculation time is dramatically reduced with the MCS.

Unfortunately, ANSYS can only be used to run the MCS thermal problem analysis. ANSYS can not run mechanical analysis problems with the MCS. The SYSWELD FEA commercial software was used to overcome this problem.

Comparisons of the calculation results of the two software packages reveal that the MCS thermal history results of SYSWELD and ANSYS are comparable. In fact, not only could SYSWELD solve thermal and mechanical problems with the MCS, but also

SYSWELD was found to take less computational time than ANSYS.

With the efficient software SYSWELD, a total of five 3D models were analyzed. One 3D model with welding speed of $3x10^{-4}$ m/s, plate thickness of 0.08 m and plate length of 6.12 m was run for both thermal and mechanical problem in very short time compared with that in transient analysis. This model is named SYSWELD Model1A. The weld shape effect was studied in another 3D model which was run with weld pool shape coming from the measurement results in Chapter 3. This model is named as SYSWELD Model2. Note that there was also a slight thickness increase from Model1A to reflect the plate thickness of the bridge weldments. The effect of welding speed, plate thickness and materials properties were also analyzed with the same geometry and mesh as SYSWELD Model1. These were named as Model1B, Model1C and Model1D, respectively. In order to evaluate the effect of material properties on residual stress inside the ESW weldments, Model1D used temperature dependent material properties while other SYSWELD models used constant material properties. The parameters that were used in the 3D models are listed in Table 7-1.

7.2 BACKGROUND

Using MCS to solve heat transfer problem was started in 1941 by Rosental.[79,80] He was the first one to use the MCS to derive the analytic solution of heat transfer problem with moving point heat source. Radaj[157] reviewed the literature using the MCS to get analytic solutions in 1992. Radaj states that, when a thermal process involves movement of a heat source at a constant velocity, the problem may be transferred from a dynamic problem to an equivalent static problem. The time derivatives can be replaced by an equivalent spatial derivative.

However, because of its direct relationship to reality and the limitation of commercial codes, most finite element analysis is based on the FCS. FCS requires very dense mesh around heat source along the whole moving direction. Compared with the FCS, the MCS requires less data storage capacity because very dense mesh is only needed at one position where heat source is positioned. At the same time, with less nodes,

elements and static state calculation condition (instead of transient analysis calculation condition for the FCS), the calculation time of MCS is dramatically reduced. In addition, MCS is more accurate, compared with the FCS, in simulating the activity of heat source movement because it simulates the heat source moving continuously which is the true case in practice. The FCS simulates the process with many time steps. During each time step, the problem is calculated in static state. In order to be close to the real continuous moving process, fine time steps are required. The computational procedure for FCS is very time consuming because of this.

Bergheau and Leblond[158] reported incorporating moving coordinate for analyzing heat transfer, stress and strain into the computer code SYSWELD used by the French company FRAMASOFT/CSI. The first result they reported is the application of laser surface treatment. The "moving reference frame medium" enables one to connect nodes and elements in order to account for a rate.[162] So, the metallurgical and mechanical equations are not solved in the FCS but in a MCS. Figure 7-1 illustrates the procedure which is based on the definition of element trajectories and on integration point trajectories. The trajectories are parallel to the heat source moving direction. In this way, the thermal and mechanical history undergone by each point of the structure can be determined and accounted for.[159] The non-linear thermal equations are solved by changing the time derivative to spatial derivative. With the thermal results, the mechanical equations are solved with help of the procedure which defines each integration point sequence. The initial values are ones of the previous integration point if the moving direction of the material is considered.

Gu, Goldak and Hughes[160] reported the results of thermal analysis in MCS with finite element methods. With the assumptions that the material properties were independent of temperature and position of the structure, i.e., uniform material properties, the following equation can be applied to heat transfer analysis.

$$T = T_0 + \phi e^{\left(-\frac{vx}{2\alpha}\right)} \qquad (7\text{-}1)$$

where,

T	=	Temperature.
T_0	=	Initial temperature.
ϕ	=	Variable.
v	=	Moving speed of heat source.
x	=	Dimension value along x coordinate system.
α	=	Thermal diffusivity.

The equation involved symmetric matrices and could be solved in a conventional computer code. The authors compared the results with one from conventional transient analysis and one from static state analysis under the MCS. The results are very consistent. With the MCS, the calculation efficiency increased dramatically with acceptable accuracy.

As for the ES welding process, 2D numerical analysis has been applied on both thermal and stress analysis with ANSYS. In this chapter, in order to compare the results of the FCS and the MCS, one 3D transient thermal analysis and one 3D static thermal analysis under MCS have been conducted with ANSYS commercial software. In order to get clearer information about residual stress in weldments, five 3D static state thermal analyses and mechanical analyses were performed under MCS with SYSWELD computer code.

7.3 MODELS

ASSUMPTIONS

The ESW process is simplified with the following assumptions in this MCS analysis:

1) The melting point of the metal is used as the boundary conditions at the contact layers between molten metal/base metal, molten metal/plate, molten slag/plate.
2) The heat generated by the deformed solid is negligible.

3) All of the thermal coefficients that have been used in this study remains constant through the welding process simulation.

4) The material is isotropic and homogeneous.

5) Welding process analyzed was in steady state, i.e., a representation of being in the middle of a long weld where heat input, travel speeds, etc. are constant.

6) The heat source is assumed at a zero-volume area.

7) There is no Joule (I^2 R) heating.

8) The non-linear thermoelastic-viscoplastic model is reduced to a linear thermoelastic model. A linear elastic-plastic stress-strain relation was assumed. The elastic and plastic regions were defined by elastic modules and plastic modules with yield stress separating them.

9) Ignore potential defect or crack formation.

10) Ignore creep and hardening, as well as introduce simplification in yield laws. Von-Mises yield criterion and associated flow rule with kinematic hardening were assumed to consider the Bauschinger effect.

11) The phase transformation expansion effect was considered to be similar during heating as well as during cooling because of the lack of available thermal expansion coefficient values. Plastic strain due to the change in volume during allotropic phase transformation is neglected in this study.

12) The same material properties were used for base metal, weld metal and HAZ.

GOVERNING EQUATION

The fundamental principle for heat flow analysis in FCS is as following:

$$\frac{\partial}{\partial x}(K_x\frac{\partial T}{\partial x})+\frac{\partial}{\partial y}(K_y\frac{\partial T}{\partial y})+\frac{\partial}{\partial z}(K_z\frac{\partial T}{\partial z})+Q=\rho C\frac{\partial T}{\partial t} \tag{7-2}$$

With MCS, the time derivative can be replaced by the spatial derivative:

$$\frac{\partial T}{\partial t}=-v\frac{\partial T}{\partial x} \tag{7-3}$$

With Equation 7-3, Equation 7-2 can be rewritten as following equation:

$$\frac{\partial}{\partial x}(K_x\frac{\partial T}{\partial x})+\frac{\partial}{\partial y}(K_y\frac{\partial T}{\partial y})+\frac{\partial}{\partial z}(K_z\frac{\partial T}{\partial z})+Q+\rho Cv\frac{\partial T}{\partial x}=0 \qquad (7\text{-}4)$$

where,

Q	=	Internal heat generation rate per unit volume (w/m^3).
K_x, K_y, K_z	=	Thermal conductivities along x, y and z principal axes, respectively (w/m^oC).
ρ	=	Density of Material (kg/m^3).
C	=	Mass specific heat (J/kg^oC).
T	=	Temperature (^oC).
v	=	Heat Source moving velocity (m/s).
x	=	Dimensional value along x coordinate system (m).

GEOMETRY DEFINITION AND SPATIAL DISCRETIZATION

The fixed and moving coordinate models had basically the same geometry just different mesh density. The geometry of the models is illustrated in Figures 7-2 (a) and 7-2 (b). The geometry for ANSYS models have curved boundary fusion zone which is shown in Figure 7-2. As for the ANSYS fixed coordinate model, the heat source moved from plate bottom to the top until the fusion zone moved out of the welded plate, which is the same as in 2D model. As for the ANSYS moving coordinate model, the heat source is positioned at a plane about 0.04 m from the top of welded plate to the heat source.

As for the mesh, weld metal and HAZ regions were discretized with smaller elements than regions far away from the heat source. Both the height of the weldment and the effect of the copper shoe were included in the 3D models. The effect of the copper shoes was simulated with a high heat transfer coefficient. Among the 3D models, one was run with ANSYS commercial software in transient analysis FCS. In this model, the shape of the heat source remained the same for every increment of time. The mesh

of this model is shown in Figure 7-3 (a) and the geometry of the model is shown in Figure 7-2 (a). A nonuniform mesh with 5568 elements and 8901 nodes was generated over the domain for the 3D model for transient analysis with ANSYS.

In order to compare the results of the MCS and the FCS, another model was run with ANSYS commercial software using the static analysis MCS. The mesh of this model is shown in Figure 7-3 (b). A second model with a nonuniform mesh of 3476 elements and 5490 nodes was used for static analysis in the MCS with ANSYS. The geometry of the model is shown in Figure 7-2 (b). ANSYS only has the code capability to solve thermal problems using the MCS. It does not have the code to solve the mechanical problems with the MCS. The commercial code SYSWELD was also used in this study to overcome this problem. In order to study the effect of weld pool shape, two distinct 3D models were performed in SYSWELD computer code. The weld pool shape of SYSWELD Model2 comes from the experimental results. The difference of weld pool shape of these two models was explained in Figure 7-4. The reason for two kind of fusion zone models is that the straight fusion zone model is easily modified to analyze changes in welding parameters. At the same time, the calculation results from fusion zone model with straight boundary are almost the same as those from curved boundary fusion zone model. Point A, B, C and D for the straight line fusion zone model in the Figure 7-4 (a) were in same relative position as AC and BD were for the curved model in Figure 7-4 (b). The coordinates of the four points can be described as A(0, t, 0), B(0, 0, -0.02), C(0.02, t, 0), D(0.04, 0, -0.02) where t is the plate thickness. A nonuniform mesh with 8112 elements and 10650 nodes shown in Figure 7-3 (c) was used for SYSWELD model1. A nonuniform mesh with 7872 elements and 10345 nodes was used for SYSWELD Model2 as shown in Figure 7-3 (d). Only a part of the welded plate has been modeled, i.e., a quarter of the welded plate was used in 3D models in order to save calculation time. Planes $A_{11}A_{1n}A_{21}A_{2n}$ and $B_{2n}D_{21}C_{21}B_{21}$ (see in Figures 7-2 (a) and 7-2 (b)) are the symmetric planes in the models. In addition, the $C_{11}D_{11}D_{21}C_{21}$ plane (see in Figures 7-2 (a) and 7-2 (b)) is not the actual end of the welded plate. The heat flow behavior through the unmodeled part of the welded plate can be simplified by utilizing a heat convection boundary condition which is the same as that in 2D model (Chapter 5).

The only additional step needed is to calculate the convection coefficient from the conductivity and length of the welded plate, i.e., h=k/L was prescribed as the convection coefficient on the $C_{11}D_{11}D_{21}C_{21}$ plane, where L is the unmodeled plate length.

HEAT SOURCE

The heat source distribution can be modeled by utilizing the essential boundary condition ($T(x, y, z)=T_s(x, y, z)$). The melting temperature of the welded plate is represented by $T_s(x, y, z)$. That is to say, a temperature boundary versus a heat flux heat source model was used in this study which is also the same as in 2D model. For example, the nodes on both $A_{11}A_{21}B_{11}B_{21}$ plane and $B_{11}B_{12}B_{21}B_{22}$ plane where the heat source was positioned at a certain time step in Figure 7-2 (a) are prescribed melting temperature of the metal for transient analysis model. Just one heat source is present in the model for the static analysis model shown in Figure 7-2 (b). The nodes on both $A_{1m}A_{2m}B_{1m}B_{2m}$ plane and $B_{1m}B_{2m}B_{1m+1}B_{2m+1}$ plane where the heat source was positioned are set at the prescribed melting temperature of the metal.

INITIAL AND BOUNDARY CONDITIONS

The heat transfer field equation is solved under the given initial and boundary conditions. Essential boundary condition, natural boundary condition and adiabatic boundary condition were used during the thermal analysis. Only symmetry boundary condition was used for mechanical analysis.

Initial Condition for Thermal Analysis

Room temperature (T=298K) is prescribed to all points in the domain except the points at heat source boundary as the initial condition for the thermal calculation.

Boundary Condition for Thermal Analysis

The melting temperature of welded plate T=1773 K is prescribed at the heat source boundary. Therefore, a temperature boundary versus a heat flux heat source model was used in this study.

The heat transfer through the surrounding medium can be specified through the heat transfer coefficients.

$$K_n \frac{\partial T_s}{\partial n} + h_c (T_s - T_A) = 0 \tag{7-5}$$

where,

K_n = Thermal conductivity normal to the surface.

h_c = Film coefficient for convectional heat transfer at the boundary.

T_s = Surface temperature.

T_A = Ambient temperature.

The convection heat transfer boundary condition for the FCS analysis model (see in Figure 7-2 (a)) is prescribed by the $B_{12}B_{22}B_{1n}B_{2n}$ plane (when heat source is at the position on $A_{11}A_{21}B_{11}B_{21}$ surface and $B_{11}B_{12}B_{21}B_{22}$ plane), $B_{1n}B_{2n}D_{21}D_{11}$ plane, $D_{11}D_{21}C_{21}C_{11}$ plane, $B_{21}C_{21}C_{11}B_{11}$ plane and $B_{1n}D_{11}C_{11}B_{11}$ plane . The convection heat transfer boundary condition for MCS analysis model (see in Figure 7-2 (b)) is prescribed by the $B_{1m+1}B_{1n}B_{2m+1}B_{2n}$ plane, $B_{1n}B_{2n}D_{21}D_{11}$ plane, $D_{11}D_{21}C_{21}C_{11}$ plane, $B_{21}C_{21}C_{11}B_{11}$ plane, $B_{1n}D_{11}C_{11}B_{11}$ plane and $A_{11}B_{11}A_{1m}B_{1m}$ plane. It should be noted that the effect of copper shoe was included in the 3D transient analysis model. $A_{1n}B_{1n}B_{11}A_{11}$ plane and $B_{1n}FEB_{11}$ Plane is the position where copper shoe was pressed to the welded plate for the FCS analysis model. $A_{1m}B_{1m}B_{11}A_{11}$ plane and $B_{1n}FEB_{11}$ Plane is the position where copper shoe was pressed to the welded plate for the MCS analysis model. $B_{1n}FEB_{11}$ plane is the position where copper shoe contacts with base metal $A_{1n}B_{1n}B_{11}A_{11}$ and $A_{1m}B_{1m}B_{11}A_{11}$ plane is the position where copper shoe contacts with fusion zone (see in Figure 7-2 (b)). A higher thermal coefficient was used in copper shoe area to simulate the effect of copper shoe, as mentioned above. According to temperature field calculation results of literature

[150-152], a thermal coefficient value of 130 Jm/sK on $A_{1n}B_{1n}B_{11}A_{11}$ plane, $A_{1m}B_{1m}B_{11}A_{11}$ plane and $B_{1n}FEB_{11}$ Plane, were used in this study.

The symmetry surfaces in the ANSYS and SYSWELD program were prescribed by the adiabatic boundary condition. Plane $A_{11}A_{1n}A_{21}A_{2n}$ and Plane $B_{2n}D_{21}C_{21}B_{21}$ for FCS model are the symmetry planes with adiabatic boundary conditions prescribed (see in Figure 7-2 (a)). Plane $A_{11}A_{1m}A_{21}A_{2m}$ and Plane $B_{2n}D_{21}C_{21}B_{21}$ for MCS model are also symmetry planes with adiabatic boundary conditions prescribed (see in Figure 7-2 (b)).

Boundary Condition for Mechanical Analysis

Only symmetry boundary conditions were used during the residual stress analysis. The residual stress was modeled under self-restrain only with no external restrains applied in the analysis. To prevent rigid body motion during the finite element analysis, only two nodes on the domain edge were fully restrained. This suggests that the welded plate is not restrained but is pivoted around these restrained nodes and the restraint free condition is realized.

Planes $A_{1n}B_{1n}B_{11}A_{11}$ and $A_{1m}B_{1m}B_{11}A_{11}$ were constrained along x coordinate direction, plane $B_{2n}D_{21}C_{21}B_{1n}$ was constrained along y coordinate direction. (see in Figures 7-2 (a) and 7-2 (b) for direction and plane position)

MATERIAL PROPERTIES

The temperature dependent material thermal properties were the same as those that were used in 2D models in Chapter 5.

The temperature dependent elastic modules and thermal expansion coefficient were the same as those in 2D models in Chapter 6. Temperature independent material properties of yield stress of 250 MPa, poission's ratio of 0.3 and plastic modules of 19000 MPa were used in SYSWELD Model1A, Model1B, Model1C and Model2 for mechanical analysis. SYSWELD Model1D used the same temperature dependent material property as those in Chapter 6. The reason for using constant material property is that

constant material property requires less calculation time and occupying less memory and space during calculation. At the same time, the results from constant material property model has the same trend as that from temperature dependent material property model.

7.4 FINITE ELEMENT CODE

SYSWELD was used to simulate the ESW processes with 3D model. The SYSWELD program is a finite element program which has unique functions in comparison with other commercial finite element programs, especially in metallurgical analysis. It is constantly updated with new features, enhancements of existing features and error corrections.

The software has five distinct parts. Calculations are performed in three successive steps, with results from one step being the input data for the calculation of next step. The following functions are improved year by year and the powerful functions are unique compared with other finite element program.

1) Coupling the thermal and metallurgical calculation.
2) Calculation of grain size.
3) Calculation of hardness.
4) Microscopic modeling of transformation plasticity.
5) Analysis of stress relief by the introduction of viscoplasticity.
6) Moving coordinate analysis in thermal, metallurgical and mechanical analysis.
7) Simulation of welding with interactive magnetodynamic and thermo-metallurgical analysis.
8) Function of interactive magnetodynamic and thermo-metallurgical analysis for induction quenching.
9) Simulation of diffusion process.

In this study, the unique powerful function of MCS was used in thermal and mechanical analysis.

7.5 SOLUTION PROCEDURE

Both transient thermal analysis in the FCS and static thermal analysis in MCS were performed using ANSYS 5.3 commercial software. Solid 70 thermal solid element in ANSYS was chosen in thermal analysis[153]. Temperature dependent material properties were defined, followed by meshing of the domain. For MCS, mass transfer function on key point should be open. At the same time, moving velocity should be given. Preparation part of the ANSYS thermal analysis was finished by above procedures.

For the transient analysis solution part of ANSYS program, the solution procedures are the same as the one in 2D model thermal analysis. (see Chapter 5)

For the MCS solution part of ANSYS program, static analysis option was chosen first, followed by choosing a full Newton-Raphson solution procedure. The initial temperature was specified by the TUNIF command in the ANSYS program. Convection heat transfer was activated on all the sides except the symmetry plane as soon as welding was initiated which was done by selecting nodes at the heat source boundary and by prescribing the melting temperature of welded plate.

Both thermal and mechanical calculation were performed with SYSWELD commercial software. Classical quadratic element was used for both thermal and mechanical analysis. According to the model geometry in Figure 7-2 (b), nonuniform meshing of the domain was used. Material temperature dependent properties were given first. Then trajectory of heat source was specified with definition of the streamline with MEDIUM command. This is the preparation part of SYSWELD thermal analysis.

The analysis will be carried out without accounting for the dynamic behavior of the structure due to the use of the MCS in computational option. Velocities will not be computed. DIRECT solver, which is based on a complete Gauss triangulation, was used in this study. NON SYMMETRIC label is used because the CONVECTION computation option leads to non-symmetry matrix. Automatic algorithm incrementation was used with modified Newton method. INITIAL CONDITIONS command allows one to specify the initial distribution of temperature.

The preparation part of mechanical analysis with MCS in SYSWELD is normally

the same as that in thermal analysis. The thermal analysis results and material mechanical properties are the input data for the mechanical analysis. The elasto-plastic analysis was carried out by taking into account the hardening effects of the material using kinematic material hardening law. DIRECT solver, which is based on a complete Gauss triangulation and automatic incrementation algorithm, was used with modified Newton method.

7.6 RESULTS

TEMPERATURE PROFILE FOR ANSYS MODELS

The temperature profile for the fixed coordinate calculation system model and moving coordinate calculation system model during the welding process are shown in Figures 7-5 and 7-6, respectively. From Figure 7-5, it can be seen that the temperature profile around heat source is the same for the different time steps when heat source moves from plate bottom to plate top. It is consistent with the assumption of steady state heat transfer for each time step. Figure 7-6 illustrates the temperature profile for the moving coordinate calculation system. The results are very comparable with the fixed coordinate calculation system.

In order to compare the calculation results of the two calculation systems in detail, the temperature results for the nodes along the WCL and perpendicular to weld line for the two calculation systems are plotted in Figure 7-7. Figure 7-7 (a) compares the temperature results of nodes along WCL on middle plane as a function of distance from plate bottom for the FCS and MCS. Figure 7-7 (b) compared the temperature results of nodes perpendicular to WCL direction on the middle plane as a function of distance from WCL for the FCS and the MCS. It can be seen that the results are consistent. The slight difference between them may be caused by a combination of the mesh difference between the two models and the proven increased accuracy of the moving coordinate mesh over the same density in the fixed coordinated mesh in similar problem.

ANSYS VERSUS SYSWELD

One can not solve mechanical problems with MCS using ANSYS. In order to solve this type of problem, SYSWELD must be used. In order to verify that the results coming from the two program are consistent, temperature results comparison between the two programs was given in Figure 7-8. Figure 7-8 (a) illustrates the temperature as a function of distance from plate bottom along WCL on the middle plane for ANSYS and SYSWELD. Figure 7-8 (b) illustrates the temperature as a function of distance from WCL perpendicular to WCL direction on middle plane for ANSYS and SYSWELD program. The model bottom begins at -1.2 m along the y coordinate direction for the SYSWELD moving coordinate model resulting in an effective plate length of twice the actual plate length while the ANSYS fixed coordinate problem only models the actual plate length. The extra plate length was added to all SYSWELD models used for residual stress calculations because plate length in the MCS actually relates to weld cool down time and an increase in cool-down time, i.e., plate length, was needed to assure the weld reached ambient temperature prior to assessement of resultant post-weld residual stress. The results verify that the two programs give the same results. Figure 7-8 (b) illustrates the temperature as a function of distance from WCL perpendicular to WCL direction on the middle plane for the ANSYS and the SYSWELD program. The results also reveal that the two programs give the same results.

However, the calculation time for SYSWELD is much less than that for ANSYS. At least three quarters of the calculation time for ANSYS was saved in SYSWELD calculation. SYSWELD is more efficient and powerful than ANSYS from this point of view.

SYSWELD MODEL1A RESULTS

The calculation results for the SYSWELD Model1A are given in Figures 7-9 to 7-12. The temperature profile and Von Mises stress distribution profile with the heat source close to the top of the plate are shown in Figures 7-9 (a) and 7-9 (b), respectively.

The temperature profile in Figure 7-9 (a) reveals that the bottom part of the welded plate is at room temperature when the heat source moves near the top of the welded plate. The plate length is long enough in the models for mechanical analysis. Without the edge effect of the welded plate, the residual stress value should be the same along heat source moving direction when the welding process finished and weldment was cooled down. The residual stress values that were analyzed in this chapter are the residual stress results at the bottom part of the welded plate determined by mechanical analysis based on thermal analysis results. The Von Mises distribution profile in Figure 7-9 (b) reveals that the highest stress is concentrated around the heat source during ESW process.

The residual stress in the fusion zone is very complicated. The stress along x, y and z coordinate direction is named as longitudinal stress (stress in the longitudinal direction of the plate, i.e., perpendicular to welding direction), parallel stress (stress parallel to welding direction) and transverse stress (stress parallel to plate thickness direction), respectively. According to the experimental results of Chapter 4, the principal residual stress in ESW weldments were the longitudinal stress and the parallel stress. The most important stresses, from a structure integrity point of view, are the longitudinal stress and parallel stress. Figure 7-10 (a) illustrates the longitudinal stress as a function of distance from WCL on middle plane with SYSWELD Model1A. It reveals that the longitudinal stress is very low compared with the 2D model calculation results (Figure 6-7 (a)). The stress begins with low tensile stress of 30 MPa and drops to 20 MPa, then increases to 60 MPa around the boundary of fusion zone and HAZ and then drops to -60 MPa at the distance from WCL less than 0.1 m. After that the stress goes back to zero with increasing distance from WCL. Figure 7-10 (b) illustrates the parallel stress as a function of distance from WCL on middle plane with SYSWELD Model1A. The results reveal that the parallel stress begins with a tensile stress which is higher than the half yield stress, drops to low tensile stress which is around 60 MPa, then increases to the highest tensile stress of 150 MPa around the boundary of fusion zone and HAZ, then drops from highest tensile stress to low compressive stress of -50 MPa. After that the stress goes back to zero with increasing distance from WCL. The transverse stress, Figure 7-10 (c), is mostly concentrated in the fusion zone with almost zero stress in other

parts of the weldments. The complicated transverse stress oscillation in fusion zone is consistent with longitudinal stress and parallel stress which is also complicated in fusion zone.

The residual stress at the plate surface is shown in Figures 7-11 (a), 7-11 (b) and 7-11 (c). Figure 7-11 (a) illustrates the longitudinal stress as a function of distance from WCL on plate surface with SYSWELD Model1A. The results reveal that the WCL longitudinal stress at the plate surface is compressive. The stress begins with the lowest compressive stress of -80 MPa, then increases to zero with increasing distance from WCL with the stress going up and down between the lowest compressive stress and zero stress. The parallel stress is shown in Figure 7-11 (b) as a function of distance from WCL on plate surface with SYSWELD Model1A. The results reveal that the stress begins with low tensile stress, drops a little bit and then increases to its highest tensile stress of 50 MPa around the HAZ. The stress then drops to a low compressive stress of -20 MPa and then increases to zero with increasing distance from WCL. The transverse stress, Figure 7-11 (c), is only complicated in the fusion zone with almost zero stress in other areas of the weldment.

The longitudinal and parallel stress is shown in Figure 7-12 (a) as a function of distance from WCL through plate thickness with SYSWELD Model1A . The results reveal that the longitudinal stress is more complicated than parallel stress. However, the general trends for them is that both longitudinal stress and parallel stress decrease with increasing distance from middle plane towards the surface. The transverse stress through thickness remains below half yield, but varies in a nonlinear fashion. The transverse stress as a function of distance from middle plane through plate thickness with SYSWELD Model1A was shown in Figure 7-12 (b).

SYSWELD MODEL2 RESULTS

The calculation results for SYSWELD Model2 were shown in Figures 7-13 to 7-16. The difference between Model1 and Model2 is listed in Table 7-1. The physical structure of the Model2 is coming from the experimental results of Chapter 3 with plate

thickness of 0.889 m comparing with 0.08 m in Model1. In Figure 7-13, the temperature profile and Von Mises stress distribution profile with the heat source near the top of the plate were shown in Figures 7-13 (a) and 7-13 (b), respectively. The temperature profile in Figure 7-13 (a) reveals that the bottom part of the welded plate is at room temperature when the heat source moves near the top of the welded plate. The plate length, which equals to cool-down times, is long enough in the model for mechanical analysis. The Von Mises distribution profile in Figure 7-13 (b) reveals that the highest stress is concentrated around the heat source during ESW process.

The longitudinal and parallel stress as a function of distance from WCL on middle plane with SYSWELD Model2 was shown in Figure 7-14 (a). The transverse stress as a function of distance from WCL on middle plane with SYSWELD Model2 was shown in Figure 7-14 (b). Longitudinal and parallel stress as a function of distance from WCL on plate surface with SYSWELD Model2 was shown in Figure 7-15 (a). The transverse stress as a function of distance from WCL on plate surface with SYSWELD Model2 was shown in Figure 7-15 (b). Longitudinal and parallel stress as a function of distance from middle plane through plate thickness with SYSWELD Model2 was shown in Figure 7-16 (a). The transverse stress as a function of distance from middle plane through plate thickness with SYSWELD Model2 was shown in Figure 7-16 (b). All of the stress distribution have the same trend as the results in SYSWELD Model1A. The difference between the two model results from the effect of fusion zone shape which is summarized in the following section.

EFFECT OF FUSION ZONE SHAPE

The effect of fusion zone shape on residual stress inside the ESW weldments is illustrated in Figures 7-17 to 7-20 by comparing the results of SYSWELD Model1A and SYSWELD Model2. It should be noticed that the plate thickness effect also play a role in this comparison. Temperature as a function of distance from plate bottom along WCL on middle plane for SYSWELD Model1A and Model2 was shown in Figure 7-17 (a). Temperature as a function of distance from WCL perpendicular to WCL direction on

middle plane for SYSWELD Model1A and Model2 was shown in Figure 7-17 (b). The results reveal that the two models have almost the same temperature profile.

Longitudinal stress, parallel stress and transverse stress as a function of distance from WCL on middle plane for SYSWELD Model1A and Model2 were shown in Figures 7-18 (a), 7-18 (b) and 7-18 (c), respectively. The results reveal that the difference is very insignificant.

Longitudinal stress, parallel stress and transverse stress as a function of distance from WCL on plate surface for SYSWELD Model1A and Model2 were shown in Figures 7-19 (a), 7-19 (b) and 7-19 (c), respectively. The results reveal that the stress distribution gradient for SYSWELD Model2 is less than that for SYSWELD Model1A. At the same time, the stress results difference between SYSWELD Model1A and SYSWELD Model2 at surface is greater than that on middle plane, with Model2 having lower surface compressive longitudinal stresses and higher surface parallel stresses.

Longitudinal stress, parallel stress and transverse stress as a function of distance from middle plane through plate thickness for SYSWELD Model1A and Model2 were shown in Figures 7-20 (a), 7-20 (b) and 7-20 (c), respectively. The results reveal that they have the same general trends for the two models except for the stresses near the plate surface. Generally the stress for SYSWELD Model2 first decreases and then increases with increasing distance from middle plane.

EFFECT OF WELDING SPEED

Welding speed effect on residual stress inside the ESW weldments was analyzed with SYSWELD Model1B with the welding speed of $3x10^{-4}$ m/s for Model1A and $1x10^{-4}$ m/s for Model1B. Note that the weld pool geometry remained constant for these two models which means a higher heat input at higher welding speed. Figures 7-21 to 7-25 give detailed comparative information between Model1A and Model1B on the effect of welding speed on ESW process. Temperature profile and Von Mises stress distribution for Model1B were shown in Figures 7-21 (a) and 7-21 (b), respectively. It can be seen that temperature profile with welding speed of $1x10^{-4}$ m/s is less than that for welding

speed of $3x10^{-4}$ m/s as shown in Figures 7-21 (a) and 7-9 (a), respectively. Model1B Von Mises stresses (Figure 7-21 (b)) have the same trends as SYSWELD Model1A (Figure 7-9 (b)) and Model2 (Figure 7-13 (b)) results, i.e., the highest stress area is seen around heat source during welding process. However, the extent of Model1B residual stress field is much less. Temperature as a function of distance from plate bottom along WCL on middle plane with different welding speed was shown in Figure 7-22 (a). Temperature as a function of distance from WCL perpendicular to WCL direction on middle plane with different welding speed was shown in Figure 7-22 (b). The results reveal that different welding speed leads to the change of temperature profile. The thermal gradient was steeper at the higher speed weld near the fusion zone while the slower speed weld plate cooled down faster.

Figures 7-23 (a), 7-23 (b) and 7-23 (c) show the longitudinal stress, the parallel stress and the transverse stress as a function of distance from WCL on middle plane with different welding speed, respectively. The results reveal that the highest stress is the one on the WCL with slow welding speed. The highest stress on middle plane is parallel to welding direction and with near yield stress range value. Longitudinal stress on middle plane changes from tension to compression and then to zero stress with increasing distance from WCL with faster welding speed. The slow welding speed has half yield stresses at WCL and then goes to low compressive stress. The higher welding speed starts a low tensile at WCL and goes to medium compressive stress. Parallel stress and transverse stress has the same trend as longitudinal stress when welding speed slows down. The highest parallel stress is on the WCL in the range of yield stress value. The highest transverse stress is on the WCL in the range of half yield stress value.

Figures 7-24 (a), 7-24 (b) and 7-24 (c) show the longitudinal stress, the parallel stress and the transverse stress as a function of distance from WCL on plate surface with different welding speed, respectively. The results reveal that the stress distribution difference with different welding speed on plate surface is not as significant as that on middle plane. However, the longitudinal stress on the WCL is much lower with welding speed of $3x10^{-4}$ m/s comparing with welding speed of $1x10^{-4}$ m/s.

Figures 7-25 (a), 7-25 (b) and 7-25 (c) show the longitudinal stress, the parallel

stress and the transverse stress as a function of distance from middle plane through plate thickness with different welding speed, respectively. The results reveal that the stress difference at plate surface is less than for the other parts of the weldment. The slow welding speed leads to the large stress gradient inside the weldments.

In general, the effect of welding speed on residual stress distribution is greater on middle plane of weldments than on plate surface during ESW process.

EFFECT OF PLATE THICKNESS

Plate thickness effect on residual stress inside the ESW weldments were analyzed with SYSWELD Model1C for a welding speed of $3x10^{-4}$ m/s. The plate thickness in Model1C was reduced to 0.6 m versus the 0.8 m of Model1A. Note that the heat input was also reduced in proportion to the plate thickness reduction as the width of the fusion zone was reduced from 0.8 m to 0.6 m. Figures 7-26 to 7-30 give detailed information of the effect of plate thickness on ESW process. Temperature profile and Von Mises stress distribution are shown in Figures 7-26 (a) and (b), respectively. The Von Mises stress has the same trend as SYSWELD Model1A and Model2 results with the highest stress area around heat source during welding process. In order to clearly understand the effect of plate thickness, Figures 7-27 to 7-30 give a detailed comparison of each result for two different plate thickness weldments. Temperature as a function of distance from plate bottom along WCL on middle plane with different plate thickness was shown in Figure 7-27 (a). Temperature as a function of distance from WCL perpendicular to WCL direction on middle plane with different plate thickness was shown in Figure 7-27 (b). The results reveal that the two models have almost the same temperature profile. It appears that the thinner plate cooled faster than thick plate as a function of distance down the length of the plate. This effect is probably due to the increased effect of the plate surface.

Figures 7-28 (a), 7-28 (b) and 7-28 (c) show the longitudinal stress, the parallel stress and the transverse stress as a function of distance from WCL on middle plane with

different plate thickness, respectively. The results reveal that the difference is very insignificant.

Figures 7-29 (a), 7-29 (b) and 7-29 (c) show the longitudinal stress, the parallel stress and the transverse stress as a function of distance from WCL on plate surface with different plate thickness, respectively. The stress difference at plate surface is greater than on middle plane. The longitudinal stress begins with much lower compressive stress on plate surface on WCL with thinner plate thickness.

Figures 7-30 (a), 7-30 (b) and 7-30 (c) show the longitudinal stress, the parallel stress and the transverse stress as a function of distance from middle plane through plate thickness with different plate thickness, respectively. The results reveal that they have generally the same trends for the plate thickness with stress difference growing at plate surface.

Overall, it can be said that the plate thickness effect on residual stress distribution is mainly on longitudinal stress on plate surface.

EFFECT OF MATERIAL PROPERTIES

Material properties effect on residual stress inside the ESW weldments were analyzed with the SYSWELD Model1D for a welding speed of $3x10^{4}$ m/s. Temperature dependent yield stress, Poisson's ratio and plastic modules were used in the SYSWELD Model1D versus constant material properties used in other SYSWELD models in this study. Figures 7-31 to 7-33 give detailed information about the effect of material properties on ESW process.

Figures 7-31 (a), 7-31 (b) and 7-31 (c) show the longitudinal stress, the parallel stress and the transverse stress as a function of distance from WCL on middle plane with different material properties, respectively. The results reveal that the stress distribution trend to have higher stress values when constant material properties are used compared with using temperature dependent material properties. The longitudinal stress on the WCL changes from tension stress to compression stress while the material property goes from constant to temperature dependent. The temperature dependent material property

model resulted in the lowest compressive stress around fusion line.

Figures 7-32 (a), 7-32 (b) and 7-32 (c) show the longitudinal stress, the parallel stress and the transverse stress as a function of distance from WCL on plate surface with different material properties, respectively. The results reveal that the different material property models show the same general stress distribution trends. The constant material properties lead to higher tension stress at the WCL for transverse stress, but lower tensile stress at WCL for longitudinal stress and parallel stress. The model with the constant material property shows higher or equal stress with increasing distance from WCL.

Figures 7-33 (a), 7-33 (b) and 7-33 (c) show the longitudinal stress, the parallel stress and the transverse stress as a function of distance from middle plane through plate thickness with different material properties, respectively. The results reveal that material properties affect the stress distribution through the plate thickness. The longitudinal stress is in compression stress range with lower stress value at the WCL and most of the way through the thickness. However, higher longitudinal stress can be seen near the plate surface with temperature dependent material property model. Both parallel stress and transverse stress reveal lower stress value at WCL when the temperature dependent material properties were used. Therefore, material properties effect on residual stress distribution is mainly on residual stress through plate thickness.

7.7 DISCUSSION

MODEL EFFICIENCY

Comparing the fixed coordinate calculation system with the moving coordinate calculation system, the latter one is much more efficient. The calculation time for thermal analysis with MCS is only about one hundredth of the time for the FCS. It is estimated that the mechanical analysis with the FCS model in ANSYS program may take up to 120 days while only a few hours are needed for the SYSWELD model with MCS having a denser denser grid than that for the FCS model in ANSYS. With MCS, many continuous processes in practice can be simulated in acceptable time.

Comparing SYSWELD program with ANSYS program, SYSWELD is more powerful than ANSYS in MCS. Three quarters of the calculation time is saved with SYSWELD analysis compared with ANSYS program.

STRESS DISTRIBUTION

SYSWELD Model1D simulates residual stress distribution close to the real situation. Figures 7-31 to 7-33 displays the stress distribution for various position.

Stress Distribution on Middle Plane

The Longitudinal stress on middle plane of the weldment is in compressive stress region with the highest compressive stress near the boundary of fusion zone and HAZ. The highest compressive stress is one third of the yield stress. The Parallel stress on middle plane of the weldment has both tension stress and compressive stress. The highest tension stress and highest compressive stress are located around the boundary of fusion zone and HAZ. The highest tension stress is almost half the yield stress range while the highest compressive stress is only about one fifth of the yield stress range. The transverse stress on middle plane of the weldment has both tension stress and compressive stress. The stress value is low with the highest value even lower than one fifth of the yield stress. The highest value is located around the boundary of fusion zone and HAZ.

The transverse stress on middle plane is generally low compared with the longitudinal stress and parallel stress. This point is consistent with the assumption that the residual stress is mainly perpendicular to and parallel to welding direction. Between longitudinal stress and parallel stress, the latter is higher and has higher stress variation at the boundary of fusion zone and HAZ dominated by the tension stress.

Stress Distribution on Plate Surface

The longitudinal stress on plate surface of the weldment is in compressive stress

state with the highest compressive stress in fusion zone. The stress value is about one fourth of the yield stress. The parallel stress on plate surface of the weldment has both tension stress and compressive stress with less than one fifth of the yield stress. The highest tension stress is on the WCL. The highest compressive stress is in HAZ. The transverse stress on plate surface of the weldment has the lowest stress value compared with longitudinal stress and parallel stress. Both tension stress and compressive stress have been found along transverse stress direction. The highest tension stress is at the WCL and the highest compressive stress is in fusion zone.

In general, the transverse stress has the lowest stress value on plate surface. The longitudinal stress is in compressive stress range with the highest value about one fourth of the yield stress. The parallel stress value is less than that of longitudinal stress with both tension stress and compressive stress.

Stress through Plate Thickness

The longitudinal stress through plate thickness of the weldment is in compressive stress range. The lowest stress can be found at the WCL. The highest stress is located between middle plane and plate surface with the stress value in the range of one third of the yield stress. The parallel stress through plate thickness is in tension stress range. The highest tension stress can be found at the WCL with the stress value about one fourth of the yield stress. The transverse stress through plate thickness has the same trend as the parallel stress through plate thickness with lower the stress value.

In general, the longitudinal stress through plate thickness reveal compressive stress with the highest value about one third of the yield stress. The parallel stress through plate thickness is in tension stress range with the highest value about one fourth of the yield stress. The transverse stress has the lowest stress value among the three kind of stresses.

With all of the above information, it can be seen that the longitudinal stress of the weldment is in compressive stress state with parallel stress having both tensile stress and compressive stress with the parallel stress being dominated by the tension stress. Such

results are consistent with the coring results of Chapter 4.

WELDING PARAMETER EFFECTS

Among welding speed, plate thickness and plate length, the welding speed has the most profound effect on stress distribution. The effect of welding speed on residual stress distribution is mainly on middle plane of weldment during ESW process. The general trend is that both longitudinal stress and parallel stress move to the tensile stress region with slower welding speed. The welding speed has less effect on the residual stress distribution on plate surface while plate thickness mainly affects the longitudinal stress on plate surface. However, plate thickness has less effect on residual stress distribution of ESW weldment compared with welding speed. Because plate thickness is associated with the effect of copper shoe, the effect of copper shoe becomes more important for thinner plate. It can then be inferred that the effect of copper shoe is mainly on the longitudinal stress.

Material properties during calculation mainly affect the stress value of longitudinal stress and parallel stress on middle plane and on plate surface. The residual stress through plate thickness is sensitive to the material properties. The effect of the material properties is mainly on the residual stress value, not on the stress distribution trends.

7.8 CONCLUSIONS

1) The ESW 3D model predicted compressive residual stresses in and around the fusion/HAZ zones in the direction perpendicular to the welding direction.
2) The ESW 3D model predicted low level tensile residual stresses in and around the fusion/HAZ zones in the direction parallel to the welding direction.
3) When the distance from WCL is bigger than 0.1 m, both longitudinal stress and parallel stress are compressive stress and goes to zero with increasing distance from WCL when welding speed is at $3x10^{-4}$m/s and plate thickness is 0.08m.
4) When the distance from WCL is bigger than 0.4m, the plate is in zero residual

stress state with welding speed of $3x10^{-4}$m/s and plate thickness of 0.08m.

5) The effect of welding speed on residual stress distribution is mainly on middle plane of ESW weldment and has less effect on stress distribution on plate surface. Both longitudinal stress and parallel stress move to tensile stress region with slower welding speed

6) Copper shoe is very important for ESW process. The effect of copper shoe on longitudinal stress distribution inside ESW weldments is greater than that on parallel stress.

7) The effect of plate thickness on residual stress distribution of the ESW weldments is mainly on residual stress distribution on plate surface.

8) The effect of material properties on residual stress distribution of the ESW weldments is mainly on the residual stress value not on the residual stress distribution

9) Moving coordinate system is more efficient for ESW process simulation comared with fixed coordinate system.

10) Residual stress distribution is not uniform.

Table 7-1 Parameters for Three Dimensional Numerical Analysis of ESW Process

	Plate Thickness (m)	Plate Height (m)	Plate Length (m)	Welding Speed (m/s)	Material Property
ANSYS Fixed Coordinate Model	0.08	1.56	6.12	3×10^{-4}	Variable
ANSYS Moving Coordinate Model	0.08	1.56	6.12	3×10^{-4}	Variable
SYSWELD Model1A	0.08	2.76	6.12	3×10^{-4}	Constant
SYSWELD Model1B (welding speed effect)	0.08	2.76	6.12	1×10^{-4}	Constant
SYSWELD Model1C (plate thickness effect)	0.06	2.76	6.12	3×10^{-4}	Constant
SYSWELD Model1D (material property effect)	0.08	2.76	6.12	3×10^{-4}	Variable
SYSWELD Model2	0.0889	2.76	6.12	3×10^{-4}	Constant

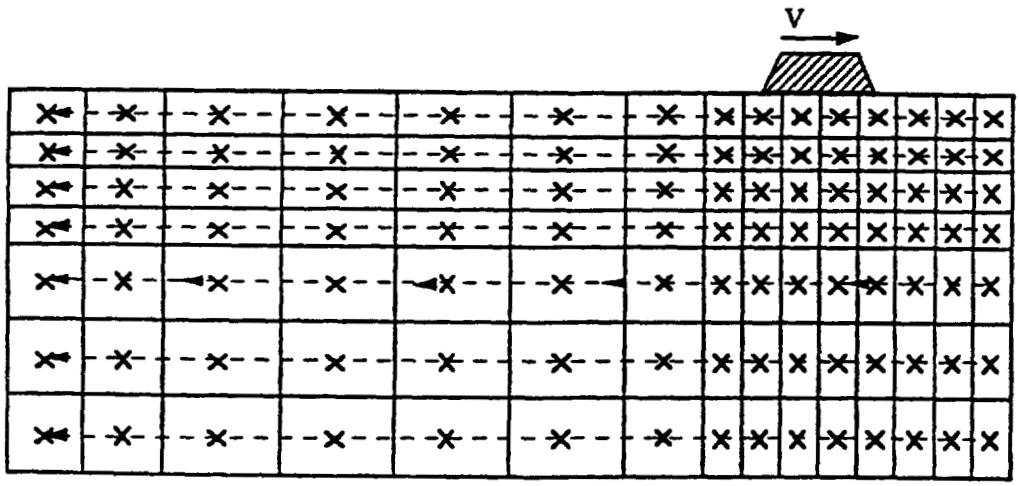

Figure 7-1 Schematic Illustration the Trajectory Notion in the Case of a Manufacturing Process

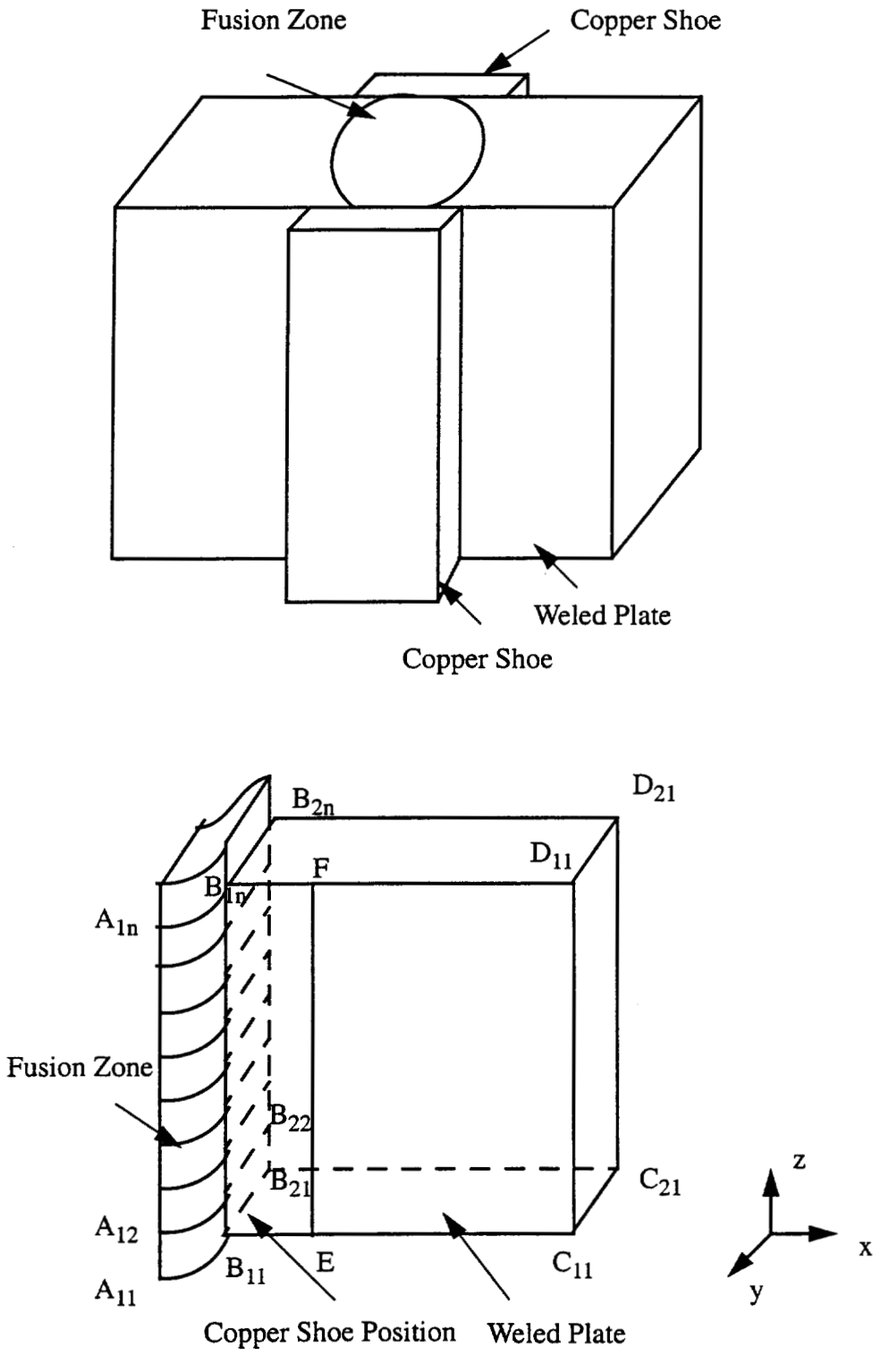

Figure 7-2 (a) Illustration of the Geometry of Fixed Coordinate System Three Dimensional Model

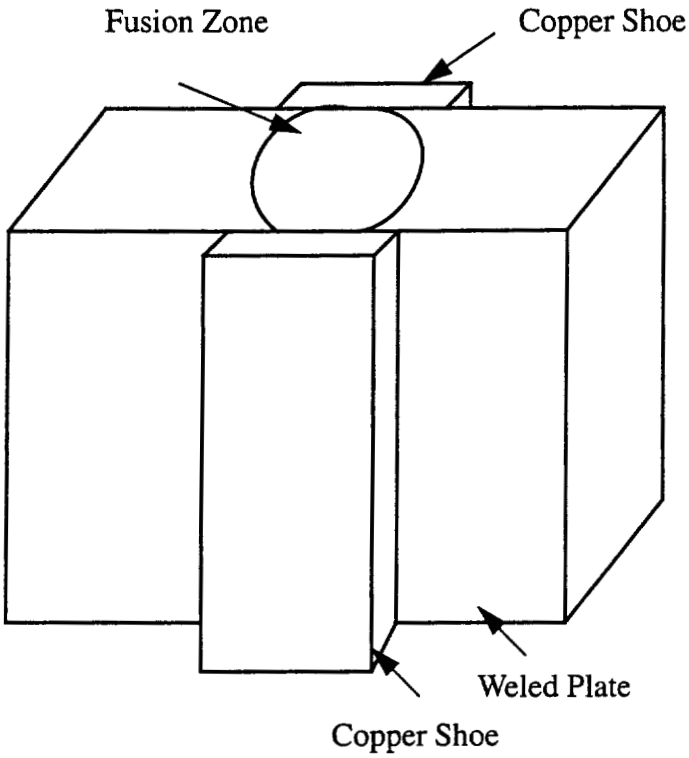

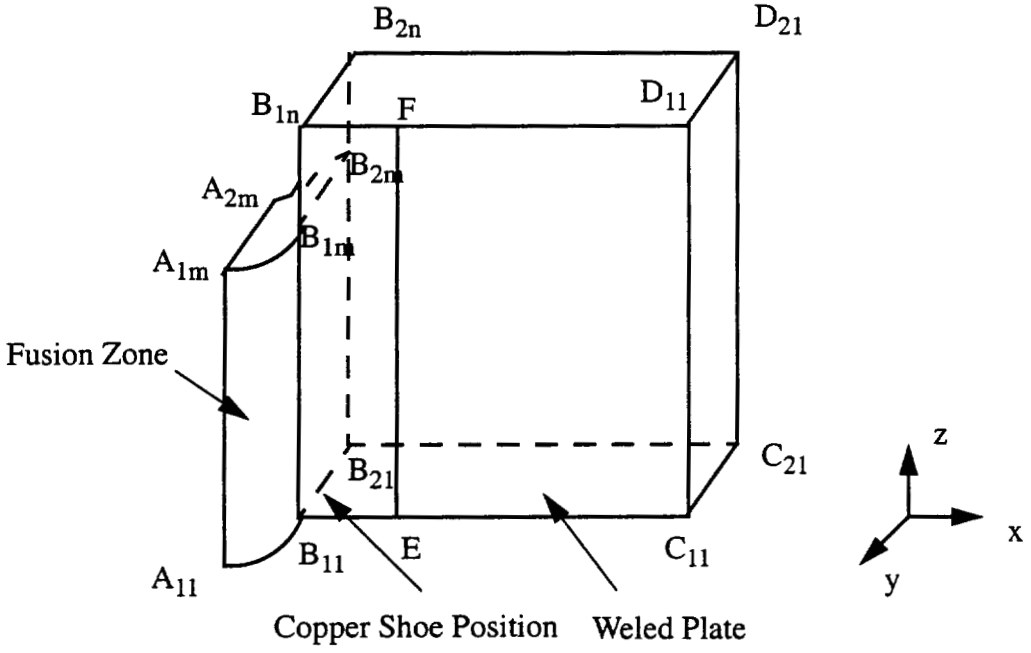

Figure 7-2 (b) Illustration of the Geometry of Moving Coordinate System Three Dimensional Model

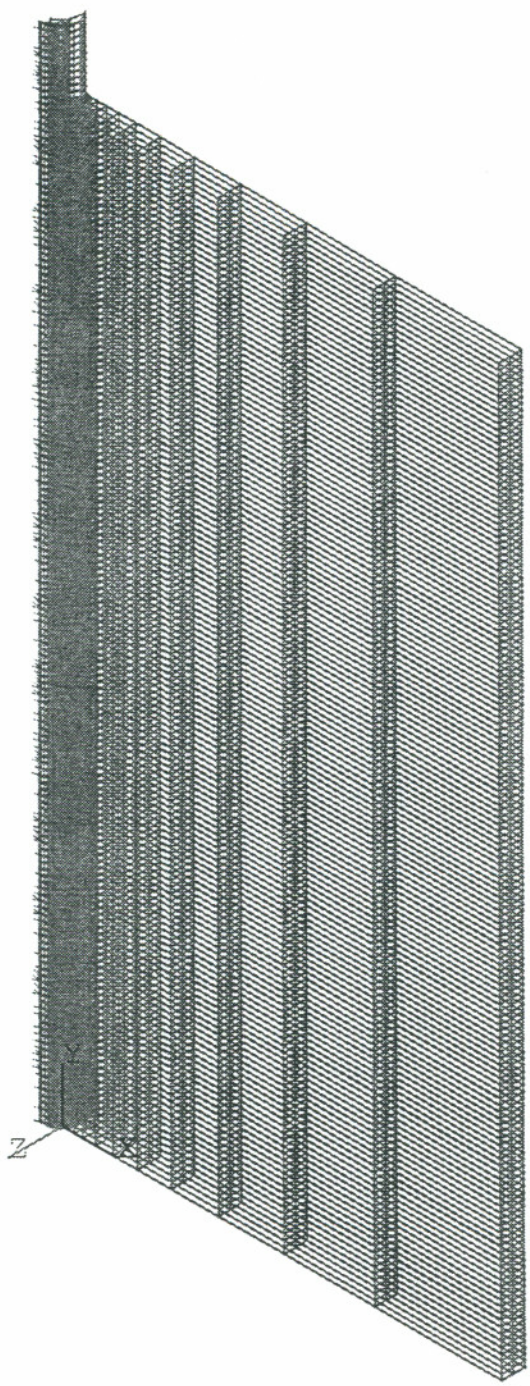

Figure 7-3 (a) Mesh of ANSYS Fixed Coordinate Three Dimensional Thermal Calculation Model

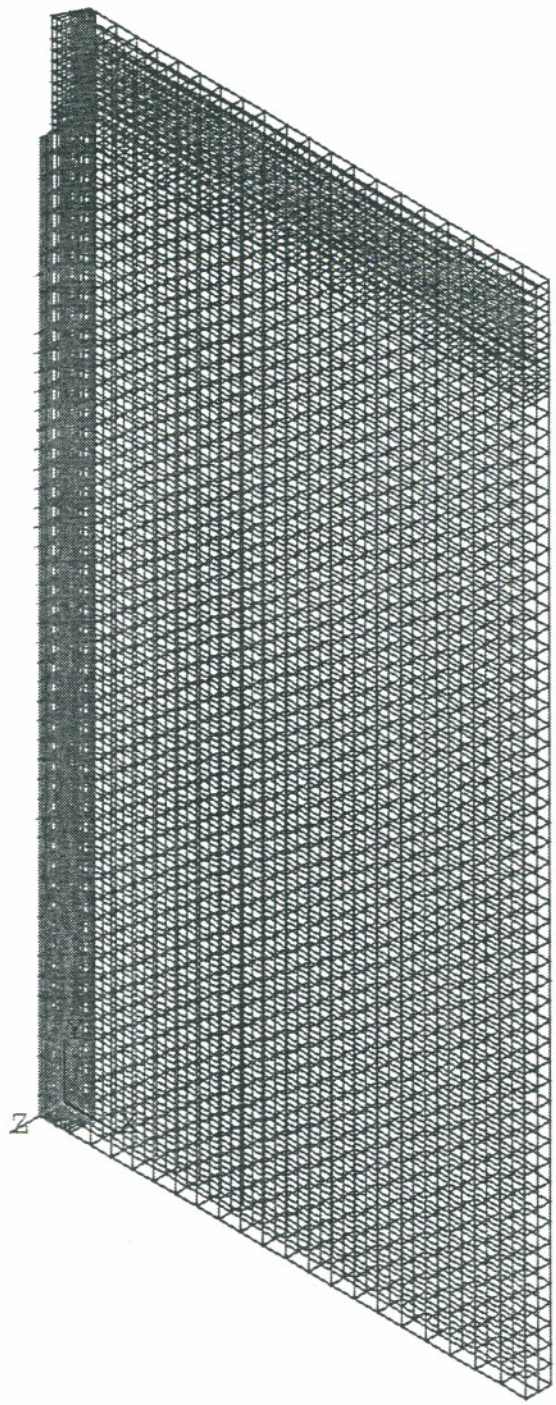

Figure 7-3 (b) Mesh of ANSYS Moving Coordinate Three Dimensional Thermal Calculation Model

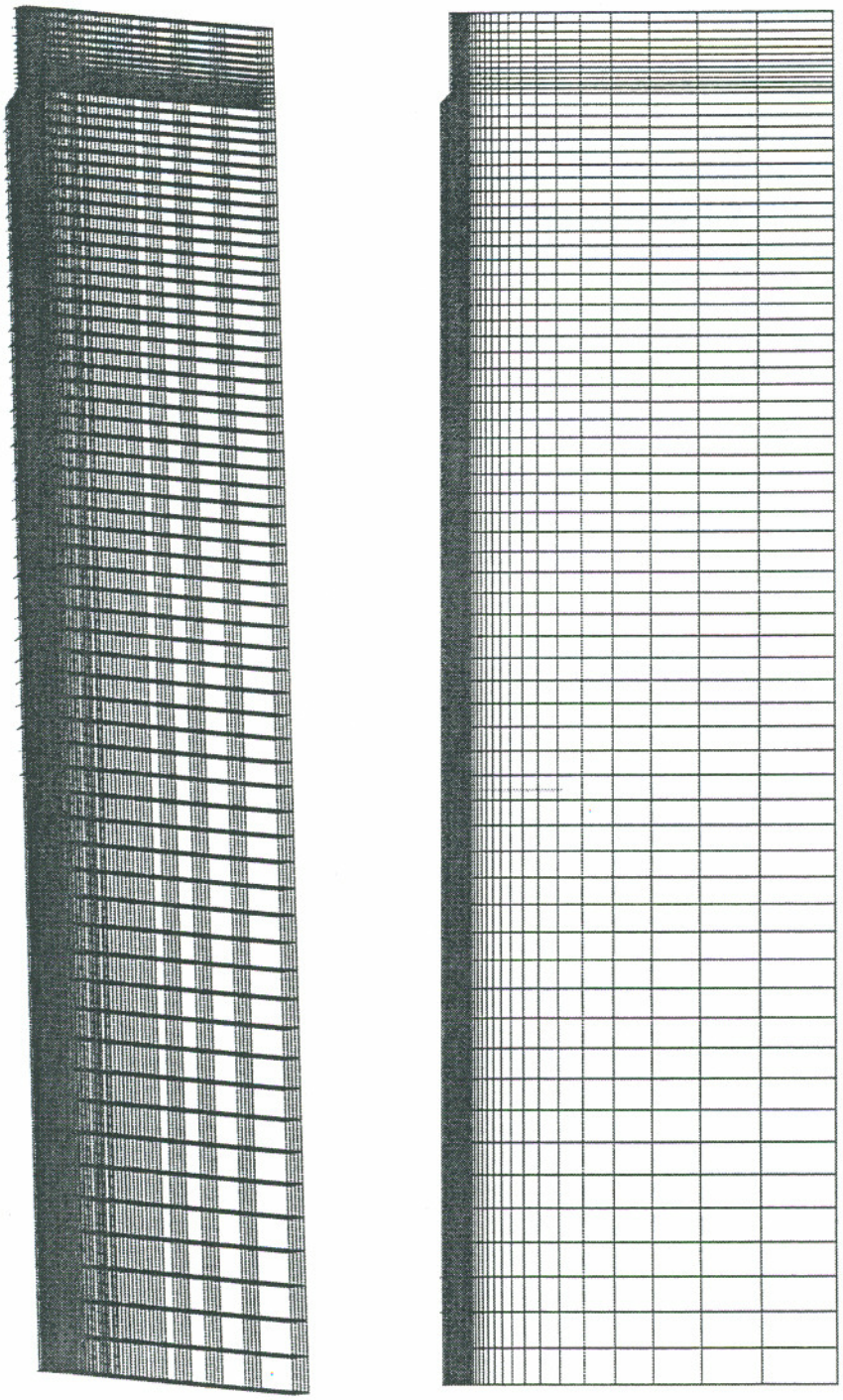

Figure 7-3 (c) Mesh of SYSWELD Model1

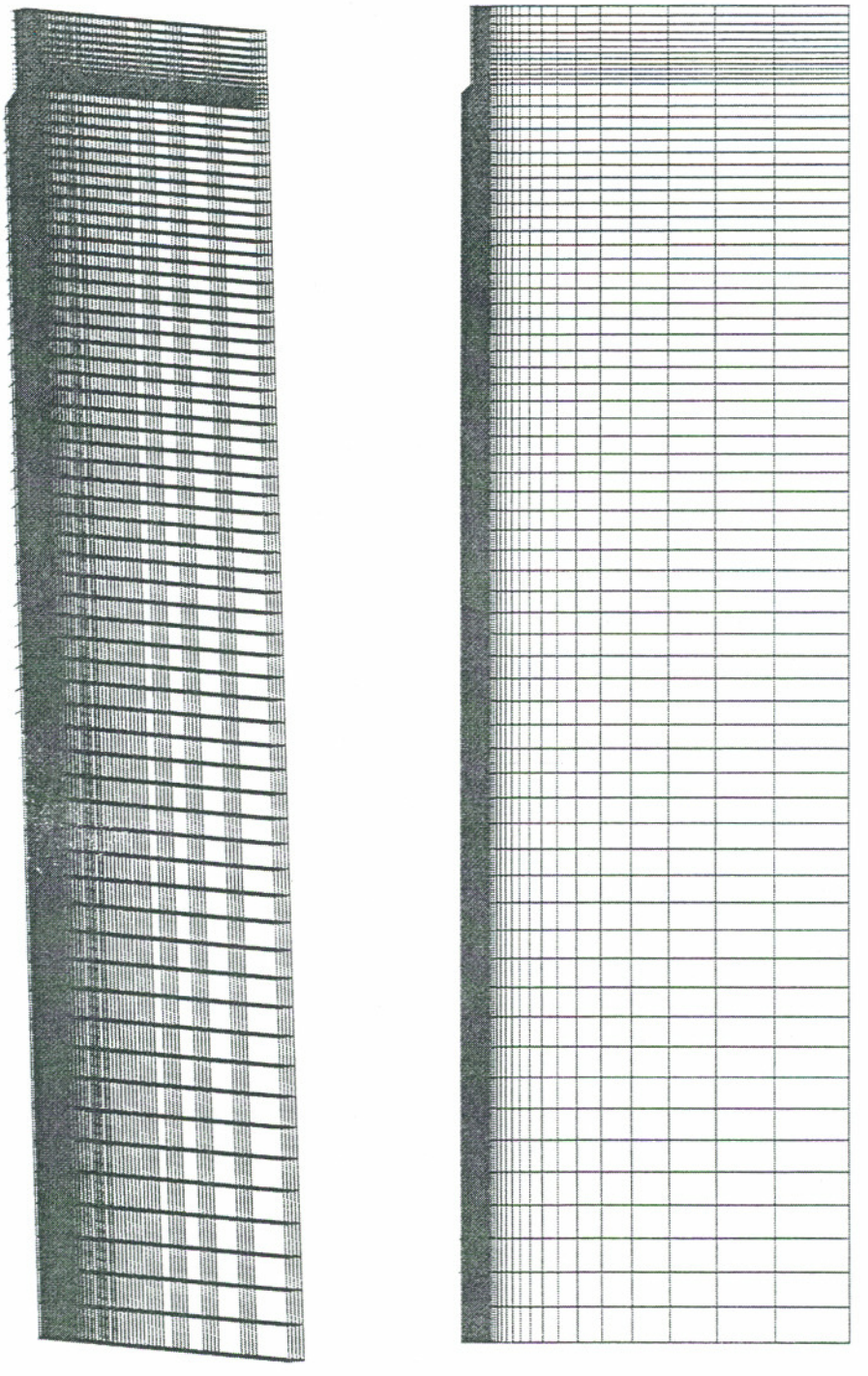

Figure 7-3 (d) Mesh of SYSWELD Model2

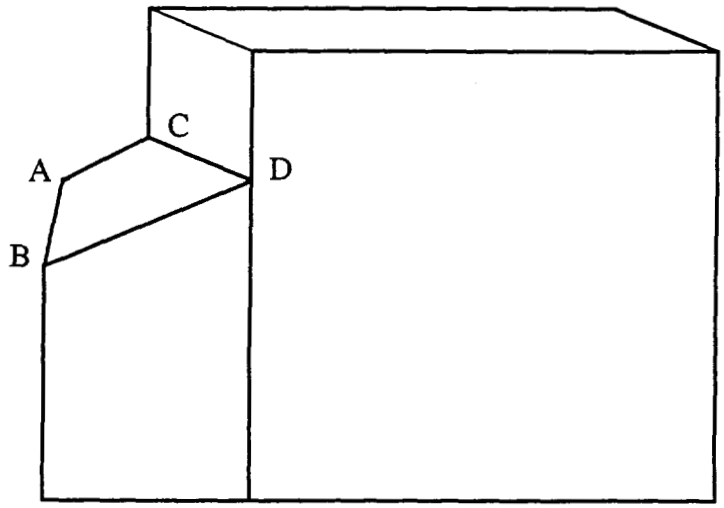

(a) Model1 in SYSWELD Three Dimensional Model

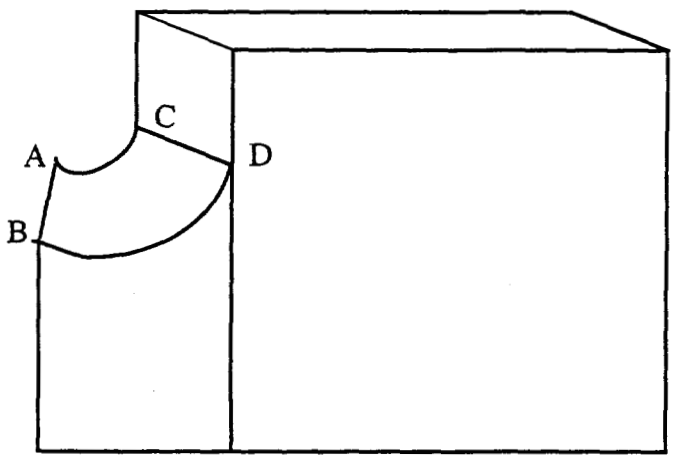

(b) Model2 in SYSWELD Three Dimensional Model

Figure 7-4 Illustration of Weld Pool Shape ABCD for (a) Model1 in SYSWELD (b) Model2 in SYSWELD

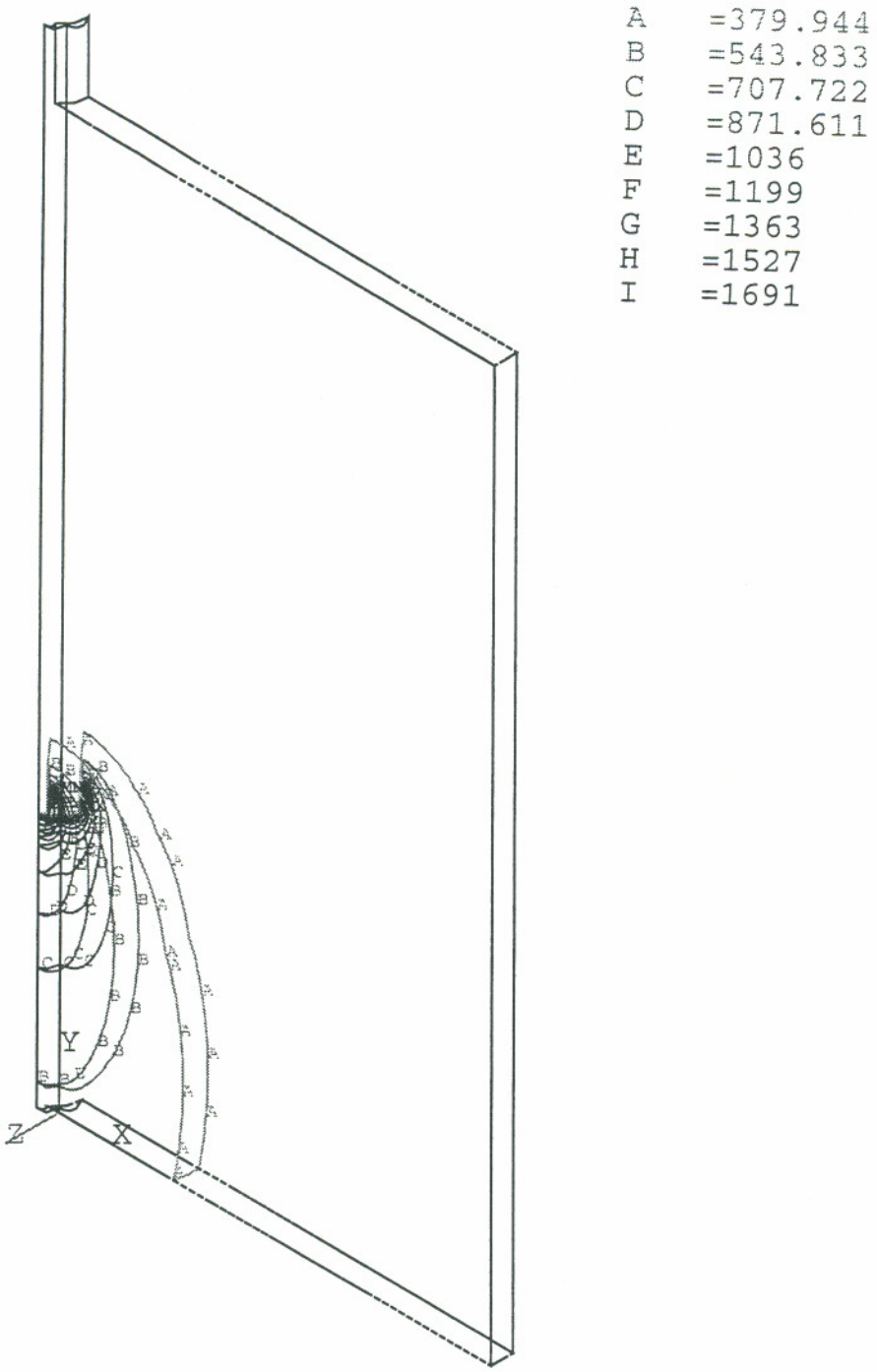

Figure 7-5 (a) Temperature Profile at Time=1600 Seconds for ANSYS Fixed Coordinate System Thermal Calculation

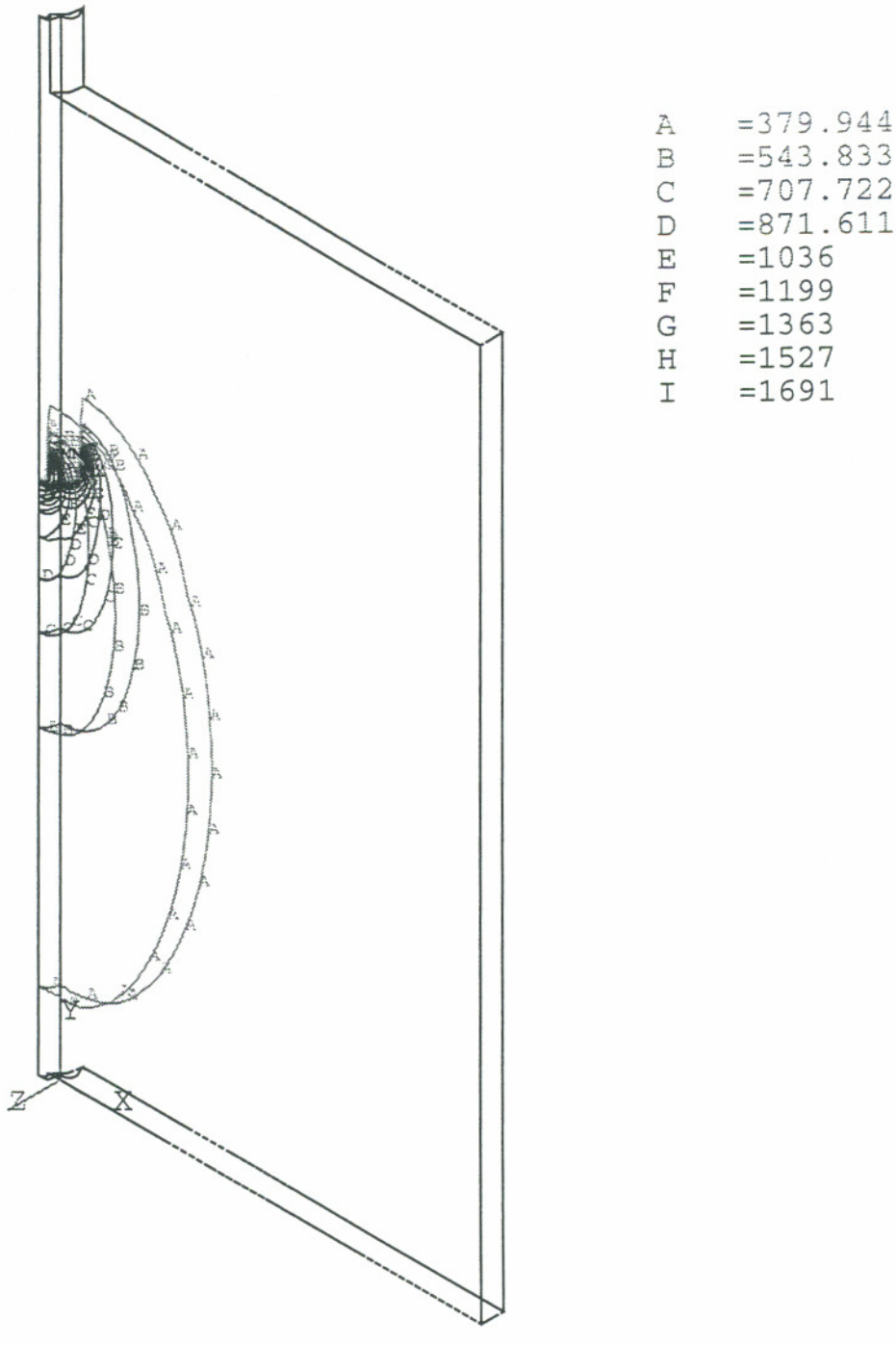

Figure 7-5 (b) Temperature Profile at Time=3200 Seconds for ANSYS Fixed Coordinate System Thermal Calculation

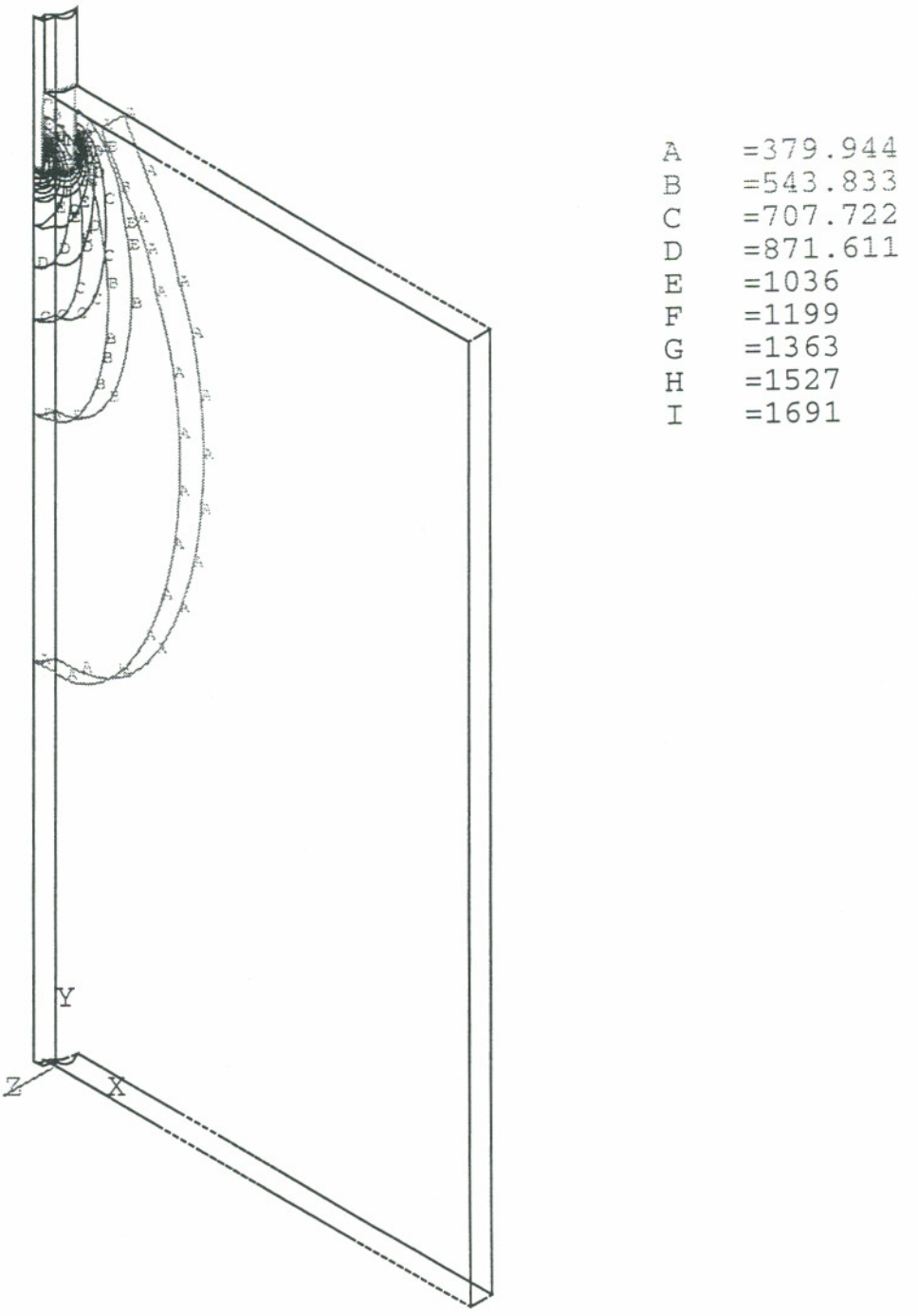

Figure 7-5 (c) Temperature Profile at Time=4800 Seconds for ANSYS Fixed Coordinate System Thermal Calculation

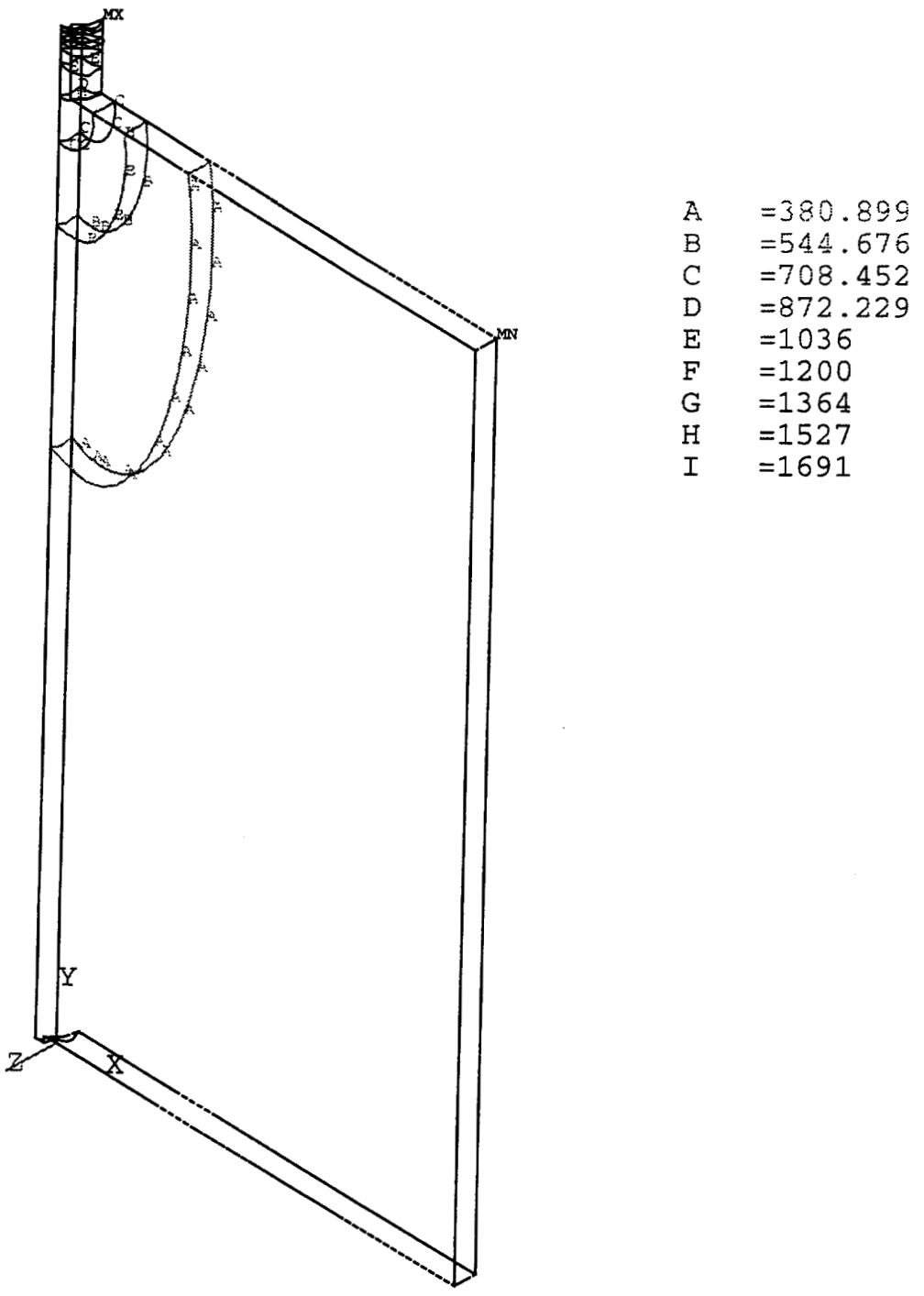

Figure 7-5 (d) Temperature Profile at Time=5600 Seconds for ANSYS Fixed Coordinate System Thermal Calculation

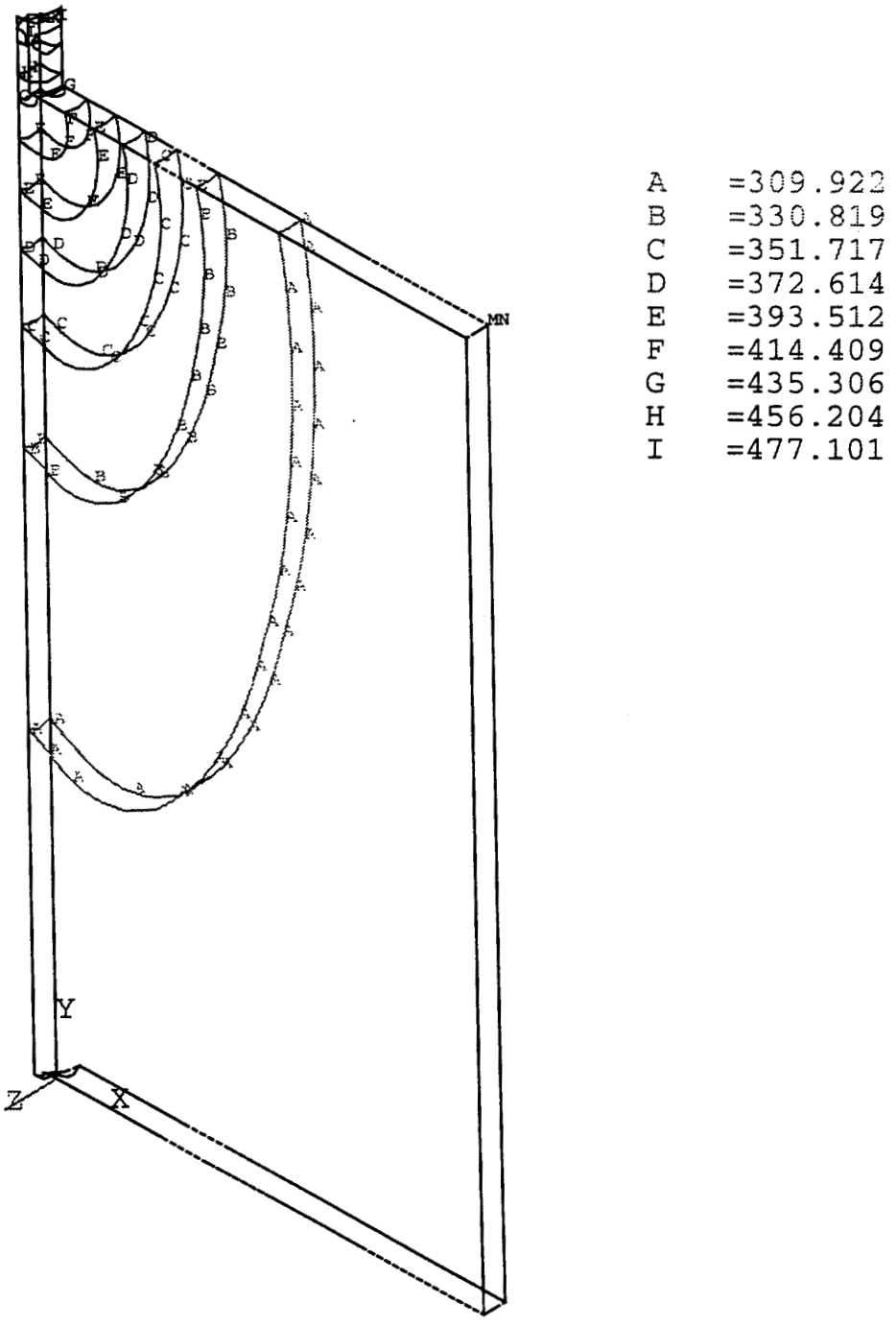

Figure 7-5 (e) Temperature Profile at Time=6300 Seconds for ANSYS Fixed Coordinate System Thermal Calculation

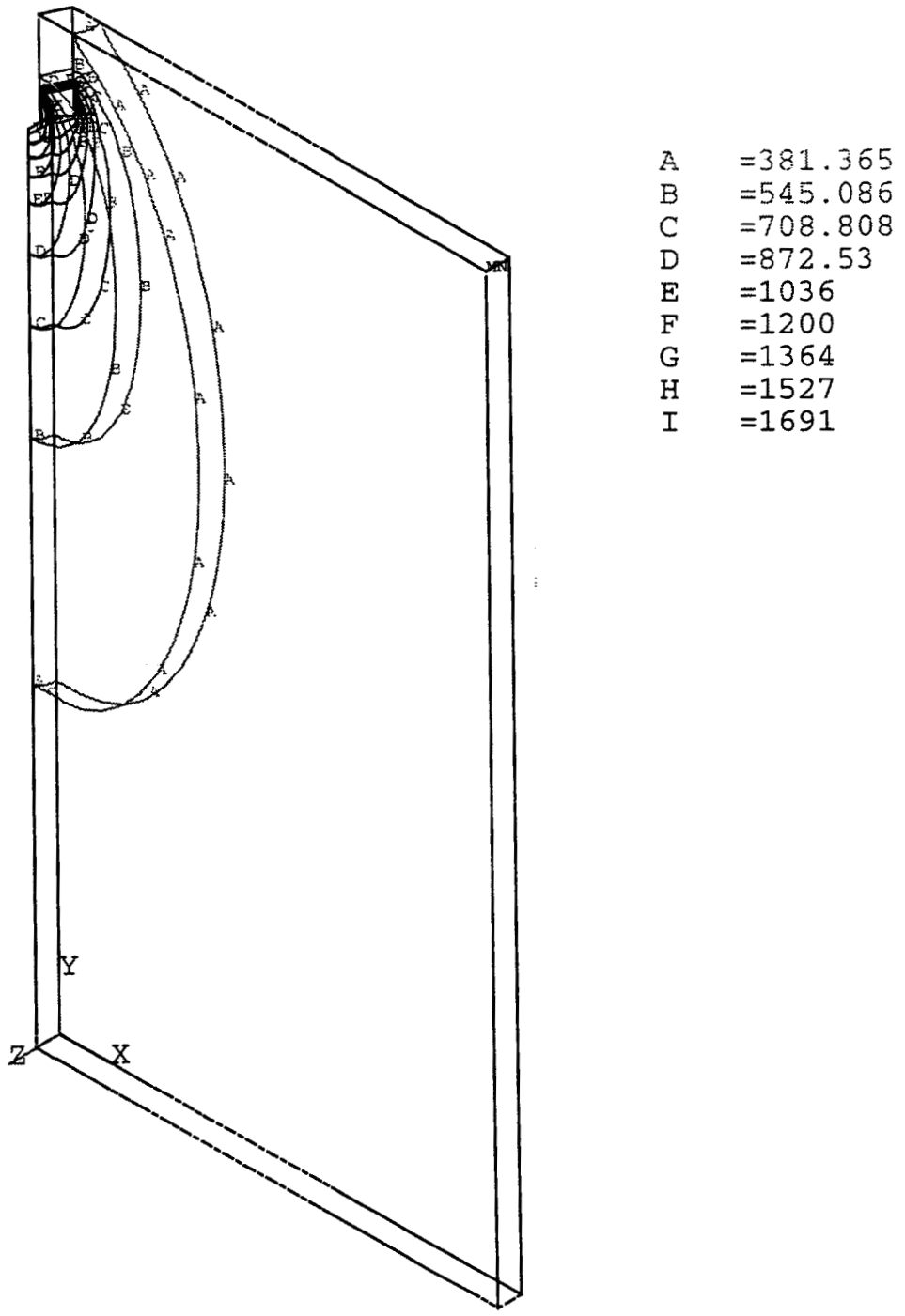

Figure 7-6 Temperature Profile for ANSYS Moving Coordinate System Thermal Calculation

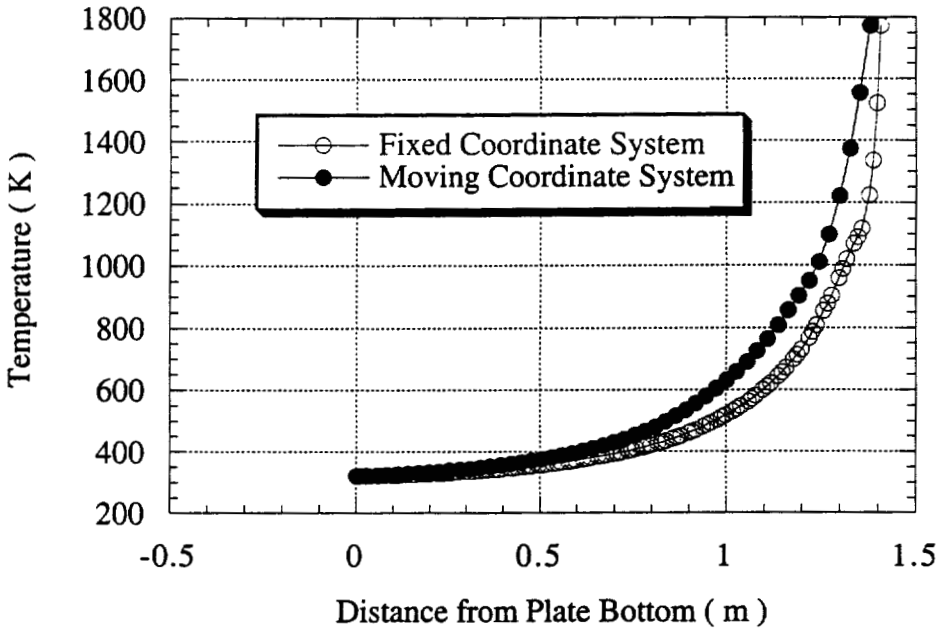

Figure 7-7 (a) Temperature as a Function of
Distance from Plate Bottom along Weld Center Line on Middle
PLane for Fixed Coordinate System and Moving Coordinate System

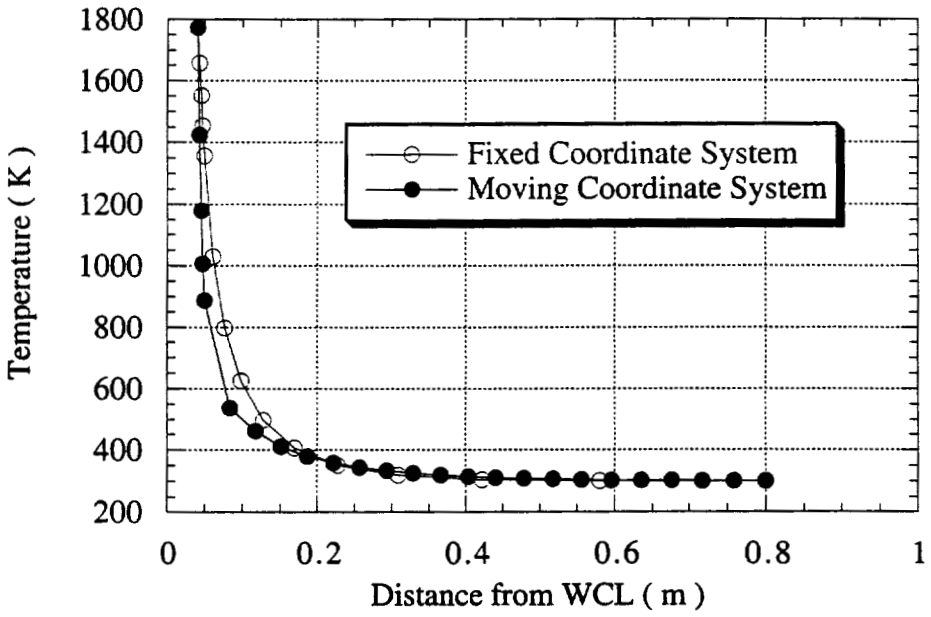

Figure 7-7 (b) Temperature as a Function of
Distance from WCL along Perpendicular to WCL Direction
on Middle Plane for Fixed Coordinate System and Moving Coordinate System

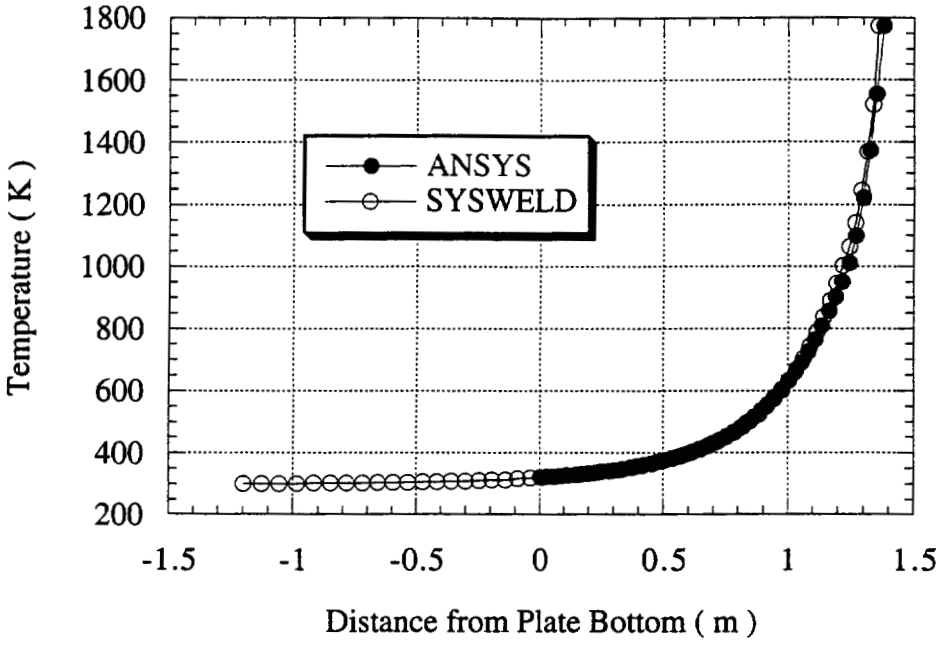

Figure 7-8 (a) Temperature as a Function of Distance from Plate Bottom along Weld Center Line on Middle Plane for ANSYS and SYSWELD with Moving Coordinate System

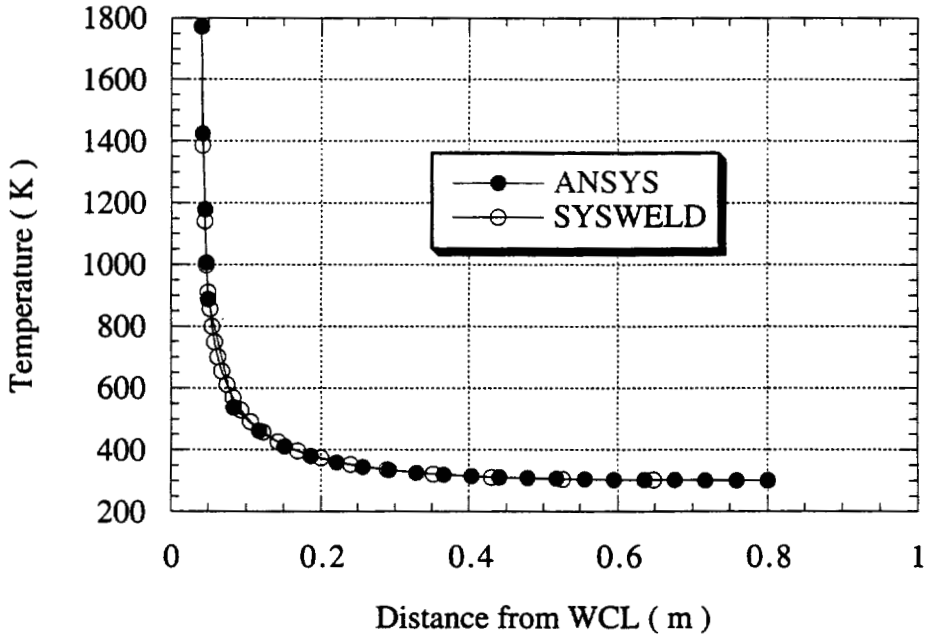

Figure 7-8 (b) Temperature as a Function of Distance from WCL along Perpendicular to WCL Direction on Middle PLane for ANSYS and SYSWELD with Moving Coordinate System

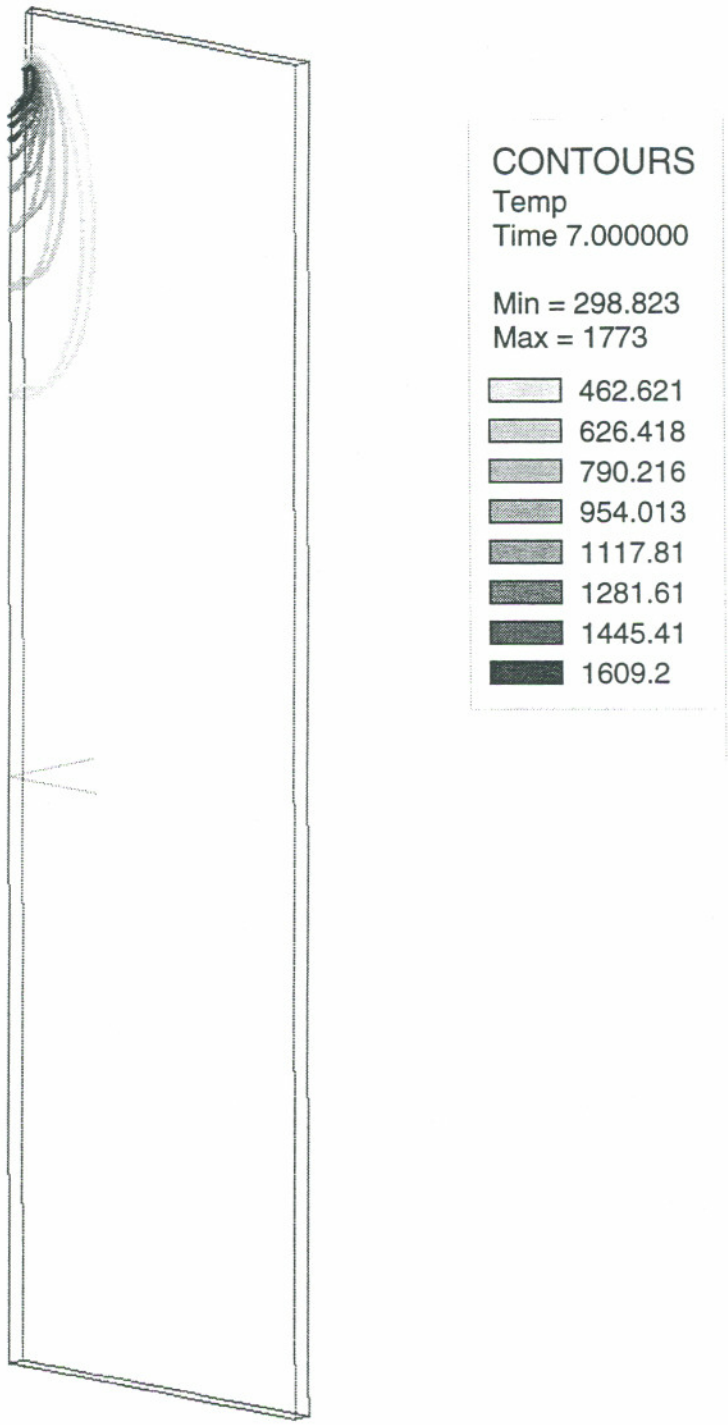

Figure 7-9 (a) Temperature Profile for SYSWELD Model1A Moving Coordinate System Thermal Calculation

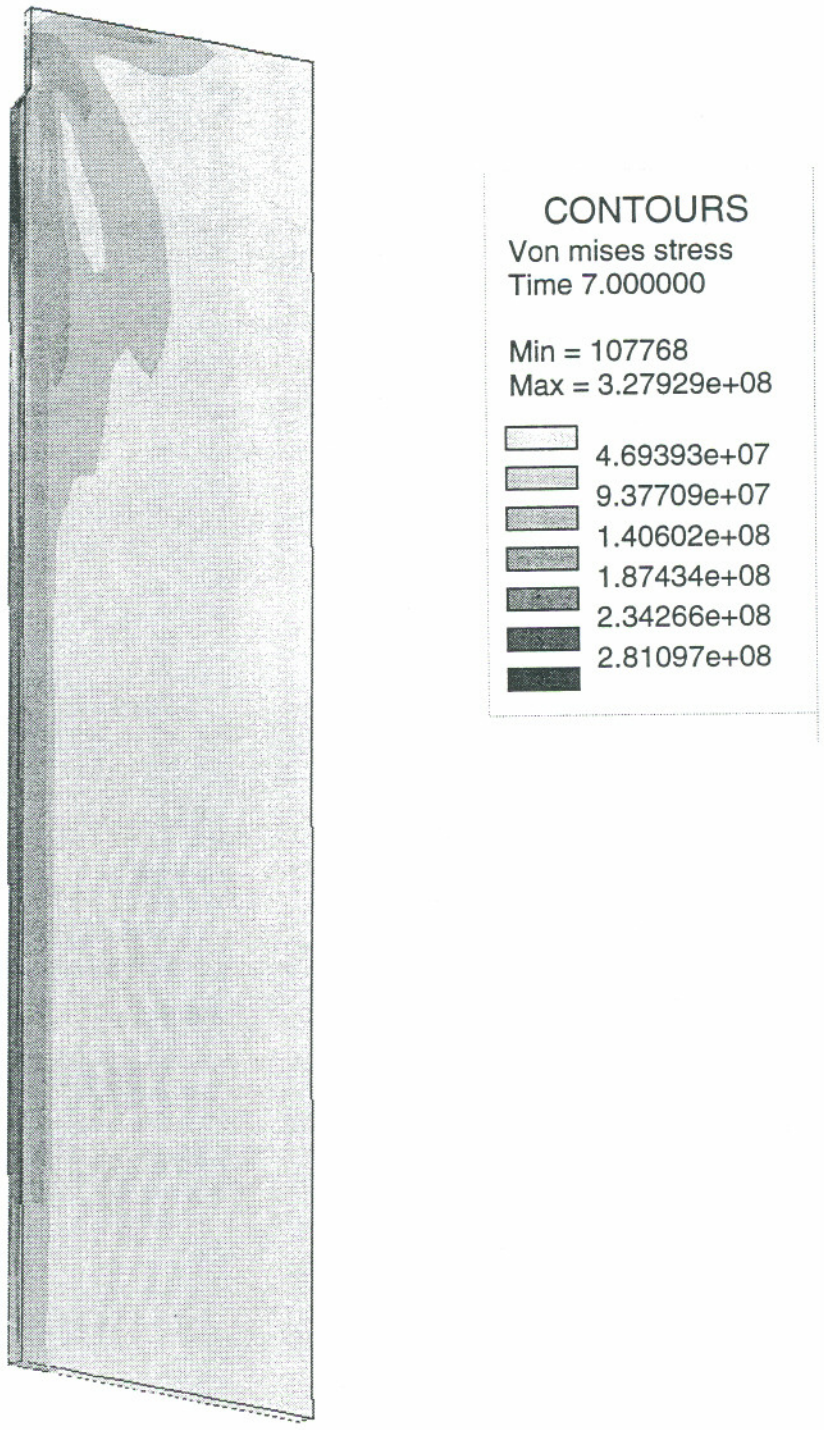

Figure 7-9 (b) Von Mises Stress Profile for SYSWELD Model1A Moving Coordinate System Thermal Calculation

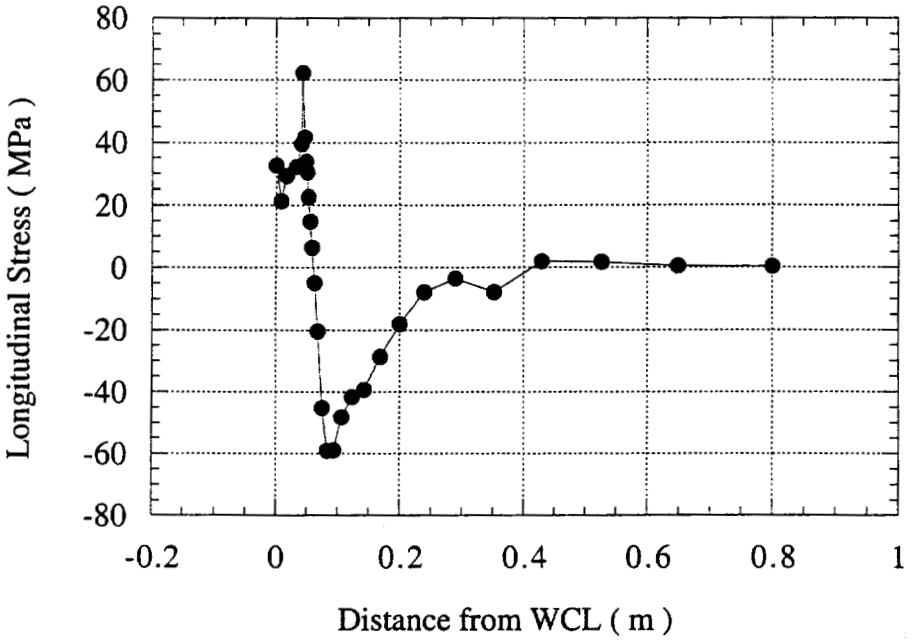

Figure 7-10 (a) Longitudinal Stress as a Function of
Distance from WCL on Middle Plane with SYSWELD Model1A

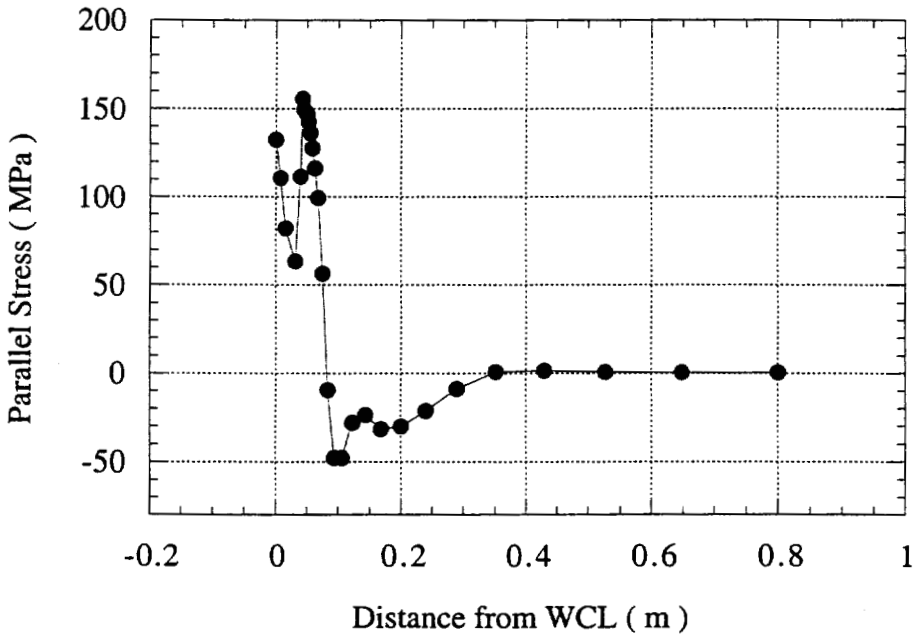

Figure 7-10 (b) Parallel Stress as a Function of
Distance from WCL on Middle Plane with SYSWELD Model1A

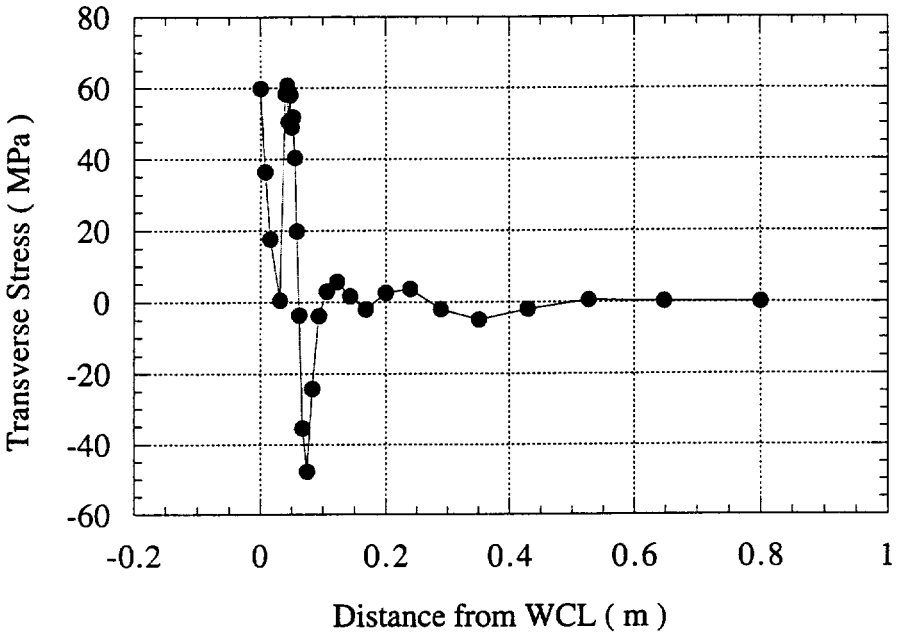

Figure 7-10 (c) Transverse Stress as a Function of
Distance from WCL on Middle Plane with SYSWELD Model1A

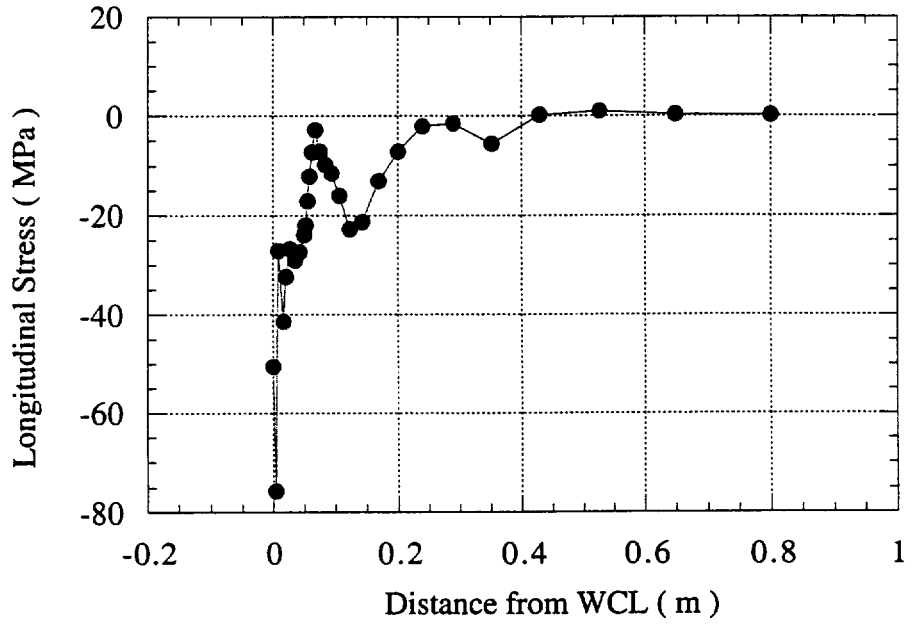

Figure 7-11 (a) Longitudinal Stress as a Function of
Distance from WCL on Plate Surface with SYSWELD Model1A

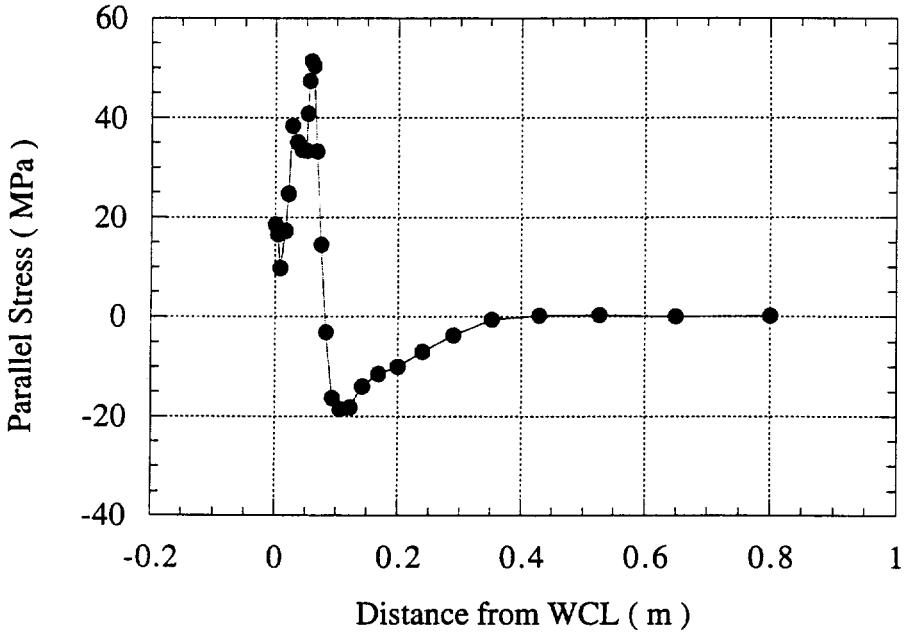

Figure 7-11 (b) Parallel Stress as a Function of
Distance from WCL on Plate Surface with SYSWELD model1A

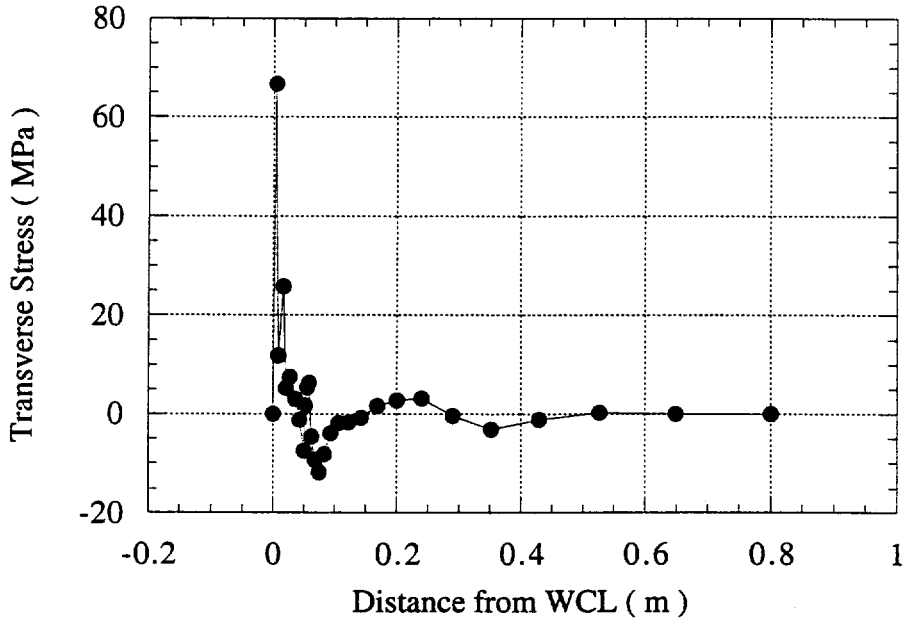

Figure 7-11 (c) Transverse Stress as a Function of
Distance from WCL on Plate Surface with SYSWELD Model1A

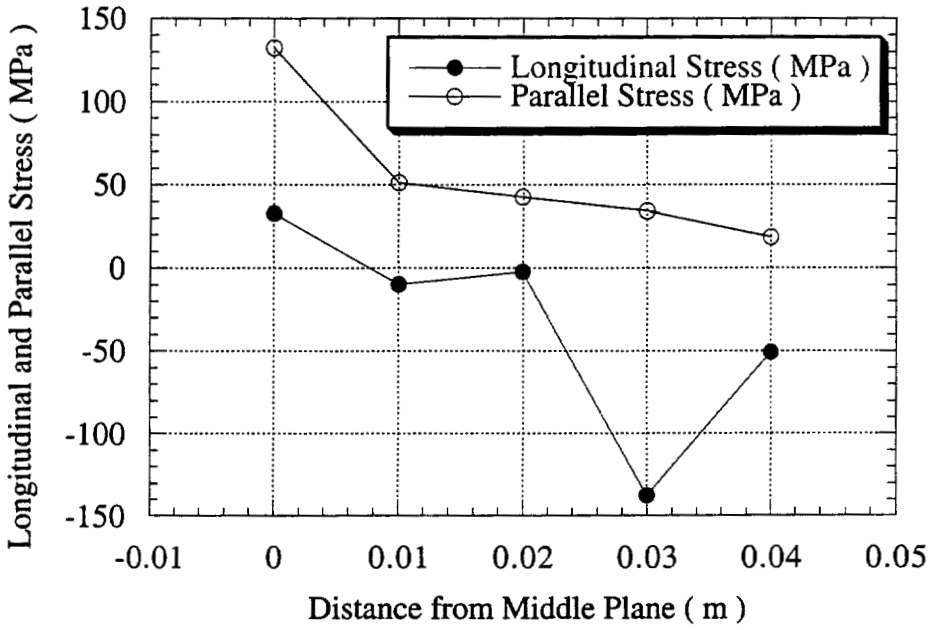

Figure 7-12 (a) Longitudinal and Parallel Stress as a Function of Distance from Middle Plane through Plate Thickness with SYSWELD Model1A

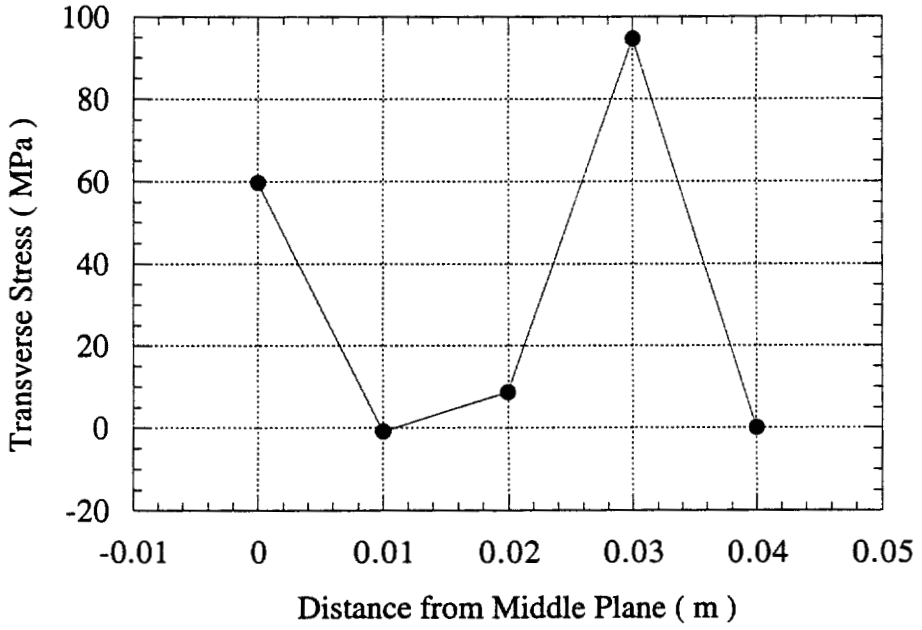

Figure 7-12 (b) Transverse Stress as a Function of Distance from Middle Plane through Plate Thickness with SYSWELD Model1A

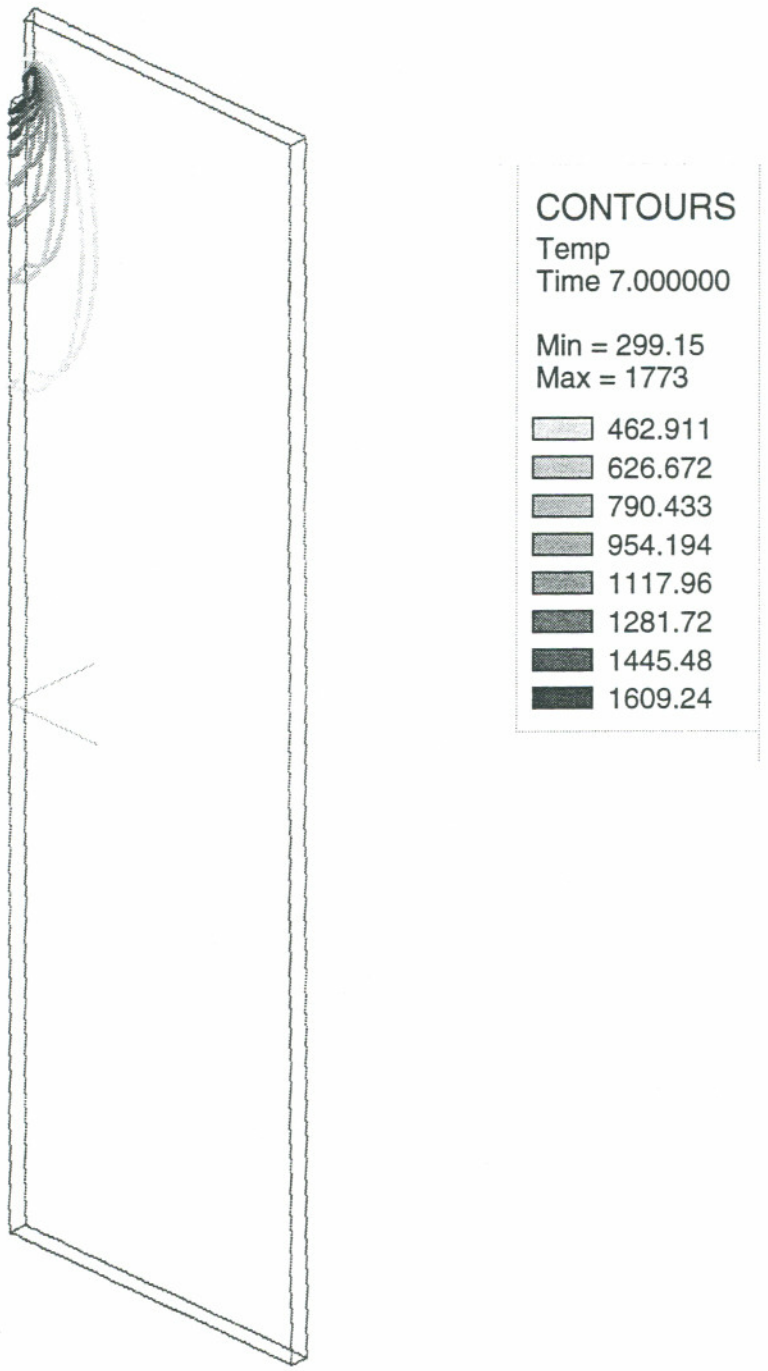

Figure 7-13 (a) Temperature Profile for SYSWELD Model2 Moving Coordinate System Thermal Calculation

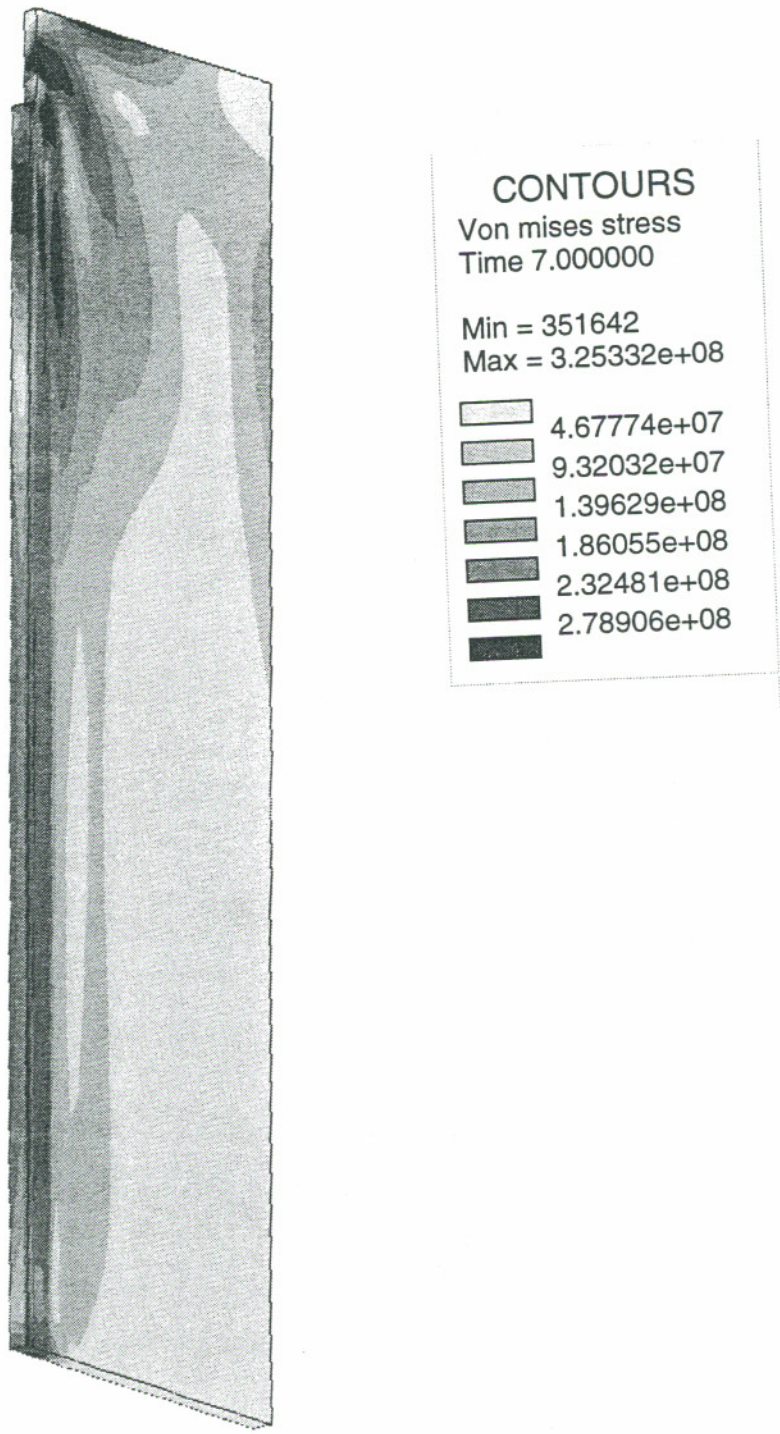

Figure 7-13 (b) Von Mises Stress Profile for SYSWELD Model2 Moving Coordinate System Thermal Calculation

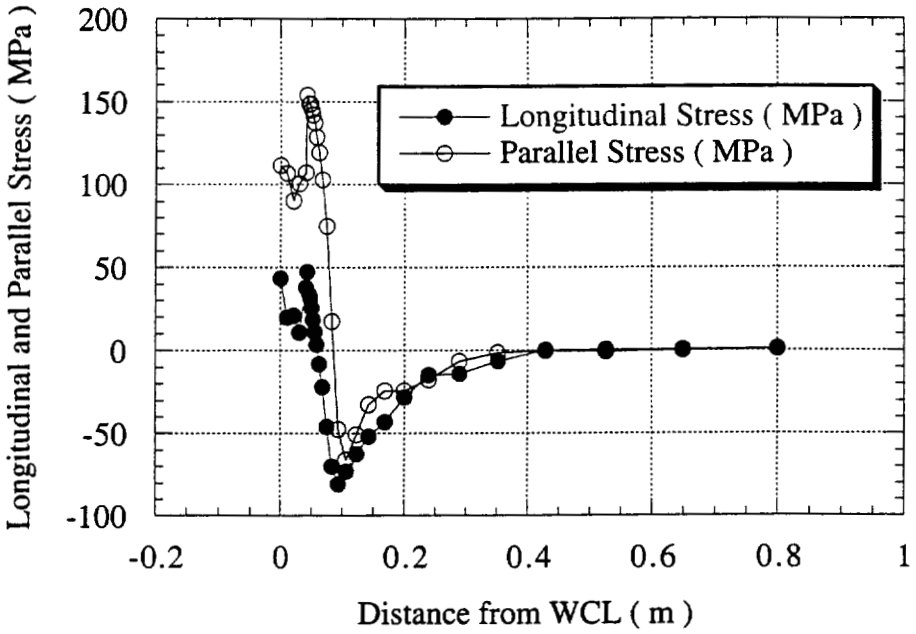

Figure 7-14 (a) Longitudinal and Parallel Stress as a Function of Distance from WCL on Middle Plane with SYSWELD Model2

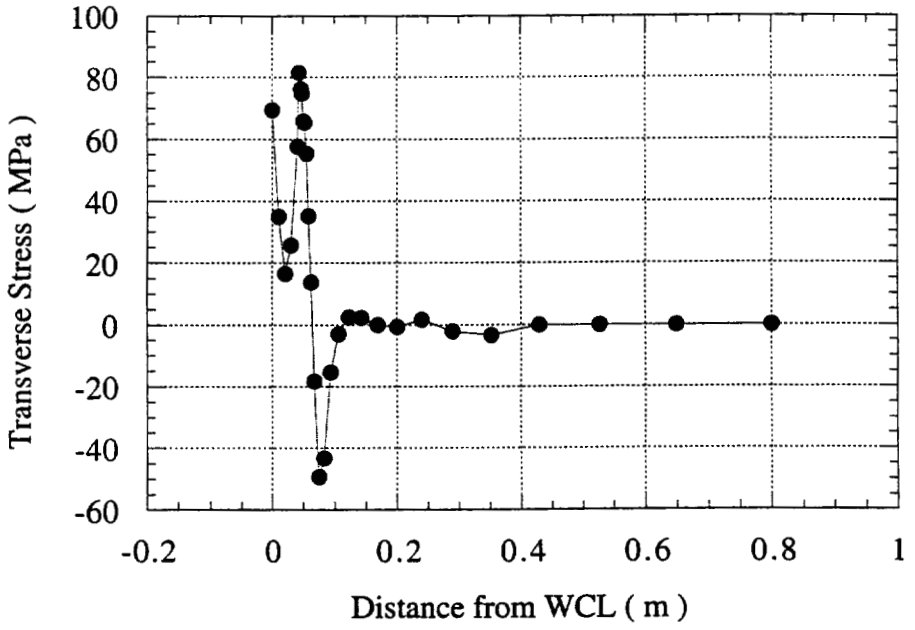

Figure 7-14 (b) Transverse Stress as a Function of Distance from WCL on Middle Plane with SYSWELD Model2

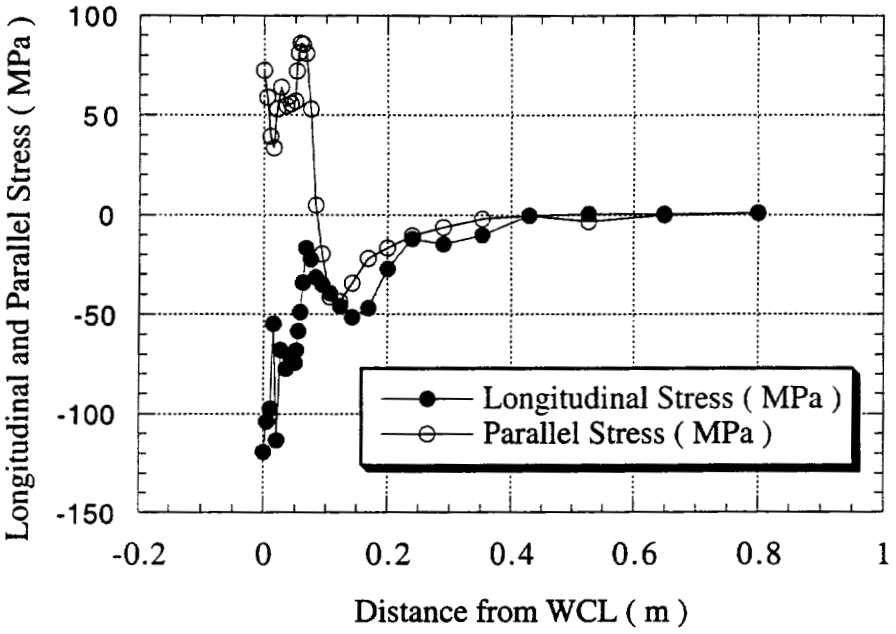

Figure 7-15 (a) Longitudinal and Parallel Stress as a Function of Distance from WCL on Plate Surface with SYSWELD Model2

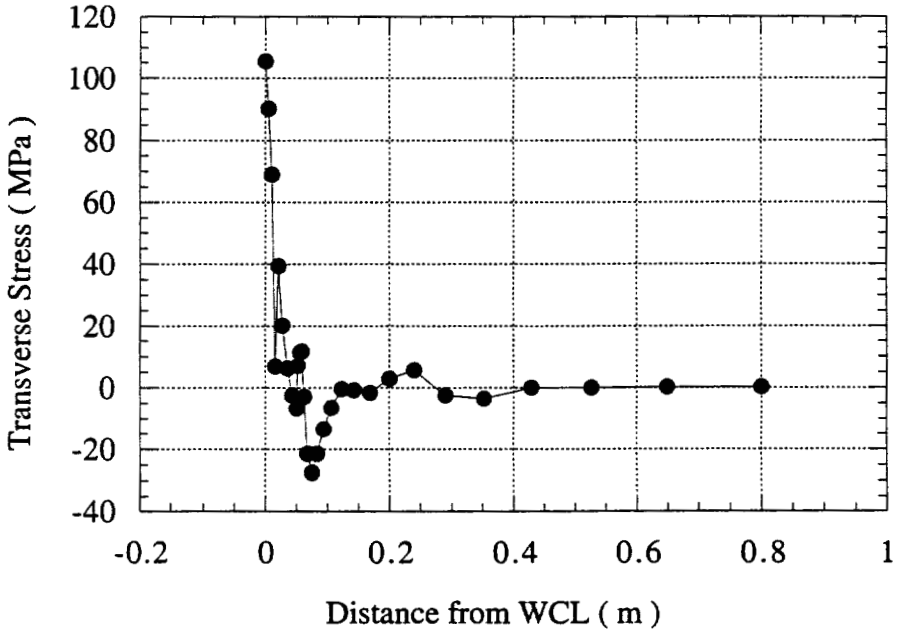

Figure 7-15 (b) Transverse Stress as a Function of Distance from WCL on Plate Surface with SYSWELD Model2

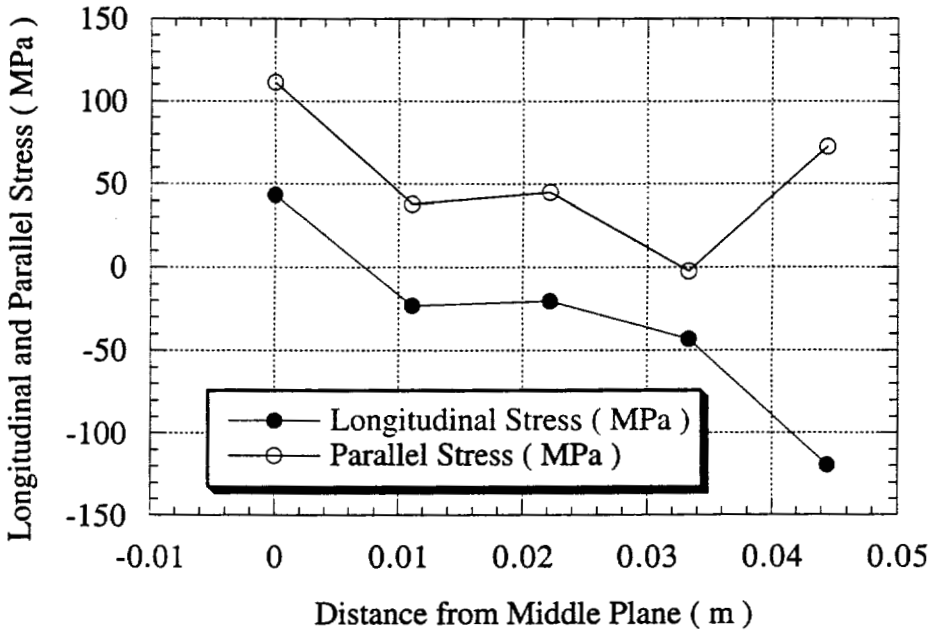

Figure 7-16 (a) Longitudinal and Parallel Stress as a Function of Distance from Middle Plane through Plate Thickness with SYSWELD Model2

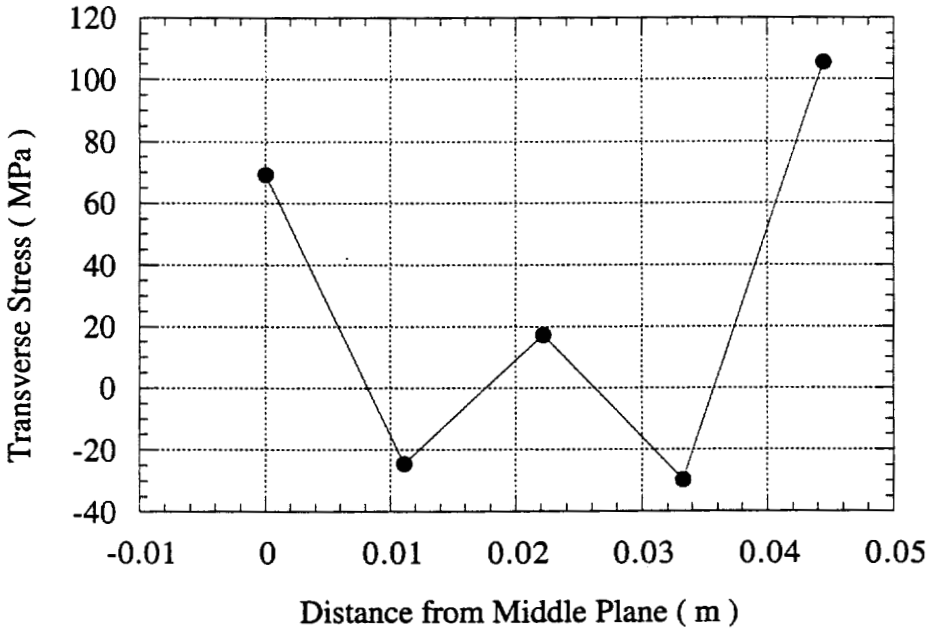

Figure 7-16 (b) Transverse Stress as a Function of Distance from Middle Plane through Plate Thickness with SYSWELD Model2

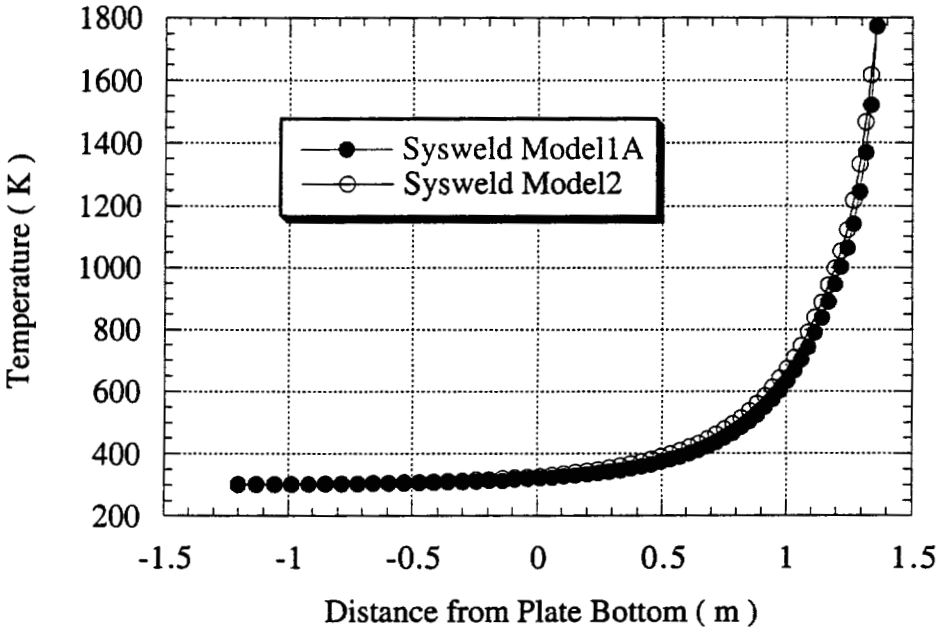

Figure 7-17 (a) Temperature as a Function of Distance from Plate Bottom along WCL on Middle Plane for SYSWELD Model1A and Model2

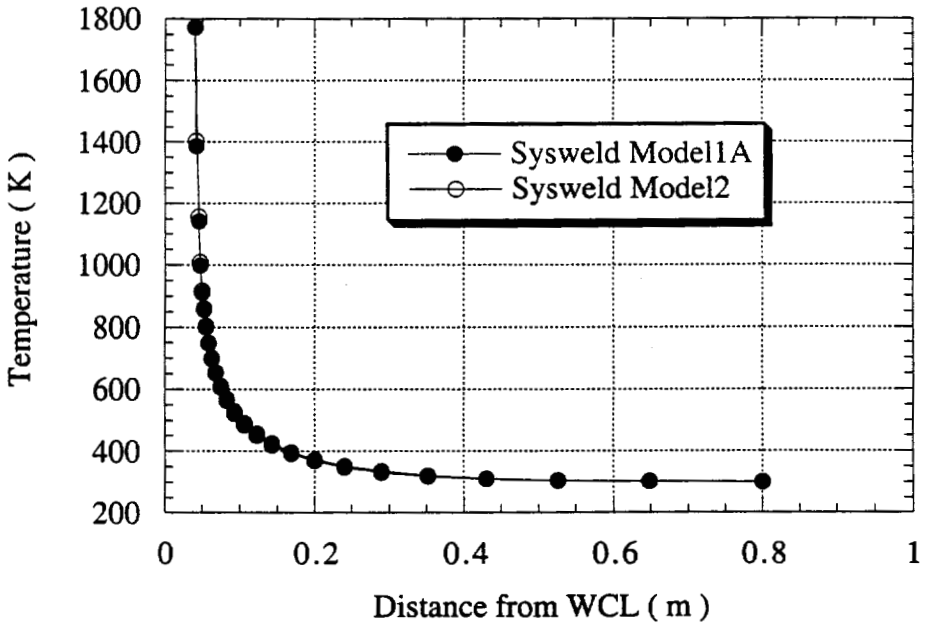

Figure 7-17 (b) Temperature as a Function of Distance from WCL along Perpendicular to WCL Direction on Middle Plane for SYSWELD Model1A and Model2

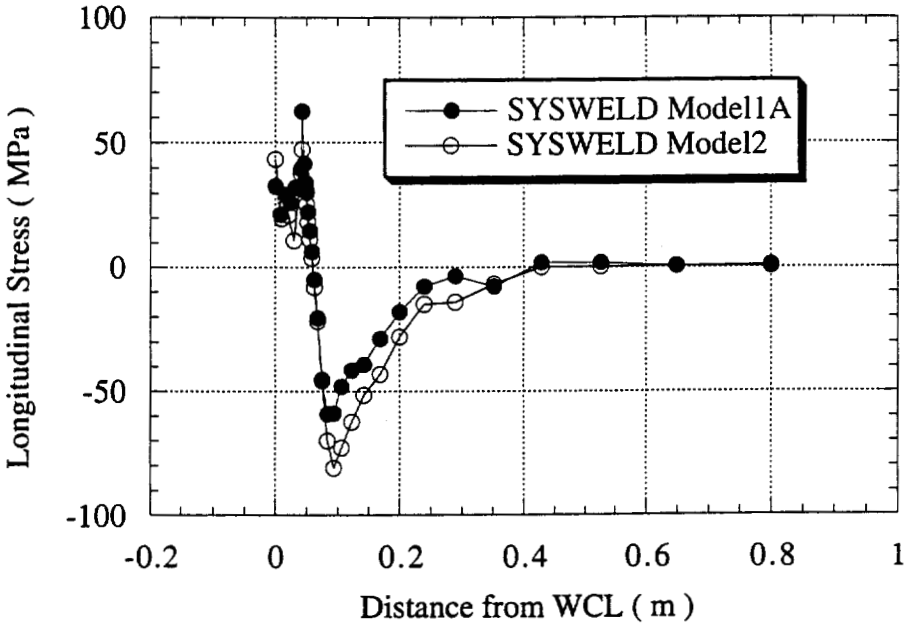

Figure 7-18 (a) Longitudinal Stress as a Function of Distance from WCL on Middle Plane for SYSWELD Model1A and Model2

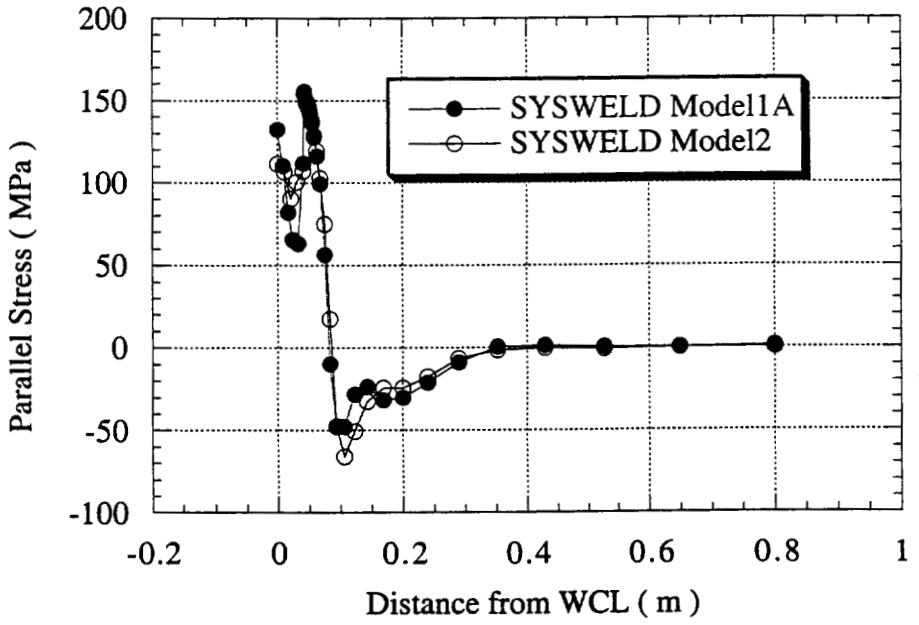

Figure 7-18 (b) Parallel Stress as a Function of Distance from WCL on Middle Plane for SYSWELD Model1A and Model2

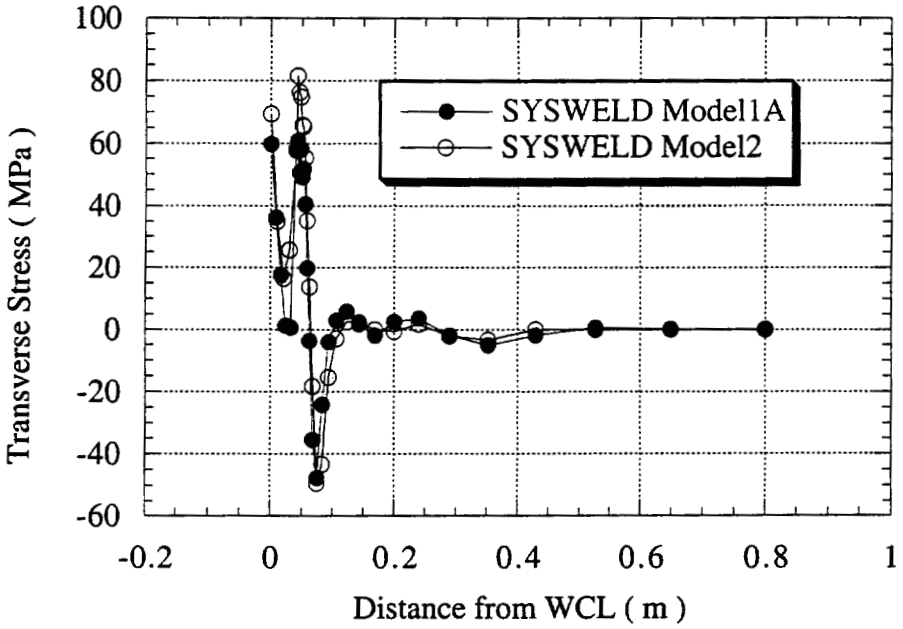

Figure 7-18 (c) Transverse Stress as a Function of Distance from WCL on Middle Plane for SYSWELD Model1A and Model2

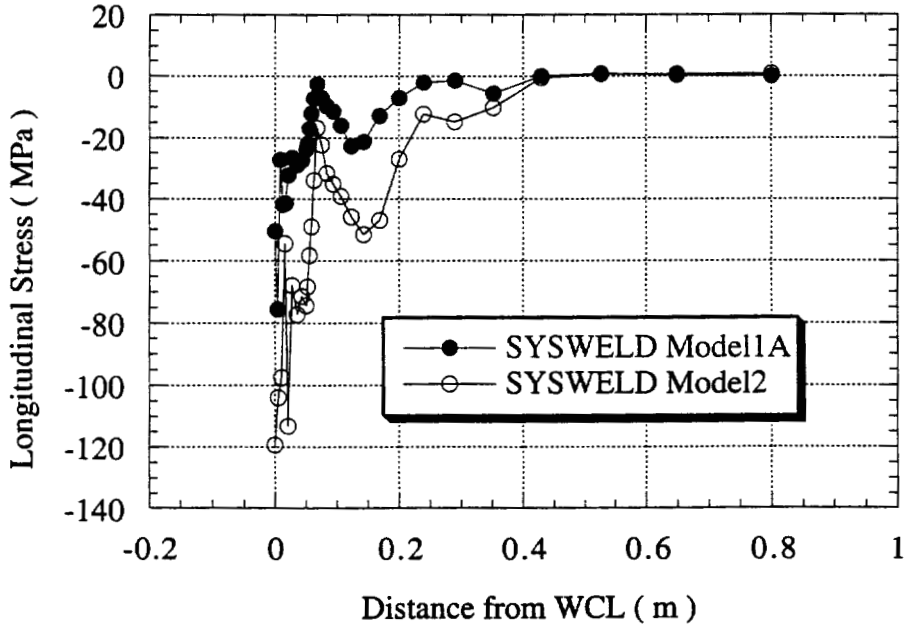

Figure 7-19 (a) Longitudinal Stress as a Function of Distance from WCL on Plate Surface for SYSWELD Model1A and Model2

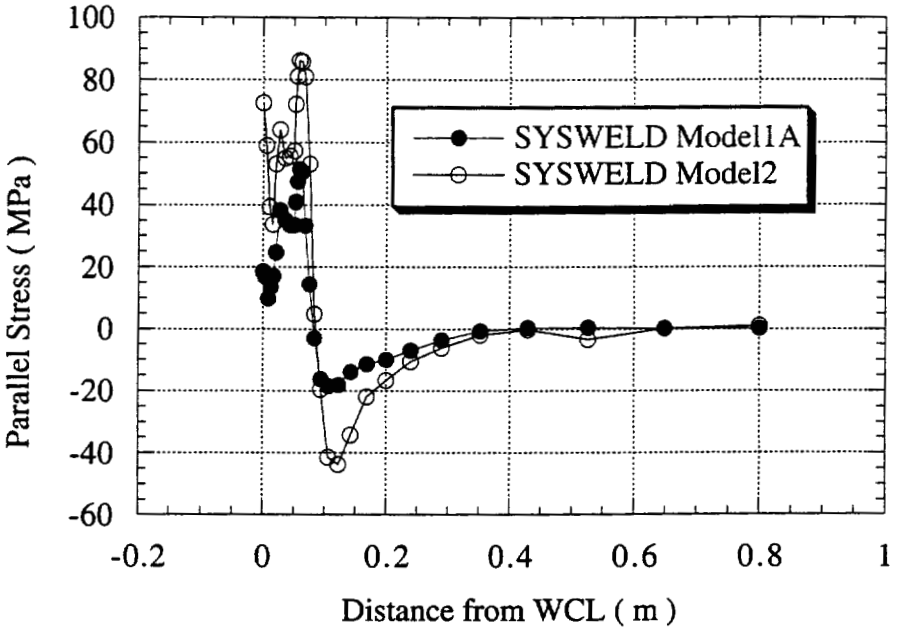

Figure 7-19 (b) Parallel Stress as a Function of Distance from WCL on Plate Surface for SYSWELD Model1A and Model2

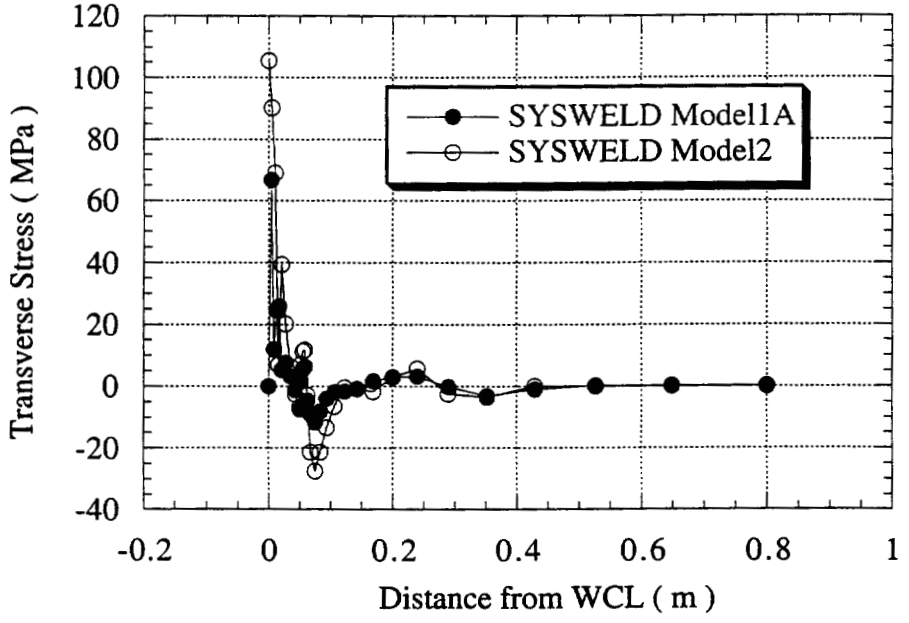

Figure 7-19 (c) Transverse Stress as a Function of Distance from WCL on Plate Surface for SYSWELD Model1A and Model2

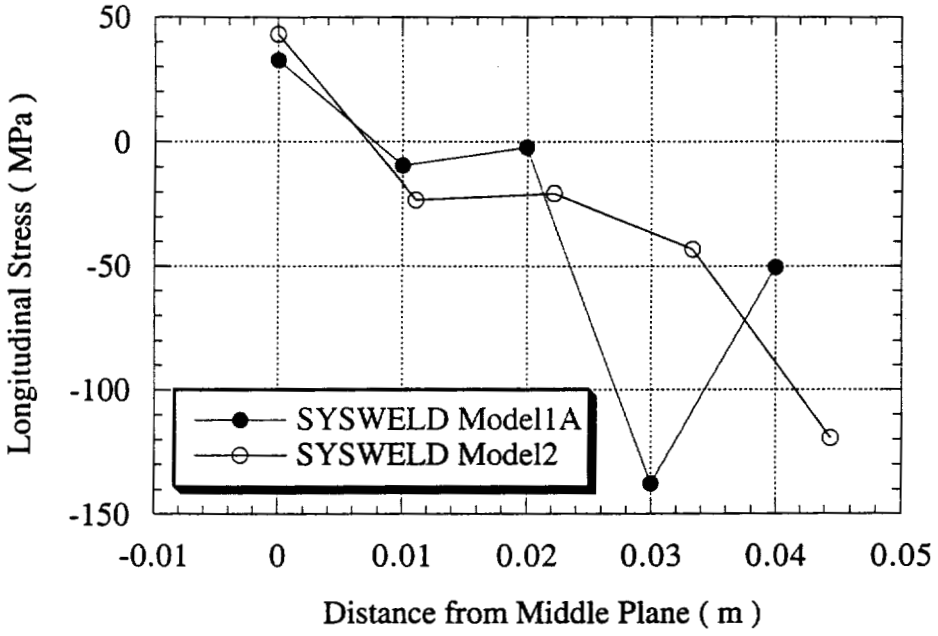

Figure 7-20 (a) Longitudinal Stress as a Function of Distance from Middle Plane through Plate Thickness for SYSWELD Model1A and Model2

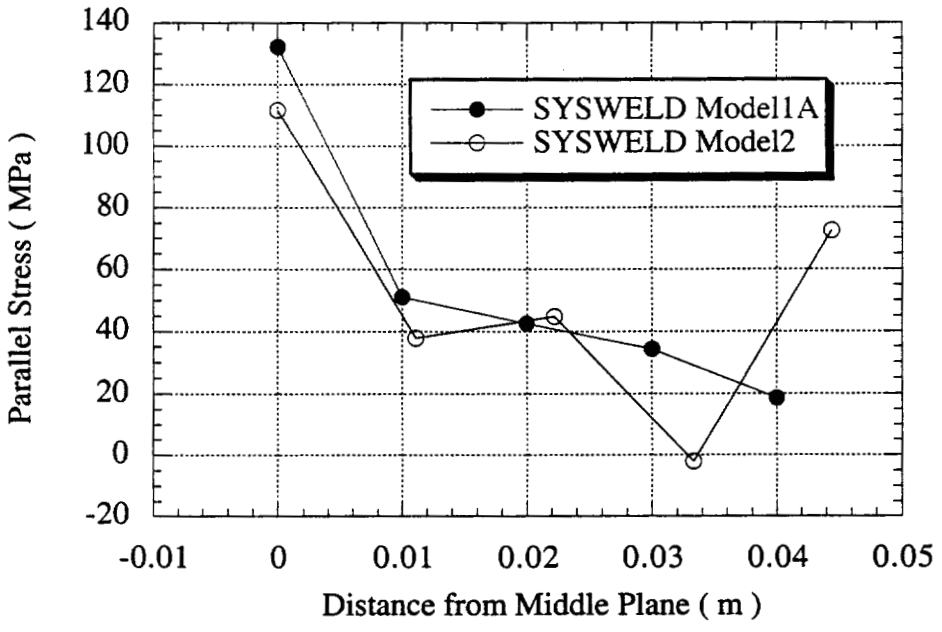

Figure 7-20 (b) Parallel Stress as a Function of Distance from Middle Plane through Plate Thickness for SYSWELD Model1A and Model2

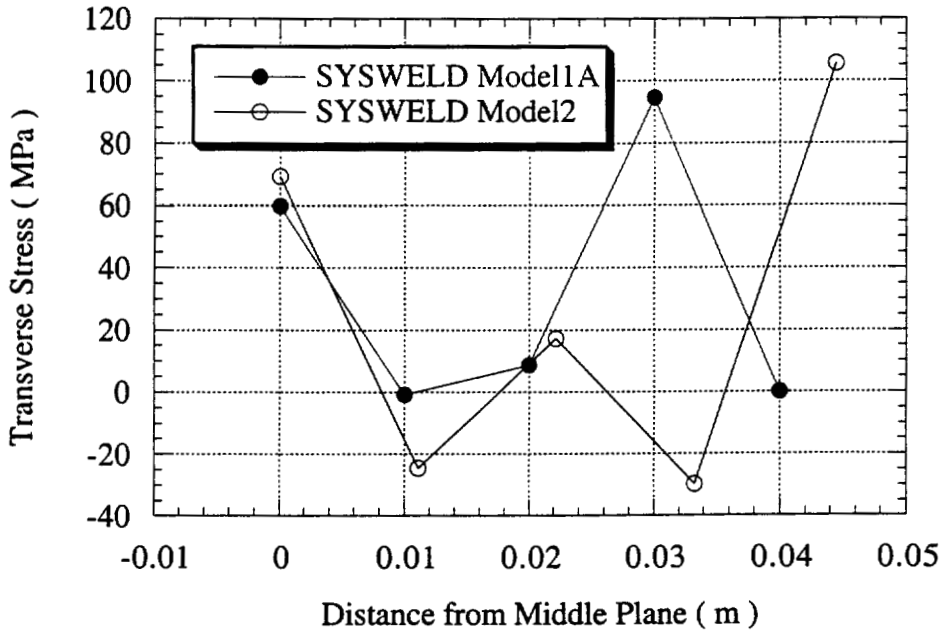

Figure 7-20 (c) Transverse Stress as a Function of Distance from Middle Plane through Plate Thickness for SYSWELD Model1A and Model2

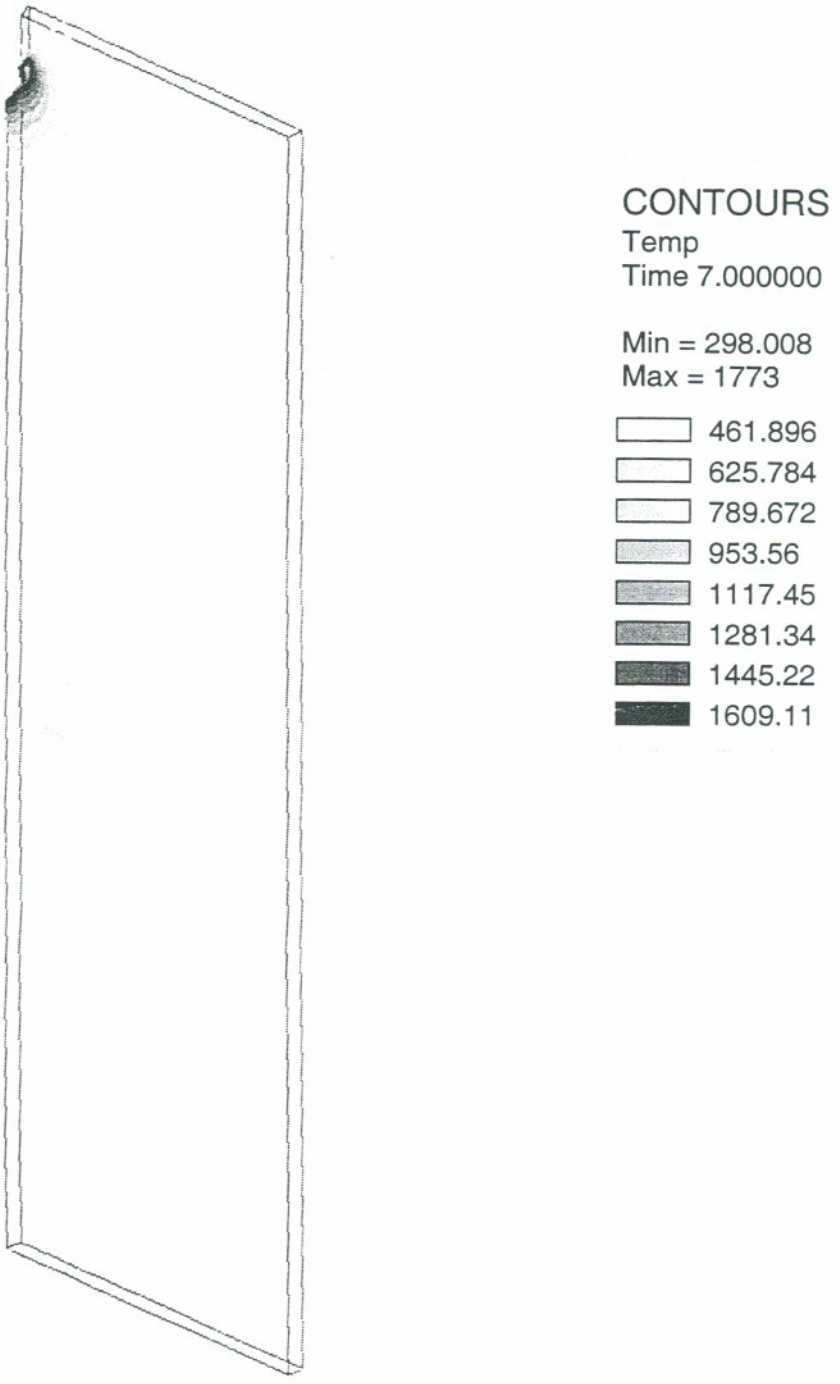

Figure 7-21 (a) Temperature Profile for Welding Speed of $1x10^{-4}$m/s with SYSWELD Model1B

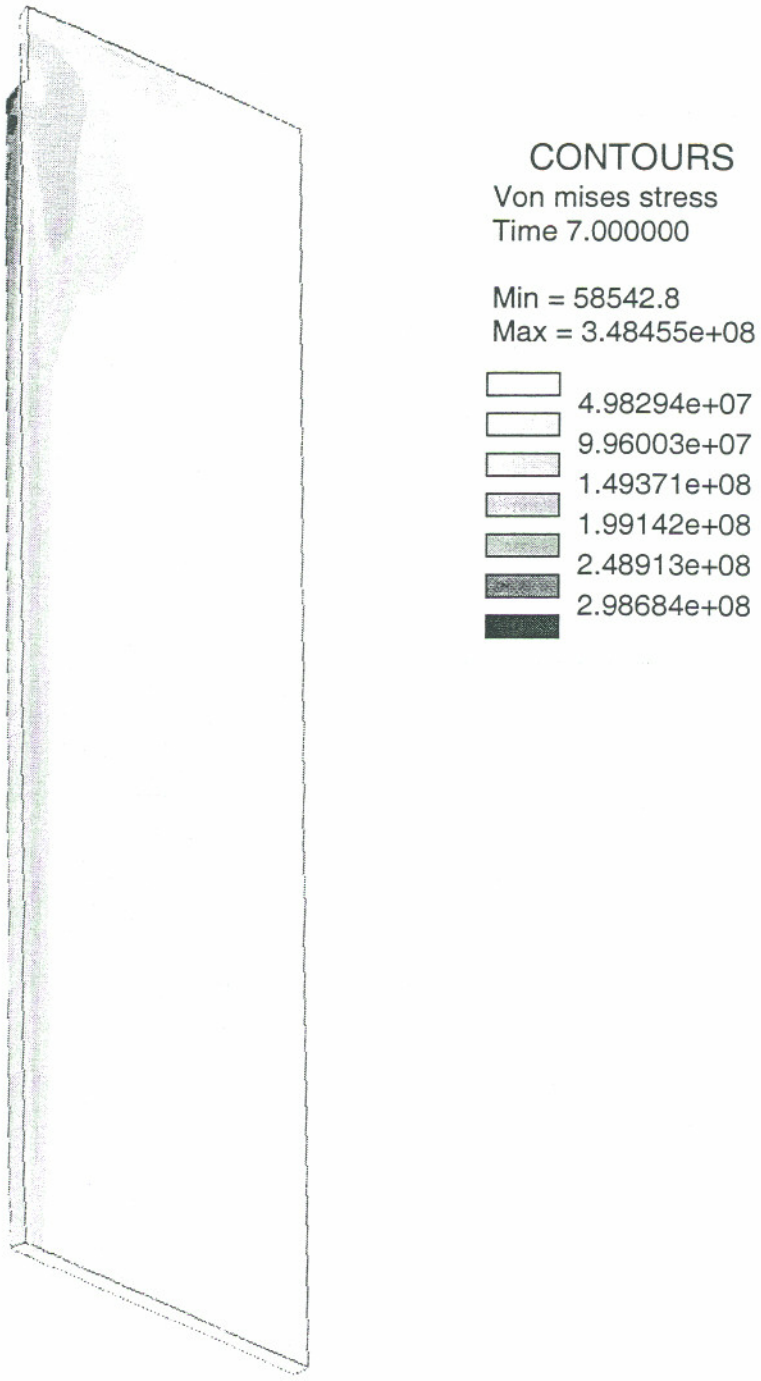

Figure 7-21 (b) Von Mises Stress Profile for Welding Speed of $1x10^{-4}$m/s with SYSWELD Model1B

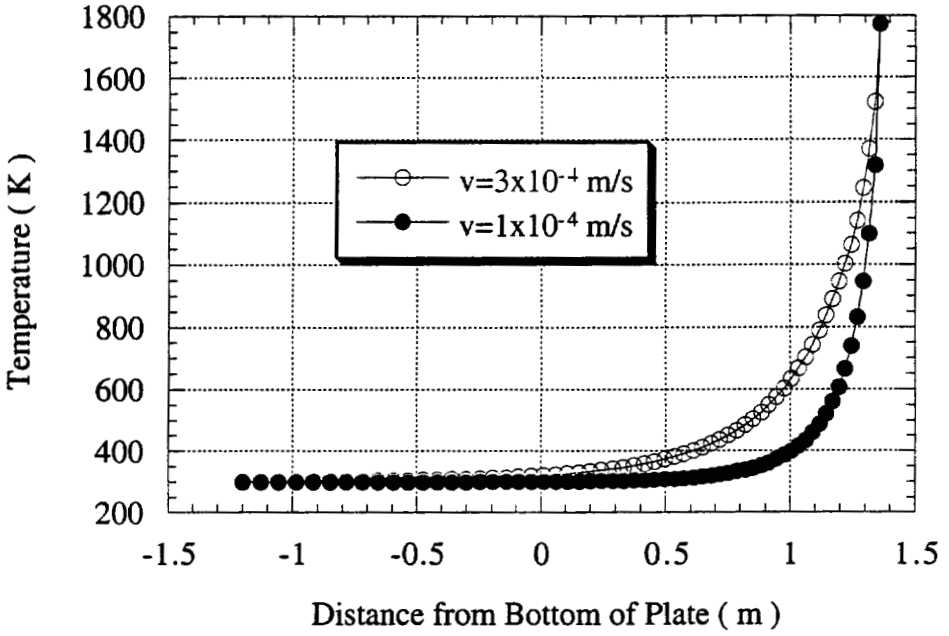

Figure 7-22 (a) Temperature as a Function of Distance from Plate Bottom along WCL on Middle Plane with Different Welding Speed

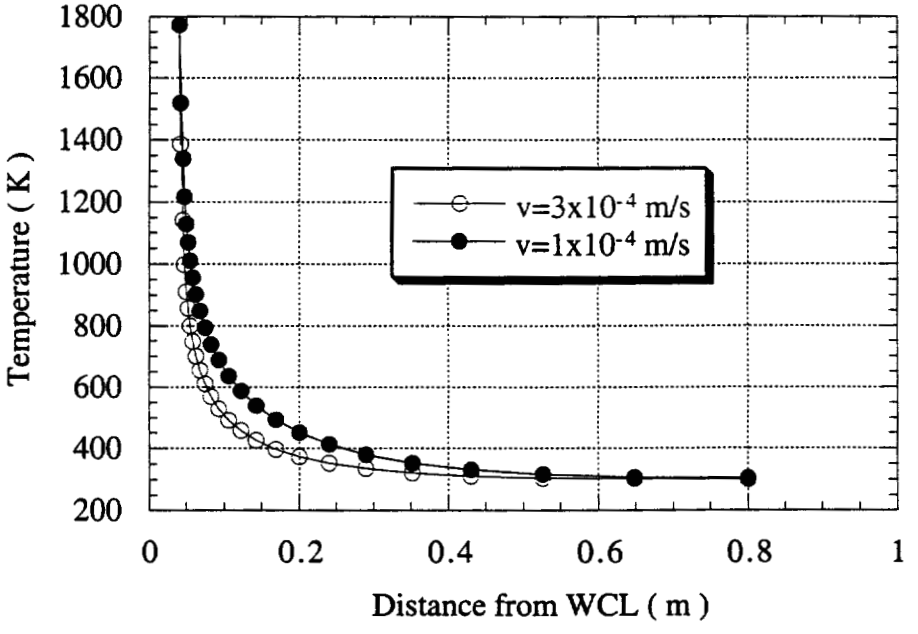

Figure 7-22 (b) Temperature as a Function of Distance from WCL along Perpendicular to WCL Direction on Middle Plane with Different Welding Speed

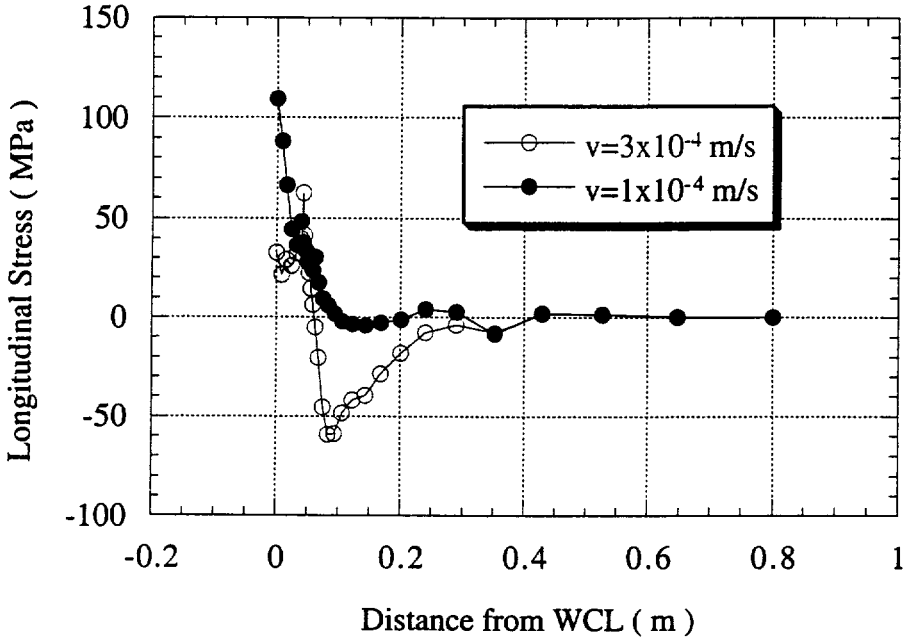

Figure 7-23 (a) Longitudinal Stress as a Function of Distance from WCL on Middle Plane with Different Welding Speed

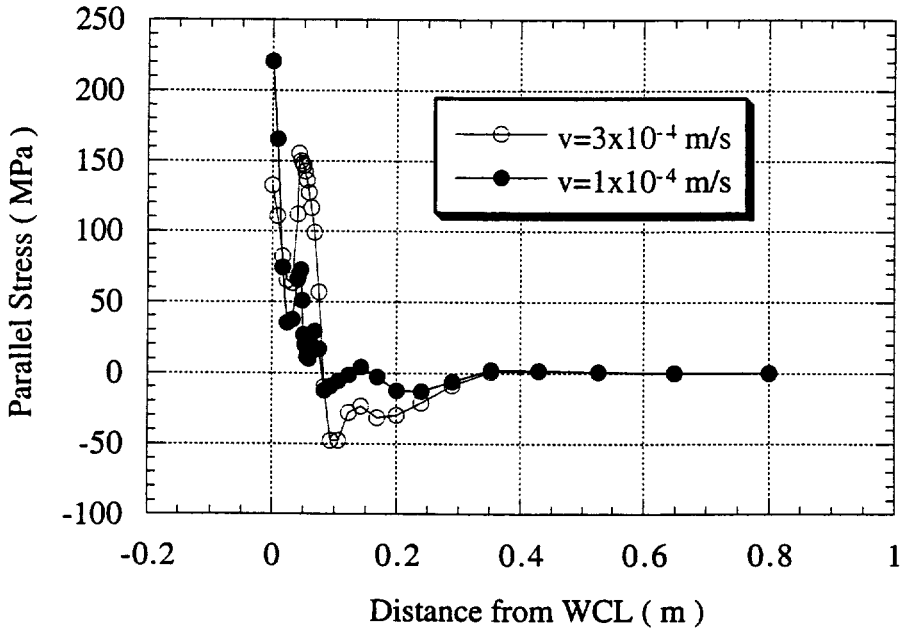

Figure 7-23 (b) Parallel Stress as a Function of Distance from WCL on Middle Plane with Different Welding Speed

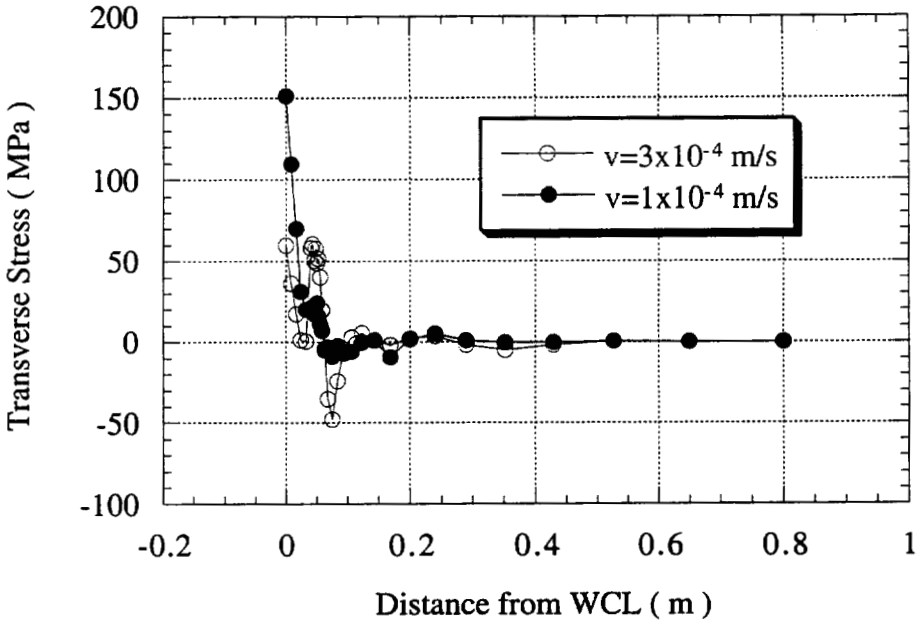

Figure 7-23 (c) Transverse Stress as a Function of
Distance from WCL on Middle Plane with Different Welding Speed

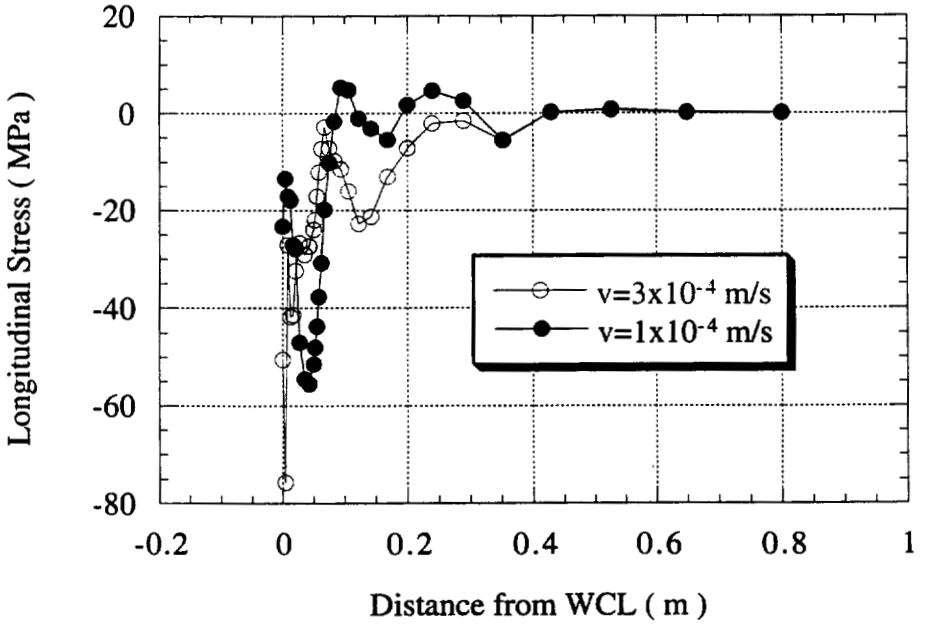

Figure 7-24 (a) Longitudinal Stress as a Function of
Distance from WCL on Plate Surface with Different Weld Speed

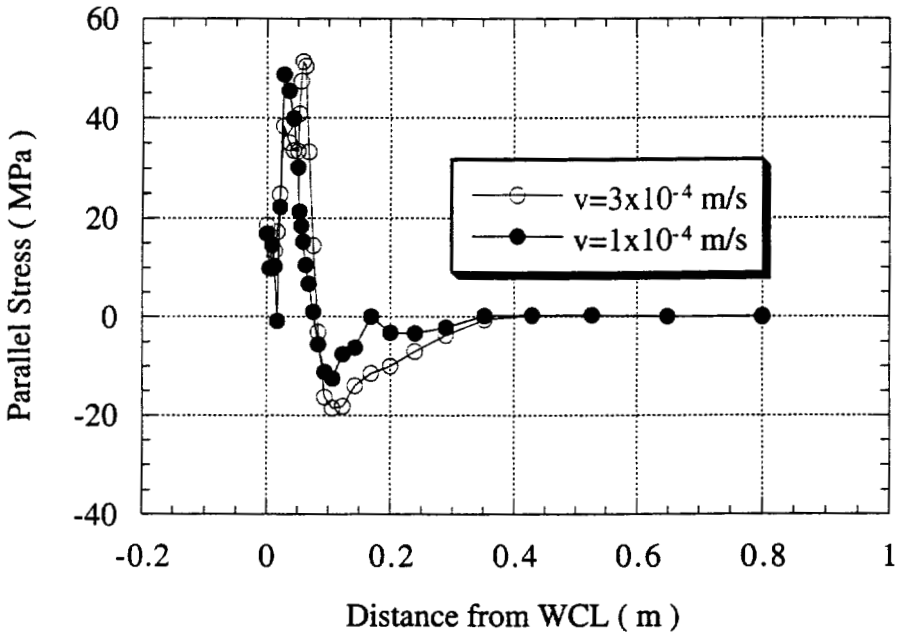

Figure 7-24 (b) Parallel Stress as a Function of Distance from WCL on Plate Surface with Different Welding Speed

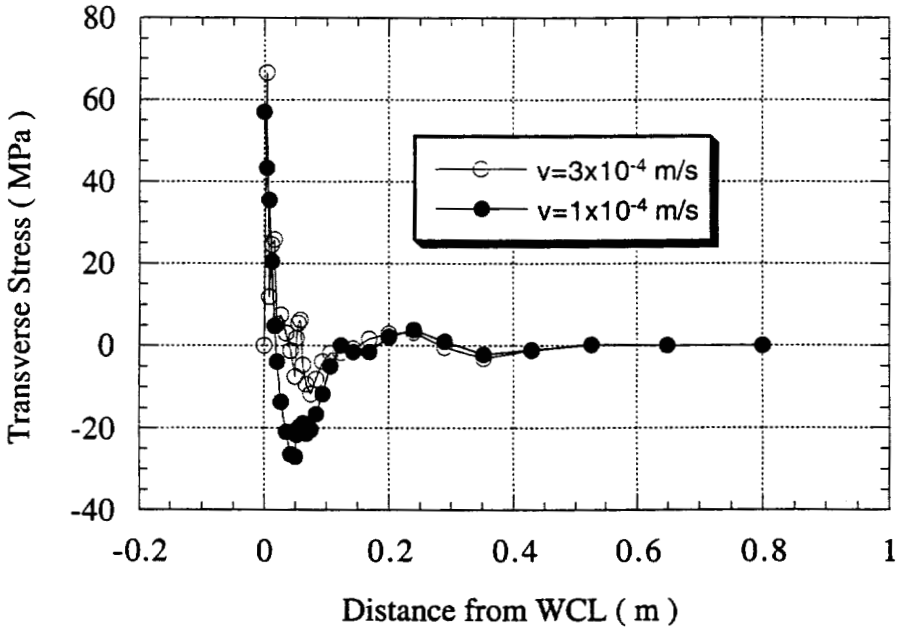

Figure 7-24 (c) Transverse Stress as a Function of Distance from WCL on Plate Surface with Different Welding Speed

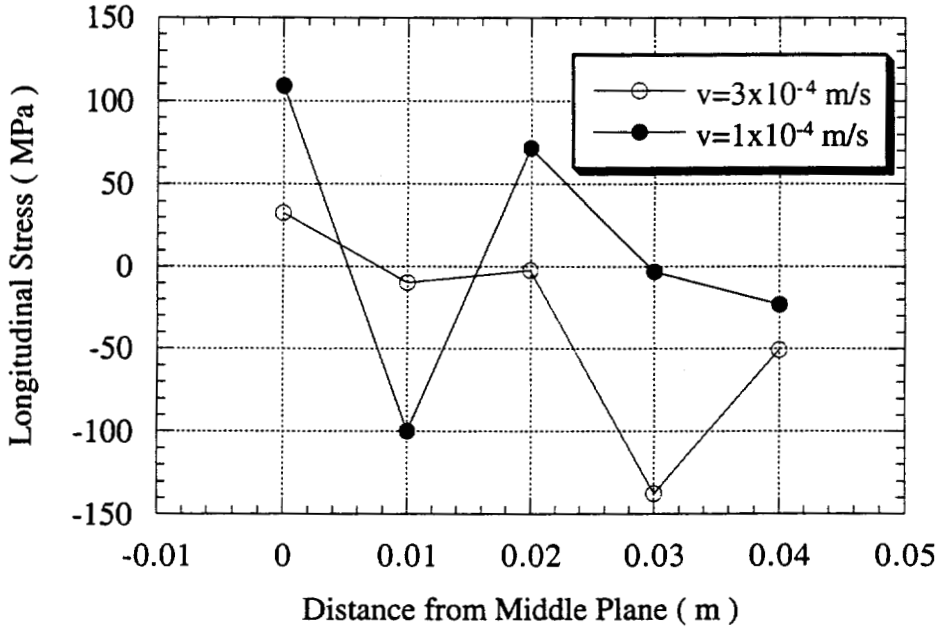

Figure 7-25 (a) Longitudinal Stress as a Function of Distance from Middle Plane through Plate Thickness with Different Welding Speed

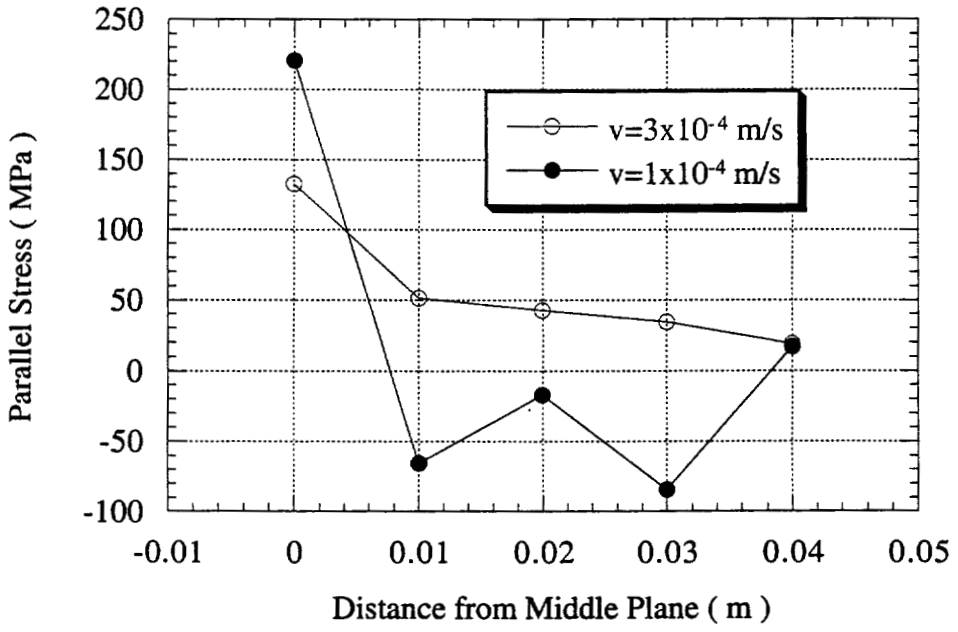

Figure 7-25 (b) Parallel Stress as a Function of Distance from Middle Plane through Plate Thickness with Different Welding Speed

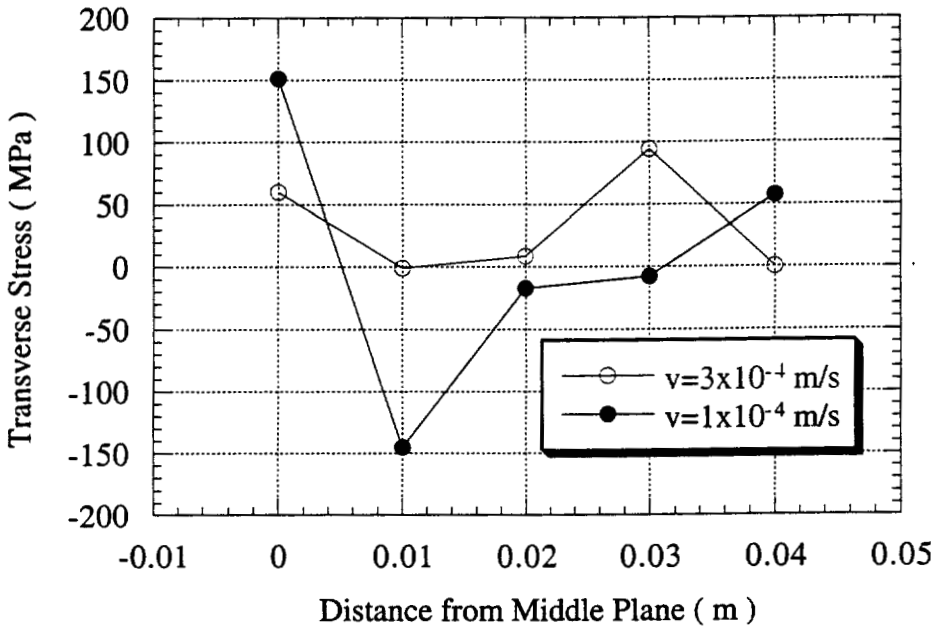

Figure 7-25 (c) Transverse Stress as a Function of Distance from Middle Plane through Plate Thickness with Different Welding Speed

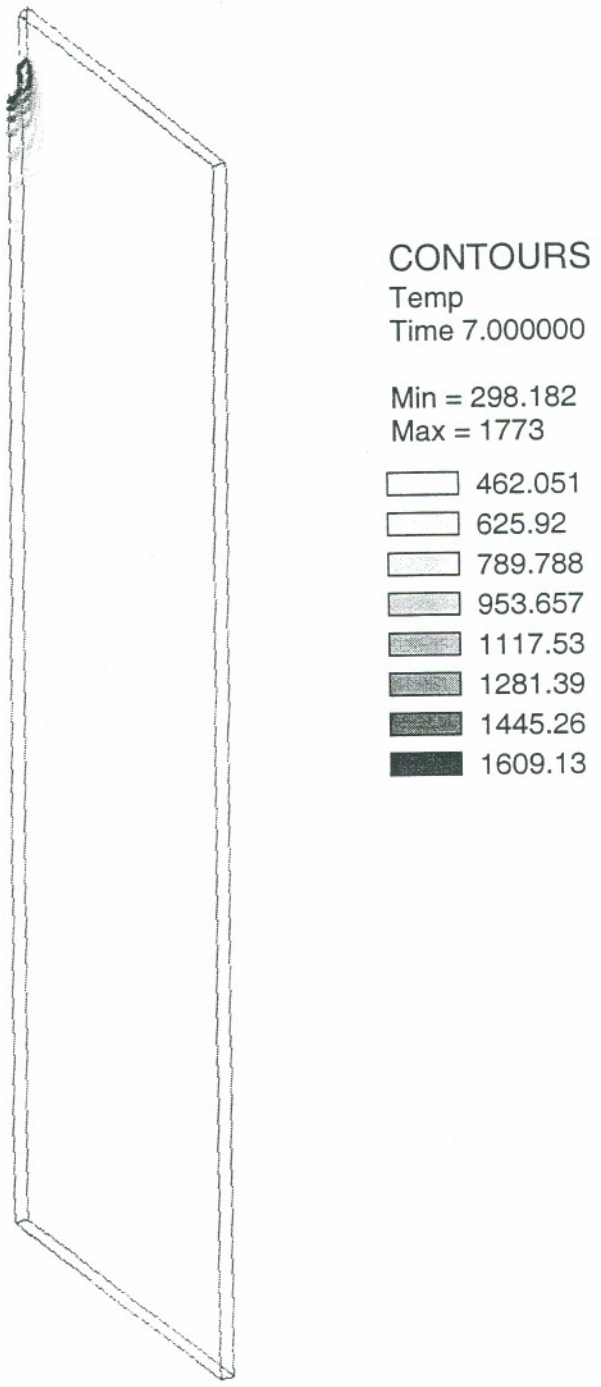

Figure 7-26 (a) Temperature Profile for Plate Thickness of 0.06m with SYSWELD Model1C

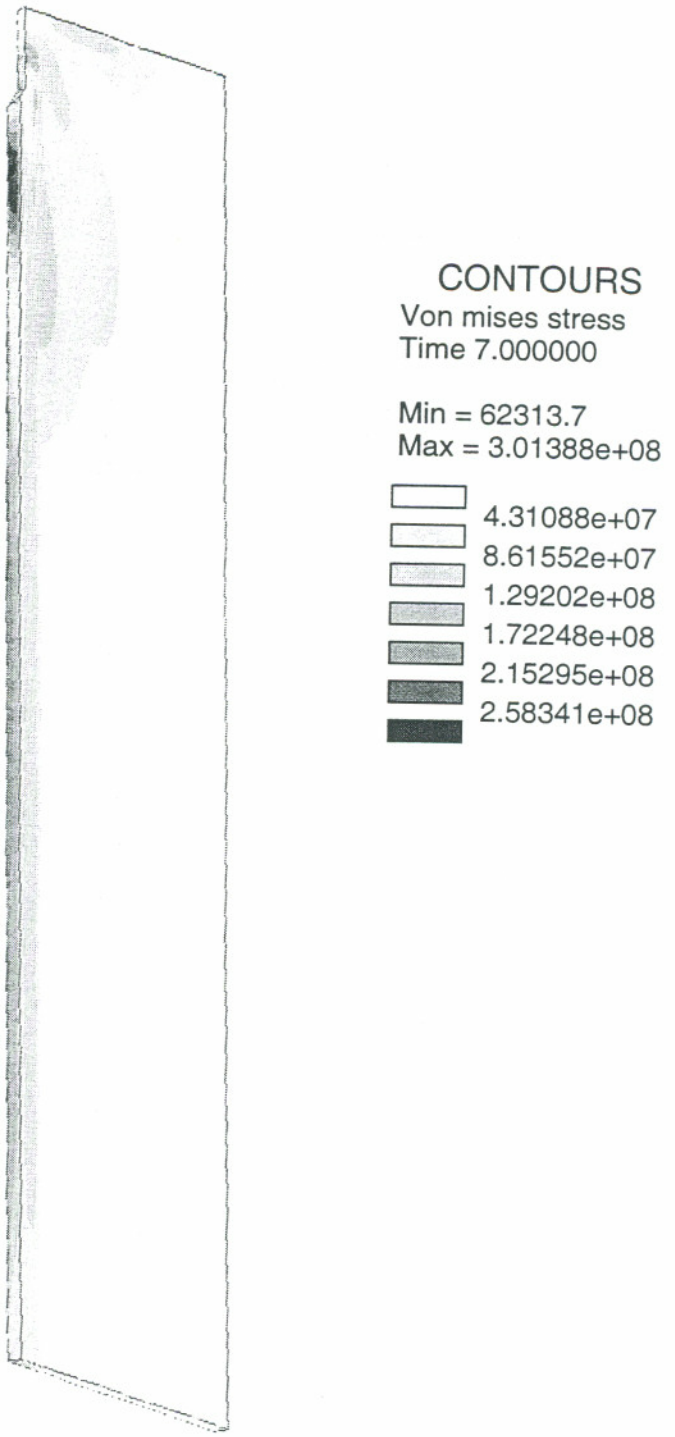

Figure 7-26 (b) Von Mises Stress Profile for Plate Thickness of 0.06m with SYSWELD Model1C

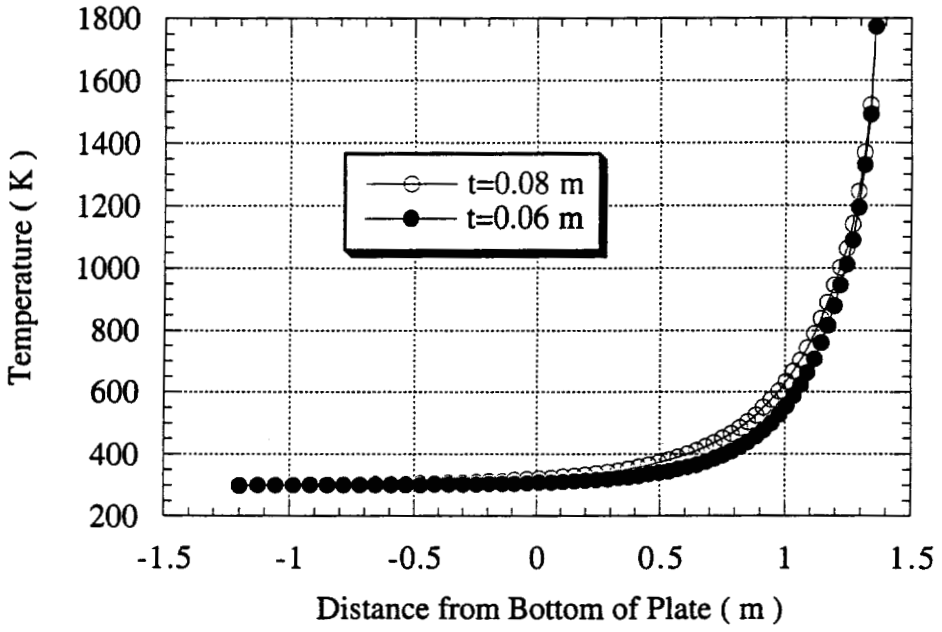

Figure 7-27 (a) Temperature as a Function of Distance from Plate Bottom along WCL on Middle Plane with Different Plate Thickness

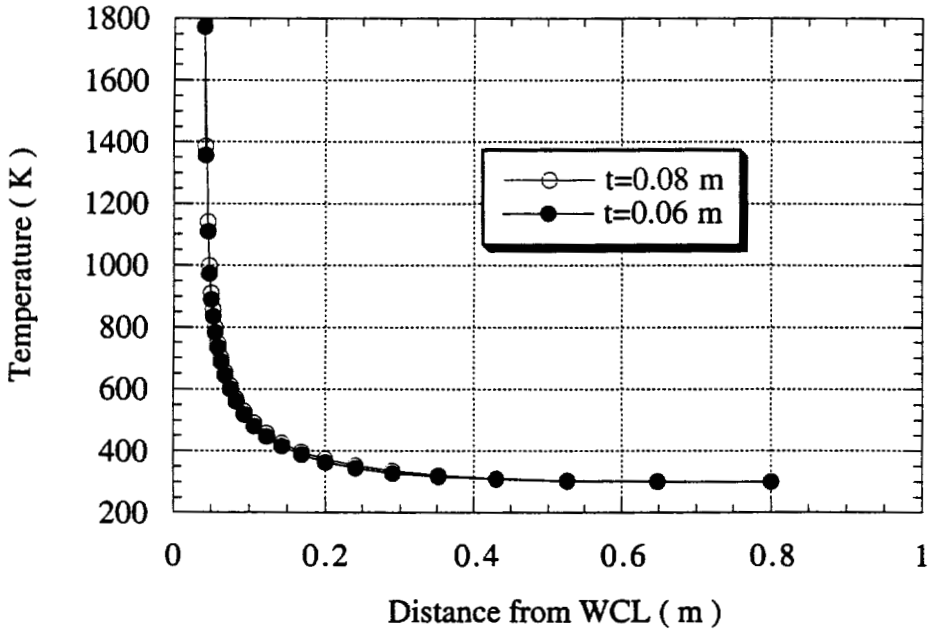

Figure 7-27 (b) Temperature as a Function of Distance from WCL along Perpendicular to WCL Direction on Middle Plane with Different Plate Thickness

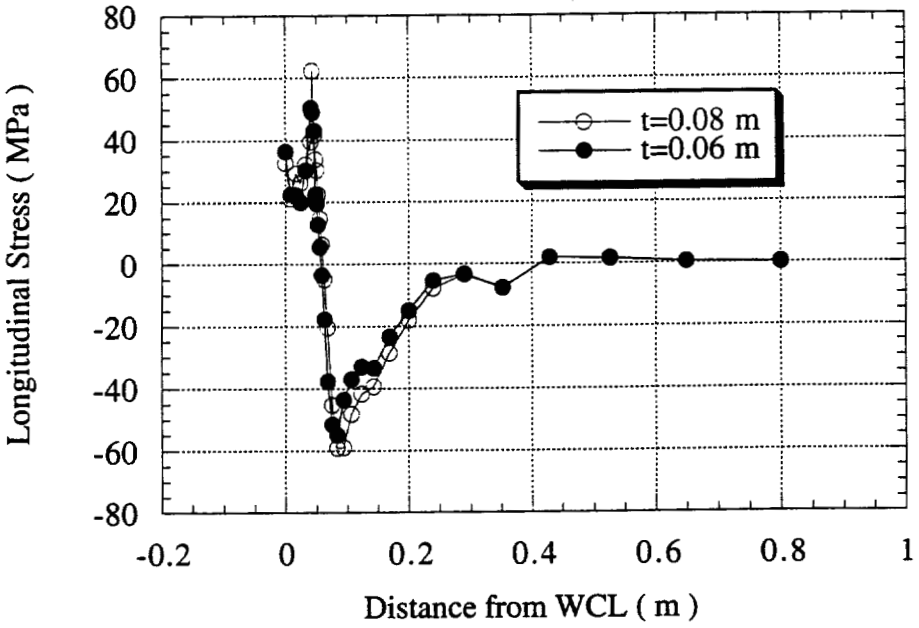

Figure 7-28 (a) Longitudinal Stress as a Function of Distance from WCL on Middle Plane with Different Plate Thickness

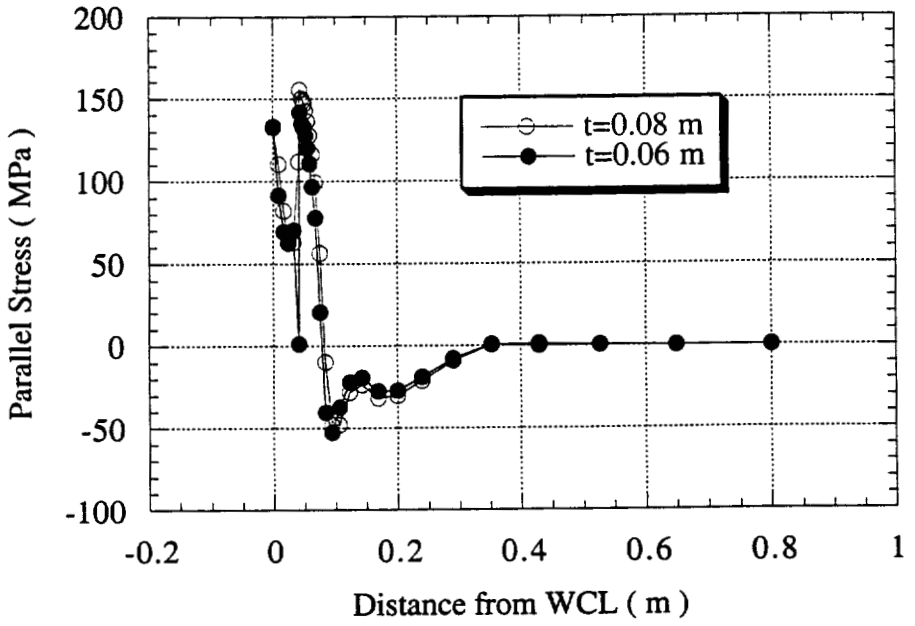

Figure 7-28 (b) Parallel Stress as a Function of Distance from WCL on Middle Plane with Different Plate Thickness

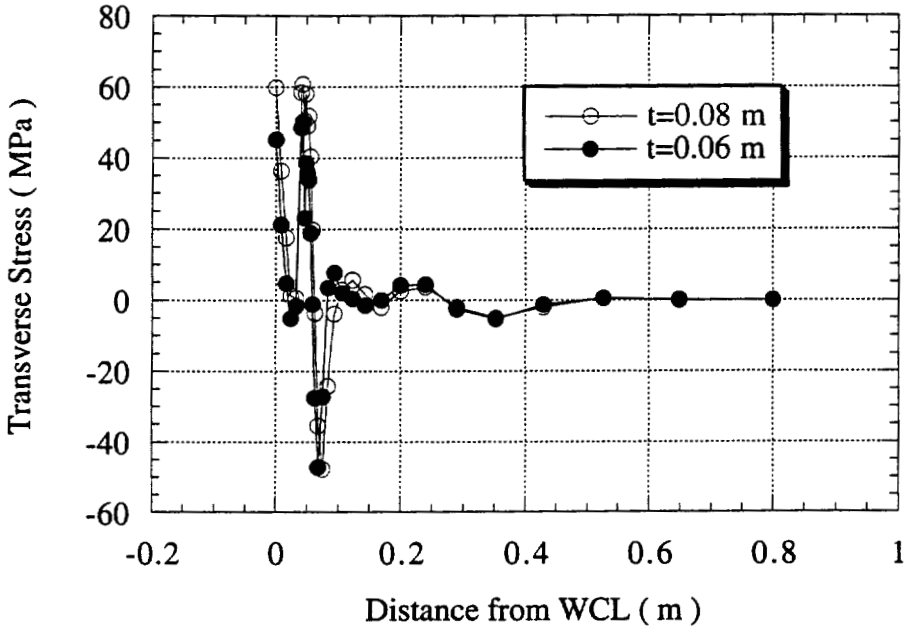

Figure 7-28 (c) Transverse Stress as a Function of Distance from WCL on Middle Plane with Different Plate Thickness

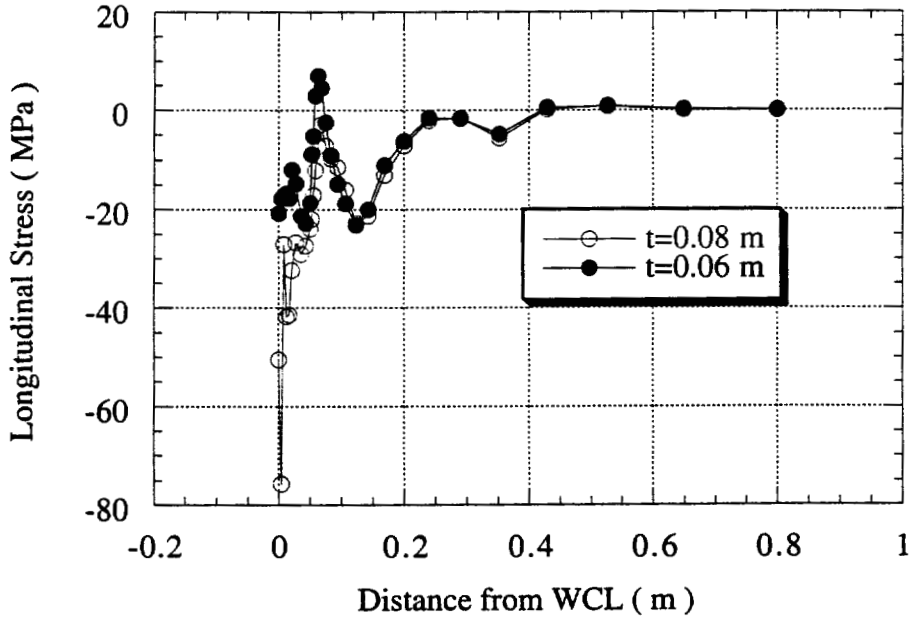

Figure 7-29 (a) Longitudinal Stress as a Function of Distance from WCL on Plate Surface with Different Plate Thickness

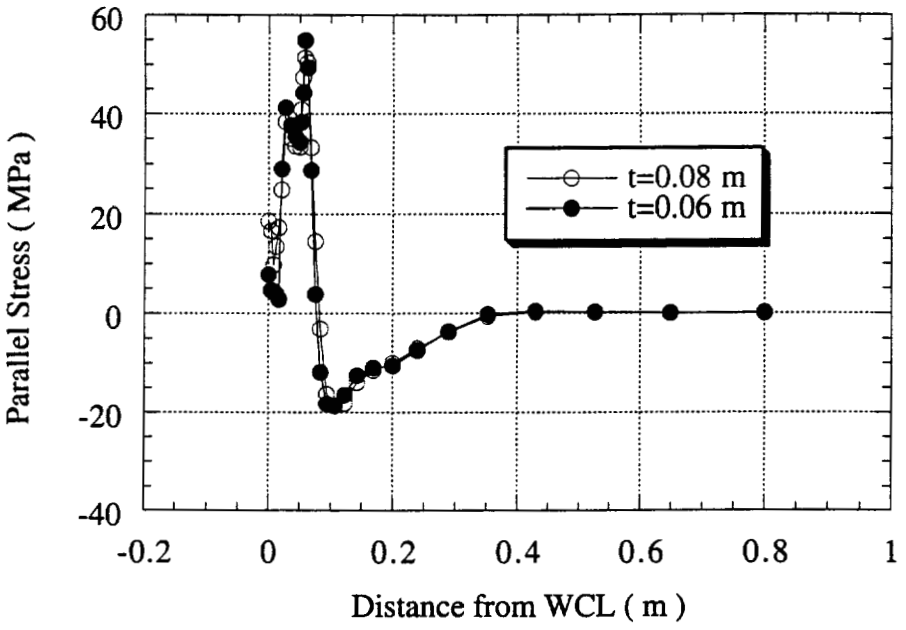

Figure 7-29 (b) Parallel Stress as a Function of Distance from WCL on Plate Surface with Different Plate Thickness

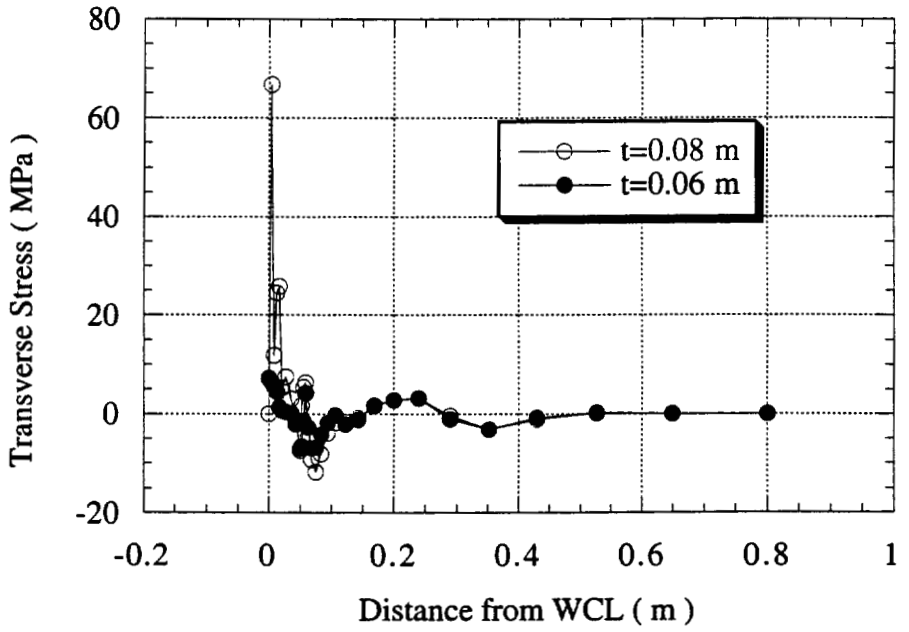

Figure 7-29 (c) Transverse Stress as a Function of Distance from WCL on Plate Surface with Different Plate Thickness

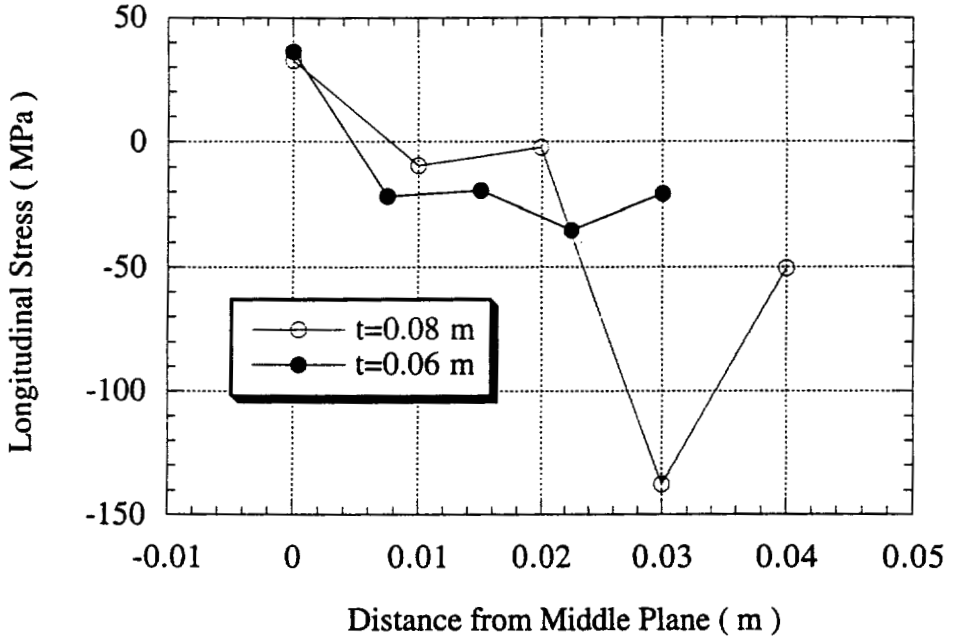

Figure 7-30 (a) Longitudinal Stress as a Function of Distance from Middle Plane through Plate Thickness with Different Plate Thickness

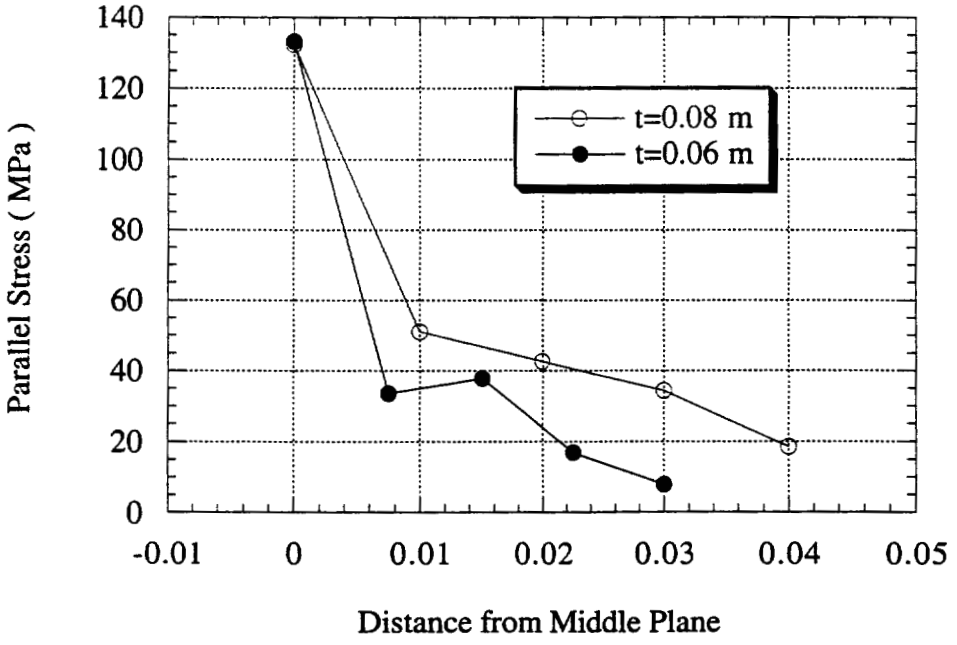

Figure 7-30 (b) Parallel Stress as a Function of Distance from Middle Plane through Plate Thickness with Different Plate Thickness

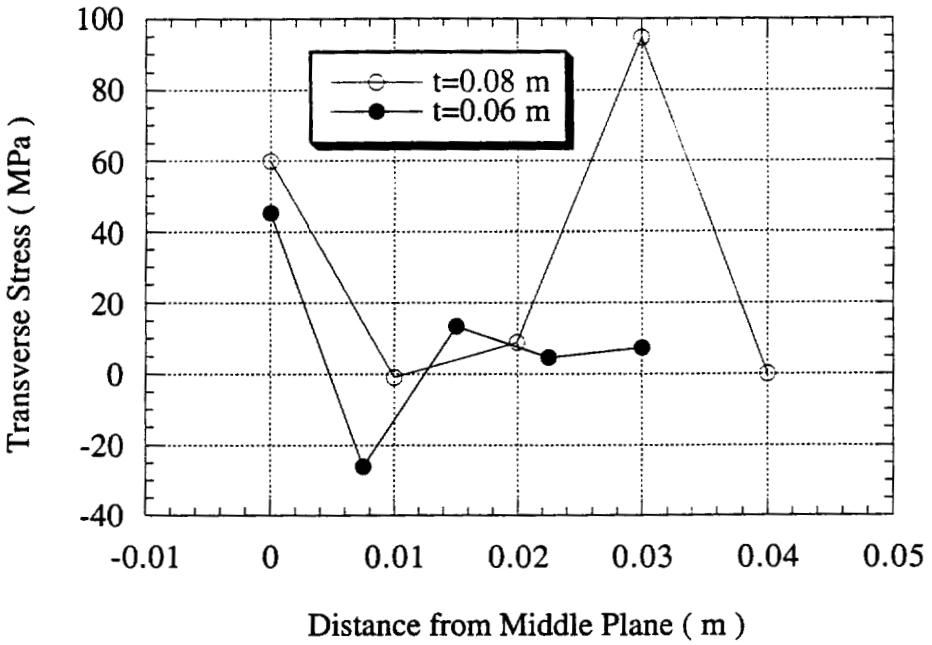

Figure 7-30 (c) Transverse Stress as a Function of Distance from Middle Plane through Plate Thickness with Different Plate Thickness

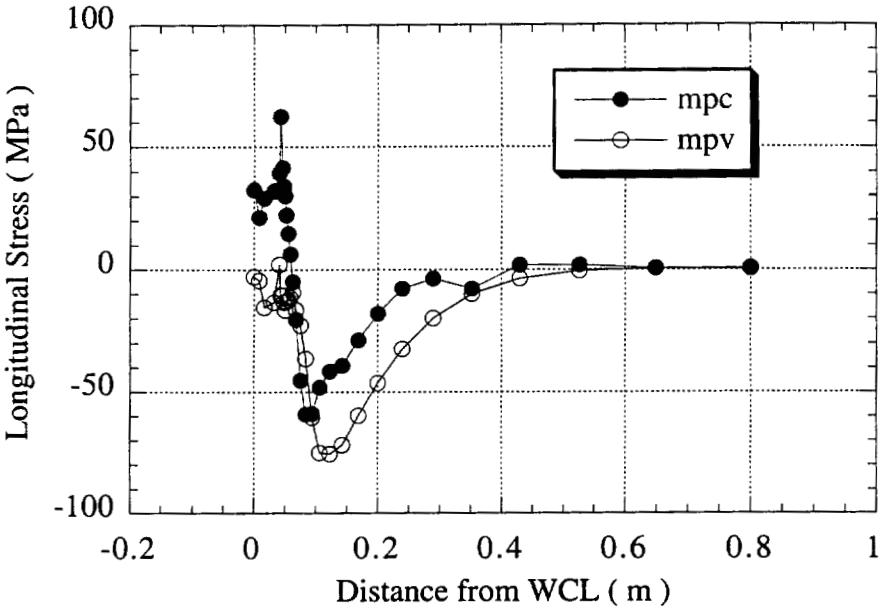

Figure 7-31 (a) Longitudinal Stress as a Function of Distance from WCL on Middle Plane with Different Material Properties

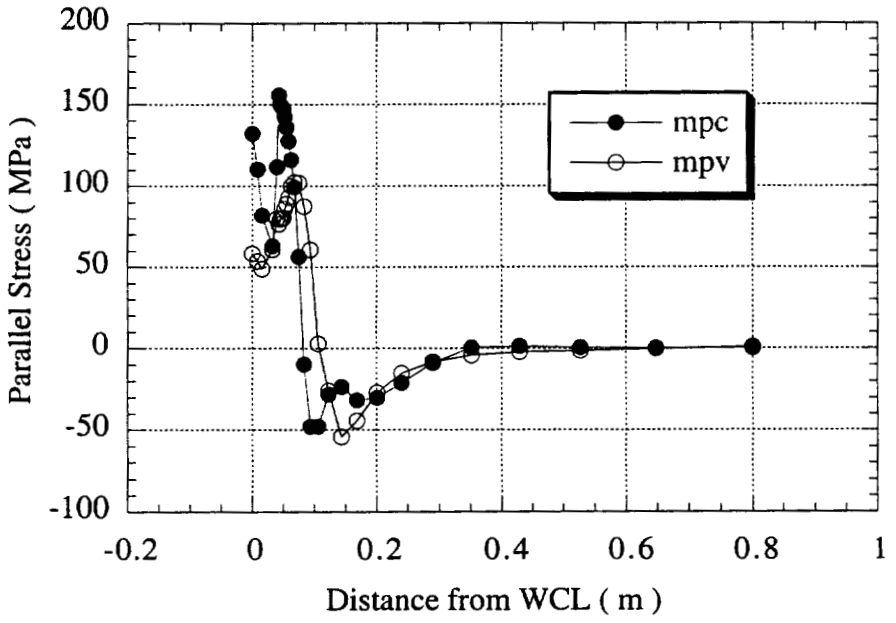

Figure 7-31 (b) Parallel Stress as a Function of Distance from WCL on Middle Plane with Different Material Properties

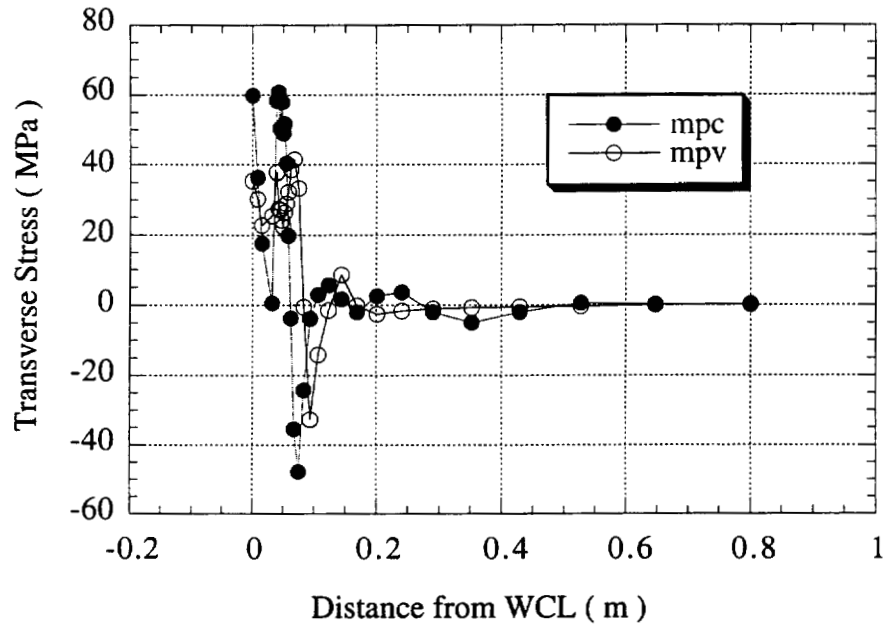

Figure 7-31 (c) Transverse Stress as a Function of Distance from WCL on Middle Plane with Different Material Properties

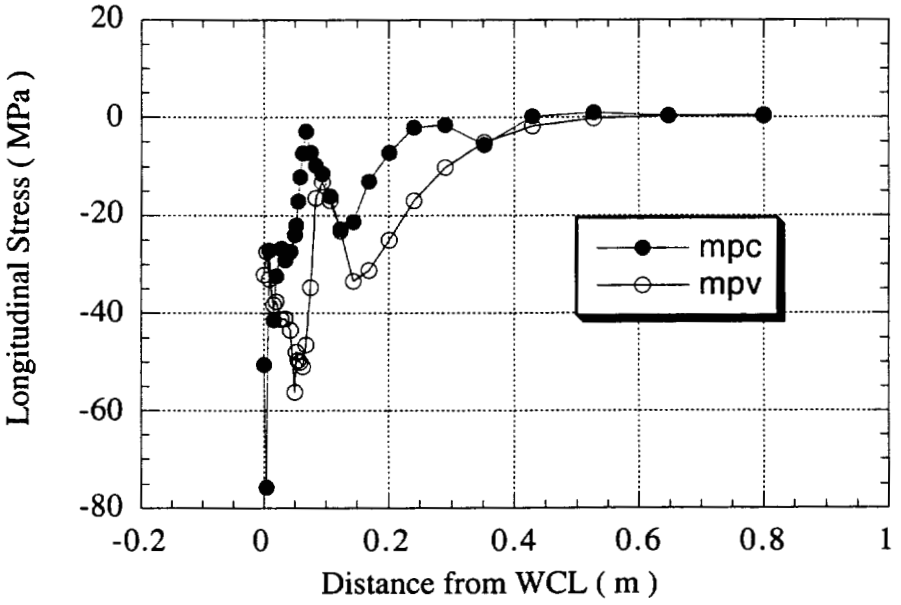

Figure 7-32 (a) Longitudinal Stress as a Function of Distance from WCL on Plate Surface with Different Material Properties

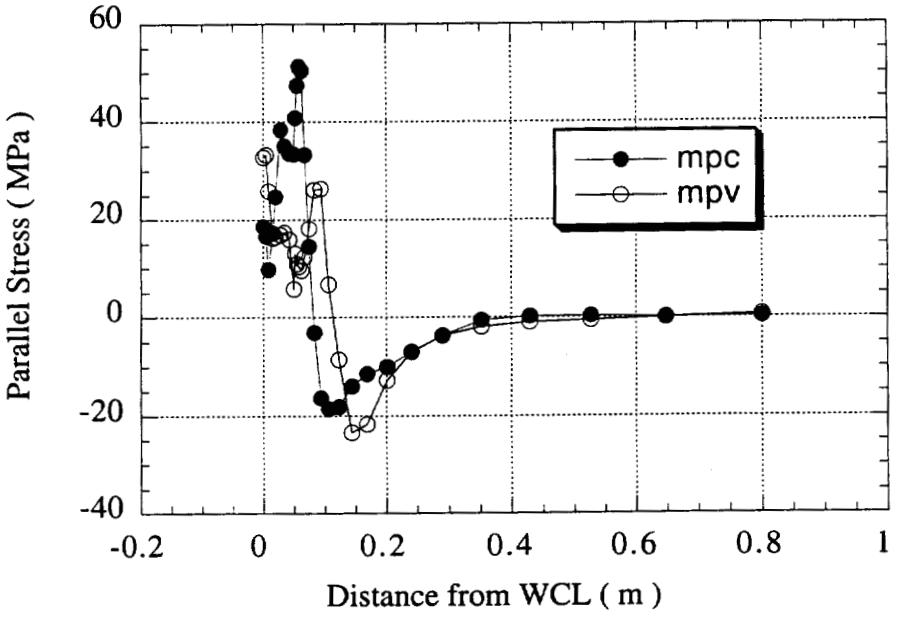

Figure 7-32 (b) Parallel Stress as a Function of Distance from WCL on Plate Surface with Different Material Properties

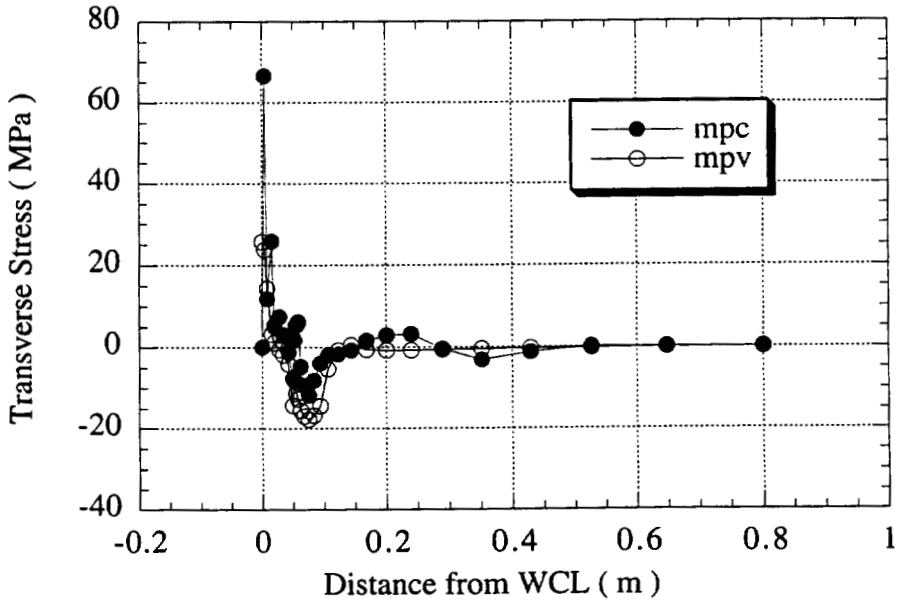

Figure 7-32 (c) Transverse Stress as a Function of Distance from WCL on Plate Surface with Different Material Properties

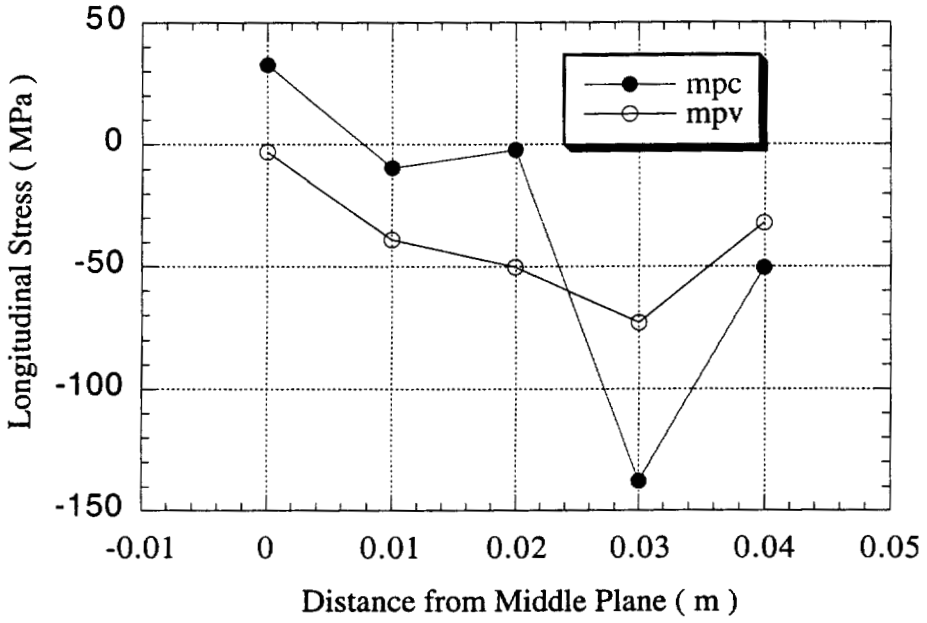

Figure 7-33 (a) Longitudinal Stress as a Function of Distance from Middle Plane through Plate Thickness with Different Material Properties

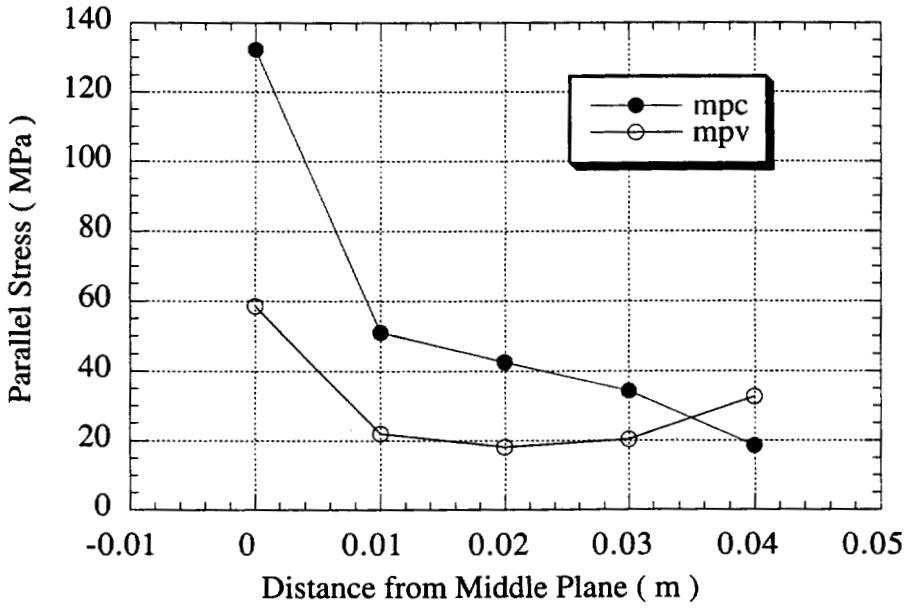

Figure 7-33 (b) Parallel Stress as a Function of Distance from Middle Plane through Plate Thickness with Different Material Properties

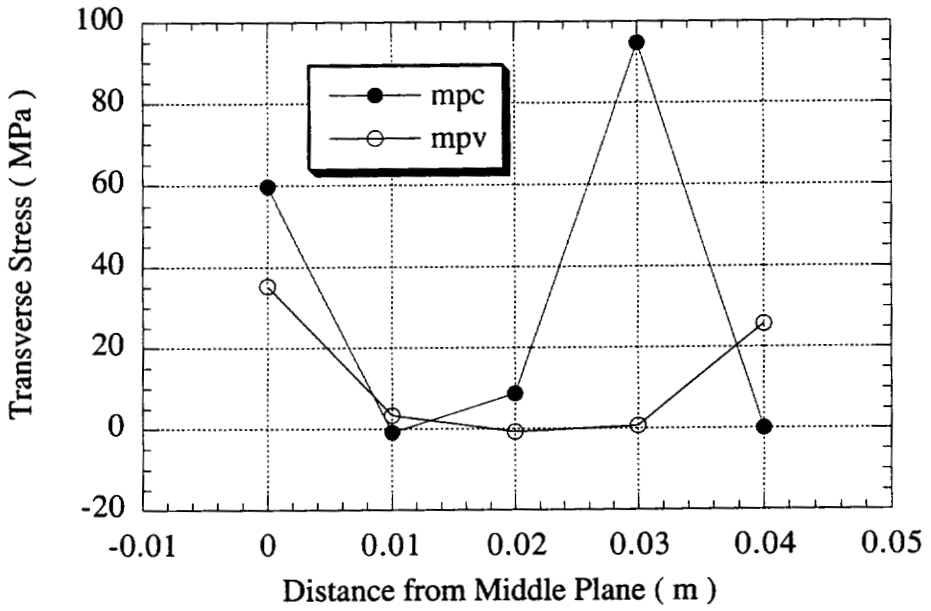

Figure 7-33 (c) Transverse Stress as a Function of Distance from Middle Plane through Plate Thickness with Different Material Properties

CHAPTER 8 SUMMARY

8.1 EXPERIMENTAL RESULTS

According to reference [166], the stress relief for A36 is at the temperature of about 650^{0}C and above. From Figure 7-19 (b), it can be seen that when the distance from WCL reaches 0.06 m, the temperature drops to 650^{0}C. For WCL core, the surface of the core, i.e., plate surface has the narrowest fusion zone with width about 0.02 m. The core dimension is about 0.0889 m. So the HAZ plus base metal on WCL core surface is (0.0889m-0.02m)/2=0.034 m. 0.034 m is less than 0.06 m, i.e., rolling stress of WCL cores was totally relieved during ESW welding process. As for HAZ cores, they ranged from 0.013 m to 0.103 m with center at about 0.06 m from WCL. That is to say, the rolling stress of HAZ cores was totally relieved during ESW welding process.

When the cores were drilled from the bridge, the rolling stress, dead load of the bridge and partial welding thermal stress were relieved. During core sectioning process, the rest of the welding thermal stress is relieved step by step, i.e., the releived stress during core sectioning is welding thermal stress.

United States Steel Corporation reported residual stress measurement results in 1979.[4] The following techniques were used to determine the through thickness residual stresses in a few weldments:

1) Obtaining slices from the weldment and measuring the residual curvature as material was removed from one surface of the weldment.
2) Obtaining slices from the weldment, placing strain gages at various locations on the surface through the thickness of the weldment, and relieving the residual stresses at these locations by splitting the slice parallel to the weldment surface.

3) Measuring the residual stresses by removal of the material around a hole drilled through the weld and instrumented with strain gages on the walls of the hole.

It should be noticed that in their report the strain which is normal to the weld axis is named as transverse strain and the strain which is parallel to the weld axis is named as longitudinal strain. Relieved tension strain indicates compressive residual stress. The measurement results are summarized as following:

1) Residual through-thickness strains normal to plate surface were measured in a 4-in-thick weldment. This showed that the residual through thickness stresses were compressive with a magnitude less than the magnitude of strain at the uniaxial yield stress.

2) The center thickness portions of the weldments contained residual tensile transverse strains and compressive longitudinal strains. The compressive residual strain was at the yield stress.

The measured residual stress along perpendicular to welding direction in this study were consistent with the results reported by the United States Steel Corporation. As for the measured residual stress along parallel to welding direction, the results of this study are not fully consistent with the results reported by the United States Steel Corporation. This may be caused by the different operation parameters used during welding process, non-traditional residual strain measurement techniques used in both sutdies, dramatically different plate lengths used in the two studies, fusion zone weld repairs on the weldment in this study and strain gage position. In general, the experimental results reported herein were consistent with the results reported by the United States Steel Corporation.

8.2 NUMERICAL SIMULATION RESULTS

The 2D and the 3D numerical simulation results demonstrate both consistency and difference. Such behavior is expected because the 2D results are a simplification of a complex 3D problem. In this chapter, only stresses parallel to and perpendicular to WCL are studied for the mid-plane 2D model, cross-sectional 2D model and 3D model. The general observation of both longitudinal stress and parallel stress reveals that all of the

stresses exhibit stress oscillations in the fusion zone/HAZ region. They all start at a given value and decrease at places away from WCL. At some distance, they reach a minimum value and then increase again. After that, they reach their highest value in the HAZ region and begin decreasing again with increasing distance from WCL. The comparison of the three type stresses is listed as following.

MIDDLE PLANE RESULTS AFTER HAZ

Mid-plane Model versus 3D Model

The 2D mid-plane model has tensile yield stress (220/250) at HAZ and then decreases to zero at about 0.2 m from WCL. The 3D model middle plane results has one fifth tensile yield stress at HAZ, then the stress goes to compressive stress (80/250) and finally reaches zero at about 0.45 m from WCL. The maximum tensile longitudinal stress is about five times greater for the 2D mid-plane model than that for the 3D model on middle plane. The difference between the zero stress point for the 2D model and the 3D model is about a factor of two. Therefore, one needs 3D model for ESW middle plane longitudinal stress analysis.

The parallel stress for the 2D mid-plane model starts at 425/250 of tensile yield stress, goes to 80/250 compressive stress at 0.15 m from WCL and then goes to zero at about 0.4 m from WCL. Similarly, the parallel stress for the 3D model starts at 150/250 of tensile yield stress, goes to 75/250 of compressive yield stress at 0.1 m and then goes to zero at about 0.4 m from WCL. Both models demonstrate that the stress changes in similar way and changes take place at about the same distance from WCL with almost the same minimum compressive stress.

The maximum tensile parallel stress is about a factor of three greater for 2D mid-plane model than that for the 3D model on middle plane. Simulation results from the 2D mid-plane model and the 3D model have better agreement for the parallel stress on middle plane of weldment than that for the longitudinal stress.

Cross-sectional Model versus 3D Model

Longitudinal stress for the 2D cross-sectional model has tensile yield stress (225/250) at HAZ and then decreases to zero at about 0.4 m from WCL. Similarly, the longitudinal stress for the 3D model on middle plane has about one fifth tensile yield stress at HAZ, goes to 80/250 compressive stress and then reaches zero at about 0.45 m from WCL. No agreement was found for the longitudinal stress between the 2D cross-sectional model and the 3D model. There is no compressive zone for the 2D cross-sectional model results. Therefore, the 3D model is needed for ESW mid-plane longitudinal stress analysis.

Parallel stress for the 2D cross-sectional model starts at 270/250 of tensile yield stress, goes to 80/250 of compressive yield stress at about 0.08 m from WCL and then goes to zero at about 0.1 m from WCL. The parallel stress changes in similar way as that in the 2D mid-plane model. Comparing with the 2D mid-plane model, the maximum tensile stress is lower for 2D cross-sectional model (270 versus 425). The minimum compressive parallel stress is about the same for two 2D models. However, the 2D cross-sectional model takes about one fourth length of cycle to reach zero compared with the 2D mid-plane model.

Parallel stress for the 2D cross-sectional model has the same trend as 3D model. The maximum tensile parallel stress for the 2D cross-sectional model is higher than that for the 3D model (270 versus 150). The minimum compressive parallel stress is about the same for both the 2D cross-sectional models and the 3D model. Simulation results from the 2D cross-sectional model and the 3D model have better agreement for the parallel stress on middle plane of weldment than that for the longitudinal stress.

WCL THROUGH THICKNESS RESULTS

Longitudinal stress for the 2D cross-sectional model starts at high tensile stress (280/250), drops to zero stress and then increases to very high tensile stress at plate surface (420/250). For the 3D model, longitudinal stress starts at low tensile stress

(45/250) and then decreases to medium compressive stress (-125/250) at plate surface.

Parallel stress for the 2D model starts at middle tension stress (110/250), decreases to middle compression stress (-80/250) and then increases to tensile stress at plate surface (20/250). For the 3D model, parallel stress starts at middle tensile stress (110/250), decreases to zero and then increases to low tensile stress at plate surface (20/250). The results show that the trend is inconsistent for the longitudinal stress for both the 2D and the 3D models while the parallel stress is more comparable. Unlike the 3D model, the parallel stress for the 2D model reveals compressive stress. Therefore, the 3D model is needed to simulate the correct trends and to obtain acceptable stress magnitudes of ESW weldments.

Both longitudinal stress and parallel stress starts at high stress, decreases and then changes their slop to end up at a high stress at surface for the 2D cross-sectional model while the longitudinal stress and the parallel stress for the 3D model stress starts at high value and continuously decreases until they reach the plate surface.

Comparison of longitudinal and parallel stresses reveal that the longitudinal stress is bigger than the parallel stress for the 2D model while the reverse is true for the 3D model parallel stress.

8.3 EXPERIMENTAL RESULTS VERSUS MODELING RESULTS

The residual stress at the plate surface near fusion zone for 3D model are compared with the WCL and HAZ coring and coring-plus-sectioning experimental results after subtraction of the expected bridge load of -15 ksi in the direction perpendicular to the welding direction in Table 4-26 and Table 4-27.

Experimental results reveal that the longitudinal stress is very low and change from tension stress to compression stress as the distance from WCL increasing to near HAZ. From Table 4-26 and Table 4-27, it can be seen that the compressive stress is about three times bigger than tension stress. The major stress state around fusion zone/HAZ is in compressive stress range. Modeling results reveal that the longitudinal stress is in low compressive stress range in and around the fusion/HAZ zone. From

Figure 7-32 (a), the very low tension longitudinal stress also existed in modeling results. Thus both experimental results and modeling results reveal that low compressive longitudinal stress around fusion zone/HAZ is to be expected.

Experimental results reveal that the parallel stress is in tension stress range and change from around material yield stress to around half yield stress as the distance from WCL increasing to near HAZ. The modeling reveal low level tensile parallel residual stresses in and around the fusion/HAZ zones in the direction parallel to the welding direction. The experimental results predicted much higher stress magnitude than modeling results. However, both of the results reveal tension parallel stress around fusion/HAZ zones. The stress magnitude difference may come from the repair weld on the experimental cores. As for the exact effect of the weld repairs, further studies are needed.

Both experimental results and modeling results reveal that the stress gradient is much greater round fusion/HAZ and the stress decreases with the increasing distance from WCL.

In general, both experimental results and modeling results are consistent.

8.4 FUTURE WORK

ES weldments differ substantially from structural arc-welded butt joints in that they are done in one pass and at very high heat input. These differences are expected to have a major effect on the resultant residual stress pattern which in turn could affect the fatigue performance and propensity to cracking. This part of study is very useful to direct the future application of ESW welding process. At the same time, the residual stress evaluation on ESW weldments were initiated on existing structure in this study. The general conclusions of this study are summarized in next section.

In order to fully understand the residual stress, work should be done on "ideal" "new" ESW welds made specifically for these study or use data from bridge welds or both. At the same time, the following future works are needed:

1) Work completed for this dissertation centered on experimental and numerical

evaluation of temperature fields and residual stresses associated with the ESW. The effect of microstructure evolution has potential influence on the residual stress fields. This needs to be explored in the future. The SYSWELD code system has a metallurgical analysis module which could be used in this future study.

2) The core drilling process can be simulated using SYSWELD program. With this model, both thermal and mechanical analysis would be carried out in the same way as that in this present study. After that, applying the zero gravity to all modeled material except the "cores" one could see the predicted stress change on the cores. The cores could then be subsequently "sliced" for further comparison of residual stress experimental measurements.

3) Pre-heating and fusion line repair weld were observed to be variable on the bridge welds. Thus an experimental and/or modeling assessment of the relevance of these bridge-specific results would require the assessment of a base ES weldment with multiple repair welds, and preheat conditions superimposed on the base ESW residual stress field.

8.5 CONCLUSIONS

1) Compressive residual stresses in and around the fusion/HAZ zones in the direction perpendicular to the welding direction was predicted in ESW weldments.

2) Tensile residual stresses in and around the fusion/HAZ zones in the direction parallel to the welding direction was predicted in ESW weldments.

3) The fusion zone analysis indicated nominally symmetrical fusion zones with various weld fabrication perturbations superimposed on the generic welding parameters.

4). Enchant studies reveal that all but one of the weld core surfaces had fusion line/zone cosmetic repair welds made the complete length of the ESW weld.

5) Coring and slicing residual stress results yielded a wide range of measured residual stresses.

6) The coring and slicing results varied from highly compressive to highly tension

covering the residual stress range predicated from the ESW 3D model as well and the results expected from a multi-pass weld.

7) The effect of welding speed on residual stress distribution of the ESW weldments is mainly on residual stress distribution on middle plane of ESW weldments.

8) The effect of plate thickness on residual stress distribution of the ESW weldments is mainly on residual stress distribution on plate surface.

9) The effect of material properties on residual stress distribution of the ESW weldments is mainly on the residual stress value not on the residual stress distribution trend.

10) 3D modeling is needed to analyze the residual stress inside ESW weldments.

REFERENCES

1. B.E. Paton, **Electroslag Welding**, New York, American Welding Society, 1962.

2. W.P. Beater, Jr., P.J. Konkol, B.M. Kapadia, A.K. Shoemaker, and J.K. Sovak, **Acceptance Criteria for Electroslag Weldments in Bridges**, Phase I. Final Report, U.S. Steel Corporation, Monroeville, PA, April 1977.

3. J. D. Harrison, "Metal Construction Bridge", **Welding Journal**, 48(8), 1969, pp. 366-371.

4. Ann, Hee-Sung, **Solidification study and improved structural integrity of electroslag welds**, Ph.D. Dissertation, Oregon Graduate Institute of Science and Technology, Portland, Oregon, 1987

5. S. Venkataraman, **Effects of Process Variables and Microstructures on Properties of Electroslag Weldments**, Ph.D. Dissertation, Oregon Graduate Institute of Science and Technology, Portland, Oregon, 1981.

6. A.W. Pense, J.D. Wood, J.W. Fisher, "Recent Experiences with Electroslag Welded Bridges", **Welding Journal**, 58(12), 1978, pp. 33-42.

7. K. Masubuchi, **Analysis of Welded Structure**, New York, NY, Pergamon Press, 1981.

8. H. Wohlfahrt, "Residual Stresses due to Welding, Their Origin, Calculation and Evaluation", **Residual Stresses**, edited by E. Macherauch, V. Alle Rechte Vorbehalten Hauk., Germany, DGM Informationsgesellschaft mbH, 1986, pp. 81-112.

9. **Metals Handbook: Welding, Brazing, and Solding, vol. 6**, Ed. 10, Materials Park, Ohio, ASM International, 1992.

10. S. Vaidyanathan, A.F. Todar, and I. Finn, "Residual Stresses due to Circumferential Welds", ASME, **Journal of Engineering Materials and Technology**, Oct. 1973, pp. 233-237.

11. Koichi Masubuchi, "Models of Stresses and Deformation due to Welding-A

Review", **Modeling of Casting and Welding Processes**, Proceedings of a Symposium Sponsored by the Solidification Committee of the Metallurgical Society of AIME, 1980, edited by Harold D. Brody and Diran, pp. 223-229

12. L. Tall, "Residual Stresses in Welded Plates-A Theoretical Study", **Welding Journal Research Supplement**, 43(1), 1964, pp. 105-235.

13. K. Masubuchi, B. Simmons, and R.E. Monre, **Analysis of Thermal Stresses and Metal Movement During Welding**, RSIC-820, Redstone Scientific Information Center, Redstone Arsenal, Alabama, July, 1968.

14. D. G. Atteridge, S. Venkataraman, and W.E. Wood, **Improving the Reliability and Integrity of Consumable Guide Electroslag Weldments in Bridge Structures**, Final Report, Federal Highway Administration, U.S. Department of Transportation, December 1982.

15. D.G. Atteridge, S. Venkataraman, and W.E. Wood, **Improving the Reliability and Integrity of Consumable Guide Electroslag Weldments in Bridge Structures**, Executive Summary Report, Federal Highway Administration, U.S. Department of Transportation, December 1982.

16. D.G. Atteridge, W.E. Anderson et al, Department of Energy, Westinghouse Savannah River Company, Aiken, SC, **Weld Residual Stress Measurement/Mitigation,** Annual Progress Report Oct. 1, 1991 through Sept. 30, 1992, Subcontract No. AA46386, report No. 17, July 1993.

17. D.G. Atteridge, J.H. Devletian, and W.E. Wood, **Heat-Affected Zone Toughness of Electroslag Weldments,** Office of Advanced Research, Federal Highway Administration, U.S. Department of Transportation, Grant No. DTFH61-86-X-00119, March 1994.

18. R. Turpin, D.G. Atteridge, J.H. Devletian, and W.E. Wood, **Repair of Process-Related Defects in Electroslag Weldments, Office of Advanced Research**, Federal Highway Administration, U.S. Department of Transportation, Grant No. DTFH61-86-X-00119, March 1994.

19. D.G. Atteridge, R.E. Page, V. Srivathsan and W. Wood, "Effect of Mechanical Vibration on Electroslag Weldment Fusion Zone Structure", **the 61st Annual American Welding Society Meeting**, Los Angles, CA, April 1980, pp. 63-67

20. S. Venkataraman, W.E. Wood, D.G. Atteridge, and J.H. Devletian, "Influence of Alloy Additions on the Toughness of Electroslag Weld Metal", **the ASM Metals Congress**, Cincinnati, OH, September 21-23, 1981, pp. 78-84

21. S. Venkataraman, W.E. Wood, D.G.Atteridge, and J.H. Devletian, "A New Method for Grain Refinement in Electroslag Welds", **the ASM Conference, Trends in Welding Research in the United States**, New Orleans, LA, November 16-18, 1981, pp. 124-128

22. J.H. Devletian, P.Wang, W.E. Wood, and D.G. Atteridge, "Toughness and Structure Changes in ES Welds Induced by SA Overwelding", **the Annual American Welding Society Meeting**, Kansas City, MO, April 26-29, 1982, pp. 67-71

23. S. Venkataraman, W.E. Wood, and D.G. Atteridge, "Influence of Process Variables on Microstructures and Mechanical Properties of Electroslag Welds", **the 63rd Annual American Welding Society Meeting**, Kansas City, MO, April 26-29, 1982, pp. 187-192

24. S. Venkataraman, W.E. Wood, D.G.Atteridge,and J.H. Devletian, "Influence of Alloy Additions on the Toughness of Electroslag Weld Metal", **the 63rd Annual American Welding Society Meeting**, Kansas City, MO, April 26-29, 1982, pp. 136-141

25. S. Venkataraman, J.H. Devletian, W.E. Wood, and D.G.Atteridge, "Grain Refinement Dependence on Solidification and Solid State Reaction in Electroslag Welds", **the TMS/AIME Fall Meeting**, St. Louis, MO, October 25-26, 1982, pp. 56-61

26. W.E. Wood, D.G. Atteridge, and W.E. Anderson, "Acoustic Emission Characterization of Defects in Electroslag Weldments", **the International Conference on Trends in Welding Research**, Gatlinburg, TN, May 1986, pp. 142-148

27. D.G. Atteridge and W.E. Anderson, "Cyclic Work Hardening Induced in the Heat-Affected Zone During Multi-Pass Welding", **the Third International Conference on Welding and Performance of Pipelines**, London, England, November 1986, pp.112-116

28. K. Khan, J. Albers, D. Atteridge, L. Meekisho, and D. Danks, "An Experimental Study of Residual Stresses in Mechanical Components", the **1992 SEM Congress**, Las Vegas, Nevada, June 8-11, 1992, pp. 91-96

29. D.G. Atteridge, J. Devletian, R. Turpin, and W.E. Wood, "Electroslag Welding of Thick Section Steel Plates", **Materials Week**, 17(10), pp. 33-37

30. H. Q. Zhao, Y.P. Gao, J. M. McCarthy, J. H. Devletian and W.E. Wood, "Microstructure Study of Ni Alloy 625 Cladding over Carbon Steel",

International Trends in Welding Science and Technology, edited by S. A.. David and J.M. Vitek, ASM International, June 1992, pp. 339-343

31. Y.P. Gao, J. H. Devletian and W.E. Wood, "Electroslag and Submerged Arc Cladding with Nickel Alloy Strip", **International Trends in Welding Science and Technology**, edited by S. A.. David and J.M. Vitek, ASM International, June 1992, pp. 449-453

32. M.R. Scholl, W.E. Wood, and D.G. Atteridge, "Acoustic Emission Characterization of Defects in Electroslag Weldments", the **29th International Instrumentation Symposium Proceedings,** Las Vegas, Nevada, May 1982, pp. 312-316

33. M. Li, D.G. Atteridge, L.L. Meekisho and V.A. Dikshit, "Finite Element Analysis of Multipass Electroslag Cladding Welds", the **74th Annual AWS Convention**, Houston, TX, April 27-30, 1993, pp. 216-221

34. M. Li, D.G. Atteridge, V.A. Dikshit and L.L. Meekisho, "Finite Element Analysis of Electroslag Cladding", **International Conference on Modeling and Control of Joining Processes**, Orlando, FL, December 8-10, 1993, pp. 53-57

35. M. Li, D.G. Atteridge, and L.L. Meekisho, "Mathematical Modeling of Microstructure Evolution in Heat Effected Zone of Electroslag Cladding", **International Conference on Trends in Welding Research**, Gatlinburg, TN, June 1995, pp. 96-101

36. C.O. Rudd, J.A. Josef, D.J. Snoha, "Residual Stress Characterization of Thick Plate Weldments Using X-ray Diffraction", **Welding Journal**, 57(3), 1978, pp. 87s-91s.

37. C.O. Rudd, P.S. Dimascio, "A prediction of Residual Stress in Heavy Plate Butt Welds", **Journal of Materials for Energy Systems**, 52(3), 1978, pp. 62-65.

38. M. Hetenyi, **Handbook of Experimental Stress Analysis**, New York, NY, John Wiley & Sons, 1950.

39. R.C. Dove and P.H. Adams, **Experimental Stress Analysis and Motion Measurement**, Columbus, Ohio, Charles E. Merrill Books, Inc., 1964.

40. A.W. Hendry, **Elements of Experimental Stress Analysis,** Oxford, UK, Pergamon Press, 1977.

41. J.W. Dally and W.F. Riley, **Experimental Stress Analysis**, Ed. 2, New York, NY, McGraw-Hill, Inc., 1978.

42. R.S. Sirohi and H.C. Randha Krishna, **Mechanical Measurements**, Ed. 2, New Delhi, India, John Wiley & Sons, 1991.

43. H. Kockelmann, "Mechanical Methods of Determining Residual Stresses", **Residual Stress, Measurement, Calculation, Evaluation**, edited by V. Hauk, H. Hougardy and E. Germany Macherauch, DGM Informationsgesellschaft mbh, 1991, pp. 37-52.

44. S. Keil, "Methods of Determining Residual Stresses in Metal Parts using Strain Gauges", **Residual Stresses, Measurement, Calculation, Evaluation**, edited by V. Hauk, H. Hougardy and E. Germany Macherauch, DGM Informationsgesellschaft mbh, 1991, pp. 53-58.

45. C.C. Perry and H.R. Lissner, **The Strain Gauge Primer**, Ed. 2, New York, NY, McGraw-Hill Book Company, 1962.

46. D. Rosenthal and J.T. Norton, "A Method of Measuring Triaxial Residual Stress in Plates", **Welding Journal**, 24(5), 1945, pp. 295s-307s.

47. D.A. Ferrill, P.B. Juhl and D.R. Miller, "Measurement of Residual Stresses in a Heavy Weldment", **Welding Journal**, 45(11), 1966, p. 504s.

48. A.J. Bush and F.J. Kromer, **Internal Residual Stress Measurements in a Thick Weldment**, Westinghouse Research Laboratories Scientific Paper 73-1P6-APMEC-P2, 1974.

49. V.A. Vinokurov and A.S. Gazaryan, "Residual Stresses in Thick Butt Welded Joints", **Welding Production**, 8(2), 1961, pp. 16-22.

50. R.G. Treuting and W.F. Jr. Reed, "A Mechanical Determination of Biaxial Residual Stresses in Sheet Materials", **Journal of Applied Physics**, 22(2), 1951, pp. 130-134.

51. J. Mathar, "Determination of Initial Stresses by Measuring the Deformations Around Drilled Holes", **Transactions of ASME,** 56(4), 1934, pp. 249-254.

52. N.J. Rendler and I. Vigness, "Hole-Drilling Strain-Gage Method of Measuring Residual Stress", **Experimental Mechanics**, 6(12), 1966, pp. 577-586.

53. H. Wolf and D.L. Sauer, "New Experimental Techniques to Determine Residual Stresses in Large Turbine-Generator Compounds", **American Power Conference**, Chicago, May 1, 1974, pp. 46-50

54. A. J. Bush and F. J. Kromer, "Residual Stresses in a Shaft after Weld Repair and

Subsequent Stress Relief", **1979 SESA Spring Meeting**, paper No. A-16.

55. E. F. Rybicki and R. B. Stonisifer, "Computation of Residual Stresses due to Multipass Welds in Piping Systems", **Journal of Pressure Vessel Technology**, 101 (5), 1979, pp. 149-154

56. C. O. Rund and G.D. Farmer, "Residual Stress Measurement by X-Rays, Errors, Limitations and Applications", **Nondestructive Evaluation of Materials**, edited by J.J. Burke and V. Weiss, Ed., Plenum Pub. Corp., 1979.

57. J.T. Norton, "X-Ray Determination of Residual Stress", **Materials Evaluation**, 10(2), 1973, pp. 21A-41A.

58. C.O. Rund, "X-Ray Analysis and Advances in Portable Field Instrumentation", **Journal of Metals**, 31(6), 1979, pp. 10-15.

59. I.C. Noyan and J.B. Cohen, **Residual Stress, Measurement by Diffraction and Interpretation**, New York, Springer-Verlag, 1987.

60. C. A. Peck, "Practical Aspects of Residual Stress Measurement by X-Ray Diffraction", **Residual Stress in Design, Process and Materials Selection**, edited by W.B. Materials Park Young, Ohio, ASM International, 1987, pp. 7-9.

61. V. Hauk, "Problems of the X-Ray Stress Analysis (RSA) and Their Solutions", **Residual Stress, Measurement, Calculation, Evaluation**, edited by V. Hauk, H. Hougardy, and E. Macherauch, E. Germany, DGM Informationsgesellschaft mbh, 1991, pp. 3-20.

62. R.R. Hosbons, E.F. Ibrahim, T.M. Holden and J.H. Root, "The Use of Neutron Diffraction to Determine Non-Destructively and Residual Strain and Texture in Welds", **Recent Trends in Welding Science and Technology**, edited by S.A. David and J.M. Vitek, Materials Park., Ohio, ASM International, 1990, pp. 103-106.

63. A.D. Krawitz and T.M. Holden, "The Measurement of Residual Stresses Using Neutron Diffraction", **MRS Bulletin,** XV, 1990, pp. 57-64.

64. M.T. Hutchings, "Neutron Diffraction Measurement of Residual Stress Fields, Overview and Points for Discussion", **Measurement of Residual and Applied Stress Using Neutron Diffraction,** edited by M.T. Hutchings and A.D. Dordrecht Krawitz, The Netherlands, Kluwer Academic Publishers, 1992, pp. 3-18.

65. P. J. Webster, "Welding Applications of Neutron Strain Scanning", **International**

Trends in Welding Science and Technology, edited by S.A. David and J.M.Vitek, Materials Park Ohio, ASM International, 1993, pp. 95-98.

66. J.H. Root, T.M. Holden, J. SchrÖder, S. Spooner, C.A. Hubbard, T.A. Dodson and S.A. David, "Residual Stresses in a Multipass Ferritic Weldment", **International Trends in Welding Science and Technology**, edited by S.A. David and J.M. Vitek, Materials Park, Ohio, ASM International, 1993, pp. 99-103.

67. S. Spooner, S.A. David, J.H. Root, T.M. Holden, M.A.M. Bourke and J.A. Goldstone, "Residual Stress and Strain Measurements in Austenitic Steel Plate Containing a Multipass Weld", **International Trends in Welding Science and Technology,** edited by S.A. David and J.M. Vitek, Materials Park, Ohio, ASM International, 1993, pp. 139-143.

68. J.H. Root, T.M. Holden, J. SchrÖder, C.R. Hubbard, C.R. Spooner, T.A. Dodson and S.A. David, "Residual Stress Mapping in Multipass Ferrite Steel Weld", **Materials Science and Technology**, 9(9), 1993, pp. 754-759.

69. N.N. Hsu and W. Sachse, "Review of Ultrasonic Techniques for Measuring Residual Stress", the **38th National ASNT Fall Conference**, Denver, Oct. 1978, pp. 67-82

70. J.S. Heyman, "A CW Ultrasonic Bolt-Strain Monitor", **Experimental Mechanics**, 17(5), 1977, p. 183.

71. N.N. Hsu, "Acoustical Birefringence and the Use of Ultrasonic Waves for Experimental Stress Analysis", **Experimental Mechanics,** 14(5), 1974, p. 169.

72. T.J. Jessop, P.J. Mudge, and J.D. Harrison, **Ultrasonic Measurement of Weld Flaw Size**, Transportation Research Board, National Research Council, Washington, D.C., 1981

73. E. Schneider and K. Goebbels, "Nondestructive Evaluation of Residual Stress States Using Ultrasonic Techniques", **Residual Stresses,** edited by E. Macherauch and V. Alle Rechte Vorbehalten Hauk, Germany, DGM Informationsgesellschaft mbh, 1986, pp. 247-261.

74. M.R. James and O. Buck, "Quantitative Nondestructive Measurement of Residual Stresses", **CRC Critical Reviews in Solid State Sciences**, Aug. 1980, pp. 16-20

75. B.D. Cullity, "Magnetic Methods", **Proceedings of a Workshop on Nondestructive Evaluation of Residual Stress**, NTIAC-76-2, 1975, pp. 35-39

76. M. Suzuki, I. Komura and H. Takakashi, "Nondestructive Estimation of Residual

Stress in Welded Pressure Vessel Steel by Means of Remanent Magnetization Measurement", **International Journal of Pressure Vessel & Piping**, 12(6), 1978, pp. 121-125

77. N.A. Vicar, A.S. Smirnov, A. Yu. Fadeev, M.M. Shel, V. F. Tokunov, V.A. Gudyoya, "Study of the Magnetoelastic Effect in Rail Steel", **Electro-Magnetic Methods**, 2, 1975, pp. 63-67

78. P.S. Myers, O.A. Uyehara and G.L. Borman, "Fundamentals of Heat Flow in Welding", **Welding Research Council Bulletin**, New York, 123, July 1967, pp. 1-46.

79. D. Rosenthal, "Mathematical Theory of Heat Distribution During Welding and Cutting", **Welding Journal**, 20(5), 1941, pp. 220s-234s.

80. D. Rosenthal, "The Theory of Moving Sources of Heat and Its Application to Metal Treatment", **Transactions of ASME**, 68(11), 1946, pp. 849-865.

81. B.H. Goldenberg, "A Problem in Radial Heat Flow", **British International Applied Physical**, 2, Aug. 1951, pp. 233-237.

82. S. Tanaka, "A Study on Heat Conduction of a Moving Heat Source", **Journal of the Japan Welding Society**, 13(9), 1943, pp. 347-359.

83. T. Naka and K. Masubuchi, "Temperature Distribution of Welded Plates-Part 1", **Journal of the Japan Welding Society**, 16(7), 1947, pp. 281-290.

84. T. Naka and K. Masubuchi, "Temperature Distribution of Welded Plates-Part 2", **Journal of the Japan Welding Society**, 16 (12), 1947, pp. 374-378.

85. K.Masubuchi and T. Kusuda, "Temperature Distribution of Welded Plates", **Journal of the Japan Welding Society**, 22(5), 1953, pp. 14-17.

86. E.F. Nippes, L.L. Merrill and W.F. Savage, "Cooling Rates in Arc Welds in 1/2 in. Plate", **Welding Journal**, 28(11), 1949, pp. 556s-564s.

87. E.F. Nippes, W.F. Savage and R.J. Allio, "Studies of the Weld Heat-Affected Zone of T-1 Steel", **Welding Journal**, 36(12), 1957, pp. 531s-540s.

88. D. Radaj, **Heat Effects of Welding-Temperature Field Residual Stress Distribution**, Springer-Verlag, 1992.

89. R.L. Ule, Y. Joshi and E. B. Sedy, "A New Technique for Three-Dimensional Transient Heat Transfer Computations of Autogenous Arc Welding",

Metallurgical Transactions, 21(B), 1990, pp. 1033-1047.

90. C. Bonacina and G. Comini, "On the Solution of the Nonlinear Heat Conduction Equation by Numerical Method", **International Journal of Heat and Mass Transfer**, 16(1), 1973, pp. 581-589.

91. C. Bonacina, G. Comini, A. Fasano and M. Primicerio, "Numerical Solution of Phase Change Problems", **International Journal of Heat and Mass Transfer**, 16(1), 1973, pp. 1825-1832.

92. O. Westby, **Temperature Distribution in the Work-Piece by Welding**, Ph.D. Dissertation, Department of Metallurgy and Metals Working, The Technical University of Norway, Trondheim, Norway, 1968.

93. V. Pavelic, R. Tanbakuchi, O.A. Uyehara and P.S. Myers, "Experimental and Computed Temperature Histories in Gas Tungsten - Arc Welding of Thin Plates", **Welding Journal**, 48(7), 1969, pp. 295s-305s.

94. Z. Parley and P.D. Hibbert, "Computation of Temperatures in Actual Weld Designs", **Welding Journal**, 54(11), 1975, pp. 385s-392s.

95. Mengnie Li, **Computational Modeling of Heat Transfer and Microstructure Development in the Electroslag Cladding Heat Affected Zone of Low Alloy Steels**, Ph.D. Dissertation, Oregon Graduate Institute of Science and Technology, Jan. 1996.

96. G. Comini, S. Del Guidice, R. W. Lewis and O.C. Zienkiewicz, "Finite Element Solution of Non-Linear Heat Conduction Problems with Special Reference to Phase Change", **International Journal for Numerical Method in Engineering**, 8(1), 1974, pp. 613-624.

97. W. Kohler and J. Pittr, "Calculation of Transient Temperature Fields with Finite Elements in Space and Time Dimension", **International Journal for Numerical Method in Engineering**, 8(1), 1974, pp. 625-631.

98. B.G. Thomas and I.V. Samarasekera and J.K Brimacomber, "Comparison of Numerical Modeling Techniques for Complex, Two-Dimensional, Transient Heat-Conduction Problems", **Metallurgical Transactions**, 15 B(6), 1984, pp. 307-318.

99. J.F. Lancaster, **The Physics of Welding**, Pergamon Press, 1984, pp. 1-293.

100. A.H. Dilawari, J. Szekely, and T.W. Eager, "Electromagnetically and Thermally Driven Flow Phenomena in Electroslag Welding", **Metallurgical Transactions**, 9B(3), 1978, pp. 371-381.

101. A.H. Dilawari, T.W. Eager and J. Szekely, "An Analysis of Heat and Fluid Flow Phenomena in Electroslag Welding", **Welding Journal**, 57(1), 1978, pp. 24s-30s.

102. J.F. Lancaster, "Energy Distribution in Argon-Shielded Welding Arcs", **British Welding Journal**, 1(9), 1954, pp. 412-426.

103. J. Szekely, "The Mathematical Modeling of Arc Welding Operations", **Advances in Welding Science and technology**, edited by S.A David, Materials Park, Ohio, ASM International, 1986, pp. 3-14.

104. Y.H. Wang and S. Kou, "Driving Forces for Convection in Weld Pools", **Advances in Welding Science and technology**, edited by S.A David, Materials Park, Ohio, ASM International, 1986, pp. 65-69.

105. P. Tekriwal and J. Mazumder, "Finite Element Modeling of Arc Welding Processes", **Advances in Welding Science and technology**, edited by S.A Materials Park David, Ohio, ASM International, 1986, pp. 71-80.

106. A. Matsunawa, "Modeling of Heat and Fluid Flow in Arc Welding", **International Trends in Welding Science and Technology**, edited by S.A David, J.M. Vitek, Materials Park, Ohio, ASM International, 1993, pp. 3-16.

107. T. Debroy, "Mass Transfer in Welding", **International Trends in Welding Science and Technology**, edited by S.A David, J.M. Vitek, Materials Park, Ohio, ASM International, 1993, pp. 17-25.

108. S.A. David, T. Debroy and J.M. Vitek, "Phenomenological Modeling of Fusion Welding Processes", **MRS Bulletin,** XIX, 1994, pp. 29-35.

109. W.M. Rohsenow and J.P. Hartnet, **Handbook of Heat Transfer**, McGraw-Hill, 1973.

110. Y.S. Touloukian, Powell, C.Y. Ho and P.G. Klemens, **Thermal Conductivity, Metallic Elements of Alloys**, McGraw-Hill, 1970.

111. The British Iron and Steel Research Association, **Physical Constants of Some Commercial Steels at Elevated Temperatures**, London, Butterworths Scientific Publications, 1953.

112. T. Kasuya and N. Yurioka, "Prediction of Welding Thermal History by a Comprehensive Solution", **Welding Journal**, 72(3), 1993, pp. 107s-115s

113. W. D. Rolphe III and K.J. Bathe, "An Efficient Algorithm for Analysis of Nonlinear Heat Transfer with Phase Changes", **International Journal for**

Numercial Methods in Engineering, 18, 1982, pp. 119-134.

114. D. Blanchard and M. Fremont, "The Stefan Problems, Computing without the Free Boundary", **International Journal for Numercial Methods in Engineering,** 20, 1984, pp. 757-771.

115. K.W. Mahin, A.B. Shapiro and J. Hallquist, "Assessment of Boundary Condition Limitations on the Development of a General Computer Model for Fusion Welding", **Advances in Welding Science and technology**, edited by S.A. David, Materials Park, Ohio, ASM International, 1986, pp. 215-224.

116. K. W. Mahin, W. Winters, T.M. Holden, R.R. Hosbons and S.R. MacEwen, "Prediction and Measurement of Residual Elastic Strain Distributions in Gas Tungsten Arc Welds", **Welding Journal**, 70(2), 1991, pp. 245s-260s

117. R.D. Krieg and D.B. Krieg, "Accuracies of Numerical Solution Methods for the Elastic-Perfectly Plastic Mode l", **Journal of Pressure Vessel Technology**, 11(1), 1977, pp. 510-515.

118. P. Tekriwal and J. Mazumder, "Transient and Residual Strain-Stress Analysis of GMAW", **Journal of Engineering Materials and Technology**, 113(1), 1991, pp. 336-343.

119. C. K. Leung, R. J. Pick and D. H. B. Mok, "Finite Element Modeling of a Single Pass Weld, New York", NY, Welding Research Council, 1990, **Bulletin** 356.

120. P. J. Yoder and R. G. Whirley, "On the Numerical Implementation of elastic-Plastic Models", **Journal of Applied Mechanics**, 51(1), 1984, pp. 1-6.

121. H. Zeigler, "A Modification of Prager's Hardening Rule", **Quarterly of Applied Mathematics**, 17(3), 1959, pp. 55-65.

122. J. Goldak, M.J. Bibby, D. Downey and M. Gu, "Heat and Fluid Flow in Welds", **Advanced Joining Technologies**, edited by T.H. North, London, UK, Chapman and Hall, 1990, pp. 69-82.

123. J. Goldak, "Modeling Thermal Stresses and Distortions in Welds", **Recent Trends in Welding Science and Technology**, edited by S.A. David and J.M. Vitek, Materials Park, Ohio, ASM International, 1989, pp. 71-82.

124. Z. Paley and P. Hibbert, "Computation of Temperature in Actual Weld Designs", **Welding Journal Research Supplement**, 54(11), 1975, pp. 385-392.

125. W. K. C. Johnes and P.J. Alberry, "A Model for Stress Accumulation in Steels During Welding", **Residual Stresses in Welds by Welded Construction and Their Effects**, edited by R.W. Nichols, London, UK, Nov. 1978, pp. 15-17.

126. G. W. Greenwood and R. H. Johnson, "The Deformation of Metals under Small Stresses during Phase Transformations", **Proceedings Royal Society**, A283(1394), Jan. 1965, pp. 403-422.

127. D.E. Rodgers and P.R. Fletcher, "The Determination of Internal Stresses from the Temperature History of a Butt Welded Pipe", **Welding Journal Research Supplement**, 17(4), 1938, pp. 4s-7s.

128. S. Vaidyanathan, A.F. Todaro and I. Finne, "Residual Stresses Due to Circumferential Welds", **Journal of Engineering Materials and Technology**, 95(10), 1973, pp. 233-237.

129. Z. Paley, L. Lynch and C. Adams, "Heat Flow in Welding Heavy Steel Plate", **Welding Journal Research Supplement**, 43(2), 1964, pp. 71s-79s.

130. C. M. Adams, "Cooling Rates and Peak Temperatures in Fusion Welding", **Welding Journal Research Supplement**, 37(5), 1958, pp. 210s-215s.

131. J. Goldak, M. Bibby, J. Moor, R. House and B. Patel, "Computer Modeling of Heat Flow in Welds", **Metallurgical Transactions,** 17B(9), 1986, pp. 587-600

132. Y. Veda and T. Amici, "Analysis of Thermal Elastic-Plastic Stress and Strain During Welding by Finite Element Method", **Transactions of the Japan Welding Society**, 2(2), 1971, pp. 90-100.

133. E. Wilson and R. Nickell, "Application of the Finite element Analysis to Heat Conduction Problems", **Nuclear Engineering and Design**, 13(4), 1966, pp. 276-286.

134. R. Kamichika, T. Yada and A. Okamoto, "International Stresses in Thick Plates Weld-Overlaid with Austenitic Stainless Steel (Report 2)", **Transactions of the Japan Welding Society**, 5(1), Apr. 1974.

135. H. Hibbitt and P. Marcal, **A Numerical Thermo-Mechanical Model for the Welding and Subsequent Loading of a Fabricated Structure,** Contract No. N00014-67-A-D191-0006, Brown University, 1972.

136. R. Nickell and H. Hibbitt, "Thermal and Mechanical Analysis of Welded Structures", **Nuclear Engineering and Design**, 22(3), 1975, pp. 110-120.

137. B.A. B. Andersson, "Thermal Stresses in a Submerged-Arc Welded Joint Considering Phase Transformation", **Journal of Engineering Materials and Technology**, 100(1), 1978, pp. 356-362.

138. E. Friedman, "Thermomechanical Analysis of the Welding Process Using the Finite Element Method", **Journal of Pressure Vessel Technology**, 97(8), 1975, pp. 206-213.

139. Y. Iwamura and E.F. Rybicki, "A Transient Elastic-Plastic Thermal Stress Analysis of Flame Forming", **Journal of Engineering for Industry**, 12(2), 1973, pp. 21-25

140. E.F. Rybicki, N.D. Ghadiali and D.W. Schmueser, "An Analytical Technique for Evaluating Deformations Due to Welding", **Winter Annual Meeting of AWS**, Nov. 27-Dec.2 1977, Atlanta Ga, PVP-PB-025.

141. J. H. Argyris, J. Szimmat and K.J. Willam, "Computational Aspects of Welding Stress Analysis", **Computer Methods in Applied Mechanics and Engineering**, 33(3), 1982, pp. 635-666.

142. J. Goldak, A. Oddy, M. Gu, W. Ma, A. Mashaie and E. Hughes, "Coupling Heat Transfer, Microstructure Evolution and Thermal Stress Analysis in Weld Mechanics", **Mechanical Effects of Welding (IUTAM Symposium Lulea/ Sweden 1991)**, edited by L. Karlsson, L.E. Lindgren and M. Berlin Jonsson, Germany, Springer-Verlag, 1992, pp. 1-30.

143. P. K. Tekriwal, **Three-Dimensional Transient Thermo-Elasto-Plastic Modeling of Gas Metal Arc Welding Using the Finite Element Method**, Ph.D. Dissertation, University of Illinois at Urbana-Champaign, 1989.

144. J. C. Muehlbauer and J.E. Sunderland, "Heat Conduction with Freezing or Melting", **Applied Mechanical Review**, 18(12), 1965, pp. 951-959.

145. R. H. Tien and G.E. Geiger, "A Heat-Transfer Analysis of the Solidification of a Binary Eutectic System", **Journal of Heat Transfer**, 67(8), 1967, pp. 230-234.

146. S. H. Cho and J.E. Sunderland, "Phase Change Problems with Phase Change Thermal Conductivity", **Transactions of ASME**, 96(5), 1974, pp. 214-217.

147. L.F. Carvajal and G.E. Geiger, "An Analysis of the Temperature Distribution and the Location of the Solidus, Mushy and Liquids Zones for Binary Alloys in Remelting Processes", **Metallurgical Transactions**, 2B(8), 1971, pp. 2087-2092.

148. J. Campbell, "Fluid Flow and Droplet Formation in the Electroslag Remelting

Process", **Journal of Metals**, 22(7), pp. 23-25.

149. K.P. Edwards and J. A. Spittle, "Temperature Distributions in the Slag and Metal Remelting of Aluminum Alloys", **Institute Metals Journal**, 100, 197

150. T. Debroy, J. Szekely and T.W. Eagar, "Heat Generation Patterns and Temperature Profiles in Electroslag Welding", **Metallurgical Transactions**, 11B(12), 1980, pp. 593-605.

151. A.H. Dilawari, T.W. Eager, and J. Szekely, "Electromagnetically and Thermally Driven Flow Phenomena in Electroslag Welding", **Metallurgical Transactions**, 9B(9), 1978, pp. 371-381.

152. T. Debroy, J. Szekely and T.W. Eagar, "Temperature Profiles, the Size of the Heat-Affected Zone and Dilution in Electroslag Welding", **Materials Science and Engineering**, 56, 1982, pp. 181-193.

153. **ANSYS 5.0 Engineering Analysis System**, Swanson Analysis System, Inc., 1992.

154. Z. Pammer, "A Mesh Refinement Method for Transient Heat Conduction Problems Solved by Finite Elements", **International Journal of Numerical Methods in Engineering**, 15, 1980, pp. 494-505.

155. B.G. Thomas, I.V. Samarasekera, and J.K. Bromacombe, "Comparison of Numerical Modeling Techniques for Complex, Two-Dimensional, Transient Heat-Conduction Problems", **Metallurgical Transactions**, 15B(9), 1984, pp. 307-318.

156. B. Patel, **Thermo-Elasto-Plastic Finite Element Formation for Deformation and Residual Stresses due to Welds**, Ph.D. Dissertation, Carlton University, Ottawa, Ontario, Canada, April 1985.

157. D. Radaj, **Heat Effects of Welding**, Berlin, Springer-Verlag, 1992.

158. J. Bergheau and J.B. Leblond, "Coupling between Heat Flow, Metallurgy and Stress-Strain Computations in Steel, The Approach Developed in the Computer Code SYSWELD for Welding and Quenching", **Modeling of Casting, Welding, and Advanced Solidification Processes V**, The Minerals Metals and Materials Society, Warrendale, PA, 1991.

159. SYSWELD+ Reference Manual, FRAMASOFT/CSI, Paris, France, 1998.

160. M. Gu, J.A. Goldak and E. Hughes, "Steady State Thermal Analysis of Welds with Filler Addition", **Canada Metallurgical**, 32(3), 1993, pp. 49-55.

VITA

The author was born on November 1, 1968 in Luoyang, The People's Republic of China. She received her Bachelor of Engineering degree and Master of Engineering degree in Materials Science and Engineering from Luoyang Institute of Technology in 1989 and 1992, respectively.

She worked at The 4th. Research and Design Institute until she joined the Oregon Graduate Institute of Science and Technology in Portland, Oregon, in 1995. She finished the requirements for the degree of Doctor of Philosophy in materials science and engineering in June, 1999.